



**UNIVERSITÀ  
DEGLI STUDI  
DI TRIESTE**

**UNIVERSITÀ DEGLI STUDI DI TRIESTE  
XXXV CICLO DEL DOTTORATO DI RICERCA IN**

**INGEGNERIA INDUSTRIALE E DELL'INFORMAZIONE**

**Energy management systems and optimization  
strategies for EV integration considering the economic  
and environmental aspects**

Settore scientifico-disciplinare: **ING-IND/31 ELETTROTECNICA**

**DOTTORANDO  
NICOLA BLASUTTIGH**

**COORDINATORE  
PROF. ALBERTO TESSAROLO**

**SUPERVISORE DI TESI  
PROF. THOMAS PARISINI**

**CO-SUPERVISORE DI TESI  
PROF. ALESSANDRO MASSI PAVAN**

**ANNO ACCADEMICO 2021/2022**

**Energy management systems and  
optimization strategies for EV  
integration considering the economic  
and environmental aspects**



# Energy management systems and optimization strategies for EV integration considering the economic and environmental aspects

PhD Dissertation

by

Nicola BLASUTTIGH

Master of Science in Electrical Systems Engineering, University of Trieste, Italy.

**Nicola Blasuttigh**

*Energy management systems and optimization strategies for EV integration  
considering the economic and environmental aspects*

PhD Dissertation, February 22nd, 2022

Supervisor: Prof. Thomas Parisini

Co-Supervisor: Prof. Alessandro Massi Pavan

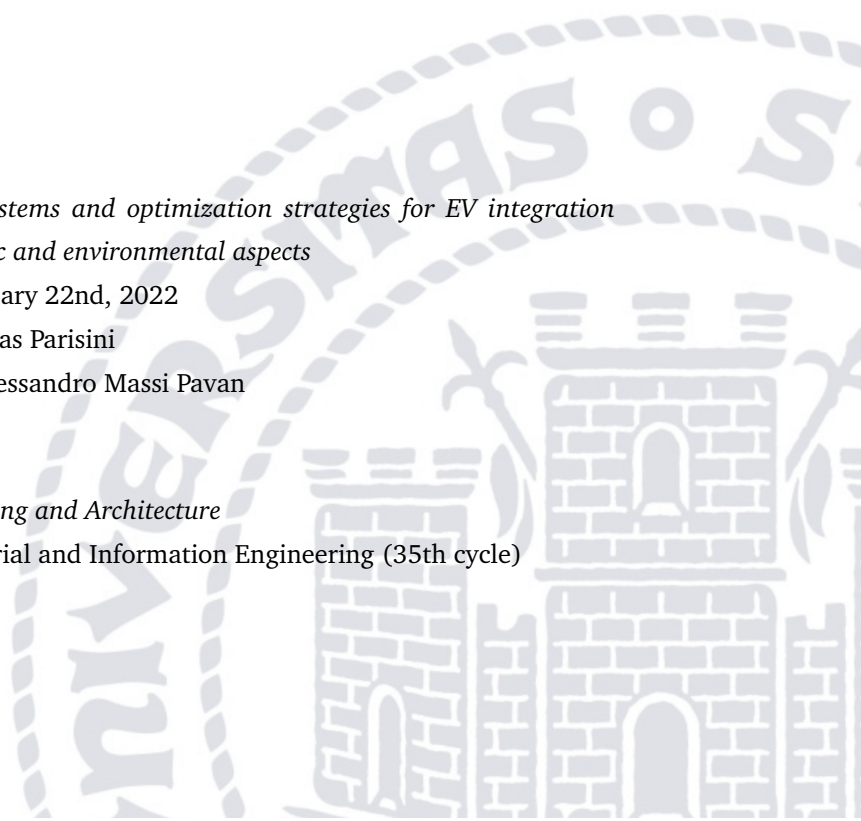
**University of Trieste**

*Department of Engineering and Architecture*

PhD Program in Industrial and Information Engineering (35th cycle)

Via Alfonso Valerio 6/1

34100 Trieste



*A Chiara e alla mia famiglia*



## ABSTRACT

Ongoing climate change is driving the need for rapid action with effective and long-term impacts. Among the major polluting sectors, energy used in buildings, industries, and transportation accounts for most of the world's greenhouse gas emissions. Electrification of these sectors is one of the optimal solutions for the decarbonization process by supporting the ongoing energy transition policies. Electricity generation from renewable sources and the exponential growth of the global electric vehicle market are the key to a sustainable future. However, despite their potential, they bear attention to their mutual integration in order to fully understand the real benefits from energy, economic and environmental perspectives. In addition, the possibility of two-way energy exchange through the advent of Vehicle-to-Grid (V2G) technology defines new opportunities for integration and support to the power grid. In the present work, optimized energy management and control for the integration of electric vehicles with the power grid and distributed renewable generation systems are studied. In the first part, the emission problem, electrification of transportation and definitions of some key concepts are introduced. Next, the integration of electric vehicles is studied from two different perspectives. The first, partially in collaboration with the Christian-Albrechts-Universität (CAU) in Kiel, focuses on aspects related to power electronics and low-level control, showing a comparison of different dual active bridge (DAB) DC-DC converter topologies, an analysis of total vehicle charging efficiency, and a simulation of an experimental V2G system for providing ancillary services. The second focuses more on the management and predictive control of energy flows for the integration of electric vehicles with microgrids, focusing on economic and environmental aspects. In particular, it shows the implementation and experimental validations of a

real-time control system for a photovoltaic charging station installed at the University of Trieste, an integrated V2G system within an Alpine ski-resort, and finally, a study related to a condominium microgrid showing the benefits related to a group of jointly acting renewables self-consumers.

## ABSTRACT (ITALIAN VERSION)

Il cambiamento climatico in atto ci spinge ad intervenire rapidamente con azioni efficaci e durature nel tempo. Tra i principali settori inquinanti, l'energia utilizzata negli edifici, nelle industrie e nei trasporti è causa della gran parte delle emissioni di gas serra a livello mondiale. L'elettrificazione di questi settori è una delle soluzioni ottimali per il processo di decarbonizzazione supportando le politiche della transizione energetica in corso. La produzione di energia elettrica da fonti rinnovabili e la crescita esponenziale del mercato dei veicoli elettrici a livello mondiale sono la chiave per un futuro sostenibile. Tuttavia, nonostante il loro potenziale, portano l'attenzione sulla loro reciproca integrazione al fine di comprendere a fondo i reali vantaggi dal punto di vista energetico, economico ed ambientale. Inoltre, la possibilità di scambio energetico bidirezionale grazie all'avvento della tecnologia Vehicle-to-Grid (V2G) definisce nuove opportunità di integrazione e supporto alla rete elettrica. In questo lavoro, vengono studiate la gestione energetica e il controllo ottimizzato per l'integrazione dei veicoli elettrici con la rete elettrica e i sistemi di generazione rinnovabile distribuita. Nella prima parte viene introdotto il problema delle emissioni, l'elettrificazione dei trasporti e le definizioni di alcuni concetti chiave. Successivamente, l'integrazione dei veicoli elettrici viene studiata da due diversi punti di vista. Il primo, in parte in collaborazione con la Christian-Albrechts-Universität (CAU) a Kiel, si focalizza su aspetti legati all'elettronica di potenza e al controllo di basso livello, mostrando un confronto tra diverse topologie di convertitori DC-DC dual active bridge (DAB), un'analisi sull'efficienza totale di ricarica del veicolo e la simulazione di un sistema V2G sperimentale per la fornitura di servizi ancillari. Il secondo invece si concentra maggiormente sulla gestione ed il controllo predittivo dei flussi energetici per l'integrazione dei veicoli

elettrici con microreti, focalizzando l'attenzione su aspetti economici ed ambientali. In particolare, viene mostrata l'implementazione e la validazione sperimentale di un sistema di controllo real-time per una stazione di ricarica fotovoltaica installata presso l'Università di Trieste, un sistema V2G integrato all'interno di uno ski-resort Alpino ed infine, uno studio relativo ad una microrete condominiale che mostra i vantaggi legati ad un gruppo di autoconsumatori che agiscono collettivamente.

# CONTENTS

<b>1</b>	<b>Introduction</b>	<b>1</b>
<b>2</b>	<b>Electric vehicle technologies and their integration</b>	<b>5</b>
2.1	Greenhouse gas emissions: a matter of energy . . . . .	5
2.2	Growth in electrification of transport . . . . .	9
2.3	Electric mobility: more than just driving . . . . .	12
2.4	Energy management solutions . . . . .	14
<b>3</b>	<b>A low-level approach to EV integration</b>	<b>21</b>
3.1	Introduction . . . . .	21
3.2	A comparative study of single-phase and three-phase DAB topology . . . . .	22
3.2.1	Motivations . . . . .	22
3.2.2	Related literature . . . . .	23
3.2.3	Single-Phase and Three-Phase DAB Comparison .	24
3.3	Efficiency Trade-off-Oriented Analysis in V2G Applications	35
3.3.1	Motivations . . . . .	36
3.3.2	Related literature . . . . .	36
3.3.3	DAB and Battery Losses Analysis . . . . .	37
3.3.4	Efficiency trade-off analysis . . . . .	45
3.3.5	Experimental Validation . . . . .	46
3.4	Optimal Charging Strategy . . . . .	48
3.4.1	Efficiency comparison . . . . .	48
3.4.2	$\eta_{max}$ -Charging Strategy Implementation . . . . .	49
3.5	Design and simulation of V2G system . . . . .	55
3.5.1	Motivations . . . . .	55
3.5.2	Related literature . . . . .	56
3.5.3	Experimental V2G apparatus . . . . .	57

3.5.4	Control system . . . . .	58
3.5.5	Simulation results . . . . .	65
3.6	Discussion . . . . .	69
<b>4</b>	<b>EMS for EV integration: applications and case studies</b>	<b>73</b>
4.1	Introduction . . . . .	73
4.2	A real-time EMS of a PV-based EV charging station accounting for uncertainties . . . . .	74
4.2.1	Motivations . . . . .	74
4.2.2	Related literature . . . . .	75
4.2.3	Description of the charging station . . . . .	78
4.2.4	Modeling and problem formulation . . . . .	79
4.2.5	Real time control using eMPC . . . . .	85
4.2.6	Experimental validation . . . . .	94
4.2.7	Discussion . . . . .	100
4.3	Vehicle-to-Ski: a V2G optimization-based cost and environmental analysis for a ski resort . . . . .	103
4.3.1	Motivations . . . . .	103
4.3.2	Related literature . . . . .	103
4.3.3	System description . . . . .	105
4.3.4	Problem formulation and EMS implementation . . . . .	115
4.3.5	EV-CS growth model . . . . .	120
4.3.6	Results and discussions . . . . .	123
4.3.7	Sensitivity analysis . . . . .	129
4.3.8	Discussion of simulation result . . . . .	131
4.4	A MPC-based control with ANN-based forecasters for jointly acting self-consumers . . . . .	133
4.4.1	Motivations . . . . .	133
4.4.2	Related literature . . . . .	134
4.4.3	JARSC system description . . . . .	136
4.4.4	System modelling and control design . . . . .	144
4.4.5	System simulation and results . . . . .	156
4.4.6	Discussion of simulation result . . . . .	170
4.5	Discussion . . . . .	172
<b>5</b>	<b>Conclusions</b>	<b>175</b>

<b>References</b>	<b>179</b>
<b>About the author</b>	<b>219</b>
<b>List of Publications</b>	<b>221</b>
<b>Acknowledgements</b>	<b>223</b>



## INTRODUCTION

Interest in renewable generation and decarbonization of energy systems is of paramount importance in reducing the effects of ongoing climate change. There are several solutions that can be implemented with the aim of countering the increase in greenhouse gas emissions. One of these is the electrification of transportation sector, whose current burden in terms of emissions is considerable. However, the sector accounts for the least contribution to the use of renewable energy which integration would lead to lower electricity purchase costs and increases power grid independence. For these reasons, the introduction of electric vehicles has opened up new avenues in the research field for this technology. In order to better manage the integration with the renewable energy production systems and to reduce the losses during their connection, it is necessary to develop intelligent components and control systems that allow both to increase their efficiency and to optimally manage energy flows while taking into account economic and environmental aspects. Moreover, recent technologies allow not only the mere vehicle charging but also the use of the energy stored within the vehicle battery as a real storage system that, when connected to the power grid, can be used as an energy generator to power local loads or provide the so-called ancillary services to the public grid by vehicle-to-grid (V2G) technology. In order to understand the best way to manage energy flows within the grid, it is necessary to study the problem vertically and holistically. Based on the above, we can pose the following questions that motivated the study of the following work:

- (Q1) In which ways can electric vehicles be integrated into the current electric system and what are the challenges to be considered?

(Q2) Which energy management strategies can be exploit and which objectives can be achieved in systems that integrate electric vehicles?

With the aim of answering these questions, this work presents the study and experimental implementation of energy control and management strategies for integrating electric vehicles with the power grid. Experimental validations of this work have been developed at the University of Trieste and at the Christian-Albrechts-Universität (CAU) in Kiel, leading to outcomes that resulted in several research publications.

The structure of this work is organized as follow.

In Chapter 2, a general discussion on global emissions, solar energy and transport electrification is proposed. Then, a literature review on EV integration with renewable energy is analysed through the definition of several concepts such as vehicle-to-grid, nanogrids, and energy management systems (EMSs).

In Chapter 3, the first goal is to study the integration of electric vehicles from the bottom level. First, the typical charging configuration of an electric vehicle with one type of DC-DC converter (DAB) is introduced, comparing two different topologies from the perspective of electrical performance and issues. Taking advantage of the interfacing of the converter and the vehicle battery, the efficiency of the overall system during its operation is studied, comparing different charging strategies in vehicle-to-grid (V2G) applications, and a new charging strategy that always operates at maximum efficiency is implemented. Finally, the design and simulation of a V2G system is examined in order to provide support to the electric grid through active and reactive power exchange.

In Chapter 4, the second goal aims to study the high-level problem of managing energy flows within the grid to which the vehicle is connected by taking into consideration photovoltaic generation, dedicated storage systems and user constraints. To this end, an MPC-based real-time energy management system that takes into account uncertainties on charging station variables is proposed and experimental results of its application on the "Photovoltaic-based charging station" installed at the University of Trieste are provided. Then, a V2G system is proposed in order to minimize the cost and environmental impact in an Alpine ski-

resort, studying different future scenarios based on a model of electric vehicle growth in future years. Finally, given recent developments on renewable energy communities, the implementation of an MPC controller along with an artificial neural network (ANN) predictor in a group of jointly acting renewables self-consumers (JARSCs) is studied by examining the results from economic, energy and environmental perspectives.

In the last chapter, a general discussion on the results obtained is presented and conclusions are drawn.



## ELECTRIC VEHICLE TECHNOLOGIES AND THEIR INTEGRATION

Global climate change is today's problem. Increased human emissions of greenhouse gases are altering the Earth's climate, which is already having a significant impact on the environment. The solutions are there but as a first step it is essential to know the problem in order to understand how to fight it. In this context, it is appropriate if not imperative to understand which sectors pollute the most, what is the potential for improvement, and how we can use this information to develop new strategies and solutions to at least mitigate the issue to help the environment and our lives.

### 2.1 GREENHOUSE GAS EMISSIONS: A MATTER OF ENERGY

The contribution of estimated greenhouse gas emissions of various economic sectors for 2019 is shown in Figure 2.1 when global greenhouse gas emissions were 59 billion tons of  $CO_2eq$  [1]. Two counting methods are used to distinguish between estimated emissions. Direct emissions, which include emissions from owned or controlled sources, and indirect emissions, where emissions associated with electricity and heat generation are reallocated to the sectors where this energy is consumed [2]. From the left-side stacked bar, it is quite easy to note that the energy sector, which includes electricity & heat and other energy, is where most of the emissions come from (almost 33% of the total). This is composed of several subcategories such as energy for industry (43%), energy for buildings (46.9%) (both commercial and residential), energy for transportation (1.6%) and other energy systems (8.5%). Most energy systems emissions are associated with the power sector, i.e. coal, gas and other plants that produce electricity and heat. The remain

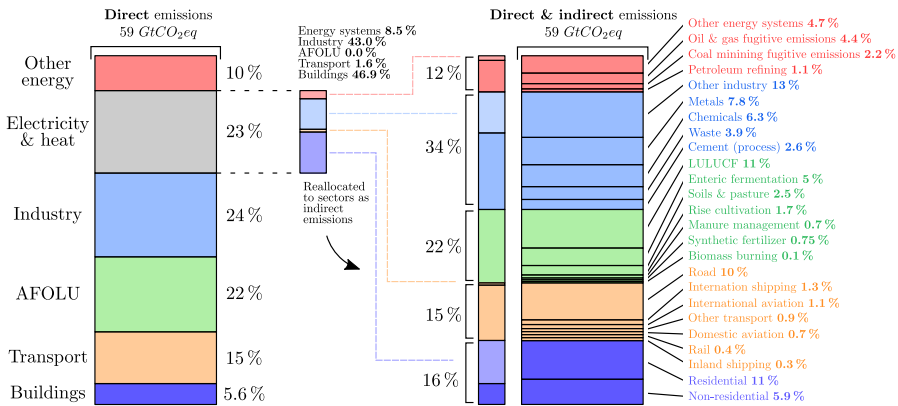


**Figure 2.1:** Direct versus indirect global GHG emissions. The stacked bar on the left shows total global GHG in 2019, split by sectors based on direct emissions accounting. The reallocation of electricity and heat sector increases the contribution to global emissions from the industry and building sector. The stacked bar on the far right indicates the shares of subsectors in GHG when indirect emissions are included. Percentages may not add up to 100 across categories due to rounding at the second significant digit

emissions belong to industry (24%), the agriculture, forestry and other land uses (AFOLU) sector (about 22%), transport (15%), and buildings (5.6%).

The electricity & heat subsector can be reallocated to consuming sectors as indirect emissions, thus highlighting the importance of energy demand as a driver of global climate change. Reallocation of indirect emissions is particularly important for the buildings and industry sectors, where some of the energy consumed is produced on-site (e.g., in gas-fired boilers), but a good portion also comes upstream from power plants through electricity consumption. From this perspective, the relative importance of the industry and buildings sectors jump dramatically, from 24% to 34%, and 5.6% to 16%, respectively.

For the decarbonization process to be effective, it is not possible to focus only on certain sectors but rather a synergistic approach is needed from all sides: therefore, the solution is certainly not unique. Relative to the energy in the industrial sector, the metals (iron and steel) production is of particular impact. Its decarbonization is made difficult by the persistent global demand for steel and the limitations on techno-economic options for making the sector low-emission [3]. De-

spite this difficulty, several studies develop innovative energy modeling and control methods for the main players in steelmaking, electric arc furnaces (EAF). Solutions to mitigate emissions in this sector range from energy recovery, optimization of the melting process, and control of the furnace through power supply based on electronic converters rather than transformers [4–8]. Moreover, leading industries are developing test facilities to reduce emissions through renewable energy [9]. The category related to *other industry* also has a significant impact. These emissions come from the paper and pulp sector, food and tobacco processing, industrial sources of fluorinated gases, and other generic industries.

The AFOLU sector and its emissions impacts are closely tied to global supply chains. A variety of land-based carbon fluxes make up these emissions, including: (a) deforestation (e.g. the clearing of natural vegetation for agricultural purposes); (b) transformations between croplands and pasture; (c) peat drainage and burning; (d) wood harvesting; (e) the regrowth of forest and other natural vegetation after agricultural abandonment and harvest; and (f) soil  $CO_2$  flux due to grassland and cropland management [2].

Regarding the energy sector, we find the emissions related to the energy for buildings. This is divided in non-residential and residential with an impact of 5.9% and 11%, respectively. Also in this area, research is advancing dramatically by seeking effective solutions to consumption reduction and optimization in both design and operational phases for both electrical and thermal sources. In [10, 11], a study of possible decarbonization scenarios for the U.S. residential sector is proposed. The results show that electrification of residential consumption would lead to a drastic reduction in emissions following, however, a drastic refurbishment of current homes and a simultaneous decarbonization of electricity generation. Among different solutions, a techno-economic comparison on different technologies for decarbonization in residential buildings is proposed in [12]. Here again, the importance of electrification and the use of renewable energy is shown, but it is emphasized that the structure of the power grid will need significant funding and incentives will be required for switching to low-carbon technologies.

In the non-residential field, however, the progress in decarbonization of commercial buildings over the past 20 years is analyzed in [13] by showing that the emission trend is continuously decreasing due to the decarbonization strategies implemented. Increased renewable energy generation (especially building-integrated), increased building efficiency, and reduced energy losses [14] will be required for further decarbonization and the realization of carbon neutrality. In [15] several commercial building electrification strategies are analyzed where the great potential of this approach in saving energy and reducing emissions is shown. However, the key issue falls on supporting decarbonization policies such as incentives and taxes on emitted carbon.

In recent years, these sectors have driven a turnaround regarding electricity generation due to the strong increase in photovoltaic power generation. Photovoltaic power generation grew by a record value of 179 TWh in 2021, increasing by 22% over 2020, and remaining the third largest renewable technology behind hydro and wind. These results, however, can be attributed to three different types of plants. Specifically, out of the total 2021 growth over 2020, utility-scale plants are responsible for 52% of the 2021 growth, followed by residential (29%) and commercial-industrial (19%).

Figure 2.2 shows the global installed PV capacity from 2010 to 2021 highlighting the share in different sectors. All these have experienced less and less growth on average during the entire period. However, in recent years, the residential sector has been growing again thanks to sustainability and incentive policies to counter the energy crisis and speed up the energy transition. More specifically, the PV residential growth in 2019, 2020 and 2021 was 29%, 38% and 40%, respectively. However, by 2030 two to four times the current value is expected to be installed to reduce carbon emissions depending on uncertainty regarding future decarbonization scenarios [16]. Thus, further growth is also expected in the other two sectors.

This development has led to two important changes. The first is related to the radical change in the management of electricity in different countries, which now has to take into account the variability of the power produced by non-controllable sources (photovoltaics and wind power). The second is related to the type of production, no longer

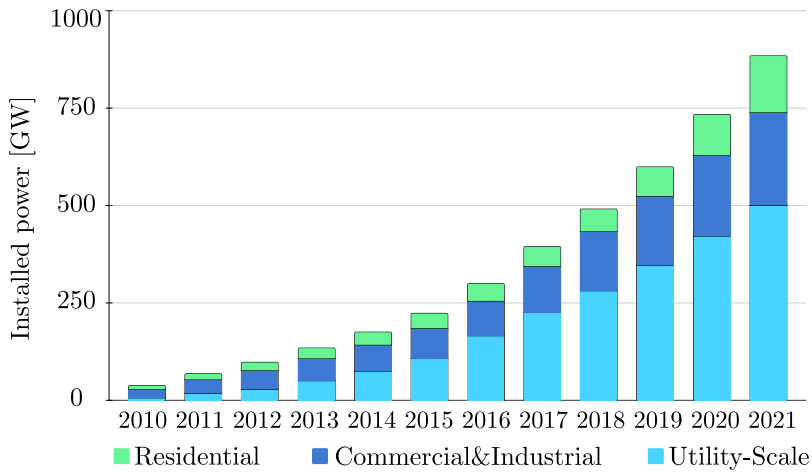


**Figure 2.2:** Photovoltaic power capacity for each sector from 2010 to 2021.

localized to only large generating plants but now distributed over the country by many plants of different sizes.

In conclusion of the analysis of polluting sectors, the transport sector impacts almost as much as the entire building sector. Road transport has the highest percentage of emissions (10%), followed by the aviation (domestic and international) (0.7% and 1.1%), international and inland shipping (1.3% and 0.3%), and to an almost negligible extent the rail transport (0.4%). Focusing on the road transport sector, almost 60% can be attributed to passenger transport and the remainder to freight transport [17]. It can therefore be understood that assuming total electrification of transport alone there is a large margin for reduction. For these reasons, the European Commission has stated a goal of reducing greenhouse gas emissions from transport by 20% before 2030 compared to 2008 and 60% before 2050 compared to 1990 [18]. Accelerating the use of low-emission alternative energy for transportation, especially electricity, and removing barriers to the electrification of transportation are two key components of this approach.

## 2.2 GROWTH IN ELECTRIFICATION OF TRANSPORT

The opportunity for electrification of the transportation sector appears to be the one with greater possibilities than the actions available in the building or industrial sectors [19], although action can be taken

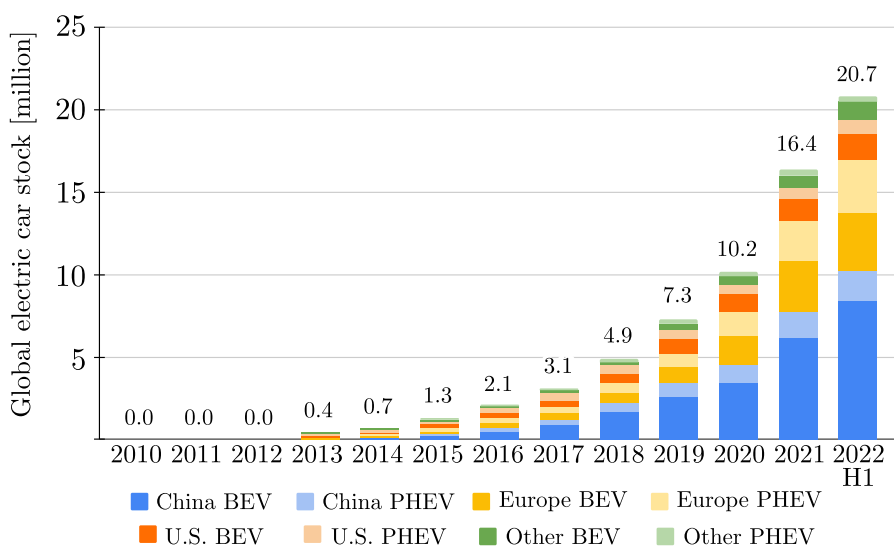
on multiple fronts in the three emission categories. For this reason, many governments have encouraged the adoption of electric vehicles through incentives and subsidies. However, decarbonization of electricity generation plays a key role in combination with electric vehicle deployment. Indeed, there is a fine balance between the emissions saved by vehicles and those generated through conventional electric generation for their electrification [20]. Nevertheless, the electrification of transportation faces several technical, social, and economic barriers to its growth. These can be vehicle cost, driving range, medium to long charging times, and lack of adequate charging infrastructure. Of these, the last is the most important for those considering switching to electric [21]. Despite these factors, electric mobility is growing steadily [22]. While this expansion is promising for the decarbonization of the sector, worries about the potential consequences, such as those related to mined mining materials, are raising [23–26]. There are different types of vehicles that can be electrified which fall into two main categories: light duty vehicles (LDV) such as car, and heavy duty vehicles (HDV) such as trucks and buses.

Figure 2.3 shows the global light-duty EV stock in China, Europe, United States and other countries<sup>1</sup> from 2010 to 2022 H1 (first half). As can be seen, the growth is significant year on year, especially in 2021 where a decrease was expected due to the Covid-19 pandemic. Sales of electric cars, including battery electric vehicles (BEVs) and plug-in hybrid electric vehicles (PHEVs), increased in 2020 despite a weak automotive industry, and they increased again to 16.4 million in 2021 with 7.8 million of those sales occurring in China and 5.5 million in Europe. A total of 4.3 million new BEVs and PHEVs were delivered during the first half of 2022, an increase of +62% compared to 2021 H1. Thus, more than 20.5 million electric cars are now on the road, two times as many in just two years. By the end of 2022, a total number of nearly 25 million EVs in operation are expected.

This trend is mainly due to the acceleration to policies and incentives from all major countries. China is the fastest growing because of

---

<sup>1</sup>Other includes Australia, Brazil, Canada, Chile, India, Japan, Korea, Malaysia, Mexico, New Zealand, South Africa and Thailand. Europe includes the EU27, Norway, Iceland, Switzerland and United Kingdom.



**Figure 2.3:** Global electric car stock, 2010-2021

government efforts to accelerate decarbonization by extending subsidies for electric car purchases for two more years due to the pandemic. Europe is also taking action in this context by growing sales by 65% in 2021. Among all countries, Norway has the largest share of electric car sales (86%) followed by other northern countries such as Iceland (72%), Sweden (43%), Netherlands (30%) and Germany (26%). In Italy, in 2021 electric cars had an annual market share equal to 9.3%, steadily growing although at lower growth rates compared with the neighboring countries such as Austria (20%), Switzerland (13%), France (19%) or Germany (26%) [27].

Regarding the HDV category, the number of 2021 registrations grew in all three world regions. In particular, more growth was noted in the sale of electric buses than trucks. So far, only 4% of the global bus fleet is electric and only 0.1% of the truck fleet. China still dominates the economics of the heavy-duty electric sector for both buses and trucks. In Europe, sales of electric buses can be attributed to municipal or regional policies for zero-impact projects. Different powertrain technologies have been developed for this sectors. In [28] a comprehensive analysis of the HDV powertrain technologies' operation, performance indicators, and most recent advancements is discussed where it is shown that electric and hydrogen technology will develop slowly by removing

barriers such as cost and infrastructure. The potential of HDV transport electrification for a case study in Switzerland is analyzed in [29], taking into account network capacity, weight constraints and the possibility of using battery swapping stations.

### 2.3 ELECTRIC MOBILITY: MORE THAN JUST DRIVING

The electric mobility is set to play an important role in achieving the European commission's goals for three reasons. The first concerns the inherent efficiency of electric powertrains which are significantly more energy efficient than conventional ones. Second, the energy for charging can directly use energy from renewable sources available for transportation and thus easily interface with current residential and non-residential technologies. Third, the connection of vehicles to the power grid allows its stabilization through the batteries of electric vehicles through a bidirectional connection [30]. In fact, we are used to thinking that an electric vehicle can only charge through the grid for the purpose of driving. However, we forget that when connected to the grid, the vehicle has a high-capacity battery that could be harnessed for purposes other than driving through bidirectional functionality.

This concept is named Vehicle-to-Anything (V2X), a term that explains the use of the electric vehicle battery to provide energy services and derive additional value from the battery asset during times of non-use [31]. There are several technologies for this purpose, which differ depending on the type of interface that is established with the vehicle. The most attractive are vehicle-to-home (V2H), vehicle-to-vehicle (V2V) and vehicle-to-grid (V2G) [32–36].

With the mentioned technologies, the vehicle becomes bidirectionally controllable and thus can be leveraged to achieve certain purposes and benefits. For example, the owner of an EV might decide to discharge it toward household loads during the highest tariffs periods during the day to minimize the total cost or might decide to maximize self-consumption in the case of integration with a residential PV system. Looking at it more widely, vehicles parked in a large parking lot could be seen as one large aggregate storage system to provide services in support to the grid.

The V2H concept shows that a vehicle can be connected to a home grid for charging or discharging and thus can provide power to small household loads and integrate with small-scale distributed generation systems. In [37], the usage of V2H is studied to evaluate the self-consumption improvements in a PV-based residential scenario by comparing optimization and rule-based algorithm. In [38] an energy optimization strategy considering renewable energy generation, energy storage and an electric vehicle is studied to optimally handle costs and user constraints. A combined V2H and vehicle-to-building (V2B) strategy is analysed in [39] where results show that peak power, energy costs and greenhouse gases emissions are reduced. An optimal EV battery management considering a residential scenario with PV plant, household loads and both thermal and cooling system is consider in [40] by using a Monte Carlo approach to evaluate different EV driving patterns. From a lower level of control, in [41, 42] other advantages and operation modes of V2H are studied by using electric vehicles as uninterruptible power supply (UPS) by protecting home appliances from power grid outages.

The V2V concept, on the other hand, exploits the possibility of sharing energy between vehicles within a local energy community. By doing so, it is possible to keep energy within the local power grid without requiring energy from the local public grid. A fair number of papers can be found on the subject. In [43] the V2V concept is exploited in a local PV-BESS charging station between donor and acceptor EV clients in order to reduce the load on the public grid and optimize recharging costs. In [44] the V2V concept is exploited on a larger scale to develop an energy exchange market to decrease costs and impact on the public grid. An holistic energy management system is proposed in [45] for a V2V energy sharing strategy by considering user satisfaction, social welfare and costs.

In contrast, the concept of V2G refers to the integration of electric vehicles with the public grid for the purpose of providing support services through a large number of connected vehicles. These services are called "ancillary services" and can be requested by the grid operator itself [46]. Some examples may be active and reactive power exchange, frequency and voltage regulation, harmonic suppression or simply peak-shaving

and load-leveling. Several works can be found on this concept with different applications like energy management systems for cost optimization [47–50], peak shaving [51–55], reactive power compensation [56–58], frequency regulation [59–64] and  $CO_2$  minimization [65].

In most of these works, a key aspect related to the battery utilization of the vehicle itself arises. In fact, from a techno-economic point of view it must be taken into account that even if on the one hand the vehicle is available in providing different types of services, on the other hand it must be considered how much the battery degradation affects the useful life of the vehicle. Thus, it is useful to find a trade-off between benefits and degradation. Different battery degradation models with several approaches are studied in literature [66–70]. These patterns are then leveraged in V2X strategies to minimize battery degradation while still optimizing the user's needs and constraints, and the services to the grid [71–77].

When referring to the *grid*, it does not always refer to the public grid but rather to any portion of the electrical system to which the user is connected. In fact, as we have seen, the different technologies that belong to V2X also differ in the scale of the system. Starting with the concept of V2H, it was possible to characterize the smallest scale of the vehicle-to-grid interaction system in the residential sector.

## 2.4 ENERGY MANAGEMENT SOLUTIONS

The use of renewable resources and distributed generation are now fundamental parts of the electricity system. The policies of many countries promote the installation of renewable distributed generation systems in order to speed up the ongoing energy transition as well as energy storage units to increase their independence from the public power grid. In the period in which we are living, driven by a strong political unrest and energy crisis that steers the strong variability of prices, the installation of a PV system becomes an attractive cost-saving alternative for many consumers. The installation of these systems, the use of energy storage facilities, and the integration with different types of loads such as electric vehicles has driven a new concept of the electricity grid formed by many small-scale local generation networks exchanging power and information. The use of these approaches has

rapidly led to the definition of a new structure of innovative grids called nanogrids.

A nanogrid is defined as a power distribution system for a single house-small building, with the ability to connect or disconnect from other power entities via a "gateway." It consists of local power production powering local loads, with the option of utilizing energy storage and/or a control system [78]. In this case, the "gateway" defines a two-way power connection to an electrical entity external to the nanogrid such as another nanogrid or the public grid. This gateway may include a communication line for information exchange. Differently, when several nanogrids are connected together they are referred to as microgrids and this defines a clear boundary between the definitions.

However, it is possible to combine these two entities under one cap if we consider that both allow the control of internal energy flows and, if any, the control of the storage system. The possible control actions on these flows present an important opportunity in a great number of aspects related to the economic, environmental and service side towards other connected electric entities [79].

For this purpose, it is therefore necessary to implement an energy management strategy that autonomously decides on the exchange of energy flows while meeting the constraints and uncertainties of the system. To solve this problem, we can rely on so-called energy management systems (EMS), tools used to monitor, control, and optimize the performance of an energy system. EMSs can be classified in different classes based on the control methods used [80–82]. A common classification divides EMSs in two major classes, rule-based (RB) control and optimization-based (OB) control. The former is based on rules dictated by human experience, engineering knowledge, or intuition that can be implemented through different approaches. The second, on the other hand, is based on analytical or numerical operations capable of minimizing a given cost function through future knowledge of given energy flows. We therefore understand that appropriate estimation or prediction of the production or load of the power grid can lead to performance improvements because it is possible to act in advance on

the evolution of the system. Several papers related to EMS classification, methods and control system can be found in [79, 81, 83–85].

Regarding the forecasting aspect, the natural fluctuation and uncertainty of the variables related to an electrical network are two major problems to overcome in order to optimally manage the entire system. Forecasting strategies to handle the stochastic nature of renewables and the fluctuating energy demand of connected loads are emerging as enabling technologies for future systems, with special regard to household and residential applications. Furthermore, it is also necessary to predict economic variables such as the price of buying or selling electricity. With the integration of rooftop solar PV along with BESS and EV, an economic and efficient operation of the whole system becomes extremely challenging, as suitable prediction of energy demand and availability is needed. It is therefore clear that EMS performance is tied to the accuracy of predictions.

From an energetic point of view, the variables that most need to be predicted are the power generated by the renewable system and the electricity consumption during the day. These in fact are the two main variables that govern the exchange of energy with the storage system and/or the power grid.

Photovoltaic power forecasting in the literature can be classified based on different aspects such as forecast horizon (short, medium and long-term), historical data and forecasting methods [86, 87]. Different forecasting methods such as physical, heuristic, statistical and machine learning are commonly used in PV power forecasting. These can be broadly classified based on two macro approaches: physical and data-driven approach. The physical approach requires prior knowledge of PV material properties and the metadata of a PV system, together with the need of weather data such as temperature, wind velocity, irradiance, etc.. [88]. The data-driven approach needs operational data to train/calibrate the model coefficients, which then generates the predictions. As a result, a data-driven method can only be used if a specific PV module or system has been exposed and sufficient data has been gathered to train and calibrate the models.

Physical models calculate the PV power using the equivalent electrical circuits. A considerable amount of works can be found in the literature regarding the estimation of model parameters [89–92] and their performance comparison [93–96]. Data-driven methods can be classified in heuristic methods, statistical methods and machine learning methods. The accuracy of the historical data is perhaps the most crucial component of such a forecasting approach. Among them, machine-learning methods are the most studied in recent years because of their accuracy, reliability and non-linear modeling. Artificial neural networks (ANN), long short-term memories (LSTM), random forests (RF) and other well-liked forecasting models are frequently employed in solar power applications as shown in [97]. The most fundamental machine learning architecture is an ANN. Similar to the neurons in the real brain, a group of connected artificial neurons forms the foundation of an ANN, and each connection can send signals to neighboring neurons. More details on this aspect will be further analysed in Section 4.4. Several works related to PV prediction are available in literature [98–105].

Load forecasting is the predicting of electrical power required to meet the different forecast horizons demand. For energy providers and other actors in the production, transmission, distribution, and markets for electric energy, load estimation is crucial. For this reason, accurate models for electric power load forecasting are necessary to optimally manage the operation of any electrical systems. Forecasting methods for load consumption are the same already mentioned for the photovoltaic production forecast. However, the complex nature of loads makes the forecasting process a demanding task. First, because the load series is complex and exhibits several levels of seasonality. Secondly, because there are many important exogenous variables that must be considered, specially weather related variables [106]. Some load consumption forecasting with different approaches and methods can be found in [107–110].

From an economic point of view, electricity price prediction can also be advantageous so as to minimize the total cost of purchase and maximize gains from possible sale. At the market level, price prediction is an important factor for electricity market participants because it influences decisions about power plant operations. As we can expect,

**Table 2.1:** Life cycle  $CO_2$  emission factors [gCO<sub>2</sub>eq/kWh] from electricity production technologies according to IPCC 2014 [117].

Production type	Min.	Median	Max.
Coal	740	820	910
Gas – combined cycle	410	490	650
Biomass	130	230	420
Solar PV – Utility scale	18	48	180
Solar PV – rooftop	26	41	60
Geothermal	6.0	38	79
Concentrated solar power	8.8	27	63
Hydropower	1.0	24	2200 <sup>2</sup>
Ocean (Tidal and wave)	5.6	17	28
Wind Offshore	8.0	12	35
Nuclear	3.7	12	110
Wind Onshore	7.0	11	56

non-stationarity, non-linearity and high volatility are constant characteristics that are highly dependent on production and consumption. Several papers on electricity price forecasting can be found in [111–116].

Going back to the discussion in Section 2.1, electrification of consumption is one of the main strategies to start a decisive decarbonization process. However, the electricity grid must also play its role by lowering the amount of  $CO_2$  emitted due to electricity production. Every country in the world produces electricity based on the availability of different energy sources and based on technical and economic constraints. For example, during a sunny day, photovoltaic production will increase and there will be a proportional decrease in another type of production so as to balance consumption and exports. As a result,  $CO_2$  emissions from electricity production are strongly dependent on source types and total consumption. Each type of production is thus characterized by a certain amount of  $CO_2$  emitted for each ton of fuel consumed or, more easily, for each unit of energy produced.

Table 2.1 shows the so-called *emission factors* that give an indication of the environmental impact for electricity production for each source.

<sup>2</sup>Dams affect the natural carbon cycle in freshwater ecosystems through floods of terrestrial vegetation and soils. The flooded organic matter decomposes causing additional GHG emissions, especially in the first years after the reservoir creation.

As can be seen, electricity production from fossil fuels has very high emission values compared to renewables. Note that these, although they do not emit any emissions during operation, contribute even if marginally through the processes of materials manufacturing, construction, operation and maintenance, and decommissioning in a life-cycle-assessment (LCA) approach [120].

Through a simple weighted-average calculation, it is possible to obtain an average value of  $CO_2$  emissions for each kWh of electricity produced, typically called *carbon intensity* defined as [121]:

$$CI_{avg} = \frac{\sum(E_i \cdot CR_i)}{\sum E_i} \quad (2.1)$$

where  $E_i$  is the electricity generated (kWh) by a source  $i$  and  $CR_i$  is the carbon-emission rate (or  $CO_2$  emission factor) (g/kWh) for that source. In this regard, numerous projects for determining and calculating carbon intensity were born in recent years [122–125].

In Italy, the share of electricity that comes from renewable energy is close to 40%, but the rest comes from other fuels such as biomass, coal, natural gas, oil, and hard coal that cause higher  $CO_2$  emissions [126]. The carbon intensity profile for the northern Italian electricity market zone (ITA-NORD) of 2019-2020 is shown in Fig. 2.4. Besides the high frequency daily variations that mainly depend on the variability of renewable energy sources, it is possible to clearly notice a slower trend caused by many other factors including energy demand. In particular, a rapid decrease in  $CO_2$  emissions can be seen just after mid-December 2019 before growing again in early 2020. This behavior is due to an abnormal increase in seasonal temperatures with unusually sunny days that have led to a drastic reduction in electricity demand and consequently in energy production from fossil fuel sources which have the highest emission factors among all the production types. This confirms the relevance of multiple factors (i.e. temperature, solar radiation, pandemics, etc..) that jointly influence the optimal management of any energy system.

---

Flooding can also increase sedimentation and decomposition in the reservoir, due to longer water residence times, which can lead to higher GHG emissions. [118, 119].

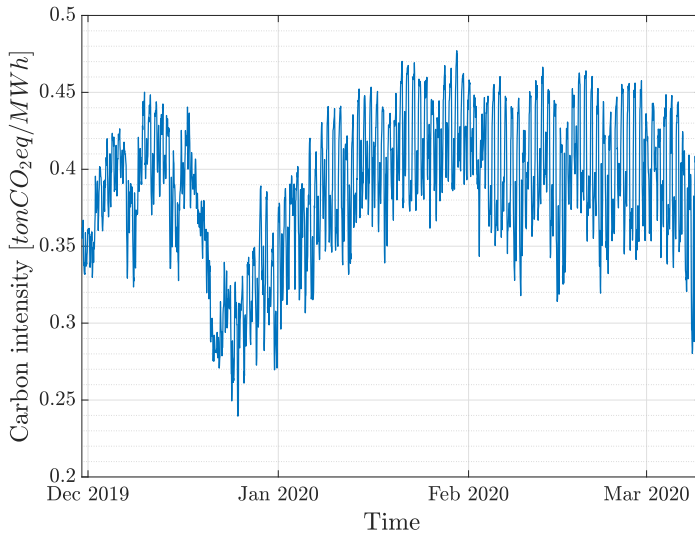


**Figure 2.4:** Carbon intensity variation during 2019-2020 for the IT-NO electrical sector with 1h resolution

A fair amount of papers regarding the calculation of emission factors, carbon intensity, and its prediction can be found in the literature [127–132].

## A LOW-LEVEL APPROACH TO EV INTEGRATION

### 3.1 INTRODUCTION

The integration of electric vehicles with the current distribution system needs to start from the bottom level, studying possible charging configurations from the power electronics point of view to achieve optimum efficiency and operation performance.

In the following sections, three different studies related to the integration between dual-active bridge (DAB) converters, batteries and the power grid are shown.

In Section 3.2, a study on two different topologies of DAB, single-phase and three-phase, is introduced, comparing the two converters from the point of view of losses, current stresses and filter sizing [133].

In Section 3.3, the efficiency aspect is taken to the next level by also including the vehicle's internal battery losses. A study is presented showing the total efficiency of the system consisting of DAB converter and battery and the existence of an optimal charging trajectory to minimize losses [134]. Furthermore, based on this, in Section 3.4 a real-time controller is proposed for tracking the maximum system efficiency during the charging process [135]. The experimental validations performed at the Christian-Albrechts-Universität in Kiel in collaboration with the University of Trieste are shown and analysed.

Finally, Section 3.5 describes the V2G system under development at the University of Trieste along with a PLECS-simulated model of its operation in order to provide V2G services [136].

## 3.2 A COMPARATIVE STUDY OF SINGLE-PHASE AND THREE-PHASE DAB TOPOLOGY

Bidirectional converters enable vehicle-to-grid (V2G) operations in electric vehicle (EV) charging stations. In this context, dual-active bridge (DAB) DC-DC converter is a preferable solution due to galvanic isolation and reduced volumes compared to other systems. Single-phase DAB (1ph-DAB) and three-phase DAB (3ph-DAB) topologies are usually compared in terms of efficiency and performances with the same rated power. Conversely, this study focus on a comparison concerning device losses and stresses, medium-frequency transformer (MFT) design and capacitor filter sizing for the same power per phase, considering DABs and batteries coupled in a V2G application. Thereby, the impact of the battery state-of-charge (SoC) variation relative to the grid-side DC voltage is studied. The 1ph-DAB consists of two identical primary and secondary side full-bridges connected together by a high frequency single-phase transformer. The 3ph-DAB consists of two identical primary and secondary side three-phase half-bridge converters connected together by a high frequency three-phase transformer. Theoretical analysis and simulations results reveal that, in some respects, 1ph-DAB performance is superior to that of the 3ph-DAB with the proposed comparison approach. While, the main advantage of 3ph-DAB over 1ph-DAB is the reduced size of filter capacitors.

### 3.2.1 MOTIVATIONS

Gas emissions restrictions and increasing air pollution suggest that other transportation technologies should be exploited leading to the future loss of oil's role. Nevertheless, conventional vehicles account for most of the global mobility fleet. EVs integration can bring several advantages related to energy sustainability such as decarbonization and renewable energy integration. A relevant aspect is related to charging stations distribution and charging time, which greatly influences the EV penetration. When EVs are connected to the grid, battery charging has always been the main target. However, new opportunities are investigated for grid support, called V2G technologies [137]. In this context, it is necessary to design highly efficient systems that provide high power levels as powerful DC solutions [138–140]. DAB converter is one of the

most popular converter for bidirectional power flow functionality given its high-power density, high efficiency and galvanic isolation [141, 142]. Two topologies are mainly used in the development of a bidirectional DC-DC bridge converter: single-phase and three-phase DABs. However, other several topologies and multi-phase structures are investigated with particular interest [143, 144].

### 3.2.2 RELATED LITERATURE

In the existing literature, 1ph-DAB and 3ph-DAB performances are usually unfairly compared from the system utilisation perspectives (i.e. same rated power), leading to the 3ph-DAB outperforming the 1ph-DAB in terms of lower device losses, lower current harmonic content and capacitor size [145, 146]. Nevertheless, a more proper and comprehensive study is shown in [147] where the two topologies are compared with the same silicon area for low-voltage high-current applications. However, the paper focuses on an on-board charger that connects the LV battery to the internal HV-DC bus while the proposed study aims to analyse an off-board charging station solution for direct charging of the existing higher voltage batteries considering V2G applications. Furthermore, the cited efficiency analysis does not accurately consider the MFT losses nor its design. Analytical calculations on filter capacitor sizing are not shown and the gate driver losses are not included in the study. For this reason, considering the higher capability of 3ph-DAB compared to 1ph-DAB, the proposed comparison approach involves analysing the two topologies for a nominal power level related to the actual difference in the switching legs of the converters. Doing this, the 3ph-DAB is not favored. The study includes devices and gate driver losses, MFT design and capacitor sizing where all these aspects are considered with different battery voltages in order to estimate DAB's losses as a function of different EV state-of-charge. This, supported by the ever-increasing studies on DAB and batteries integration as well as the impact of output voltage variations on converter losses [148].

The study of DAB converters and their use has been of great interest especially with the advent of renewable energies and in storage systems given the strong need for bi-directional energy flows together with galvanic isolation. This type of converter is used in many applications

where power density, cost, weight and reliability are key factors. Some applications can be UPSs, recharging systems, photovoltaic systems and applications related to traction in electric mobility in both the road and aviation sectors [149, 150]. The design of these converters is of crucial importance in order to achieve high efficiency values and optimise the converter characteristics. Although the purpose of this thesis goes beyond this aspect, it is nevertheless intended to provide useful references on the design of these converters to the interested reader [151–155].

### 3.2.3 SINGLE-PHASE AND THREE-PHASE DAB COMPARISON

The detailed structures for 1ph-DAB and 3ph-DAB are shown in Fig. 3.1. Both converters consist of two back-to-back bridges connected together by a transformer and a series inductance. Its operation is based on the exchange of active and reactive power between two alternating voltage sources, which is regulated through the relative phase shift between them. As it is well known, as the active power is mainly defined by phase shift, the reactive power is exchanged in relation to voltage source amplitudes. This means that, especially under unbalanced voltage conditions such as EV batteries charging and discharging process, current stresses and losses must be carefully assessed. Several modulation techniques with different purposes are developed in literature although only single phase-shift (SPS) modulation is considered in this study. More details on DAB operations can be found in [141] for both topologies. Since the aim is to compare the converters for the same power per switch, the design rated power must be chosen with appropriate values. More in general, given an  $s$ -phase converter with

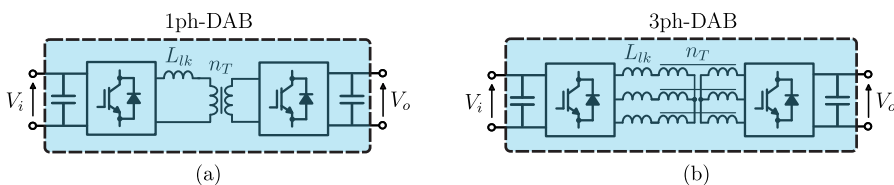


**Figure 3.1:** Schemes for (a) 1ph-DAB and (b) 3ph-DAB

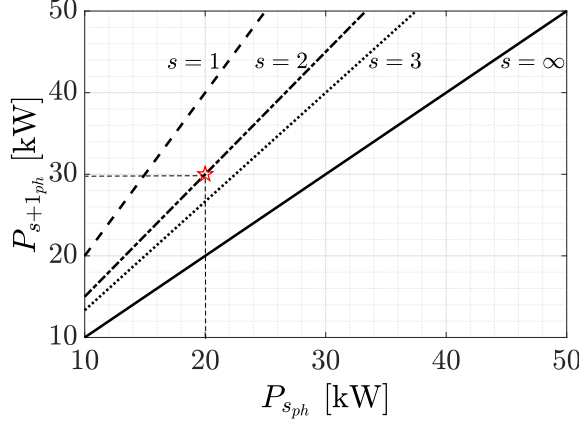


**Figure 3.2:** Characteristic of (3.2) for different number of phases  $s$  which provides the power of the  $s+1$ -phases converter ( $P_{s+1_{ph}}$ ) in order to have the same power per switch of the  $s$ -phase converter with power  $P_{s_{ph}}$ .

a power  $P_{s_{ph}}$  and a  $d$ -phase converter with  $d > s$ , the latter is able to provide a power  $P_{d_{ph}}$ , as described in (3.1):

$$P_{d_{ph}} = \prod_{M=s}^{d-1} \frac{M+1}{M} P_{s_{ph}}, \quad \forall \quad 1 \leq s < d \quad (3.1)$$

where  $s$  and  $d$  are the number of phases of the first and the second converter, respectively. A particular form of (3.1) can be defined for consecutive number of phases ( $d = s + 1$ ) as shown in (3.2):

$$P_{s+1_{ph}} = \left( \frac{s+1}{s} \right) \cdot P_{s_{ph}} \quad (3.2)$$

Figure 3.2 shows the characteristic of (3.2) for different number of phases  $s$  which, given the power of the  $s$ -phases converter  $P_{s_{ph}}$ , defines the the power of the  $s+1$ -phases converter  $P_{s+1_{ph}}$  in order to have the same power per switch. The two nominal powers of the proposed DABs are highlighted by the red mark and the converters specifications are listed in Table 3.1.

Specifically, the comparison approach focuses only on the DC-DC converters installed and operated in an existing DC grid. Thus, no assessment is made on AC grid-side rectifiers. Also, regarding a possible

**Table 3.1:** DABs parameter specifications

Topology	$P_N$ [kW]	$V_i$ [V]	$V_o$ [V]	$n_T$ [-]	$L_{lk}$ [ $\mu$ H]	$\varphi_{max}$ [rad]	$f_{sw}$ [kHz]
1ph-DAB	20	800	600-800	1:1	61.1	$\pi/12$	20
3ph-DAB	30	800	600-800	1:1	27.7	$\pi/12$	20

voltage and current imbalances in the 3ph-DAB transformer, it is assumed that the design is carefully performed to avoid them.

### 3.2.3.1 POWER LOSSES ON THE SEMICONDUCTOR DEVICES

Conduction and switching losses are the main losses for a switching device. These losses are estimated through simulations by varying the normalised power from -1 to 1 [p.u.], with different battery voltage ( $V_o$  in Fig. 3.1) to evaluate the impact of the SoC. Figures 3.3 (a) and (b) show the ratio between 3ph-DAB and 1ph-DAB switching and conduction losses in p.u., respectively, with different normalised power and output voltages. Each switching device consists of a SiC-MOSFET (Wolfspeed C2M0040120D) and its anti-parallel body-diode, both described by the manufacturer thermal model [156]. The loss increment in 3ph-DAB is noticeable in both cases for most conditions. More specifically, 3ph-DAB switching losses are up to 35% higher for specific power conditions (see  $V = 750$  V in Fig.3.3 (a)). Conversely, for all power conditions where no voltage mismatch occur switching losses are up to 30% lower with respect to 1ph-DAB. It should be noted that the results depend on the accuracy of the electrical model simulated by the software, but above all on the accuracy of the thermal model provided by the manufacturer.

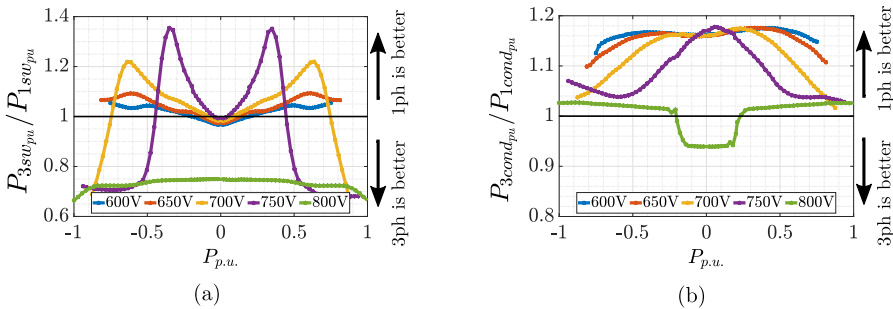


**Figure 3.3:** Different comparison analysis between the 1ph-DAB and 3ph-DAB in terms of device switching (a) and conduction (b) losses.

Also regarding conduction losses, 3ph-DAB performs worse causing losses to increase up to 18%. These considerations lead the 1ph-DAB to be more suitable in case of any type of variable voltage battery applications such as EV charging or V2G. Although gate driver losses are usually omitted due to their feeble contribution, in this work they are taken into account based on the model shown in [157]. Gate driver losses contribution has been also taken into account, resulting in 50% more losses in 3ph-DAB than in 1ph-DAB due to the larger number of devices.

### 3.2.3.2 ZVS RANGE COMPARISON

The total efficiency of DAB is highly dependent on the conditions of use. Particularly, the switching losses can worsen during hard-switching. Input and output Zero-voltage switching (ZVS) boundary conditions can be found by specifying particular constraints to the inductance current as shown in [141] and [158] for 1ph-DAB and 3ph-DAB, respectively. ZVS range is compared between the two systems to evaluate the operating range. Figures 3.4 (a) and (b) show the normalized power relative to the rated power (solid lines) and the ZVS operating range (dashed lines) for the 1ph-DAB and 3ph-DAB, respectively, where  $d = n_T V_o / V_i$  is the dc conversion ratio and  $\varphi$  the phase-shift angle. Thus, for each value of  $d$ , the normalised power increases as the phase-shift angle increases, following the corresponding solid curve. Taking the curve  $d = 1$  as an example, it can be seen that this always lies within the ZVS

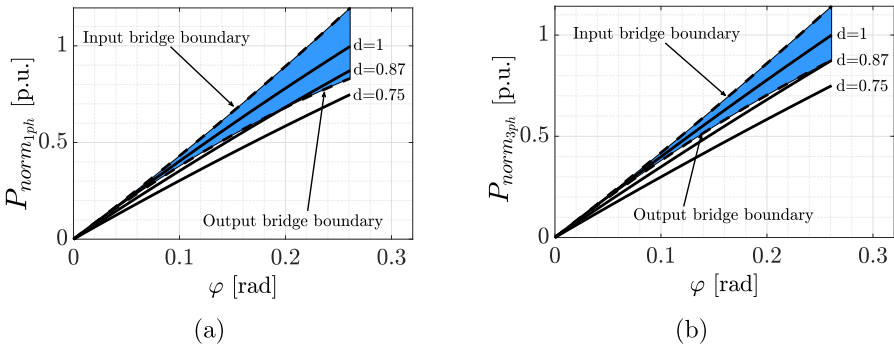


**Figure 3.4:** Different comparison analysis between the two topologies in terms of ZVS range for 1ph-DAB (a) and 3ph-DAB (b), respectively.

range, resulting in lower losses in both full-bridges (input and output). The opposite is the case where  $d=0.75$  where, due to the DC voltage difference between input and output, the output bridge is outside the ZVS range, increasing switching losses. As shown, the ZVS operating range for 1ph-DAB is wider [147], allowing it to enter soft-switching mode earlier than in the three-phase case (see  $d = 0.87$  line as reference example).

### 3.2.3.3 MFT DESIGN AND LOSSES EVALUATION

MFTs were designed based on DABs maximum voltage mismatch and rated power. The purpose of the transformer design is to evaluate its losses at all operating points of the DAB in order to calculate a more accurate overall losses than that obtained with simulations for switching devices only. The transformer apparent power is calculated as in [141]. Considering the worst case scenario (i.e.  $d = 0.75$  and  $\varphi_{max} = \pi/12$ ), the apparent power equations are obtained in (3.3).

$$S_{T_{1ph}} = \frac{1}{2} V_i I_{1_{RMS}} (1 + d), \quad S_{T_{3ph}} = \frac{1}{\sqrt{2}} V_i I_{3_{RMS}} (1 + d) \quad (3.3)$$

where  $I_{1_{RMS}}$  and  $I_{3_{RMS}}$  are the RMS primary current for 1ph-DAB and 3ph-DAB, respectively. For both topologies, 3C90 Ferroxcube E100/60/28 e-core has been used, changing the number of parallel cores to meet the design specifications. Both MFTs have a fully interleaved structure and a single layer winding. In order not to unnecessarily increase the transformer losses, the leakage inductance is made as small as possible preferring to include an external inductance to obtain the design value shown in Table 3.1. Moreover, shell-type core magnetic structure has been chosen for both MFT. A 3D sketch of both transformers is shown in Fig. 3.5.

Winding and core losses are the two main contribution to the total losses in a transformer. Since the MFT's frequency is much more higher than a line-frequency transformer, skin and proximity effects begin a crucial aspect in the correct evaluation of the AC resistance. Usually, Dowell's equations are used to determined the so-called resistance factor, which relates the DC resistance of the winding with its AC value. Following the calculations in [159], where the effect of interleaving structure on



**Figure 3.5:** The 3D structure of MFTs: a) single-phase; b) three-phase

leakage inductance and winding losses is studied, it is possible to obtain copper losses as a function of  $d$  and  $\varphi$  for both MFTs.

Core losses are due mainly to two effects: eddy currents, which are induced in the core by the time-changing magnetic field and hysteresis losses. Steinmetz's equation provides a simple and easy way to calculate core losses for sinusoidal voltages. Nevertheless, this equation is not accurate anymore with all those power electronics applications where the voltage excitation is far from sinusoidal. For all these cases, the Improved Generalized Steinmetz Equation (iGSE) [160] was introduced and it is used within this design analysis. The main variables to consider for specific core losses evaluation are the peak-to-peak value and the time derivative of the flux density  $B(t)$  as well as the magnetic material parameters. Using a T-model for the MFT as in [161], it is possible to calculate the magnetic flux density integrating the voltage across the magnetizing inductance  $v_m$  as:

$$B(t) = \frac{1}{NA_c} \int_0^t v_m(t) dt \quad \text{where} \quad v_m(t) = \frac{v_p(t) + v'_s(t)}{2} \quad (3.4)$$

where  $N$  is the primary winding turns number,  $A_c$  is the cross section area of the core column and  $v_p(t)$  and  $v'_s(t)$  are the primary and secondary reflected MFT voltages, respectively. In general, the magnetic flux density peak changes mainly with the primary and secondary voltage values (and thus  $d$ ). Many authors have studied the flux density reduction due to blanking times [162, 163]. However, only the primary voltage is considered while the total voltage across  $L_m$  should be used

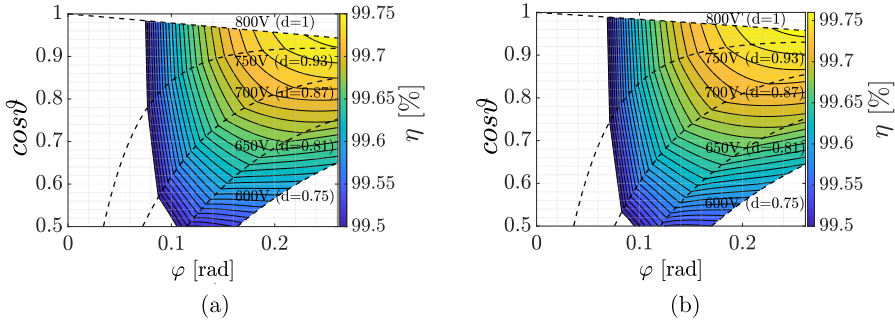


**Figure 3.6:** Different comparison analysis between the two topologies in terms of MFT losses for 1ph-DAB (a) and 3ph-DAB (b).

to calculate the right reduction of  $B(t)$  during load operations. In this way it is possible to evaluate the flux density reduction starting from the no-load condition as a function of  $d$  and  $\varphi$  allowing to add these losses to the winding losses and finally calculate the total losses of the MFT.

By substituting  $v_m(t)$  in (3.4) and integrating, flux density time-varying equation and its peak value are found. At this point, iGSE equation can be evaluated including the flux derivative over time for the entire period  $T$ . Finally, the specific magnetic losses for 1ph-MFT are shown in (3.5). The same consideration can be done for the 3ph-MFT.

$$P_{s_{1ph}} = \frac{k_i}{\pi} (2B_m)^{\beta-\alpha} \left( \frac{V_i}{2NA_c} \right)^\alpha \cdot [\varphi|d-1|^\alpha + (\pi-\varphi)(d+1)^\alpha] \quad (3.5)$$

Figures 3.6 (a) and (b) show the MFT total efficiency for both topologies as a function of phase-shift and power factor  $\cos\vartheta$ . Dashed lines highlight the MFT operation points for different battery voltages. As it can be seen, the efficiency difference between the transformers is negligible and strongly depends on the construction topology of the windings and the ferromagnetic core. It is worth noting that for  $d = 1$  (no voltage mismatch), there is a share of reactive power that increases as the phase shift increases for both cases. However, it can be shown analytically that the slope of this curve for the 3ph-DAB is  $-3/(4\pi)$  versus  $1/\pi$  for the 1ph-DAB, leading 3ph-DAB to process less reactive power for the same  $\varphi$ .

### 3.2.3.4 CURRENT EFFORTS

An important aspect of converters design is the evaluation of the thermal limits of the switching devices and the MFT stresses. In particular, attention must be paid to the peak and RMS value of the full load current with mismatched voltages. For this reason, the current on  $L_{lk}$  is analytically calculated and compared performing a sweep analysis of  $d$  and  $\varphi$ . Figure 3.7 (a) shows the percentage difference between 1ph-DAB and 3ph-DAB where it can be seen that 1ph-DAB peak currents is up to 30% lower at high  $d$  values. As  $d$  decreases, this difference varies up to 10% in favor of 3ph-DAB.

It is noticeable to see how the use of the three-phase topology is advantageous with regard to the peak current stress aspect for conditions where high power demands are paired with low DC conversion ratios. On the contrary, during all operations with low voltage mismatch, the 1ph-DAB shows a remarkable peak current reduction. RMS current values for the same working conditions are analytically calculated and the RMS reduction of 1ph-DAB with respect 3ph-DAB is shown in Fig. 3.7 (b). The RMS current difference varies between 4% and almost 9% for all the conditions, obtaining higher gap during low power. Despite the small difference, this results in the conduction loss ratio values shown in Fig. 3.3 (b), being proportional to the square of the percentage difference.

From the single MOSFET perspective, since each device conducts only for half period, the RMS current is calculated as  $1/\sqrt{2}$  times the RMS value of the inductor current whereas the peak current is the same of

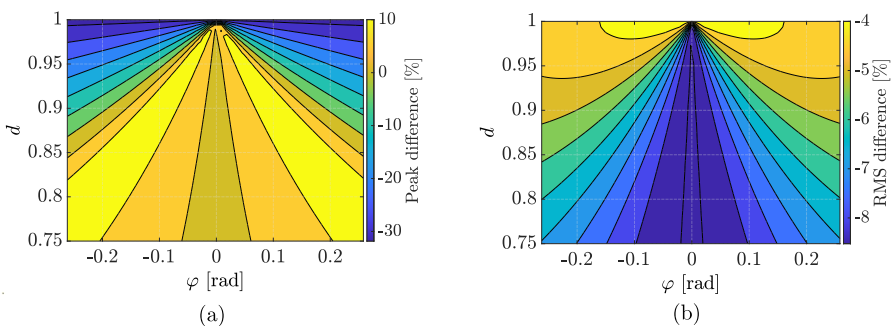


**Figure 3.7:** Different comparison analysis between the two topologies in terms of peak (a) and RMS (b) current differences.

the inductor current, for both converters. For this reason, the ratios between 1ph-DAB and 3ph-DAB single device peak and RMS currents are exactly the same as shown in Fig. 3.7 (a) and (b), respectively.

### 3.2.3.5 FILTER CAPACITOR

In order to perform normal operations, DC/DC converters need input and output capacitors which are designed to meet voltage ripple specifications by using the best capacitor technology for each application. The input and output properties of power converters, as well as the allowed maximum voltage ripple, vary depending on the converter application. Low equivalent series resistance (ESR) and equivalent series inductance (ESL) values and high capacitance densities are particularly needed for filter capacitor solutions due to the tendency towards high switching frequencies and the need for small converter volumes [164]. Electrolytic capacitors are most commonly used when high capacitance values are needed. However, when high voltages are required, it is more appropriate to use film capacitors due to their lower internal resistance and higher current capability.

The purpose of this section is to analyse the worst scenario from the point of view of battery-side filter capacitor sizing. In fact, in order to design the filter appropriately and to meet the ripple voltage and current constraints, the worst case (i.e. the one with the minimum value of  $d$  and the minimum phase-shift angle) must be considered to evaluate the maximum amount of charge variation  $\Delta Q$ .

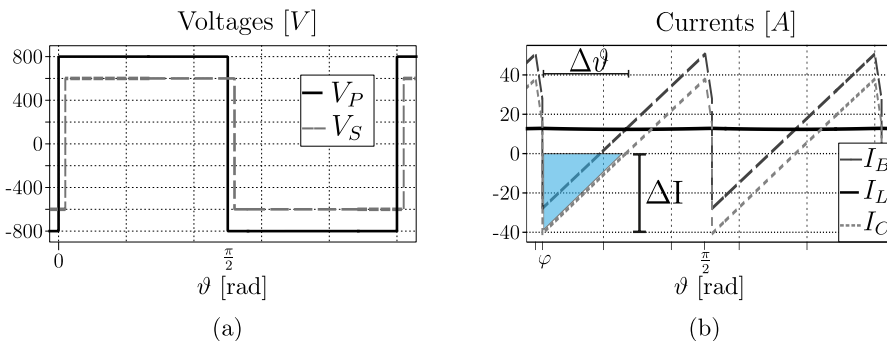


**Figure 3.8:** 1ph-DAB's voltages (a) and currents (b) waveforms for capacitor sizing calculation.

Considering the voltage and current waveform depicted in Fig. 3.8 (a) and (b), it is possible to calculate the electrical charge  $\Delta Q$  accumulated during the capacitor charging process (blue shadowed area) as in (3.6), where  $I_B$  is the output bridge current,  $I_C$  is the capacitor current and  $I_L$  is the battery current.

$$\Delta Q = \Delta V \cdot C = \frac{\Delta \vartheta}{2} \cdot \Delta I = \frac{\Delta \vartheta}{2} \cdot I_C(\varphi), \quad I_C(\varphi) = I_B(\varphi) - I_L \quad (3.6)$$

In order to calculate the angle variation  $\Delta \vartheta$ , the output current equation of the bridge from  $\varphi$  to  $\pi/2$  has to be considered and set equal to  $I_L$ , as in (3.7), whereas  $\vartheta$  is the angle variable.

$$\begin{aligned} I_B(\vartheta) &= I_B(\varphi) + \frac{V_i - nV_o}{L_{1ph}} \vartheta = \\ &= \frac{V_i (2\frac{\varphi}{\pi} - 1) + nV_o}{4fL_{1ph}} + \frac{V_i - nV_o}{L_{1ph}} \vartheta = I_L \quad \forall \vartheta \mid \varphi \leq \vartheta \leq \frac{\pi}{2} \end{aligned} \quad (3.7)$$

Solving (3.7) for  $\vartheta$ , substituting in (3.6) and solved for  $C$ , the minimum capacity needed to comply the voltage ripple constraint is obtained in (3.8) and with similar considerations for 3ph-DAB in (3.9):

$$C_{1ph} = \frac{\Delta Q}{\hat{V}_o \delta_{V\%}} 100 = \frac{V_i \left[ \pi^2(1 - \hat{d}) + 2\hat{\varphi}[n(\pi - \hat{\varphi}) - \pi] \right]^2 \cdot 100}{8\omega^2 \pi^2 L_{1ph} (1 - \hat{d}) \hat{V}_o \delta_{V\%}} \quad (3.8)$$

$$C_{3ph} = \frac{\Delta Q}{\hat{V}_o \delta_{V\%}} 100 = \frac{V_i \left[ 2\pi^2(1 - \hat{d}) + 3\hat{\varphi}[n(4\pi - 3\hat{\varphi}) - 4\pi] \right]^2 \cdot 100}{432\omega^2 \pi^2 L_{3ph} (1 - \hat{d}) \hat{V}_o \delta_{V\%}} \quad (3.9)$$

where  $\delta_{V\%}$  is the ripple voltage define as  $\delta_{V\%} = \Delta V / \hat{V}_o \cdot 100$  and  $\Delta V$  is the peak-peak DC voltage. In the above equations,  $\hat{\varphi}$ ,  $\hat{d}$  and  $\hat{V}_o$  are the minimum value of  $\varphi$ ,  $d$  and  $V_o$ , respectively, which leads to a worst condition.

As it can be seen in (3.6),  $\Delta Q$  is only valid for a specific  $\varphi$  and  $d$  ranges because, by increasing them, the blue shadowed shape changes no

longer being a simple triangle. In mathematical terms, it is possible to state that (3.6) holds only when  $-I_B(\varphi) - I_L \geq 0$  is true.

Solving  $-I_B(\varphi) - I_L \geq 0$ , two solutions are found. Whereas one is trivial ( $\varphi = 0$  and  $d \leq 1$ ), the second one gives the maximum angle for which the capacitor equation is true for a given  $d$ . Now, consider the two topologies and doing same considerations for the 3ph-DAB, (3.10) shows the  $\varphi$  range for which (3.6) holds.

$$\begin{aligned} \text{1ph-limit: } 0 \leq \varphi \leq \frac{1}{2} \left( 2\pi - \sqrt{2\pi\sqrt{d+1}} \right), \\ \text{3ph-limit: } 0 \leq \varphi \leq \frac{1}{3} \left( \pi - \pi\sqrt{2d-1} \right) \end{aligned} \quad (3.10)$$

Fig. 3.9 (a) illustrates (3.8) and (3.9) for different values of  $\hat{\varphi}$  considering a  $\delta_V\%$ =5%. The capacitors ratio ( $C_{ratio} = C_{1ph}/C_{3ph}$ ) is also calculated just to emphasize the capacitance difference which show that  $C_{1ph}$  requires more or less 6 times the  $C_{3ph}$  size. The limits of (3.10) are depicted by the dashed vertical lines for  $\hat{d} = 0.75$ . However, the previous considerations are not useful to limit the current ripple in case of a equivalent battery model, i.e. an impedance in series with a DC voltage source. In this case, the constraint is defined on the current ripple whereas the voltage ripple will be a consequence. The relationship between  $\Delta I(s)$  and  $\Delta Q(s)$  in the Laplace's domain is represented in (3.11).

$$\Delta I(s) = \frac{\Delta V(s)}{R_{bat} + sL_{bat}} = \frac{\Delta Q(s)}{C(R_{bat} + sL_{bat})} \quad (3.11)$$

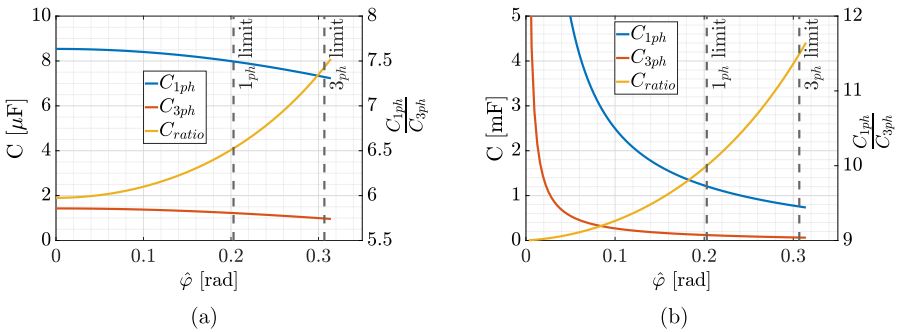


**Figure 3.9:** Different comparison analysis between the two topologies in terms of filter capacitor values for voltage (a) and current (b) ripple constraints.

where  $R_{bat}$  and  $L_{bat}$  are the total output resistance and inductance of the battery, respectively. As expected, the capacitor size is dependent on the output equivalent impedance and on the allowed current ripple. Since the battery impedance is quite small (few  $m\Omega$ ), the capacitance tends to increase to very high values. A possible solution is to introduce a LC filter to limit the current variations. Fig. 3.9 (b) shows the capacitors value for the two topologies with a 5% ripple current constraint with a pure resistive battery impedance ( $R_{bat} = 0.2\Omega$ ). With these constraints,  $C_{3ph}$  appears to be up to 10 times smaller than  $C_{1ph}$  for the considered parameters, resulting in a less expensive and less bulky capacitors to be used. Further discussions and conclusions about this section can be found in section 3.6.

### 3.3 EFFICIENCY TRADE-OFF-ORIENTED ANALYSIS IN V2G APPLICATIONS

In the electric vehicles (EVs), besides battery charging process, the EV battery pack can serve as an energy storage system (ESS) to support the grid, thanks to vehicle-to-grid (V2G) ancillary services. During the EV power exchange with the main grid, the overall efficiency depends not only on the converter but also on the battery. Typically, power converters, in particular dual-active-bridge (DAB) converters, present a low efficiency at light loads (i.e. low C-rates) and higher values at high power levels. The battery efficiency, on the other hand, decreases almost linearly as the power increases. Therefore, there is an optimum C-rate that could be selected to operate the converter and the battery when they are connected to the grid in order to minimize the losses of the overall system. In this context, this section aims to analyze the trade-off between several designed lithium-ion battery packs and DAB efficiencies to find the best compromise. Both simulation and experimental results, performed at the Chair of Power Electronics of the Technische Fakultät CAU in Kiel, are presented to validate the correctness of the theoretical analyses, which also lead to an efficiency-focused design method for V2G applications. Although the analysis focuses on V2G applications and thus on bidirectional power exchange, the same methodology can also be applied for the charging process alone. However, this is already

included in the analysis for V2G applications as it is a sub-case of the latter.

### 3.3.1 MOTIVATIONS

The sudden spread of EVs will bring new challenges on several sides, straining the electric system to meet the related energy demand. Indeed, charging electric vehicles is currently seen as a passive load towards the grid. However, due to the ever increasing spread of smart grids and their implementation [165], electric cars will play a new role within the grid by actively behaving and exchanging energy bidirectionally through V2G technologies. In the context of V2G strategies, DAB converters are increasingly studied for bidirectional applications due to their great performance in terms of efficiency, power density and volume with the benefits of isolated systems. DAB efficiency mainly depends on two factors: transferred power and voltage difference between the DC ports. The former causes an efficiency raise up to a maximum value after which it decreases again. The latter causes a vertical right downwards shift of the overall curve as the DC voltage mismatch increases. On the other hand, battery efficiency is very high at low C-rates, decreasing almost linearly as the C-rates increase. These two reversed trends produce a particular cross-behaviour layout which leads to a non-optimal operating power, causing higher losses either in the converter or in the battery and resulting in an undesirable condition.

### 3.3.2 RELATED LITERATURE

Vehicle-to-Grid (V2G) enables customers to exchange the stored energy of the battery pack with electric utilities as in conventional grid-connected energy storage systems [166, 167]. The system efficiency of these type of applications is crucial from the customer's point of view during battery energy exchange operations, since some of V2G applications can be remunerated [168, 169]. Interfacing of storage and DAB systems is widely explored in the existing literature [139, 170]. However, while it is possible to find several studies on the efficiency of batteries [171, 172] and converters [142, 173] separately, no work has been found that deals with the interfacing of vehicle batteries and power converters in the V2G environment for overall efficiency analysis. Regarding the EVs future perspectives, several studies have shown

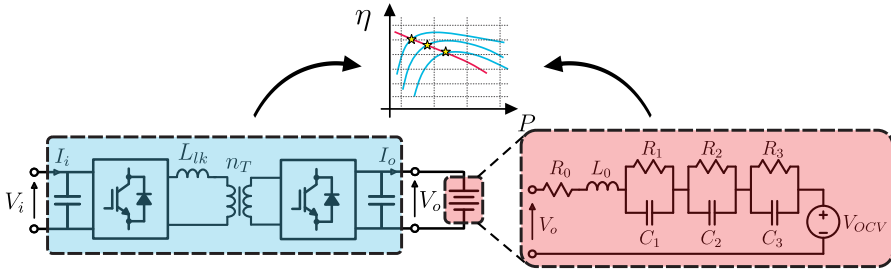


**Figure 3.10:** DAB structure, battery internal model and a graphical representation of the trade-off analysis.

that higher EV charging powers are needed to compete with internal combustion engine vehicle (ICEV) journey times. Increasing the battery pack voltage up to 800V is a possible solution to this problem, leading to considerable advantages in terms of size and weight [174–177]. For this reason, a trade-off analysis of single-phase DAB and battery is conducted in this study to define the optimum compromise in terms of efficiency with these new-trend battery packs. Without loss of generality, this analysis can be performed with any other type of DC-DC converter (e.g. three-phase DAB or other topologies).

### 3.3.3 DAB AND BATTERY LOSSES ANALYSIS

A single-phase DAB connected to a battery is depicted in Fig. 3.10, which represents a general scheme for a potential V2G application due to its bidirectional characteristics. DAB converter is used to control the charging/discharging power of the battery, which internal model is represented in the highlighted red area. In order to obtain a comprehensive overall efficiency study, both component losses are separately analysed. First, DAB efficiency is extracted from simulations and analytical results by implementing a single phase-shift (SPS) modulation. Then, cell losses during the entire charging/discharging process are calculated through several simulations at different C-rates considering the voltage profile over capacity. DAB parameter specifications are listed in Table 3.2. Battery packs designs were conducted by using a 18650-format 2.8 Ah cell, which electrical model parameters are taken from [178].

#### 3.3.3.1 DAB LOSSES EVALUATION AND ANALYSIS

DAB converter losses mainly depends on semiconductor's switching and conduction behaviour, and medium-frequency transformer (MFT) losses.

**Table 3.2:** DAB converter parameters

$P_N[kW]$	$V_i[V]$	$V_o[V]$	$n_T[-]$	$L_{lk}[\mu H]$	$f_{sw}[kHz]$
20	800	600-800	1:1	61.1	20

For the firsts, detailed simulations for the DAB under investigation are carried out providing different efficiency curves for different battery side voltages within the battery voltage range. In this way, we are able to extract only the device's losses which then will merge together with the MFT analytical losses calculations. Although the devices losses are based on simulations, a mathematical analysis based on [179] is shown for the sake of completeness. From the analytical point of view, a general equation for conduction losses calculation for each switch can be computed as:

$$P_{S,cond} = c \cdot I_S + d \cdot I_S^2 \quad (3.12)$$

where  $I_S$  is the current through the device and the coefficients  $c$ ,  $d$  are derived from device datasheet and curve fitting. Moreover, the coefficients can be computed as temperature-dependent if the temperature variation effect is considered. The switching losses are more challenging to calculate, since they also depends on other surrounding parasitic components [144]. If soft-switching operations are achieved in the DAB primary side, switching losses can be neglected. Conversely, operating points outside soft-switching range can be found for the secondary side when voltage changes during the charge/discharge process of the battery pack. A good estimation of the switching losses can be described in a form:

$$P_{S,sw} = k(I_S) \cdot I_S \cdot f_{sw} = (a + b \cdot I_S + c \cdot I_S^2) \cdot I_S \cdot f_{sw} \quad (3.13)$$

where  $k(I_S)$  is the switching-loss factor,  $f_{sw}$  is the switching frequency and the coefficients  $a$ ,  $b$  and  $c$  are obtained from curve fitting calculations. Gate drivers losses, usually neglected for the low impact on the overall performance, are also included in this study based on equations in [157]. The parasitic parameter losses such as  $C_{OSS}$  can be neglected from the calculations for frequencies around 20 kHz as considered

in this work. Further, analytical calculations are performed to obtain winding and core losses of the MFT for the same operating working points. Copper losses are computed using the well-known Dowell's equation which considers the skin and proximity effect in the transformer windings due to the high frequency waveforms behaviour. In particular, the total copper losses  $P_{Cu,loss}$  can be computed as:

$$P_{Cu,loss} = I_{RMS}^2 \cdot (R_{ac,p} + R_{ac,s} \cdot n_T^2) \quad (3.14)$$

where  $I_{RMS}$  is the transformer RMS current for each specific operating point,  $R_{ac,p}$  and  $R_{ac,s}$  are the primary and secondary transformer AC resistance, respectively, and  $n_T$  is the transformer ratio. The AC primary and secondary winding resistances are obtained through the so-called AC resistance factor [155], which is computed as:

$$\begin{aligned} F_{R_x} &= R_{ac,x}/R_{dc,x} = \\ &= A \left( \frac{\sinh(2A) + \sin(2A)}{\cosh(2A) - \cos(2A)} + \right. \\ &\quad \left. + \left[ \frac{2(N_x^2 - 1)}{3} \right] \frac{\sinh(A) + \sin(A)}{\cosh(A) - \cos(A)} \right) \end{aligned} \quad (3.15)$$

where  $A = d_f/\delta$  is the winding conductor thickness normalised with respect to the conductor skin depth,  $N_x$  is the number of winding layers and  $R_{dc,x}$  is the DC winding resistance where  $x$  denotes the primary or secondary winding.

Core losses depend on core materials and magnetic flux density within the transformer core. Since the primary and secondary voltages are non-sinusoidal, the flux density will be too, leading to the need to calculate losses with the Improved Generalized Steinmetz Equation (iGSE) [160] rather than the original Steinmetz Equation (OSE). In particular, the trapezoidal waveform of the flux density  $B(t)$  during square-wave operation of the SPS modulation is considered. Under this assumption, as the phase-shift angle increases, the maximum value of the flux density  $B_m$  decreases and its derivative becomes zero within the time intervals where the primary and secondary voltage have opposite

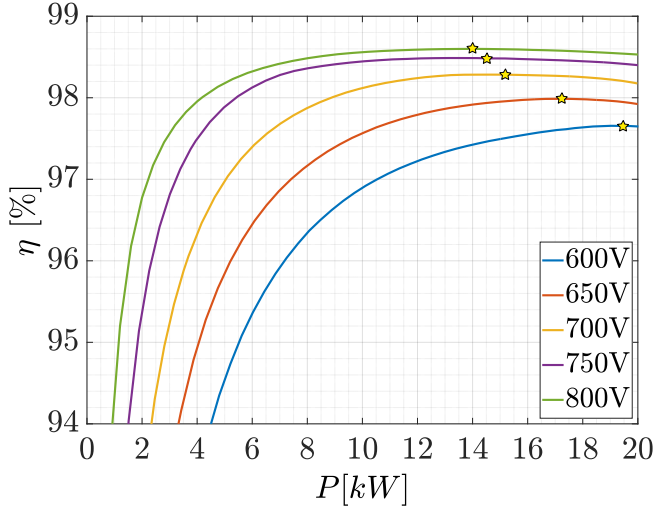


**Figure 3.11:** Simulated efficiency curves of 20kW DAB for  $V_i=800\text{V}$  at different  $V_o$  values

sign [161]. Considering the magnetic material properties, the core losses are calculated as:

$$P_{Core,loss} = \frac{k_i}{\pi} (2B_m)^{\beta-\alpha} \left( \frac{V_i}{2NA_c} \right)^\alpha \cdot [\varphi|d-1|^\alpha + (\pi-\varphi)(d+1)^\alpha] \quad (3.16)$$

where  $N$  is the primary winding turns number,  $A_c$  is the cross section area of the core column,  $V_i$  the input voltage,  $d = n_T V_o / V_i$  is the dc conversion ratio and  $\varphi$  the phase-shift angle. The constant parameters  $k_i$ ,  $\alpha$  and  $\beta$  are obtained by the core material datasheet.

A further loss contribution is due to losses in the external inductance. The calculations for this component are very similar to those used for transformer losses. Since the voltage drop across the inductance is very small and so is the resistance, the losses of this component are not considered in this work.

Figure 3.11 shows the simulated efficiency curves for the DAB converter at 800V primary voltage for different secondary voltages. When the two DAB's DC side voltages are at the same value, so there is no voltage mismatch, the reactive power exchange is minimal and the efficiency curve is the highest. As soon as the voltage mismatch is increased (in

our case the voltage on the battery side is decreased) the reactive power exchanged increases and the efficiency curve shifts downwards due to conduction losses in the devices and in the transformer windings. Of greater interest is the shift of the points of maximum efficiency (yellow stars) towards higher powers as the voltage mismatch increases. As it can be seen, the maximum efficiency point for  $V_o = 800\text{ V}$  is obtained for a power of about 14 kW.

Differently, for the curve at  $V_o = 750\text{ V}$  the maximum point is obtained at a power of about 14.5 kW and so on for the other voltage values. In this situation, the smaller the phase-shift angle, the greater the switching losses of the output bridge which is outside its soft-switching boundaries. In addition, even to a small extent, core losses increase towards no-load condition as it can be seen in (3.16). It is important to mention that these shifts in the efficiency curves and in the maximum efficiency points always exist also with lower voltage range since the effect is mainly caused by the voltage difference between the two DC ports.

### 3.3.3.2 BATTERY MODEL AND LOSSES EVALUATION

Several dynamic cell models are used and published with different complexity and accuracy. In addition to mathematical and electrochemical models, circuit-oriented models have high potential regarding precision, parametrization efforts and usability. For electric vehicle battery modelisation, different models can be found in [70, 180].

Typically, battery losses can be divided into ohmic, reversible and irreversible reaction losses. However, the terminal behavior of the battery can be described by a series of RC-pairs where the power losses can be estimated by resistances. Several models can be used to estimate cell dynamics and characteristics in different applications. In fact, the number of poles and zeros ( $RC$ -pairs) greatly influences both the transient and the power loss estimation, which makes complicated the choice of model structure. Nevertheless, the model used in this study (Fig. 3.10) should be chosen for losses-calculation purposes, as presented in

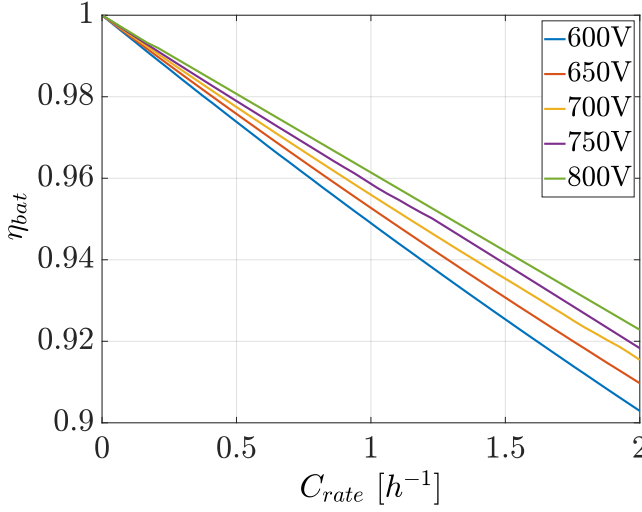


**Figure 3.12:** Simulated efficiency curves of 20kWh battery pack for different battery voltage (i.e. SoC)

[178]. The battery losses are calculated by adding the Joule's losses as in (3.17):

$$\begin{aligned}
 P_{bat,loss} &= P_{cell,loss} \cdot N_{tot} = R_{bat,eq} \cdot I_{bat}^2 = \\
 &= \sum_{j=0}^3 R_j \cdot \frac{N_{sc}}{N_{ps}} \cdot I_{bat}^2
 \end{aligned} \tag{3.17}$$

where  $R_j$  is the  $j$ -th resistive element,  $I_{bat} = I_o$  is the total battery current,  $N_{sc}$  is the number of series cells,  $N_{ps}$  is the number of parallel strings,  $R_{bat,eq}$  is the equivalent battery pack resistance and  $N_{tot} = N_{sc} \cdot N_{ps}$  is the total number of cells. Since the only measurable quantities are voltage and current at the battery terminals, the efficiency equation during charging process can be obtained as:

$$\eta_{bat} = 1 - \frac{R_{bat,eq} \cdot I_{bat}^2}{V_{bat} \cdot I_{bat}} = 1 - \frac{R_{bat,eq} \cdot I_{bat}}{V_{bat}} \tag{3.18}$$

where  $V_{bat} = V_o$  is the DAB output voltage.

As noted, in a stationary voltage condition a linear efficiency curve is obtained. Conversely, as the voltage changes, the slope of the curves changes as shown in Fig. 3.12. As it can be seen, in addition to

the estimated value of  $R_{bat_{eq}}$ , the estimation of instantaneous battery efficiency depends on the measured values of voltage and current. The internal battery pack resistance changes with several factors. The most important are temperature, SoC and the C-rate during the opera-

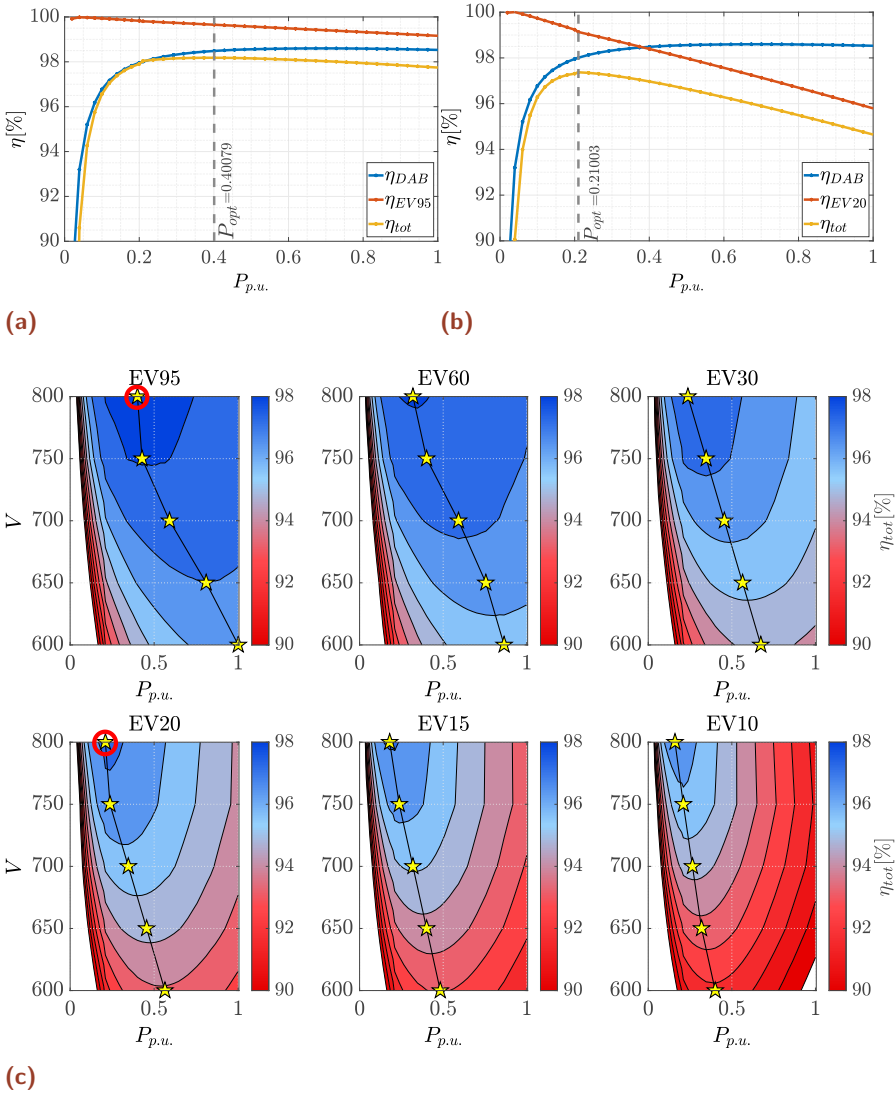


**Figure 3.13:** a) 20 kW DAB, EV95 battery and total efficiency curves for full SoC (800V) b) 20 kW DAB, EV20 battery and total efficiency curves for full SoC (800V) c)  $\eta_{tot}$  efficiency values in the complete SoC range (600-800V) for different battery packs coupled with the designed 20 kW DAB: optimal points of Fig. 3.13a and 3.13b are marked with a red circle.  $P_{p.u.}$  is the p.u. power referred to the DAB's nominal power.

tions. In general, the resistance value is higher at very low temperatures and then decreases and increases again as the temperature increases as described in [181], following a quadratic function. Regarding the influence of the other factors, [182] shows typical Li-Ion internal resistance variation for different SoC and C-rate by fitting the experimental measurements as a polynomial of the third order with respect to the SoC and as an exponential function with respect to temperature. From these results, it can be said that the internal resistance increases as the SoC decreases and for SoC greater than 50% the internal resistance decreases as the C-rate growth. Further, although not treated in this work, different techniques can be used to estimate battery impedance online as a function of SoC and temperature [183–186].

In this study, several simulations have been performed in order to calculate battery pack losses in different voltages and C-rates working points, which are then used to obtain the total losses of the system. To this end, a cylindrical 18650-format 2.8 Ah cell is modelled by using the charge characteristic according to the most important variables, such as SOC and C-rate.

### BATTERY PACKS DESIGN

Following the new battery voltage trend already discussed and to study the trade-off analysis in a wider battery capacity spectrum, six different batteries with the same voltage level but different capacities are designed with the 18650-format cylindrical cell under investigation. The battery pack capacities have been chosen related to DAB's nominal power in order to appreciate the coupling of the designed converter with different types of batteries to compare the efficiency behaviour. In particular, the idea is to compare the behaviour of the system when the capacity of the battery pack is lower ( $C\text{-rate} > 1$ ), equal ( $C\text{-rate} = 1$ ) and higher ( $C\text{-rate} < 1$ ) than the rated power of the DAB. The design deals with the number of cells in series and parallel to achieve battery pack specifications. A battery management system (BMS) is supposed to correctly optimise cell operation according to the relevant parameters such as temperature and voltage. In order to obtain the nominal battery voltage of 800 V, 187 series cells are used for all the battery packs, whereas the other design parameters are listed in Table 3.3.

**Table 3.3:** 800-V battery pack parameters with 187 series cells.

	EV95	EV60	EV30	EV20	EV15	EV10
Capacity [Ah]	117.6	75.6	39.2	25.2	19.6	14
$N_{ps}$	42	27	14	9	7	5
$N_{tot}$	7854	5049	2618	1683	1309	935

### 3.3.4 EFFICIENCY TRADE-OFF ANALYSIS

If the losses of the DAB and the battery pack are added together for the design voltage levels and for all the operating points, the total system efficiency  $\eta_{tot}$  is obtained. In particular, as the two systems are cascaded, the total efficiency is the product of the two efficiency curves. Figures 3.13a and 3.13b show an example of two simple trade-off cases for two different battery size at full capacity (800V): EV95 for left and EV20 for right figure, respectively. From the total efficiency curves the corresponding working points to achieve the overall maximum efficiency are highlighted (vertical dashed lines), showing precisely the power at which the DAB should operate to optimize the overall system losses. The first difference standing out from the comparison between the two cases is the shift in the two optimum points according to the total battery capacity ( $P_{opt}=0.21$  and  $P_{opt}=0.4$ ). This is due to the significant difference in efficiency between the two battery packs due to the lower C-rate value for the EV95. More in general, since DAB efficiency changes with the battery voltage (i.e. SoC), different total efficiency curves are obtained for a variable voltage and for each battery pack. Figure 3.13c shows the results of the total efficiency curves for the proposed battery packs, where each star represents a maximum efficiency point for that specific battery voltage. It is highly noticeable the difference in maximum efficiency between each battery and the shifting of the optimum power points even during the operation of a single battery. This shift is mainly due to the DAB's maximum efficiency point translation already discussed and shown in Fig. 3.11, now even more pronounced due to the contribution of the battery efficiency curve. This approach can be used to optimize the DAB design process with respect to the maximum capacity of the battery in such a way as

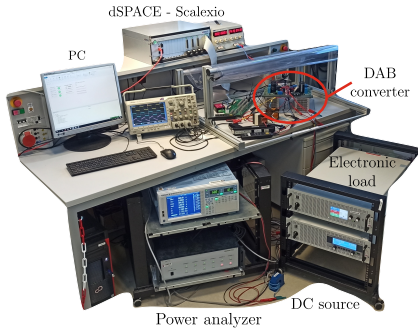


**Figure 3.14:** The experimental setup used to validate the DAB efficiency curves.

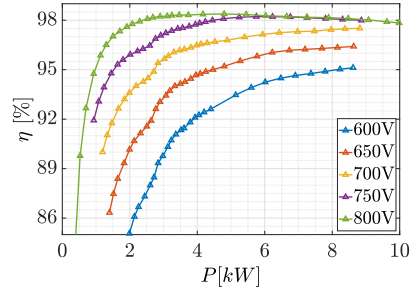


**Figure 3.15:** Experimental efficiency measurements on 10kW DAB for  $V_i = 800V$  at different  $V_o$  values

to design the correct sizing in a given working range and at a given efficiency range.

### 3.3.5 EXPERIMENTAL VALIDATION

In order to validate the simulation results regarding the efficiency curves, several experiments were carried out to measure the efficiency of the DAB through the setup shown in Fig. 3.14. The measurements are performed during the operation of a DAB with a rated power of 10 kW and a rated voltage of 800 V. The converter operates at a frequency of 20 kHz. The MFT has a ratio  $n_T = 1$  and an external inductance of value  $L_{lk} = 91.76 \mu H$  is added. The SPS controller is implemented within a dSPACE Scalexio system that generates the control signals for the MOSFETs via dedicated FPGAs. All the input and output voltages and currents (i.e.  $V_i$ ,  $V_o$ ,  $I_i$ ,  $I_o$ ) are measured through a Yokogawa power analyzer which allows the calculation of the total system losses and thus the efficiency of the DAB. Primary DC voltage  $V_i$  is kept constant by a voltage DC source, whereas battery side voltage  $V_o$  is changed by a DC load emulator within the desired battery voltage range. Figure 3.15 shows the experimental efficiency curves of DAB for  $V_i = 800V$  and different  $V_o$  values where a maximum efficiency of 98.4% is achieved at  $V_o = 800V$ .

With the aim of evaluating DC fast-charging, a further analysis is made by considering the losses of four identical DABs connected in parallel. In contrast with the simulated tests, three different designs of 40 kWh

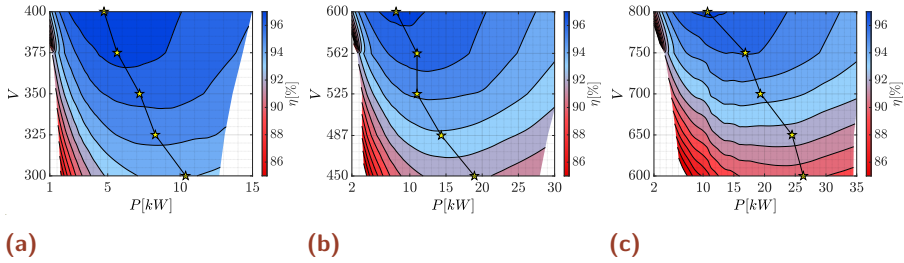


**Figure 3.16:** Total efficiency values with four 10 kW DAB in parallel and 40 kWh battery: a) 300-400 V, b) 450-600 V, c) 600-800 V

battery packs with different voltage ranges are analysed with this parallel DAB structure. In particular, three different voltage ranges are evaluated, both for the DAB and for the battery pack: 300-400 V, 450-600 V and 600-800 V for the entire charging process. The battery losses have been calculated mathematically through the model presented in Section 3.3.3.2 and additively included to the measured losses of the four parallel DABs for all working points.

Figures 3.16a, 3.16b and 3.16c show the overall efficiency for the three voltage ranges. Due to the lower voltage range with respect to the nominal one, it can be noticed the maximum power limitation of the DAB during high-mismatch voltage operations owing to the limits on the maximum current of the MFT. However, even in this case it is possible to note the existence of an optimal trajectory that minimises the total system losses at the expense of the charging time, which in this case will be more than doubled with respect to the case in Figure 3.16c. Similar considerations can be extended to the cases of Figure 3.16b and Figure 3.16c where it can be seen that the increase in C-rate significantly reduces the overall efficiency of the system owing to the higher battery losses. These behaviours demonstrate the correctness of the simulations and the results discussed in Section 3.3.4. Further discussions and conclusions about this section can be found in section 3.6.

### 3.4 OPTIMAL CHARGING STRATEGY

From the analysis presented in the previous section, it is easily understood that it is always possible to find an optimal charging trajectory that minimizes the losses of the system consisting of converter and battery. To this end, this section is concerned with developing and implementing a real-time control system for regulating the charging power to maximize the overall efficiency of the system. This control strategy is called  $\eta_{max}$  charging strategy in the current work.

#### 3.4.1 EFFICIENCY COMPARISON

First of all, let's analyze the efficiency of the optimal trajectory compared with two strategies typically used for EV charging such as constant-current (CC) and constant-power (CP). Total calculated efficiency of the DAB converter coupled with a 20 kWh battery are shown in Fig. 3.17 (a) where the three strategies charging trajectories are highlighted. The CC and CP values have been chosen in such a way as the charging time is the same for all the three cases. The efficiency points for each case are depicted in Fig. 3.17 (b) as a function of the battery voltage where the optimal trajectory performance in a full charging process is shown compare to CC and CP charging strategies. The proposed strategy has a much higher efficiency value than its rivals, especially during the initial charging phase. Due to the intersections of the trajectories visible in Fig. 3.17 (a), the efficiency at average voltage is very similar among the three strategies. However, once crossed this point, the trajectories

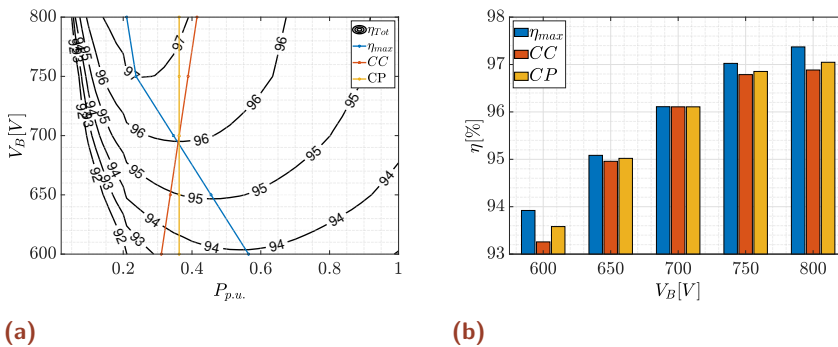


**Figure 3.17:** Representation of  $\eta_{max}$ , CC and CP strategies in discharging process of the battery system

split and only the proposed strategy follows the values at maximum efficiency until the end-of-charge voltage where the efficiency difference is again remarkable.

### 3.4.2 $\eta_{max}$ -CHARGING STRATEGY IMPLEMENTATION

This section describes the proposed  $\eta_{max}$ -charging strategy implementation where the instantaneous overall efficiency of the system including DAB converter and battery pack is maximized at each SoC. The strategy works exploiting the Perturb and Observe (P&O) principle as it is done by the well-known Maximum Power Point Tracking (MPPT) method for PV systems. However, some integration have been included for the specific application due to the particular process behaviour.

#### 3.4.2.1 MEPT CONTROL SYSTEM AND ALGORITHM EXPLANATION

The implementation of the  $\eta_{max}$ -charging strategy is straightforward. Fig. 3.18 illustrates the control loop of the proposed  $\eta_{max}$ -charge strategy together with the DAB converter controller. The DC voltages and currents from grid and battery side are measured by the Signal Processing Units (SPU) that samples the ADC inputs at 20 kHz. Here, a filtering process is performed on the measured values to remove noise. A moving average filter of 30 samples and a digital low-pass filter with 1 kHz bandwidth are used. Since the MEPT control works on the derivative of both efficiency and current is crucial that the efficiency variation is due to the actual reference and not due to disturbances. The Efficiency Estimation Unit (EEU) is tasked with calculating the efficiency of the converter and estimating the efficiency of the battery pack from the

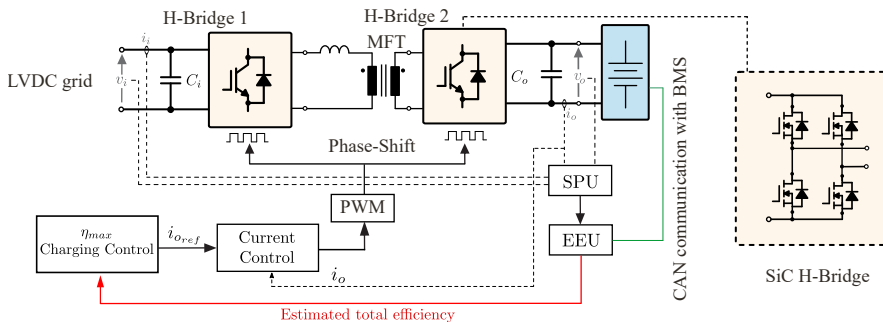


**Figure 3.18:** The charging station under study with an integrated  $\eta_{max}$ -charging strategy.

parameters delivered by the Battery Management System (BMS). Once the total efficiency is achieved, the  $\eta_{max}$  Charging Control block aims to change the battery side current reference  $i_o$  based on the efficiency measurements. Finally, a simple Current Control system is used to follow the set current reference which output provides the phase-shift angle between the two H-bridges.

A flowchart of the  $\eta_{max}$  charging control is shown in Fig. 3.19 which is repeated each 2 s. The difference between the new and the old value of the total efficiency and the reference current are calculated. Since the efficiency curve at maximum point is almost flat, the MEPT will struggle to achieve a significant change in efficiency by varying the current reference. In order to avoid useless reference variation at maximum efficiency, the moving standard deviation (MSD) of  $\eta_{tot}$  is calculated. In this way, this index can be used to detect when the efficiency has reached its maximum value and freeze the current reference variation when the MSD is below a threshold  $\sigma_{thr}$ .

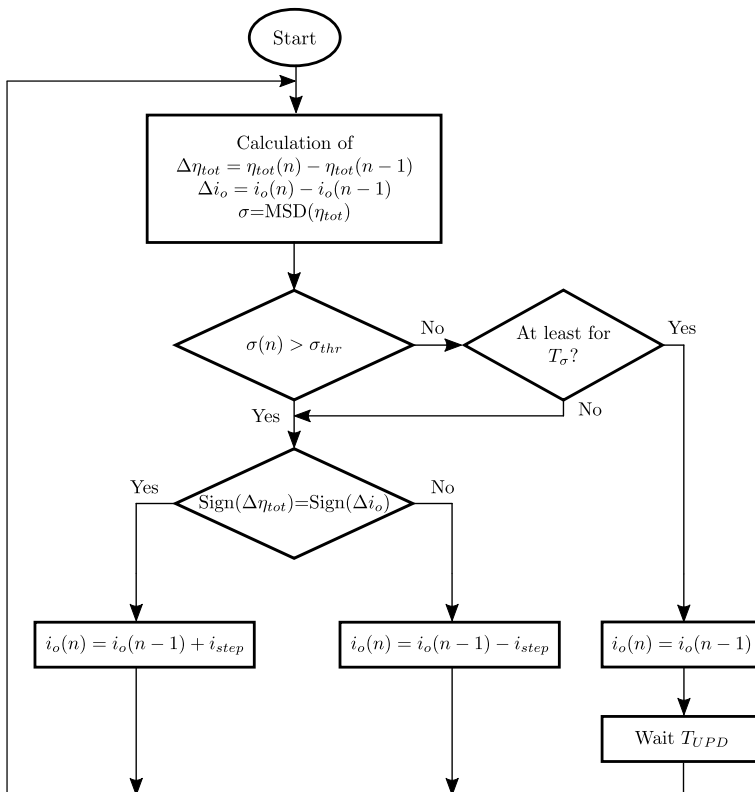


**Figure 3.19:** Control flowchart of  $\eta_{max}$ -charging strategy implementation.

For example, starting from very low current reference, a current change will result in a large change in efficiency due to the high slope of the curve. In this case, the MSD will always be greater than the threshold and the algorithm continues by varying the reference according to the sign of  $\Delta\eta_{tot}$  and  $\Delta i_o$ . As the calculated efficiency variation is gradually smaller and smaller, the MSD will be as well until it falls below the set threshold. At this point, if this trend is kept for at least a certain amount of time  $T_\sigma$ , the reference current is frozen, otherwise the efficiency tracking is continued. Since the battery voltage variation is a slow process and it depends on the battery capacity and battery charging power, the efficiency has also very slow variation. For this reason, the algorithm will start again after a certain amount of time  $T_{UPD}$  to track the efficiency when it has actually changed in a detectable way. The MEPT algorithm is simple: if  $\text{Sign}(\Delta\eta_{tot}) = \text{Sign}(\Delta i_o)$  means that the efficiency curve derivative is positive and the actual point must shift rightwards increasing  $i_o$  by  $i_{step}$ . Conversely, if the two signs are not equal, the efficiency derivative is negative and a negative value of  $i_{step}$  must be set.

#### 3.4.2.2 PARAMETERS SELECTION APPROACH

$i_{step}$

The selection of the current step depends on several factors. In general, since the MEPT control always works close to the maximum efficiency, the flatness of the efficiency curve in that specific point is a crucial aspect. As shown in Fig. 3.13a and 3.13b, the bending of the two  $\eta_{tot}$  efficiency curves at the maximum point are so different, mainly depending on the capacity of the battery related to the nominal power of the converter. In the first case, a bigger  $i_{step}$  value should be chosen in order to detect an efficiency variation. However, a much smaller step is needed in the second case. In our experiments,  $i_{step}$  is set to 0.1 A, which is approximately the 0.5% of the nominal current of the converter (12.5 A) multiplied by the kWh capacity of the battery (2 kWh). More in general, the current step should be proportional as in (3.19):

$$i_{step} \propto \frac{P_n}{V_n} \cdot C_{bat} \quad (3.19)$$

where  $P_n$  [kW] and  $V_n$  [V] are the nominal power and voltage of the converter and  $C_{bat}$  [kWh] is the battery capacity.

### $T_{UPD}$

In order to avoid useless oscillation of the current reference, an update time  $T_{UPD}$  has been included to the algorithm. The selection of this interval is challenging since depends on the overall charging time and on the maximum points efficiency variation between the beginning and the end of the charging process. In our experiments, a simple fixed  $T_{UPD}$  interval of 1 min has been set. However, a more sophisticated approach based on minimum efficiency variation or based on the actual C-rate value can be implemented. More in general, the interval should be reduced for higher C-rate which would lead to a higher efficiency variation. On the contrary, if the C-rate is smaller the interval can be increased since the efficiency variation will be slower. The same behaviour can be achieved based on the integral of the efficiency over time. As soon as the variation is above a fixed threshold (e.g. 0.2%) the tracking starts again and the integral reset.

### $\sigma$ WINDOW AND $\sigma_{thr}$

The moving standard deviation of the measured efficiency is a key parameter as it provides an indication of whether the steady-state of the efficiency has been reached. However, the size of the moving window is related to the measurements noise, filtering, and so on. Clearly, the window size narrowing leads to a higher volatility of the calculated value and the threshold should be increased accordingly to avoid incorrect conditions. Conversely, an efficiency variation could not be detected if the window is too large due to the filtering behaviour of MSD. Based on several simulations, where different values of window samples have been evaluated, a good compromise between volatility and detectability has been found with 20 s window with a threshold equal to 0.006. It can happen that if the efficiency variation after the  $T_{UPD}$  interval is too small,  $\sigma$  is always below the set threshold. In this case, the tracking is performed in any case due to the time  $T_\sigma$ , which is set to 30 s in our experiments. In any case, this is not detrimental as in the worst case the control will reach the same efficiency.

### 3.4.2.3 EXPERIMENTAL VERIFICATION OF $\eta_{max}$ -STRATEGY

A 10 kW DAB converter is realized as shown in Fig. 3.14. Two bidirectional sources are used to emulate the behavior of the grid side voltage, fixed at 400 V, and the 400 V-2 kWh battery. A charging voltage curve is obtained and load in the function generator of the DC-load based on the voltage profile of a single cylindrical cell. In this way, the DC-load voltage will vary over time simulating the charging of the battery pack. Measured efficiencies ( $\eta_{DAB}$ ,  $\eta_{Bat}$  and  $\eta_{tot}$ ) as well as primary and secondary currents ( $i_o$  and  $i_i$ ) and battery voltage ( $v_o$ ) are shown in Fig. 3.20 during an entire charging process to validate the  $\eta_{max}$  strategy. At the beginning of the process, the MEPT strategy increases the reference up to 8 A and after some fluctuations at the maximum efficiency, it stops the tracking by freezing the current reference. After the time period  $T_{UPD} = 60\text{ s}$  it calculates the new values and it finds the new current reference which maximizes the efficiency  $\eta_{tot}$ . As it can be noticed, the reference current decreases as the SoC increases in order to follow the maximum efficiency trajectory, by showing the same trends found in Fig. 3.13c. Three particular tracking periods are shown in Fig. 3.21 which represents the zoomed area  $Z_1$  in Fig. 3.20. As noted, at the end of each tracking period an increased value of  $\eta_{tot}$  is achieved after some fluctuations due to the flatness of the efficiency curve at the maximum point.

An interesting behaviour is shown in Fig. 3.22 which represents the zoomed area  $Z_2$  in Fig. 3.20. Right after the beginning of the tracking phase, a voltage step of few volts due to the DC-load resolution happened. For this reason, at  $t = 51\text{ min}$ ,  $\eta_{tot}$  increases abruptly. This event increased the standard deviation calculation above the set threshold leading to a longer tracking period to stabilize the efficiency variation and finally freeze the reference. Despite this unlucky event, this demonstrates the robustness and the correctness of the control method. The obtained experimental results confirm the correctness of the conducted numerical studies in previous sections and show the  $\eta_{max}$ -charging strategy implementation in a real-time environment. Further discussions and conclusions about this section can be found in section 3.6.

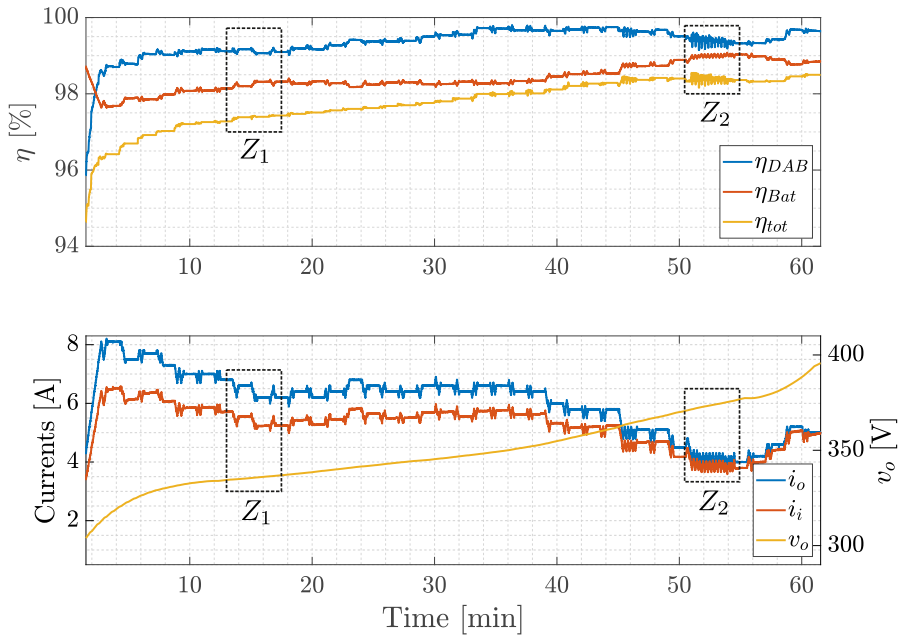


**Figure 3.20:** Efficiency tracking behaviour and main measured variables during the complete charging process of 400 V, 2 kWh battery.

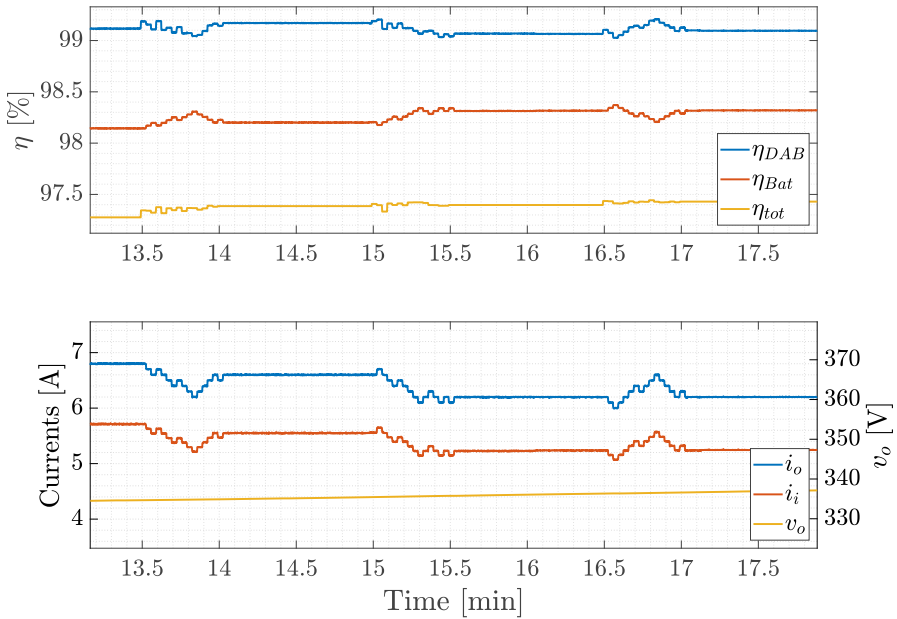


**Figure 3.21:** Three specific tracking periods during the charging process related to the  $Z_1$  area of the overall charging process.

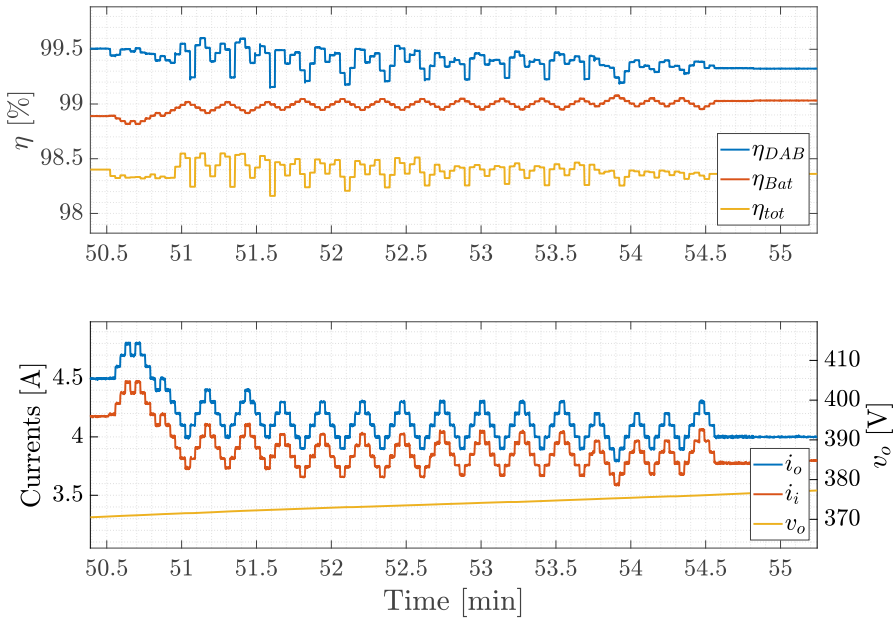


**Figure 3.22:** A longer single tracking period due to a voltage step of the DC-load related to the  $Z_2$  area of the overall charging process.

### 3.5 DESIGN AND SIMULATION OF V2G SYSTEM

Batteries of electric vehicles have to be charged by power electronic converters connected to the electric grid. If these power converters are bidirectional they can be exploited to provide vehicle-to-grid (V2G) services. At the University of Trieste an experimental V2G apparatus is under construction. Its control system has been developed and the first simulation tests has been performed. This section describes the V2G experimental apparatus with its control system and reports the results of the preliminary simulation tests.

#### 3.5.1 MOTIVATIONS

Battery-powered electric vehicles (BEVs) and plug-in hybrid electric vehicles (PHEVs) are entering more and more in the market. The use of the today's battery chargers that are able only to drawn power from the grid represents merely a load for the grid. On the contrary, if the EV batteries were connected to the grid by means of bidirectional power apparatuses able not only to charge the batteries but also to exchange power with the grid, the EV power capability could be exploited to execute services in support of the grid operations.

In order to study the integration between electric mobility and renewable energy sources, a micro-grid has been recently installed at the main campus of the University of Trieste [187]. It is composed of a 3.9 kWp photovoltaic generator, a 10 kWh storage battery interfaced to the micro-grid through a 4.6 kVA inverter, a unidirectional charging station for electric cars with two 22 kW charging terminals and an interface board connecting the micro-grid to the 400 V university grid. An under-construction prototypal V2G apparatus is going to be added to the micro-grid, with the purpose of enhancing the potentialities of the micro-grid and enlarging the research topic.

### 3.5.2 RELATED LITERATURE

The supporting services to the grid are commonly termed ancillary services and the expression vehicle-to-grid (V2G) has been coined to denote the services when due to the power transactions of the EVs with the grid [137, 188–190]. Typical ancillary services are voltage and frequency regulations, filtering of line harmonics, balancing of unbalanced loads, compensation of reactive power, spinning reserve and peak shaving. Under this perspective, the V2G power transactions are expected to play an important role in the future scenario of the electric energy systems. The V2G apparatuses are able to carry out ancillary services which can involve either a net flow of active power with the grid or not [56]. In the first case the V2G services can be directed to support the grid by acting the EV batteries as an energy buffer. In the second case, the V2G services can be directed both to stabilize the grid voltage and to improve the power quality. An effective exploitation of the V2G apparatuses is undoubtedly obtained when they are connected to a smart grid [32, 191–193]; this means that the control systems of the V2G apparatuses are networked with the grid administrator via communication devices to send it data on the operability of the apparatuses and to receive from it the requests of ancillary services. For V2G apparatuses of low power, it appears evident the convenience that a number of them operate in an aggregate way so as to be seen by the grid as a single apparatus of reasonable power. Typical energy sources of a smart-grid are renewable sources (wind turbines, photovoltaic fields, mini-hydro). Each of them has specific

operational features which influence the strategies of utilization of the sources, the design of the power converter interfacing the sources with the smart-grid, and the control of the sources. Due to the non-programmable energy generation of most of the renewable sources, the smart-grids are expected to include energy buffers. This functionality can be easily played by the batteries of the EVs and, furthermore, is done on a distributed basis because of the location of EVs over the country [194, 195].

### 3.5.3 EXPERIMENTAL V2G APPARATUS

As mentioned above, a low-scale V2G experimental apparatus was designed and is under construction at the University of Trieste. Many different structures of a V2G power electronics apparatus can be found in the literature [139]. As regards the connection of the V2G apparatus to the AC grid, the most immediate choice was to use a three-phase Voltage-Source Converter (VSC). On the other hand, the choice of the bidirectional DC/DC converter connecting the battery of the vehicle to the DC-side of the grid-connected VSC required the evaluation of a certain number of different possible structures [139]. Among them, we chose the most diffused in the literature, i.e. the dual-active bridge (DAB) [196, 197], thanks to its high power density symmetrical structure and the possibility to include a high frequency isolation transformer. Anyway, the final choice fell on the isolated three-phase dual-active bridge (DAB3), composed of two three-phase VSCs and a three-phase high frequency transformer [141]. The choice of the DAB3 in place of the more diffused DAB, is due to the additional advantage of being composed of two bridges which have one more leg, offering a greater average current sharing, suitable mainly for the battery connected VSC, and giving the possibility of providing fault tolerant operation in case of a faulty leg. Even if fault tolerance may appear to be not essential for battery charges, nevertheless it is an important feature helping to increase energy availability for electric cars and therefore to reduce the so called “range anxiety”, which is one of the major obstacles to diffusion of EVs. Moreover, in V2G systems, it increases the reliability of ancillary services offered to the electric network. Usually, in a charging station more than one vehicle can be connected to charge

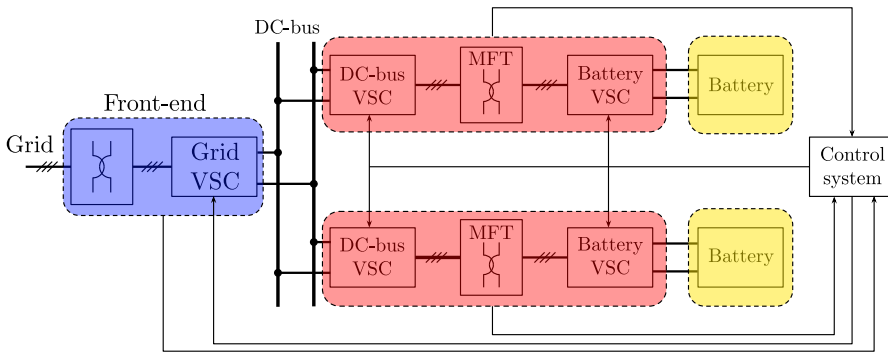


**Figure 3.23:** Block scheme of the experimental V2G apparatus.

its battery. Consequently, the V2G apparatus schematized in Fig. 3.23 was designed to be connected to two 3.3 kWh 52 V lithium-ion polymer (LiPo) batteries, each one connected to the 750 V DC-bus of the V2G apparatus via a DAB3 DC/DC converter. The battery three-phase VSC of the DAB3 is sized to be able to charge the 63 Ah battery at a rate of about 2 C and to draw from it the same current, i.e. 130 A. The V2G apparatus is completed by a grid VSC with the DC side connected to the 750 V DC-bus, endowed with a 4 mF capacitor  $C$ , and the AC side connected to the 400 V university grid via 2 mH filtering inductances  $L_f$  and an isolation transformer. By a modification of the transformer connections, the three-phase VSC has also the possibility to work in single-phase mode. In an advance experimental stage, when the V2G apparatus and its control system will have been extensively tested, the grid VSC can be directly connected to the university power system, excluding the isolation transformer.

### 3.5.4 CONTROL SYSTEM

The control system of the V2G apparatus is based on a dSPACE [198] platform endowed with FPGA boards allowing fast dynamic control. The control algorithm is divided into four different units, namely the DAB3 control unit, the frontend control unit, the DC-bus control unit and the V2G control unit, i.e. a higher level control unit controlling the whole V2G apparatus.

#### 3.5.4.1 DAB<sub>3</sub> CONTROL UNIT

The control system of the V2G apparatus includes two DAB3 control units, one for each DAB3. The DAB3 control unit is devoted to the

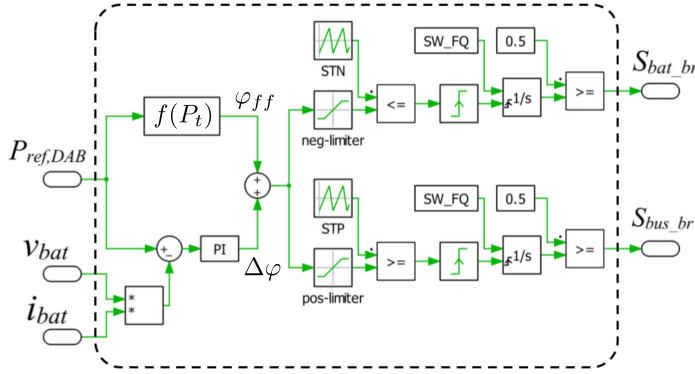


**Figure 3.24:** PLECS block scheme of the DAB3 control unit.

control of the power flowing through the DAB3 in order to transfer energy from the DC-bus to the battery and vice versa. The two VSCs composing the DAB3 are controlled with a switching frequency of 20 kHz in order to obtain a 50% duty cycle square wave at their AC side. As explained in [141], the average power flowing through the DAB3 is a function of the displacement (phase-shift) angle  $\varphi$  between the two square waves produced by each VSC and applied at the primary and secondary winding of the high-frequency transformer connecting the two VSCs. The schematic of the DAB3 control unit captured from the graphical interface of the simulation platform PLECS [199] is shown in Fig. 3.24. The DAB3 control unit receives as an input the reference power  $P_{ref,DAB}$  to be absorbed or to be delivered by the DAB3. By  $P_{ref,DAB}$ , the angle  $\varphi_{ff}$  is calculated using the inverse of the equation, found in [141], giving the average transmitted power  $P_t$  for  $\varphi$  in the range  $(-\pi/3, \pi/3)$ , i.e.

$$\varphi = f(P_t) = \frac{2\pi}{3} \left[ 1 - \sqrt{1 - \frac{9wLP_t}{2\pi dV_1^2}} \right] \quad (3.20)$$

In order to obtain a robust and precise power control, a closed loop control is added to the feedforward control. Angle  $\varphi$  is therefore obtained by adding  $\varphi_{ff}$  to an angle  $\Delta\varphi$  given by a PI controller processing the error between  $P_{ref,DAB}$  and  $P_t$ , being  $P_t$  calculated as the product between the measured battery current  $i_{bat}$  and the measured battery voltage  $v_{bat}$ . Parameters of the PI controller are calculated in order to

obtain a control bandwidth of 1.5 kHz when  $\varphi$  is equal to its maximum value  $\pi/3$ . Since the function  $f(P_t)$  linking  $\varphi$  to  $P_t$  is not linear, the bandwidth changes with  $\varphi$ . Actually, when  $\varphi$  decreases the bandwidth increases. The maximum increase is reached when  $\varphi = 0$  and is equal to one third. As a consequence, the control loop bandwidth varies from 2 kHz to 1.5 kHz for  $\varphi$  varying from zero to  $\pi/3$ . Angle  $\varphi$  is limited between zero and  $-\pi/3$  by the neg-limiter and between zero and  $\pi/3$  by the pos-limiter. Outputs of the limiters are respectively  $\varphi_{neg}$  and  $\varphi_{pos}$ . Angle  $\varphi_{neg}$  is compared to the negative sawtooth wave STN of peak value  $-2\pi$ . When STN becomes lower than  $\varphi_{neg}$ , the output of the comparator switches to one and triggers the positive edge detector which outputs a pulse resetting the integrator  $1/s$ . The input of the integrator is the switching frequency, so that during a switching period its output varies from zero to one. Finally, the output of the integrator is compared to 0.5 in order to produce a square wave signal  $S_{bat,b,r}$  with 50% duty cycle, driving the battery VSC. On the other hand,  $\varphi_{pos}$  is compared to the positive sawtooth wave STP of peak value  $2\pi$ . A square wave signal  $S_{bus,b,r}$  of 50% duty cycle is then produced in the same way as the previous one. It drives the DC-bus VSC.

When the battery has to be charged  $P_{ref,DAB}$  is negative, thus causing  $\varphi_{neg}$  to be negative and  $\varphi_{pos}$  to be zero. In this way the square wave produced by the battery VSC is delayed by  $\varphi$  from the one produced by the DC-bus VSC and the energy flows from the DC-bus to the battery. When the battery has to deliver power,  $P_{ref,DAB}$  is positive, thus causing  $\varphi_{neg}$  to be zero and  $\varphi_{pos}$  to be positive. In this way the square wave produced by the DC-bus VSC is delayed by  $\varphi$  from the one produced by the battery VSC and the energy flows from the battery to the DC-bus.

#### 3.5.4.2 FRONT-END CONTROL UNIT

The front-end control unit is devoted to the control of the grid VSC. Its PLECS schematic is shown in Fig. 3.25. The front-end control unit receives as an input the reference instantaneous real power  $p_{ref}$  and reference instantaneous imaginary power  $q_{ref}$  (defined by the p-q theory [200]) to be exchanged with the electric grid according to the active sign convention. Given  $p_{ref}$ ,  $q_{ref}$  and the measured grid voltages  $v_{sa}$ ,  $v_{sb}$ ,  $v_{sc}$ , transformed to  $v_{s\alpha}$ ,  $v_{s\beta}$  according to the amplitude

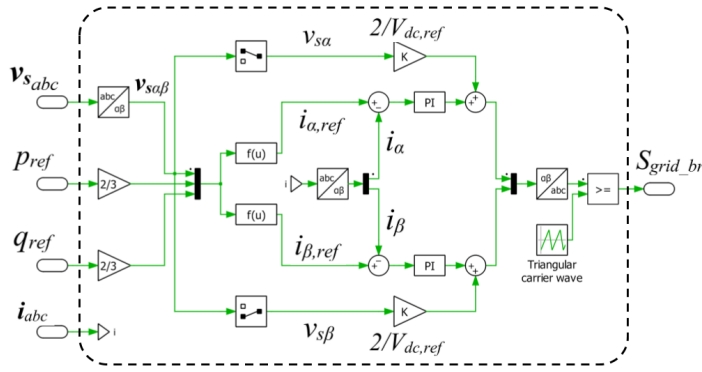


**Figure 3.25:** PLECS block scheme of the front-end control unit.

invariant abc- $\alpha\beta$  transformation, the reference currents  $i_{\alpha,ref}$ ,  $i_{\beta,ref}$  of the grid VSC are then calculated as follows [200]:

$$\begin{aligned}
 i_{\alpha,ref} &= \frac{v_{s\alpha} \cdot p_{ref} + v_{s\beta} \cdot q_{ref}}{v_{s\alpha}^2 + v_{s\beta}^2} \\
 i_{\beta,ref} &= \frac{v_{s\beta} \cdot p_{ref} + v_{s\alpha} \cdot q_{ref}}{v_{s\alpha}^2 + v_{s\beta}^2}
 \end{aligned} \tag{3.21}$$

The measured currents  $i_a$ ,  $i_b$ ,  $i_c$ , transformed to  $i_\alpha$ ,  $i_\beta$  according to the amplitude invariant abc- $\alpha\beta$  transformation, are then subtracted to  $i_{\alpha,ref}$ ,  $i_{\beta,ref}$  and the errors are processed by two PI controllers outputting the voltage drops across  $L_f$ . The outputs of the PI controllers are added to  $v_{s\alpha}$ ,  $v_{s\beta}$  divided by half the DC-bus voltage  $V_{dc}$  in order to obtain  $v_{FE\alpha,ref}$ ,  $v_{FE\beta,ref}$ , i.e. the p.u. reference values of the grid VSC output voltage in the  $\alpha\beta$  reference frame. Finally,  $v_{FE\alpha,ref}$ ,  $v_{FE\beta,ref}$  are submitted to the inverse amplitude invariant abc- $\alpha\beta$  transformation, obtaining the modulating signals for the sub-oscillation PWM producing the 20 kHz driving signals  $S_{grid,br}$  for the grid VSC. Parameters of the PI controllers are calculated in order to obtain a control loop bandwidth of 2 kHz. If the non-optimal quality of the grid voltage or dynamic demanding services such as harmonic filtering require higher performance current control, the PI-based control loops can be substituted with more sophisticated current control systems such as the ones developed in [201].

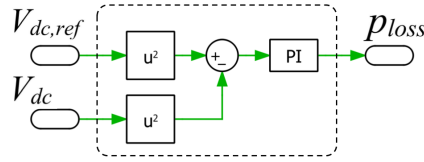


**Figure 3.26:** PLECS block scheme of the DC-bus control unit.

### 3.5.4.3 DC-BUS CONTROL UNIT

The DC-bus control unit is devoted to the control of  $V_{dc}$ , assuring the balance between losses, power exchanged by the DAB3s and power exchanged by the front-end. It is based on the following power balance s-domain linear equation:

$$s \frac{C}{2} V_{dc}^2 = P_{DAB1} + P_{DAB2} - 3V_s I_a \quad (3.22)$$

where  $P_{DAB1}$ ,  $P_{DAB2}$ ,  $V_s$ ,  $I_a$  are respectively the output powers of the two DAB3s, the RMS value of the grid voltage and the RMS value of the grid VSC output current component in phase with the grid voltage. By (3.22) the controlled variable is  $V_{dc}^2$ , as it is shown by the PLECS schematic of Fig. 3.26, where the squared value of the measured  $V_{dc}$  is subtracted to the squared value of its reference  $V_{dc,ref}$ . The error is then processed by a PI controller in order to obtain the instantaneous real power  $p_{loss}$  needed to restore the losses and assure the power balance inside the V2G apparatus. Parameters of the PI controller are calculated in order to obtain a loop bandwidth of 200 Hz. The output  $p_{loss}$  of the DC-bus control unit is sent to the V2G control unit.

### 3.5.4.4 V2G CONTROL UNIT

The V2G control unit includes a high level control algorithm coordinating the control units described above and controlling the charge and discharge of the batteries according to a strategy conciliating the charging needs with the requested ancillary services requiring an exchange of active power. Moreover, it has to exchange information with the grid, receiving the requests of ancillary services and giving feedbacks about the actual possibility to provide them. The PLECS schematic of the implemented V2G control unit is shown in Fig. 3.27. It receives the following inputs: the request of active power  $P_{req}$  and reactive power  $Q_{req}$  to be delivered to the grid, the charging commands  $CHG_1$

and  $CHG_2$  for the batteries (set to 0 for charge not required and 1 for charge required), the SOCs and voltages of the two batteries and  $p_{loss}$ . The algorithm of the V2G control unit operates as explained in the following. If both  $CHG_1$  and  $CHG_2$  are set to 0, then the V2G apparatus can satisfy the request  $P_{req}$  within the limits of its capability and according to a strategy based on SOC of batteries, as described in the following.

1.  $P_{req}$  is positive, i.e. the V2G apparatus is requested to deliver active power to the grid.
  - a) If both batteries have  $SOC \geq 10\%$  then  $P_{ref,DAB}$  is set equal to  $(P_{req} + p_{loss})/2$  and sent to both DAB3 control units. The reference  $p_{ref}$  for the grid VSC is set equal to  $P_{req}$ .
  - b) If one of the two batteries has  $SOC < 10\%$   $P_{ref,DAB}$  is set to zero for its DAB3 while  $P_{ref,DAB}$  is set equal to  $(P_{req} + p_{loss})$  for the other DAB3, which will deliver it or, if it is higher than its capability, the maximum possible. Again,  $p_{ref}$  is set equal to  $P_{req}$  or to the actual power delivered by the DAB3.
  - c) If both batteries have  $SOC < 10\%$ , then  $P_{ref,DAB}$  is set to zero for both DAB3s and  $p_{ref}$  is set equal to  $p_{loss}$ .
2.  $P_{req}$  is negative, i.e. the V2G apparatus is requested to absorb active power to be stored in the batteries.
  - a) If both batteries have  $SOC \leq 90\%$  then  $P_{ref,DAB}$  is set equal to  $P_{req}/2$  and sent to both DAB3 control units. The reference  $p_{ref}$  for the grid VSC is set equal to  $P_{req} - p_{loss}$ .
  - b) If one of the two batteries has  $90\% < SOC < 100\%$ , then power absorbed by the corresponding DAB3 is halved and the other DAB3 absorbs the rest of  $P_{req}$  or the maximum allowed by its capability. Again,  $p_{ref}$  is set equal to  $P_{req} - p_{loss}$  or to the actual total power absorbed by the two DAB3.
  - c) If one of the two batteries has  $SOC = 100\%$ , then power absorbed by the corresponding DAB3 is zeroed and the other DAB3 absorbs all  $P_{req}$  or the maximum allowed by its capability. Once again,  $p_{ref}$  is set equal to  $P_{req} - p_{loss}$  or to the actual power absorbed by the working DAB3.

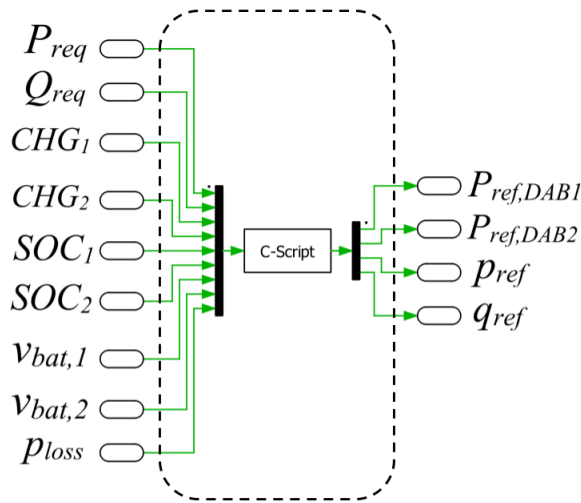


**Figure 3.27:** PLECS block scheme of the V2G control unit.

- d) If both batteries have  $SOC = 100\%$ , then  $P_{ref,DAB}$  is set to zero for both DAB3s. In this case  $p_{ref}$  is set equal to  $-p_{loss}$ , so that the V2G apparatus absorbs only its losses from the grid, thus not being able to satisfy the request to store energy in the batteries.

The request of battery charging has priority over any other request. Therefore, if  $CHG_1$  or  $CHG_2$  is set to 1 the corresponding  $P_{ref,DAB}$  is negative and calculated in order to charge the battery at 130 A up to  $SOC = 90\%$  and then current is halved until the SOC reaches 100%. The other DAB3, depending on the SOC of its battery and the value and sign of  $P_{req}$ , can totally, partially or cannot satisfy the power request. For instance, if  $P_{req}$  is negative the request can be satisfied up to the V2G apparatus capability. On the contrary, if  $P_{req}$  is positive the request cannot be satisfied, but the power absorbed from the grid can be zeroed or at least reduced transferring energy from one battery to the other. Finally, if both  $CHG_1$  and  $CHG_2$  are set to 1,  $P_{ref,DAB}$  is negative, calculated in order to charge the batteries at 130 A and sent to both DAB3 control units. In this case delivery of  $P_{req}$  is inhibited and  $p_{ref}$  is set equal to  $(2P_{req} - p_{loss})$ , i.e. the grid VSC has to absorb from the grid  $2P_{ref,DAB}$  plus the losses.

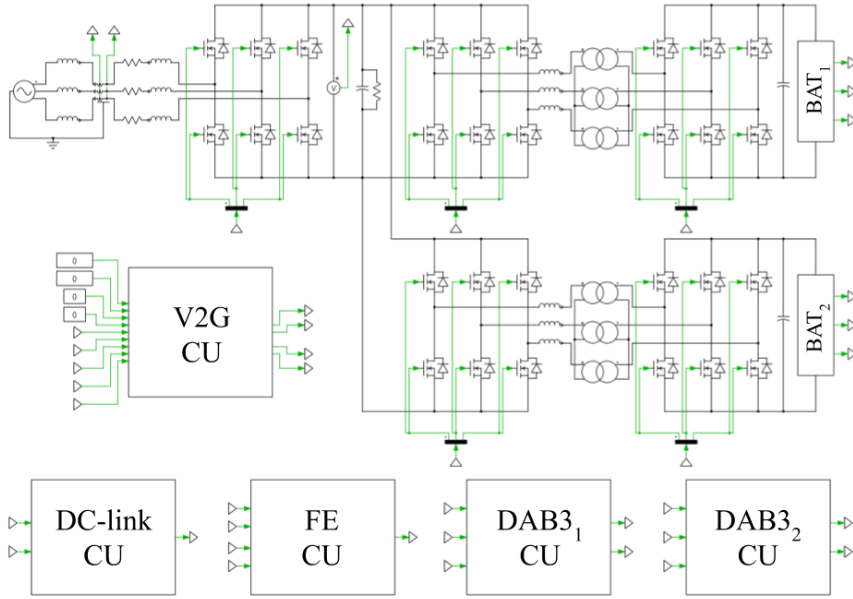


**Figure 3.28:** PLECS schematic of the V2G apparatus and its control system.

### 3.5.5 SIMULATION RESULTS

The described prototypal V2G apparatus and its control system has been modeled in the PLECS simulation environment. Its schematic, captured from the PLECS graphical interface, is shown in Fig. 3.28 and includes both the circuitry and the control system. The circuitry is composed of two batteries (modeled with the equivalent circuit and equations found in [202]), two DAB3s (composed of the battery VSC, the high-frequency transformer and the DC-bus VSC), the DC-bus with its capacitor, the grid VSC with its filtering inductances and the power system. The control system is composed of two DAB3 control units ( $DAB3_1$  CU and  $DAB3_2$  CU), the front-end control unit (FE CU), the DC-bus control unit (DC-bus CU) and the high level control unit, i.e. V2G control unit (V2G CU).

The V2G apparatus has been submitted to a number of tests to check the good operation of the system also in the most demanding transient conditions, where reference power variations are limited by a rate limiter of 2.5 kW/ms. The most significant quantities useful to evaluate the operation of the system are the DC-bus voltage  $V_{dc}$ , the battery currents  $i_{bat1}$ ,  $i_{bat2}$  and the AC output currents of the grid VSC  $i_a$ ,  $i_b$ ,

$i_c$ . The results of three tests, where the starting SOC of both batteries is set to 50%, are described in the following. In the first test, both the charging signals  $CHG_1$  and  $CHG_2$  are zero and the V2G apparatus is supplying the grid with a reactive power  $Q_{req} = 4$  kVAR and an active power  $P_{req} = 4$  kW, being the last one supplied half by  $DAB3_1$  and half by  $DAB3_2$ . Also the losses are supplied half by  $DAB3_1$  and half by  $DAB3_2$ . Traces of the quantities listed above are displayed in Fig. 3.29, showing the good operation of the apparatus in steady state condition and also during a transient, after that, at time  $t_1 = 0.2$  s,  $CHG_1$  is switched to 1. At this event, the V2G control unit commands:

- a)  $DAB3_1$  to stop delivering power and start absorbing power in order to charge the battery
- b)  $DAB3_2$  to deliver all  $P_{req}$  plus all the losses
- c) the grid VSC to continue to deliver  $Q_{req}$  and to absorb the rest of the power needed to charge the battery at the desired current of 130 A.

Fig. 3.29 shows that transient of battery currents and AC output currents last a few milliseconds, while transient of  $V_{dc}$  lasts almost 50 ms, but the amplitude fluctuation is negligible. A different possible strategy could be the one to command the  $DAB3_2$  to deliver the maximum power allowed by its capability. In this way, battery 1 would be charged only with the energy of battery 2 and the active power absorbed from the grid would be zeroed. In the second test, the ability of the V2G apparatus to face the wide power variations required by the most demanding grid requests is checked. Both  $CHG_1$  and  $CHG_2$  are zero during the whole test. At the beginning the V2G apparatus is supplying the grid with  $Q_{req} = 9$  kVAR and  $P_{req} = 12$  kW, being the last one supplied half by  $DAB3_1$  and half by  $DAB3_2$ . At time  $t_1 = 0.2$  s, the grid request is suddenly changed to  $P_{req} = -12$  kW, i.e. the V2G apparatus is requested to absorb power in order to store excess available energy in the batteries. The V2G control unit commands:

- a)  $DAB3_1$  and  $DAB3_2$  to stop delivering power and start absorbing  $P_{req}/2$  each

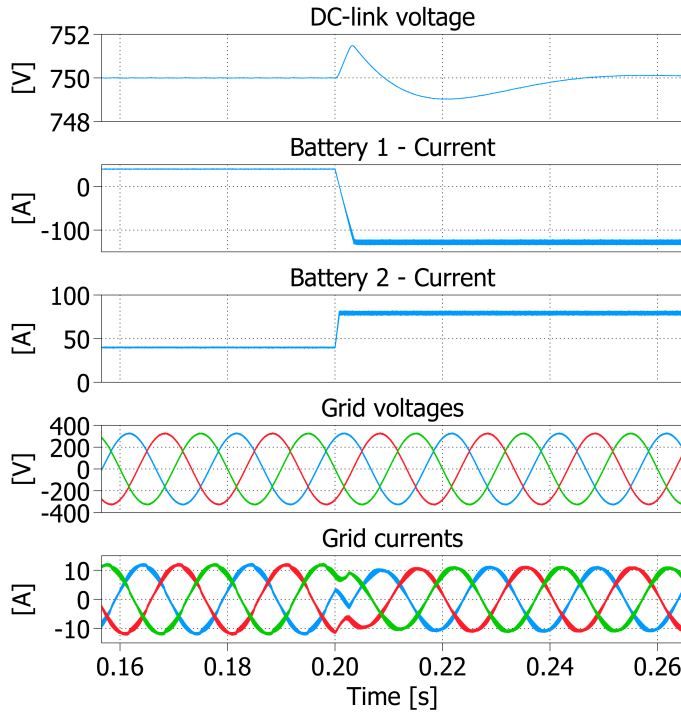


**Figure 3.29:** Test 1: DC-bus voltage, battery currents, grid voltages and output currents of the grid VSC.

- b) the grid VSC to continue to deliver  $Q_{req}$  and to absorb  $P_{req}$  plus the losses from the grid. Test results are displayed in Fig. 3.30, where it is shown that transient of battery currents and AC output currents last roughly 10 ms, while transient of  $V_{dc}$  lasts almost 60 ms. In this case the amplitude fluctuation of  $V_{dc}$  is not negligible, but it is definitely acceptable, being limited to about 3%.

In the third test, at the beginning both  $CHG_1$  and  $CHG_2$  are zero and the V2G apparatus is supplying the grid with  $Q_{req} = 12$  kVAR, while it absorbs from the grid only the losses, because  $P_{req} = 0$ . At time  $t_1 = 0.18$  s,  $CHG_1$  is switched to 1 and the V2G control unit commands:

- a)  $DAB_{31}$  to start absorbing power in order to charge the battery at 130 A
- b)  $DAB_{32}$  to stay in standby
- c) the grid VSC to continue to deliver  $Q_{req}$  and to absorb the power needed to charge the battery plus the losses.

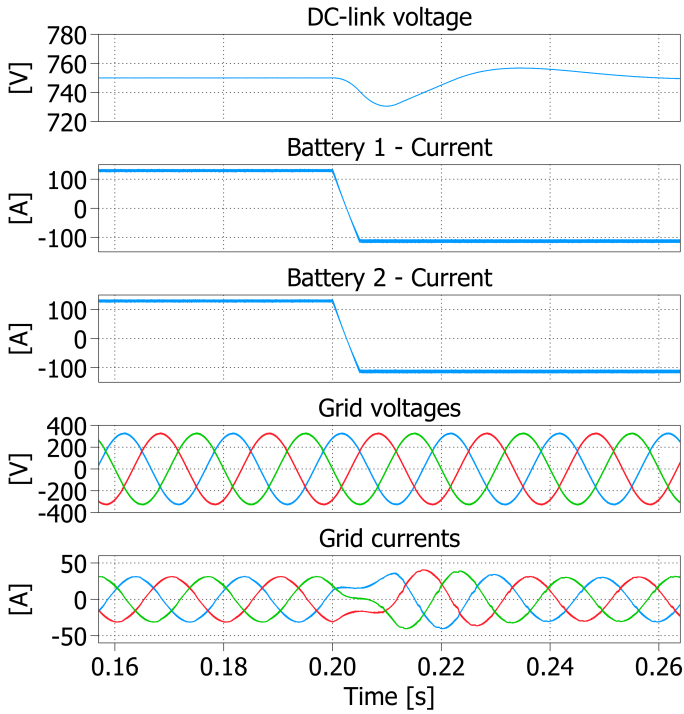


**Figure 3.30:** Test 2: DC-bus voltage, battery currents, grid voltages and output currents of the grid VSC.

As mentioned in the explanation of the first test, a different possible strategy is to take the energy to charge battery 1 from battery 2. At time  $t_2 = 0.22$  s, also  $CHG_2$  is switched to 1 and the V2G control unit commands:

- a) both  $DAB_{31}$  and  $DAB_{32}$  to absorb power in order to charge the batteries at 130 A
- b) the grid VSC to absorb the power needed to charge the batteries plus the losses and to reduce to 6 kVAR the delivered reactive power in order not to exceed its capability.

Of course, in this case the reactive power request is only partially satisfied. Fig. 3.31 shows the test results highlighting once again the good performance of the V2G apparatus, proved by the very fast transients of battery currents and AC output currents and completely negligible fluctuations of  $V_{dc}$ . Further discussions and conclusions about this section can be found in the following section (3.6).

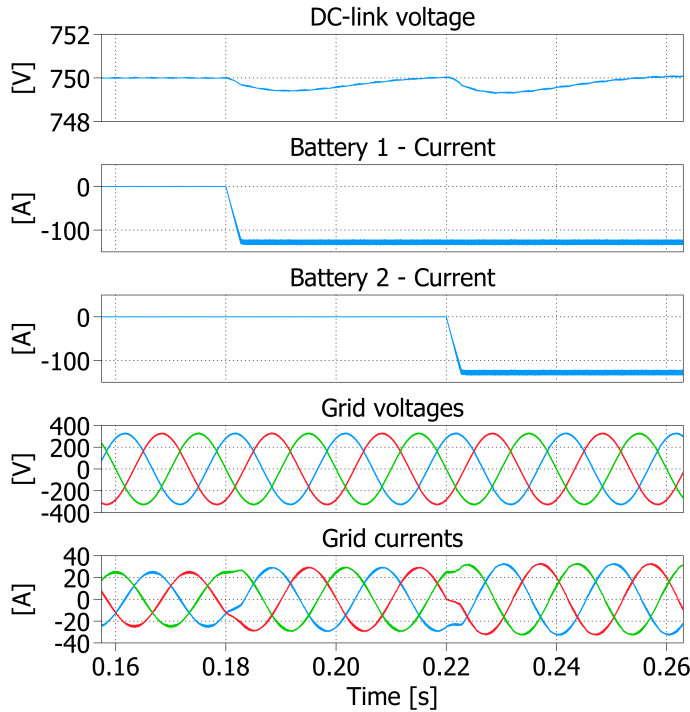


**Figure 3.31:** Test 3: DC-bus voltage, battery currents, grid voltages and output currents of the grid VSC.

### 3.6 DISCUSSION

This chapter presented some studies regarding the integration of electric vehicles from the bottom level, trying to answer the first research question (Q1). In particular, aspects related to the efficiency of DAB converters used for vehicle charging and bidirectional power exchange (V2G), their control to optimize the overall efficiency of the charging system in real-time, and the integration of vehicles with the power grid in case they provide ancillary services to the grid such as active and reactive power exchange were discussed.

In case of variable conditions typical of battery charging process, the first study in Section 3.2 aims to fairly evaluate 1ph-DAB and 3ph-DAB. Device and MFT losses, ZVS ranges, peak and RMS current stresses as well as capacitor filter sizing have been compared between the two topologies, leading to the following findings and considerations. (1) For most conditions, 3ph-DAB switching and, more clearly, conduction losses are higher compared with 1ph-DAB up to 30% and 18%, respec-

tively. (2) ZVS boundaries for 1ph-DAB result in wider soft-switching operations and thus, for a greater range of normalised transferred power than in the 3ph-DAB case, the 1ph-DAB working points lie within the soft-switching region. (3) Particular operating conditions can reduce peak current stress by up to 30% for the 1ph-DAB while 3ph-DAB RMS current is up to 9% higher despite its lower harmonic content. (4) 3ph-DAB requires much smaller capacitors due to reduced voltage and current ripple resulting in smaller volumes and weights.

A trade-off-oriented analysis between dual-active-bridge and lithium-ion batteries efficiency curves is studied and analysed in Section 3.3, showing that an optimal efficiency charging trajectory always exists. Based on the efficiency curves of the DAB at different battery-side voltage levels, the total charging system efficiency is calculated through the losses analysis of different designed lithium-ion battery packs. Supposing the operation of the same DAB with the proposed batteries, optimal operating points for different working conditions are shown, by highlighting the opposite behavior of the efficiency curves of the two components. In particular, optimum efficiency trajectory always exists during the charging process depending on the converter power rating versus battery capacity rating. Several experimental measurements on a 10 kW DAB prototype demonstrate the correctness of the simulated results. This study shows that the interface between converter and battery is a critical step from the point of view of energy efficiency. Consequently, in Section 3.4 it has been possible to develop a control that, by measuring the efficiency of the DAB and estimating the equivalent battery resistance, maximises the efficiency of the total system in real-time with a simple algorithm named Maximum-Efficiency-Point-Tracking (MEPT).

In the last Section 3.5, a prototypal V2G apparatus under construction at the University of Trieste is presented. The apparatus is described, modeled in the PLECS environment and preliminarily tested by simulations. The different control units composing the control system are described in detail and the results of three tests are shown and commented. The good operation of the V2G apparatus and its excellent performance are proven. Upcoming developments concern the experi-

mental test of the grid VSC and further development of the V2G control unit with more sophisticated control strategies.



## EMS FOR EV INTEGRATION: APPLICATIONS AND CASE STUDIES

### 4.1 INTRODUCTION

EMSs are a fundamental tool for managing energy flows within power grids and, if properly designed, allow considerable improvement in economic, technical-energy and environmental aspects based on the constraints considered. With the introduction of storage systems and the strong diffusion of electric vehicles in the grid, it is even more necessary to control the power of the different components in a way that optimizes the different objectives.

In the following sections, three different studies related to the use of EMS for energy flow management within nano-micro grids integrating electric vehicles, storage systems and photovoltaic generation are proposed and analyzed. All of the studies exploit a Model Predictive Control (MPC) approach in order to optimize flows based on future predictions of key variables.

In Section 4.2, an explicit MPC control for energy management within a PV-based EV charging station installed at the University of Trieste is presented and experimentally validated [203]. The main purpose is to assess the economic and environmental improvements of the proposed technique by taking into account the most relevant uncertainties in the system such as PV power, BESS state of charge, EV charging power and both electricity and environmental costs. Further results inherent to the charging station can be found in [204] and the implementation of a two-stage optimization control can be found in [205].

In Section 4.3, the photovoltaic generation and the V2G technology are exploited and integrated in an Alpine ski-resort by using the skier's

EVs as aggregate storage [206]. An MPC-based EMS is implemented in order to minimize the ski resort's costs, its environmental impact and the EVs battery degradation. These aspects are evaluated for future scenarios with different number of charging stations, EV battery capacity and PV system size.

As a last point, a special emphasis was given to the aspects related to one of the latest and most promising strategies for the decarbonization process through the deployment of renewable energy: the energy communities. For this reason, in Section 4.4 the economic and environmental performances of an MPC-based control with ANN-based forecaster for a group of jointly acting self-consumers (JARSCs) are evaluated [207]. Twelve dwellers consumption profiles and common loads such as lighting, elevators and EV charging stations have been used to compare different optimization scenarios in order to analyse several multi-objective optimization results.

## 4.2 A REAL-TIME EMS OF A PV-BASED EV CHARGING STATION ACCOUNTING FOR UNCERTAINTIES

In this section, an Explicit Model Predictive Control (eMPC) for the energy management of an e-vehicle charging station fueled by a photovoltaic plant (PV), a battery energy storage system (BESS), and the electrical grid is proposed. The method computes offline an explicit solution of the MPC, which is stored and then used for real time control. Multi-parametric programming is used to calculate the explicit solution by mapping the MPC laws as a function of uncertain parameters. The uncertainties introduced into the multi-parametric programming are the photovoltaic power production, the electricity price, the battery's state of charge, and the electric vehicle power consumption. Moreover, the environmental impact of the charging station operation is considered through the  $CO_2$  emissions level.

### 4.2.1 MOTIVATIONS

The use of clean and sustainable energy is mandatory to keep  $CO_2$  emissions at a low value. Consequently, the electrical system must face new challenges to supply the necessary power when requested by the EVs with the lowest possible environmental impact. Hence,

suitable solutions are photovoltaic (PV) charging stations, including a battery energy storage system (BESS) connected to the electrical grid. The Energy Management System (EMS) of such stations must provide the energy requested to charge the vehicle with the minimum environmental impact and at the minimum price.

This intelligent charging should consider parameters such as the fluctuation of PV production, the EV charging time, the EV power consumption, the State of Charge (SoC) of the BESS, the electricity price, and the  $CO_2$  emissions related to the energy drawn from the electrical grid. These parameters are commonly treated as certain when scheduling by deterministic optimization is developed. However, in the real time operation of these charging stations, some of these parameters are forecasted with a degree of error, such as PV production,  $CO_2$  emissions, and electricity price, or they are random, like the EV charging time, its arrival, and departure time. The uncertain nature of these parameters could lead to cumulative errors during the day, generating higher environmental and economic costs. Consequently, energy management techniques accounting for uncertainties appear to help improve the energy management quality.

#### 4.2.2 RELATED LITERATURE

In the literature, techniques such as fuzzy, information gap decision theory, and robust optimization have been applied to manage EV charging stations by accounting for uncertain parameters. In [208], fuzzy optimization is applied, where the energy market price fluctuation, the EV's arrival and departure time, and the EV battery's state of charge are considered uncertainties. However, it does not include an electrical power generator employing renewable energy or a storage unit in this case. In contrast, the system studied in [209] includes a PV generator, a storage unit, and a fuel cell. The algorithm used for optimization is information gap decision theory, where the uncertainty accounted for is the load. In [210], it is concluded that affine arithmetic and robust optimization approaches are helpful tools for keeping track of the parametric uncertainties, but at the price of a high computational cost and can result in costly, respectively. However, the downside of these techniques is that the schedule is done once for a certain period.

Despite these are accounting for uncertainties, the schedule calculated cannot be changed in real time operation, which leads to sub-optimal performance of the charging station.

Thus, Model Predictive Control (MPC) is a more suitable algorithm for real time operation by taking into account uncertainties such as disturbances and the future behavior of the system [211]. The control law is determined by optimizing the value of a suitable objective function by considering several constraints and a predictive model. The control law is computed at every sampling time for a particular horizon time by refreshing the state of the system, and the corresponding prediction values [212].

The MPC sampling time can range from several seconds to several hours. In microgrids that include PV systems and EVs, the performance of the control algorithm can be affected by the uncertainty of the solar irradiance level and by the EV's connection/disconnection time and its power demand. Thus, the smaller the sampling time, the smaller these uncertainties affect the control laws. Unfortunately, this may result in a higher computational burden and lower economic efficiency. For instance, in [213], the authors present a MPC for controlling a microgrid where the optimization algorithm is treated by a multi-integer linear programming (MILP). The MPC-MILP calculates the schedule of the energy flow for the different distributed generators every 15 minutes and predicts the system's state for one hour. The computation time takes 24 s, and it is repeated every 15 minutes on an Intel Core 2 Duo CPU, 3GHz. The scheduling is based on the price forecast, power generation, and load, where no error is assumed. When a disturbance to the parameters occurs, the schedule is recalculated. MPC has been used jointly with other techniques to account for uncertainties. In [214], the use of a robust-MPC for a PV-BESS scheduling is proposed, with the economic incentive revenue being considered uncertain. The latter is modeled as a box uncertainty set to get the control law as a function of its robustness. However, the uncertainty set's limits negatively affect the optimal performance of the PV-BESS. The computational time is around 20 ms using a 4.3 GHz CPU. In [215], a MPC-based chance-constraints stochastic optimization is adopted to manage the power flow in a microgrid. The power generation forecast, the demand, and

the EV's connection and disconnection times are the uncertain variables. Although the chance-constraints stochastic optimization benefits from the MPC, this technique significantly affects the computation time, so it is unsuitable for a sampling time lower than one hour.

Explicit MPC (eMPC) reduces the online optimization time and algorithm complexity. This method operates offline to create an explicit function that is a map of the optimal control laws depending on the uncertain parameters and on the active sets related to the given constraints [216]. It inherits the MPC advantages without requiring online optimization. Indeed, during the online operation, it only evaluates the explicit function calculated beforehand, thus offline, by using the actual values of the parameters considered uncertain in the offline MPC based optimization. This approach drastically reduces the online computation time compared to a classical MPC, as stated in [217]. For this purpose, Multi-Parametric Programming (MPP) is a mathematical tool that helps solve the explicit solution of the eMPC problem. The MPP allows creating the optimized control laws as functions of the uncertain parameters, the latter being modeled as bounded ranges of values, thus not as historical sequences of data.

The MPP has been widely used to implement eMPC approaches in batch scheduling, control, and optimization of process system engineering [218]. Instead, in energy, this approach has not been exploited. Few examples use this technique for EMS, accounting for uncertainties in the literature. In [219], MPP has been used to dispatch energy by minimizing a microgrid cost operation. The uncertainties affecting the load consumption, the wind and the PV power production forecasts were accounted for. The computation time for the real time operation is only  $34.8 \mu s$  in contrast with 372 ms using a traditional online optimization. The offline optimization is carried out on a remote cloud platform, and the real time operation on a digital signal processor. In [220] the same technique is used to manage the energy schedule of a combined heat and power energy system. Uncertainty in a rolling horizon framework affects the demand and state of the power units and the heating system. Unfortunately, this approach was not applied to a real system. In [221], an eMPC battery charging control based on eMPC was presented, but no parameters were considered uncertain.

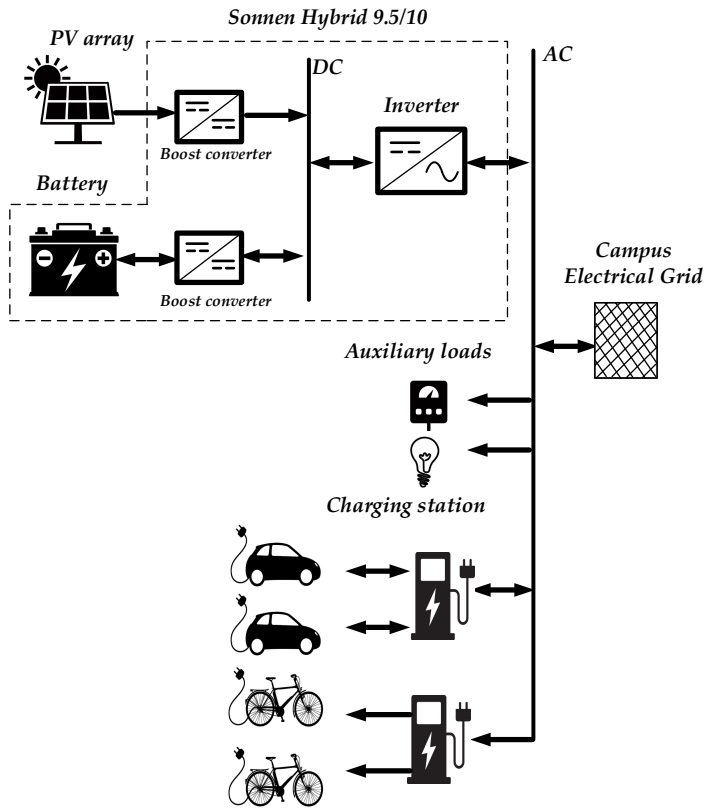


**Figure 4.1:** Main components of the PV based charging station at the University of Trieste

#### 4.2.3 DESCRIPTION OF THE CHARGING STATION

The University of Trieste, thanks to the project MUSE [187], has recently installed a PV based charging station including a Sonnen inverter with an embedded battery. The system is connected to the electrical grid feeding the University campus (Fig. 4.1) The PV array consists of two strings with 7 PV modules each and has a nominal power of 3.9 kWp. The single-phase inverter Sonnen Hybrid 9.5/10 has a maximum power equal to 3.3 kW, and it converts the DC power from the PV array and the Battery to AC. The lithium iron phosphate 10 kWh battery embedded into the Sonnen inverter can deliver a maximum power equal to 3.3 kW. Each of the two charging stations, one dedicated to EVs and the other to electric bikes, has two sockets. The EV and bike charging stations can have a maximum power of 22 kW and 440 W per socket, respectively.

However, the station only charges a specific EV, a Nissan Leaf, for the current study. This car has a 40 kWh battery and an embedded 6.7 kW battery charger.

#### 4.2.4 MODELING AND PROBLEM FORMULATION

To capture the dynamic of the charging station, state space model is commonly used specially for applications in eMPC. This model includes a vector of state variables ( $x(k)$ ) and a vector of control variables ( $u(k)$ ) and takes the following form:

$$\begin{aligned} x(k+1) &= Ax(k) + Bu(k), \\ y(k) &= Cx(k). \end{aligned} \quad (4.1)$$

$A$  is the state-space matrix,  $B$  depends on the coefficients of the control variables and  $C$  is the matrix identity so that the output  $y(k)$  is equal to state variable  $x(k)$  and  $k$  is the time step for a discrete state space model.

For the current application, the BESS's SoC ( $SoC(k)$ ) is the state variable, while the battery charging/discharging power ( $P_{bat}(k)$ ) and the power from/to the main grid ( $P_{grid}(k)$ ) are the control variables ( $u(k)$ ). Thus, the vectors appearing in the state space model are:

$$x(k) = [SoC(k)] \quad (4.2)$$

$$u(k) = \begin{bmatrix} P_{bat}(k) & P_{grid}(k) \end{bmatrix}. \quad (4.3)$$

The system's dynamic is based on the storage unit (BESS) and the balance equation of power of the charging station. In this model, the power fed into the grid is positive, and the one extracted from the grid is negative. In the case of the BESS, the power is positive when it is discharging and negative otherwise. The BESS's  $SoC$  depends on its previous state and the ratio between the current battery capacity and its maximum value  $C_{max}$ . The battery capacity varies with time and depends on its efficiency ( $n_{bat}$ ), the current  $P_{bat}(k)$  and the sampling time ( $T_s$ ):

$$SoC(k+1) = SoC(k) - \frac{n_{bat}T_s}{C_{max}}P_{bat}(k). \quad (4.4)$$

In this model, the efficiency for charging and discharging is assumed to be equal for both cases and positive. Then, the main equation that governs the charging station is the power balance which is the net sum between  $P_{bat}(k)$ ,  $P_{grid}(k)$ ,  $P_{pv}(k)$ ,  $P_{EV}(k)$  at the point of common coupling. The sum should be equal to zero at every time instant, thus:

$$P_{bat}(k) + P_{grid}(k) + P_{pv}(k) - P_{EV}(k) = 0. \quad (4.5)$$

#### 4.2.4.1 PROBLEM FORMULATION

The main goal of the optimization problem is to reduce the  $CO_2$  emissions and operational costs. This goal is gained by minimizing the grid power feeding the EV for a specific prediction horizon ( $N_p$ ), thus maximizing the exploitation of the PV/BESS system. Moreover, the BESS should charge only when PV power is available. Thus, the objective function includes three terms: the power from the grid, the BESS, and finally, the power from the PV. The three weights ( $\alpha_1$ ,  $\alpha_2$ ,  $\alpha_3$ ) assign the priority to each power source. The objective function is expressed as follows:

$$\min J(k) = \sum_{k=1}^{N_p-1} \alpha_1 P_{grid}^2(t+k) + \alpha_2 (P_{bat}^2(t+k)) + \alpha_3 (P_{pv}^2(t+k)) \quad (4.6)$$

According to the strategy explained above, the highest priority is given to the group of the PV/BESS. Meanwhile, the lowest priority is given to the grid, as the main objective is to minimize the energy consumption from the grid. These values remain fixed during this study. The weight factors,  $\alpha_1$ ,  $\alpha_2$ , and  $\alpha_3$  have been selected by using the guidelines presented in [222], and by testing different weight factors to check the system's performance. The testing of these weight factors was performed with the main goal of the grid energy minimization. On this, it is important to mention that the BESS should not be charged during night hours by the grid. During the day, the BESS can be charged by the available PV production. However, if the EV connects during the day and the BESS is not fully charged, the BESS and the EV could have power coming from the PV production. Thus,  $\alpha_2$  and  $\alpha_3$  are equal. For this application,  $\alpha_1$  is 0.016, ( $\alpha_2$ ) and ( $\alpha_3$ ) are set to 0.014. These

values allow a good trade-off between minimizing the power provided by the grid and the MPC controller stability.

#### 4.2.4.2 CONSTRAINTS

The constraints are formulated by considering the safety limitations of the system. The  $SoC$  should be inside some safety limits in order to prevent the battery degradation. The maximum and minimum power limitations for the battery and the PV system are considered too:

$$\begin{aligned} SoC^{min} &\leq SoC(k) \leq SoC^{max}, \\ P_{grid}^{min} &\leq P_{grid}(k) \leq P_{grid}^{max}, \\ P_{bat}^{min} &\leq P_{bat}(k) \leq P_{bat}^{max}. \end{aligned} \quad (4.7)$$

In the real system considered for the experimental validation of the eMPC, the PV system, and the BESS are both managed by the same inverter ( $P_{inv}$ ), so that the following additional constraints are accounted for:

$$\begin{aligned} P_{inv}^{min} &\leq P_{inv}(k) \leq P_{inv}^{max}, \\ P_{inv}(k) &= P_{pv}(k) + P_{bat}(k). \end{aligned} \quad (4.8)$$

#### 4.2.4.3 MPP FORMULATION

Because the online solving of the previous problem formulation can be time-consuming in a real implementation, MPP is formulated in order to solve the problem offline over predefined ranges of parameters treated as uncertain.

In the current case, the cost objective function presented in (4.6) is translated to a MPP-Quadratic Programming (MPP-QP), which obeys the following expression:

$$\begin{aligned} J(\theta) = \min_{u \in \mathbb{R}} & (Qu + H\theta + c)^T u \\ \text{s.t. } & G(\theta)u \leq W + E\theta \\ & \theta \in \Theta \subset \mathbb{R}^q \\ & \theta_l^{min} \leq \theta_l \leq \theta_l^{max}, l = 1, \dots, q. \end{aligned} \quad (4.9)$$

On this equation,  $\Theta$  is the space of the uncertainty parameters,  $Q \in \mathbb{R}^{(nxn)}$ ,  $H \in \mathbb{R}^{(nxq)}$ ,  $c \in \mathbb{R}^n$ ,  $G \in \mathbb{R}^{(mxn)}$ ,  $E \in \mathbb{R}^{(mxn)}$ ,  $W \in \mathbb{R}^m$ , and

$E \in \mathbb{R}^{(mq)}$ . The objective function (4.6) is formulated according to the quadratic MPP function presented in (4.9), thus  $Q$ ,  $H$ ,  $c$ ,  $G$  and  $W$  are computed from the matrices  $A$ ,  $B$  and  $\alpha$ . The mathematical transformation is explained in [223].

The solution to the problem is a piecewise affine function defined by the active sets constructed due to the constraints and the limits given by the uncertainties. Every function defines a polygon, known as a Critical Region (CR). By definition, in the CRs, the objective function relates to each of the uncertainties and their combination. Each CR gives the optimal value of the control variable vector ( $u(\theta)$ ) when the uncertain parameters assume values falling in that CR [218].

#### 4.2.4.4 UNCERTAINTIES

In MPP formulation, the uncertainties are modeled as bounds defining the uncertain ranges that could correspond to forecasting errors, variance, or minimum and maximum values. For an MPP formulation, the uncertainties should be those parameters that can be measured in real time. In the present application, these parameters are the PV production ( $\theta_{pv}$ ), the EVs power consumption ( $\theta_{EV}$ ), the BESS's  $SoC$  ( $\theta_{SoC}$ ), all provided by the charging station. Furthermore, electricity price ( $\theta_p$ ) and  $CO_2$  emissions ( $\theta_{CO_2}$ ) are also parameters that can be known in real time and are given by the Transmission System Operator (TSO). Thus, the vector of the uncertainty parameters is defined as:

$$\theta(k) = [\theta_{pv}(k), \theta_{EV}(k), \theta_{SoC}(k), \theta_p(k), \theta_{CO_2}(k)]. \quad (4.10)$$

For the current case, the uncertain parameters assume values within given bounds as follows:

$$\begin{aligned} P_{pv}^{min} &\leq \theta_{pv} \leq P_{pv}^{max}, \\ P_{EV}^{min} &\leq \theta_{EV} \leq P_{EV}^{max}, \\ SoC^{min} &\leq \theta_{SoC} \leq SoC^{max}, \\ Price^{min} &\leq \theta_p \leq Price^{max}, \\ CO_2^{min} &\leq \theta_{CO_2} \leq CO_2^{max}. \end{aligned} \quad (4.11)$$

In order to obtain a possible solution of the MPP for any given day, the ranges assumed for  $\theta_{pv}$  and  $\theta_{EV}$  go from 0 to the maximum PV power and the maximum EV load respectively. In the case of  $\theta_{SoC}$ , the minimum and maximum values are the same as the limitations chosen in (4.7). For the limitations of price and  $CO_2$  emissions, it is necessary to analyze the data given by the TSO from the previous years, in order to see which are the minimum and maximum possible value. In this study, the ranges chosen are wide enough in order that the mapping of the critical regions guarantee the solution for any given case, even for quick variations of the uncertainties.

Two further constraints are added concerning to the two last uncertain parameters. These constraints give a threshold regarding the  $CO_2$  emissions and the electricity price. This threshold is limited by  $\Gamma_1$  and  $\Gamma_2$  for the electricity price and the  $CO_2$  emissions, respectively. The lower the value of  $\Gamma_1$  and  $\Gamma_2$ , the lower the chance to recharge the EV with power from the grid when  $CO_2$  emissions and electrical price are higher in the day. These two constraints are written as:

$$0 \leq \theta_p * P_{grid}(k) \leq \Gamma_1, \quad (4.12)$$

$$0 \leq \theta_{CO_2} * P_{grid}(k) \leq \Gamma_2. \quad (4.13)$$

#### 4.2.4.5 MPP MODEL SOLVING

In literature, a few algorithms for multi-parametric quadratic programming are available. They have three main objectives:

1. the creation of the CRs in the multidimensional space of the uncertain parameters;
2. the calculation of the control law corresponding to each region;
3. the capability to enter into the corresponding CR once the actual value of the parameter that was considered as uncertain during the optimization process becomes known.

Regarding the first objective, the partition of the problem in different CRs is based on computational geometry. This algorithm creates piecewise quadratic models into polyhedral regions limited by the given

constraints, the inputs, and the space of states. The geometric computation algorithm divides the space for every time step of the corresponding prediction horizon. This approach is explained in detail in [216]. As for the second objective, a Parametric linear complementary programming is applied to every created CR. This repeats for the complete parameter space and it is performed offline. Finally, regarding the last goal, a Point location problem is used in order to find the CRs and the corresponding control law [224]. This third step operates on the real values of the parameters, thus it is effectively developed online. More information about these algorithms can be found in [217]. As for the offline optimization procedure, the algorithm steps are summarized as it follows:

1. Divide the parameters space in a range of finite values ( $i$ );
2. Select a parameter ( $\theta$ );
3. Set the constraints and the initial state of variables;
4. Calculate the corresponding critical region ( $CR_i$ ) for the specific ( $\theta_i$ );
5. Solve the MPP quadratic problem to obtain the control law as a function of the parameter ( $u(\theta_i)$ );
6. Store the control function;
7. Repeat this for every time step into the prediction horizon;
8. Repeat the procedure until all the parameter space is analyzed.

Once the critical regions have been created for the entire parameter space, these are used at each time step during the real time operation, when the actual values of the parameters that were considered as uncertain in the offline optimization procedure are known. Thus, the CRs are evaluated as follows:

1. Measure the real values of  $\theta$ ;
2. Search the corresponding  $CR_i$ , such that  $\theta \in CR_i$ ;
3. Calculate the control variables ( $u(\theta)$ ) for the complete  $N_p$ .

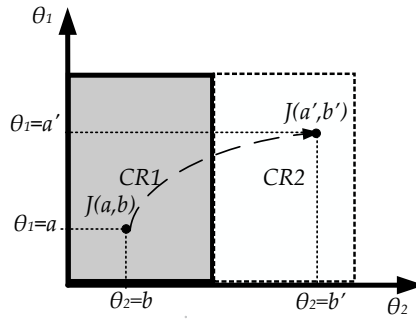


**Figure 4.2:** Simple example of CRs in the space of the uncertain parameters

Fig. 4.2 shows an example of a bi-dimensional space of two uncertain parameters  $\theta_1$  and  $\theta_2$  in which two CRs, i.e., CR1 and CR2, have been generated through MPP. If, during the real-time operation of the system, it is  $\theta_1 = a$  and  $\theta_2 = b$ , then the objective function value  $J(a, b)$  falls within CR1, thus the system control variables are settled according to this. Instead, if  $\theta_1 = a'$  and  $\theta_2 = b'$ , then the objective function value falls in CR2, so that the control variables are settled differently from the previous case. For the current application, the quadratic MPP problem is solved by using the toolbox MPT 3.0 available in MATLAB, with an interface to YALMIP. This toolbox is specialized for parametric optimization, computational geometry and model predictive control. The main solver is Parametric Linear Complementary Programming (PLCP). Additionally, this toolbox permits saving the CRs defined by the control laws in C code, which can be used by other software or platforms.

#### 4.2.5 REAL TIME CONTROL USING EMPC

In this section, the real time control is formulated based on eMPC. The common operation of this technique is to provide an optimal solution for the future, which yields in the current state, constraints, and the given dynamics of the system. In the specific framework of the charging station, this means that, at the current point in time ( $k$ ), an optimal plan is formulated for a prediction horizon ( $N_p$ ) based on the prediction of the response of the BESS, the current  $\theta_{SoC}$ , and the real values of  $\theta_{pv}$ ,  $\theta_{ev}$ ,  $\theta_{CO_2}$ , and  $\theta_p$ . Then, the CRs are evaluated to search for the control law, taking into account the actual values of the uncertainties.

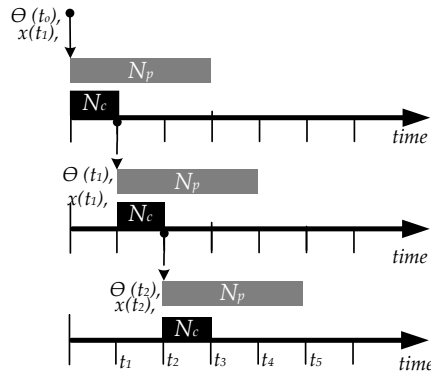


**Figure 4.3:** Example of the eMPC operation ( $N_p$ : Prediction Horizon,  $N_c$ : Control Horizon)

The control variables ( $P_{bat}$  and  $P_{grid}$ ) are chosen from these CRs for the next time step ( $k + 1$ ) known as control horizon ( $N_c$ ). The decision is implemented for this  $N_c$ . At the next step, the new values of the uncertainties and the current state of the battery are measured, and a new optimal schedule is planned. As a result, the horizon is shifted (see Fig. 4.3) at every sampling time. This rolling horizon approach helps to compensate for the optimal solution when new information is available, e.g., uncertainties.

In the current study, the offline mapping of the CRs occurs only once, and it is not repeated at any time of eMPC operation. If the problem formulation changes, e.g., because of the ranges of the uncertain parameters, the constraints, the horizon  $N_p$  and  $N_c$  change, then the CRs have to be recalculated. The operation of the eMPC is summarized in Fig. 4.4.

#### 4.2.5.1 NUMERICAL SIMULATION

This section presents the simulation results of the proposed EMS based on eMPC. It first presents a basic case study to explain the operation of the proposed algorithm. Then, it presents the performance under different settings. The data for the numerical simulation is obtained from the PV/BESS based EV charging station at the University of Trieste. The main parameters of the charging station are summarized in Table 4.1, while those referring to the BESS are collected in Table 4.2. The

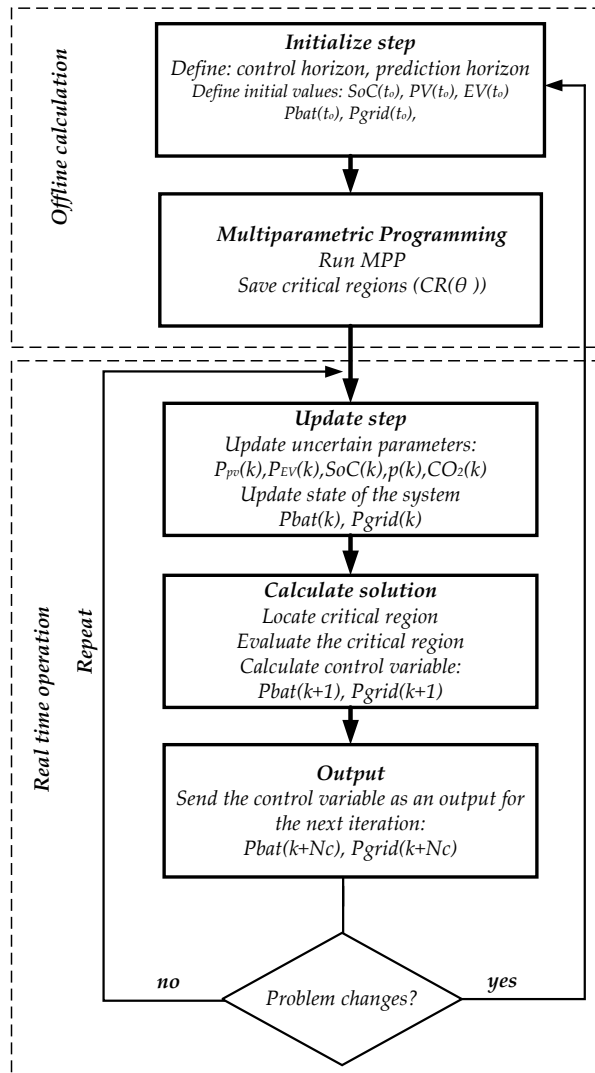


Figure 4.4: eMPC framework

**Table 4.1:** Charging station's main parameters

Parameters	Value	Units
Maximum PV power	3900	W
Maximum battery power	3300	W
Maximum inverter power	3300	W
EV charging power	6700	W

**Table 4.2:** BESS main parameters

Parameters	Value	Units
Technology	Lithium iron phosphate battery	
Normal capacity	10	kWh
Number of max cycles	10000	cycle
Vdc	50	V
Efficiency	98	%
Warranty	10	years
Maximum Power	3.3	kW

data of PV production, EV power consumption, and the SoC of the BESS have been saved with a  $T_s$  of five minutes.

#### 4.2.5.2 CASE STUDY DESCRIPTION

This case study aims to show the way the proposed algorithm works. Thus, the set of uncertain parameters has been limited to  $\theta_{PV}$ ,  $\theta_{EV}$ , and  $\theta_{SoC}$ , so that the CRs can be visualized in three-dimensional space. The ranges of these uncertain parameters (4.11) are listed in Table 4.3. As for  $\theta_{PV}$  and  $\theta_{EV}$ , the upper bounds are set by taking into account the rated power presented in Table 4.1. The upper and lower bounds of the  $\theta_{SoC}$  range have been fixed by considering the safety limits of 10 % and 90 %, respectively.

**Table 4.3:** Lower and upper bounds of the uncertainties

Uncertainties	Min	Max	Units
$\theta_{PV}$	0	3900	W
$\theta_{SoC}$	10	90	%
$\theta_{EV}$	0	6700	W
$\theta_{SoC}$	10	90	%

**Table 4.4:** Vertices corresponding to CR2

$\theta_{PV}$ (W)	$\theta_{EV}$ (W)	$\theta_{SoC}$ (%)
3300	0	90
0	0	90
3300	3300	90
3300	0	68.57

The sampling time chosen for the model formulated in Section 4.2.4 is 5 min. In the objective function presented in (4.6), the weight values are:  $\alpha_1 = 0.016$ ,  $\alpha_2=0.014$ , and  $\alpha_3=0.014$ . For the eMPC, the  $N_p$  is set to 12 time steps and  $N_c$  is equal to one time step. The time step corresponds to the sampling time, i.e., 5 minutes. For this case study, experimental data acquired on the 22nd of July 2020 have been considered.

#### 4.2.5.3 MPP SOLUTION

MPP solves the optimization problem and determines four CRs (Fig. 4.5). These polyhedral regions in the three-dimensional space of the uncertain parameters correspond to 33 variables, 154 inequality constraints, 22 equality constraints. Additionally, 33 lower and upper bounds corresponding to each time step of the  $N_p$  have been considered.

As an example, it is worth noting that CR2 is a pyramid where the  $\theta_{PV}$  varies in the range  $[0, 3300]$  W, the  $\theta_{SoC}$  in the range  $[80, 90]$  %, and the  $\theta_{EV}$  in the range  $[0, 4000]$  W. It has in total four vertices, taking the values presented in Table 4.4. This region is represented as follows:

$$\begin{bmatrix} 1 & 0 & 0 \\ 0 & -1 & 0 \\ 0 & 0 & 1 \\ -0.0065 & 0.0065 & -0.9999 \end{bmatrix} \times \begin{bmatrix} \theta_{PV_k} \\ \theta_{EV_k} \\ \theta_{SoC_k} \\ u_{(k+1)} \end{bmatrix} \leq \begin{bmatrix} 3300 \\ 0 \\ 90 \\ -89 \end{bmatrix}$$

Every CR is associated with a specific set of control variables values and does not mesh up with other regions. The total solution is saved in a look-up table using a memory space of 9 kB.

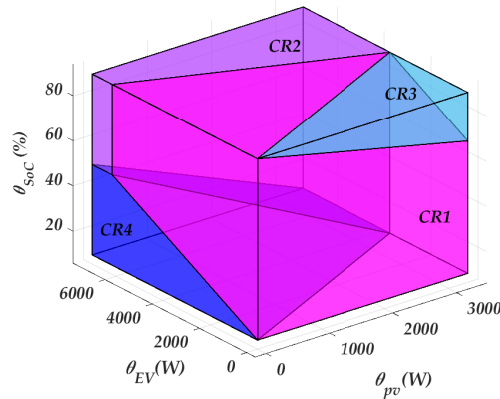


**Figure 4.5:** Critical Regions constructed by the MPP when  $\theta_{PV}$ ,  $\theta_{EV}$  and  $\theta_{SoC}$  are taken into account

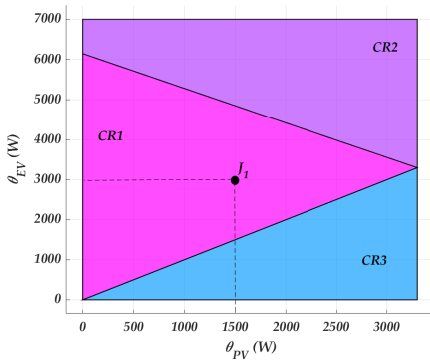


**Figure 4.6:** Critical Regions when  $\theta_{SoC}$  is known and equal to 90 %.

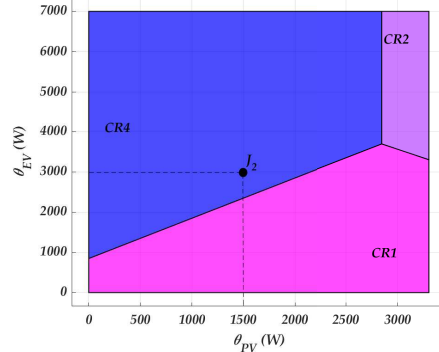


**Figure 4.7:** Critical Regions when  $\theta_{SoC}$  is known and equal to 11 %

#### 4.2.5.4 eMPC PERFORMANCE

The eMPC moves in these CRs by reading the set of actual uncertain parameters values and by evaluating in which CR they fall to get the optimized values of the control variables. For instance, in the case  $\theta_{SoC} = 90\%$ , the solution falls inside one of the CRs that are visible in Fig. 4.5 at the top face of the parallelepiped. This plane is shown in Fig. 4.6, where are three critical regions that depend on two parameters:  $\theta_{pv}$ , and  $\theta_{EV}$ .

As an example of the eMPC operation through the CRs shown in Fig. 4.6, at the first time instant, with  $\theta_{SoC} = 90\%$ ,  $\theta_{pv} = 1500W$  and

$\theta_{EV} = 3000W$ , the objective function takes the value  $J_1$ . The optimized schedule is determined for the  $N_p$ , and only the samples for the corresponding  $N_c$  are implemented. In this case,  $N_c$  is equal to the sampling time. As a result, the EV is fed from the grid for the next sampling time by 694 W, by 805 W from the BESS, and the PV array provides the remaining part.

In another instant, the current values of the uncertain parameters are again measured, and they are:  $\theta_{SoC} = 11\%$ ,  $\theta_{pv} = 1500W$ , and  $\theta_{EV} = 3000W$ , so  $J_2$  is obtained. It falls in CR4, and it is in the plane illustrated in Fig. 4.7. For this value, the EV is fed from the grid by 1045 W, by 455 W from the battery and the remaining part is provided by the PV array.

The evaluation of the CRs with the current values of the parameters that were considered as uncertain during the MPP formulation is repeated every sampling time. The power profiles, computed as described above over the whole day, are shown in Fig. 4.8. In the day considered in this example, the EV connects for recharging early in the morning, at 9 am, when the PV production is still low and the BESS  $SoC$  is close to 90%. The algorithm calculates the optimized control values of  $P_{grid}$  and  $P_{bat}$ . As long as the PV array delivers more power, the battery reduces its contribution. The EV battery recharging terminates after three hours from its connection. Afterward, the PV system recharges the BESS until the  $SoC$  approaches 90%. The maximum PV power is close to 3.1 kW and the BESS recharges in 5 hours.

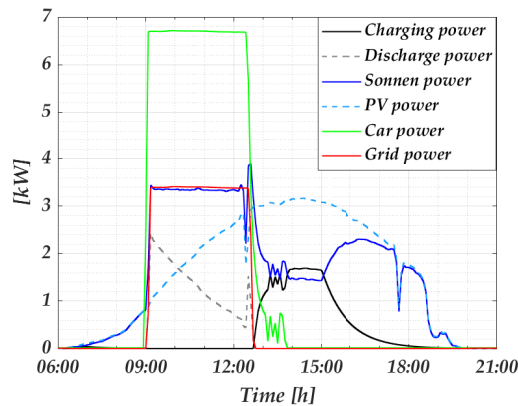


**Figure 4.8:** Power profiles for the simulation test

#### 4.2.5.5 EFFECT OF CHANGING PREDICTION HORIZON AND NUMBER OF PARAMETERS

The prediction horizon and the number of uncertain parameters affect the eMPC performance. This subsection examines their effect on the proposed study from the operational point of view.

First, a number of different  $N_p$  values has been tested with the same number of uncertain parameters presented in Section 4.2.5.2. All the other parameters and the data set remains unchanged.  $N_p$  takes the following values: 3, 12, 24, 36, and 144, which correspond to 15 minutes, 1 hour, 2 hours, 3 hours, and 12 hours, respectively. Fig. 4.9 shows the charging and discharging power of the battery for each of the five  $N_p$  values considered. The EV is connected at 9 am; thus, the battery proceeds supplies power to the charging station. There is no difference among the performance for  $N_p = 3$ ,  $N_p = 12$ , or  $N_p = 24$ . However, this power reduces slightly for the case of  $N_p = 36$ .

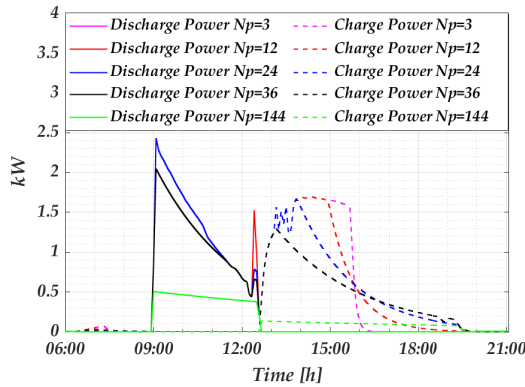


**Figure 4.9:** Battery power profiles for different prediction horizon ( $N_p$ )

Instead, for  $N_p = 144$ , the battery supplies only  $P_{bat}=0.5$  kW. Additionally, at the end of the EV's connection, there is a sudden reduction of the PV production (Fig. 4.8), thus, the battery needs to compensate for the loss of power. In the case of a  $N_p \leq 12$ , the compensation for the quick variation is 1.2 kW. The compensation is less than 0.8 kW for  $N_p = 24$  and  $N_p = 36$ . However, this compensation does not occur when  $N_p = 144$ . After the EV disconnection, the higher the  $N_p$  the smoother the charging power of the battery. For  $N_p = 144$ , the charging power is reduced as the battery has not been fully depleted from the

first interaction with the EV. In any case (charging or discharging), the slow control is because the objective function is evaluated for a longer time. Although the battery shows a slow dynamic, its charging profile varies with the  $N_p$  value.

A further analysis has been conducted by varying the number  $q$  of the uncertain parameters ( $\theta$ ) and thus the number of constraints (see (4.9)). The test is developed for a)  $q = 3$  and b)  $q = 5$ . The prediction horizon is the same for both studies and equal to  $N_p = 12$ . For  $q = 3$ , the main parameters and the study case are described in Section 4.2.5.2. For  $q = 5$ , adds to the previous study  $\theta_{CO_2}$  and  $\theta_p$ . Their bounds and the additional parameters are in Table 4.5 and 4.6. The dataset of PV production and EV consumption are the same as Section 4.2.5.2. The power profile of the both cases remains the same, and it does not present any variation under the performed parameters. This is because  $\theta_{CO_2}$  and  $\theta_p$  affects directly on the amount of power bought from the grid but not the one related to the battery. The variation of these parameters and its effect on the system are tested on the real time operation.

**Table 4.5:** Lower and upper bounds of the uncertainties

Uncertainties	Min	Max	Units
$\theta_{PV}$	0	3900	W
$\theta_{SoC}$	10	90	%
$\theta_{EV}$	0	6700	W
$\theta_p$	0.03	0.1	€
$\theta_{CO_2}$	0.3	1	kg

**Table 4.6:** Main parameter's values

Parameter	Value	Unit
$\Gamma_1$	2	€/W
$\Gamma_2$	2	kg/W
$N_p$	12	
$N_c$	1	

#### 4.2.5.6 EVALUATION OF COMPUTATIONAL PERFORMANCE

The evaluation of the computational operation is performed by varying the number of uncertain parameters and the prediction horizon. As first, it is tested for  $q = 3$  and a  $N_p$  that varies from 3 to 144. Afterwards, the analysis is performed for  $q = 5$  with the same variation of  $N_p$  as the case before. The number of regions created, variables, inequality and equality constraints are summarized in Table 4.7. Additionally, the computation time and the size of the file containing the data describing the CRs for each case are also shown. The increase of the number of parameters determines an increase of the number of regions. In this case, the number of CRs does not change with  $N_p$ . Instead, the computation time increases as the number of  $\theta$  and  $N_p$  increase. On the same processor mentioned above, it can go from 0.15 s to 2400 s by only varying  $q$  and  $N_p$ . However, for  $q = 5$  and  $N_p = 144$ , the solution is infeasible after 12 hours of simulation. As the number of parameters increases, the file's size where these values are stored also increases, but it keeps in the order of kB. These files can be used in any hardware or platform to do the real-time control. The larger file is obtained when the  $N_p = 144$  with a  $q = 3$ , but it is only 84 kB. It can be easily saved and used by any low cost platform. To access the file in online optimization only takes 0.019 s. Thus, it did not change with any variation of  $N_p$  or the number of  $\theta$ .

In conclusion, the eMPC parameters affect performance and the offline optimization computation time. Although the offline computation time increases with the number of parameters, the online use of the CRs resulting from the offline optimization of the eMPC always needs the same computation time. This is because the online procedure only searches for the specific control laws by inspecting the CRs according to the system's current status. This one represents the significant advantage of eMPC with respect to a simple MPC.

#### 4.2.6 EXPERIMENTAL VALIDATION

Two testbeds were used to evaluate the proposed EMS strategy's control and computing performance. The first testbed (Testbed 1) is completely based on a personal computer (PC), while the second includes a dSPACE Scalexio (Testbed 2) as shown in Fig. 4.10.

**Table 4.7:** Computational performance

$q$	Np	CR	Variables	Inequality constraints	Equality constraints	Time [s]	File size [kB]
3	3	4	6	28	4	0.15	2.76
3	12	4	33	154	22	0.605	9
3	36	4	105	490	70	5.15	25
3	144	3	429	2002	286	506.7	84
5	3	4	6	44	6	0.188	4
5	12	6	33	242	22	2.213	10
5	36	6	105	770	70	2400	33
5	144			Infeasible		43200	-

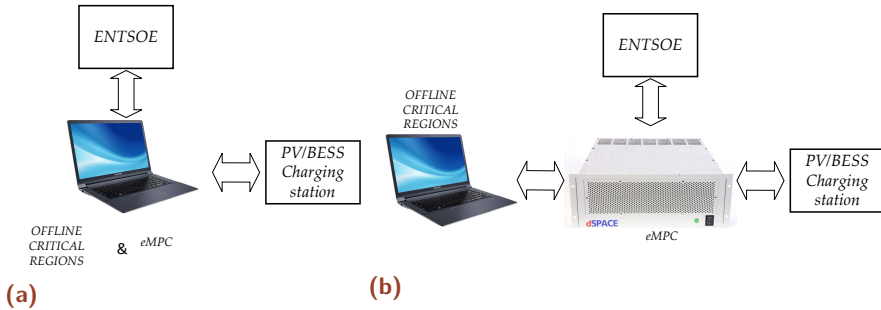


**Figure 4.10:** Testbed layout for the experimental validation: (a) Testbed 1 and (b) Testbed 2

There are two purposes of this experimental validation. The first one is to overview the EMS's performance under the effect of five uncertain parameters. The uncertainties considered are  $\theta_{pv}$ ,  $\theta_{EV}$ ,  $\theta_{SoC}$ ,  $\theta_{CO_2}$  and  $\theta_p$ . The upper and lower bounds of these uncertain parameters (4.11) are listed in Table 4.5. The bounds for  $\theta_p$  and  $\theta_{CO_2}$  are fixed by considering the historical data of the electrical system in Italy, referring to the years 2020 and 2021 [225]. The second purpose is to overview the computing performance under different hardware.

In both testbeds, the  $CO_2$  emissions are calculated by using the type of power generation given by ENTSO-E along the day. For comparison, the variation of the price and the  $CO_2$  emissions are assumed to be equal to the ones presented in Fig. 4.11 for all the tests.

Table 4.6 collects the used values of the factors and the constants involved in the optimization model. The results achieved by using the two testbeds are described in the following subsections.

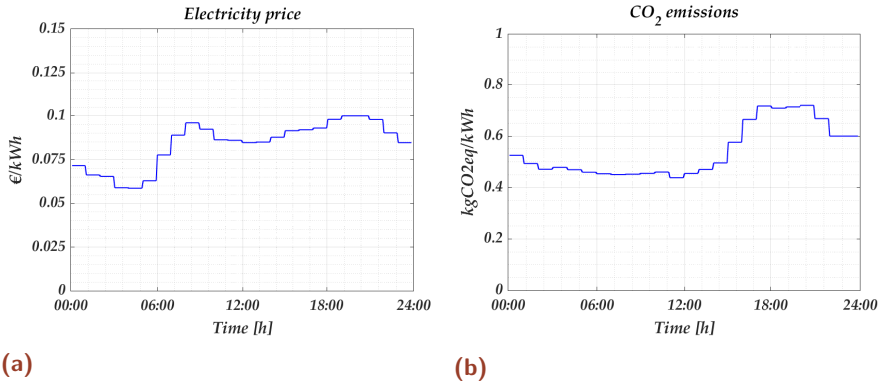


**Figure 4.11:** Single day data of (a) electricity price and (b)  $CO_2$  emissions

#### 4.2.6.1 TESTBED 1

The PC used is an Intel i5-8500 processor with a frequency of 3 GHz and a memory RAM of 16 GB. The eMPC runs in Matlab/Simulink. It interacts with the charging station through a TCP/IP protocol to set the control signals and to receive the actual  $P_{pv}$ ,  $P_{EV}$ , and  $SoC$  values. It also receives from ENTSO-E the prices and type of power generation. In this case, the communication between the PC and the charging station occurs every 5 minutes, i.e. the sampling time. The control horizon is equal to the sampling time ( $N_c=5$  min) and the prediction horizon is fixed at three times the  $N_c$ , thus at  $N_p=15$  min.

The MPP is run offline to map the CRs. Then, the eMPC operates at every  $N_c$  by reading its inputs, accessing the CRs to fix the optimal values of the control variables, and finally sending these values of the control signals to the charging station. For each  $N_c$ , the eMPC takes 0.019 s to access the CRs and 2.5 s to read its actual input values and settle the optimal values of the control variables of the charging station. The MPP needs 0.34 s of computing time to determine the 4 CRs.

The power profiles referring to the 1st of July 2021 are shown in Fig. 4.12. The EV connects for recharging at 9 am. During the four hours of charging, the PV array and the BESS feed the charging station with their maximum power, i.e. 3.3 kW. Afterward, when the EV is fully charged, the PV array recharges the BESS (40 to 90 %). The rest of the power comes from the electrical grid.

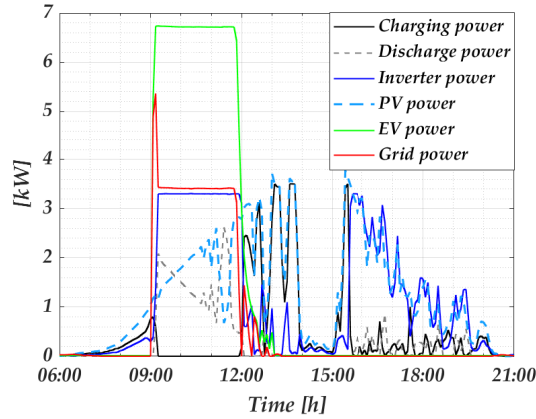


**Figure 4.12:** Power profile for Testbed 1 (Day 1)

In this result, it is important to notice that the PV/BESS has a slow response to the variations of PV production and load due to the chosen value of the sampling time and  $N_p$ . Phenomena occurring on a shorter timescale, thus within two consecutive  $N_p$ s, receive a delayed counteraction from the EMS.

#### 4.2.6.2 TESTBED 2

The second testbed uses dSPACE for implementing reactive scheduling. The processor board is a DS6001 equipped with an Intel i7-6820EQ processor with a frequency of 2.8 GHz. This processor has four cores and a memory of 4GB RAM plus 8 GB of flash memory.

In testbed 2, the dSPACE communicates with the charging station through the TCP/IP protocol to receive the values of  $P_{pv}$ ,  $P_{EV}$  and  $SoC$  at each sampling time and to set the control signals ( $P_{bat}$ ). Additionally, it communicates with ENTSO-E to get the prices and the type of power generation every hour. As for Testbed 1, the MPP is run offline to get the CRs which are saved in the dSPACE as a lookup table. The eMPC runs in the dSPACE platform and evaluates the CRs at every sampling time with the actual data. For testbed 2, the sampling time chosen is one second; thus  $N_c=1s$ , and the prediction horizon is  $N_p=3s$ .

Two days have been chosen to evaluate this configuration's performance. On day 1 (7 July 2021), the EV is connected for recharging in the morning. The PV/BESS and the grid supply power to the EV. During the day, when the PV production rises, the BESS reduces its contribution

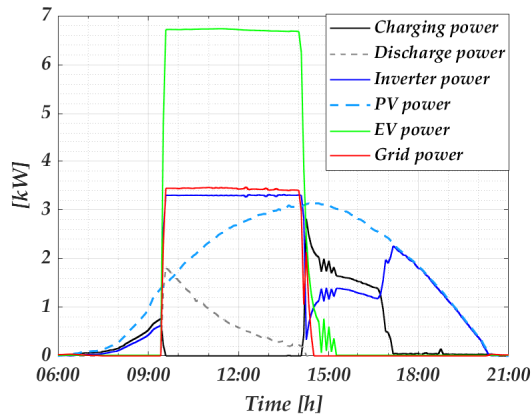


**Figure 4.13:** Power profile for Testbed 2 (Day 1)

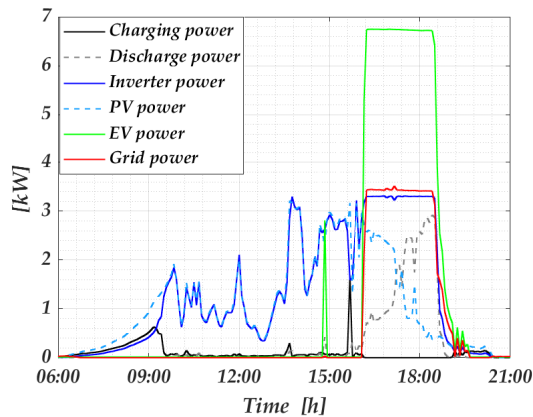


**Figure 4.14:** Power profile for Testbed 2 (Day 2)

proportionally. As a result, the BESS's  $SoC$  drops from 90 % to 42 %, and it is recharged in the afternoon. On day 2 (8 July 2021), the EV was connected at 4 pm, during a day characterized by a large PV production variability. Unlike Testbed 1, thanks to the shorter  $N_c$ , the PV/BESS response is not delayed; thus the fast fluctuations of the PV production and the EV usage are accounted for properly. The  $SoC$  of the BESS decreases from 90 % to 40 %. The BESS is not recharging from the grid at night and remains at 40 % until the next day.

#### 4.2.6.3 COMPUTING PERFORMANCE ON BOTH TESTBEDS

Table 4.8 summarizes the computing times required by the two testbeds. In both cases, the mapping of the CRs is performed offline, on the PC, and only once. The eMPC in any testbeds takes less than one second as

**Table 4.8:** Comparison between Testbed 1 and Testbed 2

	Testbed 1	Testbed 2
MPP	0.34 s	0.34 s
eMPC	0.019 s	0.001 s
Online communication	2.5 s	1 s
Sampling time	300 s	1 s

**Table 4.9:** Variation of  $CO_2$  emissions and price by considering different values of  $\Gamma$ 

$\Gamma_1 = \Gamma_2$	Parameters	Day 1	Day 2
1	$P_{grid_{max}}$ [W]	554	245
	Maximum Power PV/BESS [W]	3300	3300
	$CO_2$ [kg]	0.6474	1.199
	Price [€]	0.1001	0.1707
	Number of critical regions	5	5
1.2	$P_{grid_{max}}$ [W]	1557 -3300 W	1983
	Maximum Power PV/BESS [W]	3300	3300
	$CO_2$ [kg]	61.71	44.2121
	Price [€]	11.49	5.9743
	Number of critical regions	6	6
1.4	$P_{grid_{max}}$ [W]	3700.00	3700.00
	Maximum Power PV/BESS [W]	3300	3300
	$CO_2$ [kg]	91.06	75.8168
	Price [€]	17.12	10.23
	Number of critical regions	4	4

execution time. Thus, regardless of the testbed considered, this time remains the same. The most significant difference between the two platforms is the time needed to communicate with the charging station.

#### 4.2.6.4 ANALYSIS OF COST AND $CO_2$ EMISSIONS

To analyze the cost and the  $CO_2$  emissions, different values for  $\Gamma_1$  and  $\Gamma_2$  are explored and evaluated using the data from day 1 and day 2. Three specific values are chosen: 1, 1.2, and 1.4 and it is assumed that  $\Gamma_1 = \Gamma_2$ . The results are summarized in Table 4.9.

The variation of  $\Gamma_1$  and  $\Gamma_2$  affects the charging station's response. If  $\Gamma$  is less than 1, the power from the grid will be limited, and only PV/BESS,

thus not the grid, are allowed to supply power to the EV (3300 W). This lengthens the EV's charging time or the charging process terminates before the full charge is reached. If  $\Gamma$  is settled at 1.2, the grid delivers a maximum power of 1557 W from 9 am to 11 am on day 1, and 3300 W in the next 2 hours as the electricity price is lower. On day 2, however, the charging station provides 5283 W, whereas the grid only provides 1983 W. This is owing to the fact that prices and  $CO_2$  emissions are higher in the afternoon, limiting the amount of power supplied from the grid. In the case  $\Gamma$  is greater than 1.4, the EV can be charged to its maximum capacity of 6900 W and be fully charged in roughly 4 hours for any of the two days tested.

#### 4.2.6.5 COMPARISON WITH TRADITIONAL METHOD

To show the advantages of the proposed eMPC, a comparison with a conventional MPC is proposed. The problem formulation is the same presented in Section 4.2.4 for the proposed eMPC. The constraints and limits of the parameters are also the same. The uncertainties are defined as part of the constraints with the same bounds. The MPC, in this case, reads at every sampling time the actual values of the PV power production, the BESS  $SoC$ , the EV power absorption, the electricity price and the  $CO_2$  emissions. Then, it runs the optimization algorithm and calculates the values of  $P_{bat}$  and  $P_{grid}$  to settle at every sampling time. Next, it sends the values of the control variables as outputs to the charging station. The values  $P_{bat}$  and  $P_{grid}$  calculated by the deterministic optimization are the same as the ones from the eMPC approach. The power profiles are equal to the ones presented in Fig. 4.13 and Fig. 4.14. Instead, the computation time required by the optimization at every time step varies from 0.06 to 0.1 s, while the eMPC approach only requires 0.019 s to access the CRs at each sampling time (Table 4.8).

#### 4.2.7 DISCUSSION

In this study, the application of the eMPC to an e-vehicle charging station based on PV/BESS by accounting for five main uncertainties is shown. The uncertainties affect:  $\theta_{pv}$ ,  $\theta_{SoC}$ ,  $\theta_{EV}$ ,  $\theta_{CO_2}$ ,  $\theta_p$ . The main advantages by using this approach can be summarized as follows:

- the general problem formulation assembles to a common MPC, making it easier to code and to implement for any application. The MPT toolbox by MATLAB helps to transition from MPC to a MPP to create the CRs in offline mode;
- the uncertainties are modeled by fixing a range of real values for each of them. These bounds can be min/max operation values or forecast errors. In this application, it was chosen to use bounds characterized by min/max operation values. This comes in handy, especially for uncertainties that are difficult to forecast and for which no historical data is available. For instance, in the current application, the main uncertainty is the one related to the EV's connection, disconnection and power consumption. This uncertainty is modeled by a range of values between 0 and 7 kW. Also, the uncertainty of PV production, the price and  $CO_2$  emissions are modeled in the same way. In the case of PV power, the boundaries allow considering sudden changes of solar irradiance during the day. For instance, the 2nd of July 2021 in Trieste, the PV production reduced to 0 in less than 1 minute in the afternoon due to a cloud passing. Because of this behavior, the limits for the PV production are set between 0 and 3.3 kW. The modeling of price and  $CO_2$  emissions by using means of a couple of bounds allows considering a wide range of values;
- the main advantage of using this technique is the computation time in online mode. eMPC is based on two main aspects: creating the CRs in offline mode and the rolling control horizon in online mode. The second one, only evaluates the CRs saved beforehand. For the evaluation, it only takes 0.019 seconds to extract the control values from the CRs. By using other approaches as stochastic-MPC, reported in [215], it takes 1.04 seconds for a  $N_p = 12$ ,  $N_c = 3$ . Plus, it only takes into account one uncertain parameter. In our case, the number of uncertainties is 5 and the evaluation is 55 times less than the cited example. Because the EV can come at any time, the optimization online has to be fast. Thus, calculating the control laws beforehand offers a great advantage for this type of application;

- the control laws can be exported in C and python language, making them independent of MATLAB or the MPT toolbox for the real time control. This helps the porting of the real time control to any platform. Its use in FPGAs [226] and chips [219] makes eMPC suitable for low-cost platforms.

The main drawbacks of the proposed eMPC technique are summarized as follows:

- The offline computation time and memory usage increase with the problem's dimensions. The number of CRs increases with the number of parameters, constraints, and number of components. Thus, the offline computation time increases. Therefore, the proposed approach fits with low dimensional systems.
- The use of license software to construct the critical regions as MPT Toolbox and that runs under Matlab framework. The mathematical approach behind the construction of the CRs can be complex. Thus, the use of a toolbox or a programming tool is necessary. This can be a drawback in the case it is required to reconstruct the CRs.

## 4.3 VEHICLE-TO-SKI: A V2G OPTIMIZATION-BASED COST AND ENVIRONMENTAL ANALYSIS FOR A SKI RESORT

Ski resorts are becoming perfect demonstrations for the integration of renewable sources. This section aims to study the implementation of a vehicle-to-grid (V2G) application and the development of an MPC-based energy management system (EMS) within a ski resort in the Trentino-Alto Adige Italian region. Using real data for load and production power estimation, the study analyses the economic and environmental impact in three different scenarios by considering the resort's future trends.

### 4.3.1 MOTIVATIONS

Tourism plays a key role in a country's economy. Especially in countries with large mountain ranges such as the Alps, winter tourism attracts up to 15% of the world tourism flow [227]. Tourism depends on a combination of environmental, economic, political, and technological factors. Ski tourism benefits from snowy landscapes with climate characteristics playing a decisive role. Climate change is becoming a concern for the sector, demanding timely solutions due to rising temperatures and snow shortages. Research might help understanding how climate change impact winter tourism identifying the correlations and incidence of different meteorological variables [228, 229]. Ski resorts are the core of winter tourism. Their services include not only the ski-lifts but also catering, water management, slope maintenance and snowmaking. A ski resort is extremely energy intensive throughout the day, absorbing large amounts of electricity and consequently contributing to the environmental impact in terms of equivalent  $CO_2$  emissions. Moreover, ski resorts commonly use diesel-powered vehicles, thus exacerbating the  $CO_2$  emissions. Nevertheless, ski-resorts can become important assets for the development of an energy sustainable community thanks to the introduction of renewable energy sources.

### 4.3.2 RELATED LITERATURE

In the literature, different studies aims to analyse ski-resort energy flows from different point of view. For instance, [230] presented a study of distributed energy generation in a Colorado ski resort, assessing the economic and technical feasibility of feeding both electrical and thermal

loads. Their results indicated that solar and wind generation are not yet cost-competitive as a CHP (Combined Heat and Power) plant for the annual base load. However, [231] demonstrated in study focusing on solar, wind and hydro power that the three technologies can be implemented for any ski resort with some consideration of individual barriers and constraints. [232] evaluated an Alpine microgrid through the integration of RES (Renewable energy sources), focusing mainly on the study of voltage drops on power lines. However, the integration of electric mobility is only mentioned with the aim of increasing the sustainability of the system. Due to the global EV acceptance, an increasing number of EVs in the coming years will lead to a necessary expansion of the electric charging facilities at the ski resorts. If bidirectional charging stations are developed, it would be possible to exploit the aggregate capacity of EVs to provide V2G services. Considering the amount of energy flow involves in the ski resort, one wonders what is the best way to manage energy flows within the local energy system aiming to maximize or minimize specific objectives. Research has dedicated considerable effort to the development of EMS, EVs management and V2G technology [233, 234], including both optimisation and real-time aspects [235–237]. For example, [238] presented a multi-objective EMS for EV charging and discharging strategy based on particle swarm optimization by optimally handle costs and load variance whereas [239] developed an EMS for industrial virtual power plant with the aim of maximizing profits including EV integration.

An optimization model investigates the integration of EVs and smart grids in [240] with the aim of minimizing electricity and  $CO_2$  costs, proving that the grid system might be sustained when EVs are parked reducing the cost of the overall system. A technical and environmental analysis of different storage mechanisms including EVs with V2G, batteries and pumped hydro storage is evaluated in [241] showing great advantages and opportunities especially regarding the  $CO_2$  reduction. [50] presented a V2G integration on residential microgrids with different control scenarios by optimizing the environmental and economic impact. The results showed that controlling EVs reduces total system costs while also lowering  $CO_2$  emissions compared to the uncontrolled strategy.

Typically, electricity is sold under two different price bands, the so-called Time-of-Use (TOU) tariffs, to encourage customers to shift their energy use to other periods. The energy arbitrage process takes advantage of this price difference by using a storage system so that energy is bought at the lower price and then used when the cost increases during the day. Several authors studied this technique providing information regarding its usefulness. In [242] different energy arbitrage scenarios are studied where an aggregator aims to minimize energy costs and  $CO_2$ -emissions with different battery technologies in a Community Energy Storage (CES) system. Peak shaving and price arbitrage processes are studied by [243] to analyse the benefits of Li-Ion batteries as energy storage in commercial buildings with PV generation. In [244] an energy arbitrage strategy is developed for an EV fleet using departure and arrival time predictions. However, battery degradation is not considered leading the results to be too optimistic. Another energy arbitrage strategy considering battery degradation and electricity price forecasts is studied in [73]. Nevertheless, different markets prices are evaluated without any consideration on future prices and there is no information regarding batteries availability to exchange energy.

To the knowledge of the authors, no works on V2G integration and EMS implementation on ski-resorts with real data has been found in the current literature.

#### 4.3.3 SYSTEM DESCRIPTION

A main feature of a ski resort is its considerable energy consumption and its countless electrical loads. The purchase of this energy is a major cost to which attention is always paid. There are different electrical energy-intensive components in a ski-resort. Ski-lifts and artificial snow production are the most relevant contributions of electrical energy and water consumption. Both are the main operating costs and account for about 40% and 50% of total electricity consumption for lifts and snow making, respectively [245]. Therefore, it is extremely beneficial to properly manage them by minimising costs and wastes as much as possible. A further cost, not related to electrical energy but to diesel consumption, is the usage of snow groomers for slopes maintenance. The study of an EMS allows an optimised handling of the electrical flows

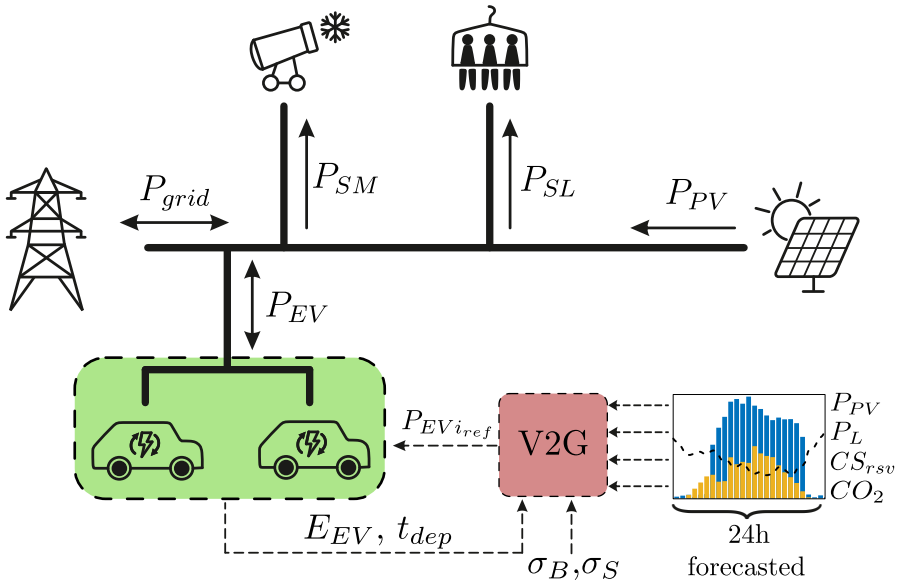


**Figure 4.15:** System representation with the main elements of the proposed system.

within the ski area, considering the operational costs and constraints of the ski operator. The proposed system consists of several interconnected elements that perform different functions (see Fig. 4.15). The ski resort is connected to the grid by means of several MV substations and it includes several power flows such as the photovoltaic production ( $P_{PV}$ ), the ski-lift load ( $P_{SL}$ ), the snow-making plants ( $P_{SM}$ ) and the V2G contributions due to EVs ( $P_{EV}$ ). The photovoltaic production system is assumed to be installed on the roofs of the facilities (restaurants, hotels and ski-lift stations) producing energy that is directly used by the resort. The V2G module optimizes the EV reference charging/discharging power  $P_{EViref}$  by using data predictions such as PV power, total load power  $P_L$ , charging stations (CS) reservation data  $CS_{rsv}$  and the  $CO_2$  emission intensity ( $gCO_{2eq}/kWh$ ) in order to minimize the specific objective function. The purchased ( $\sigma_B$ ) and sale ( $\sigma_S$ ) energy prices are not forecasted since they are both known in advance and fixed by the Distribution system operator (DSO).

The proposed electric vehicle parking lot is seen as an aggregated bidirectional component as it can both absorb and deliver power according to the resort and to the EV's owners needs. The ski resort's loads are

divided into two main groups: the total electrical power required for snow making and the total power absorbed by the ski-lifts.

The proposed EMS consists of an MILP-MPC-based V2G optimization that aims to minimize electricity cost and environmental impact by optimizing EV charging and discharging process exploiting 24-h forecasting data with 30-min resolution. The control law is calculated by optimising the value of an appropriate objective function, considering the different constraints and the system model. The optimisation is performed at each sampling time throughout the time horizon, allowing the system state to be updated and the predictions to be re-evaluated.

#### 4.3.3.1 SKI RESORT

The ski-resort area analysed in our study is located in Italy, in the Trentino-Alto Adige region and is considered a medium-sized ski resort with approximately 50 km of total slopes length. The ski resort includes several sub-resorts and this study examines only one of them, with about 15 km of slopes length at an average altitude of 2000 m. However, the work can easily be scaled up for a larger one, simply by adding more variable, parameters and constraints. The ski season typically lasts three to four months with considerable dependence on temperatures and availability of snowfall and water for proper snow making of the slopes.

A skiing day usually lasts eight hours in total throughout the season. Although the days get longer in spring, it is preferred not to extend the operating hours as skiers lose energy even before the scheduled closure [245].

#### 4.3.3.2 PHOTOVOLTAIC PRODUCTION

As already mentioned, the installation of a certain number of photovoltaic systems is assumed to account for the power balance. By analysing the ski resort facilities and calculating the total area, an assessment of the available photovoltaic power can be made. The estimation does not take into account technical and environmental constraints and only wants to provide a correct order of magnitude. The areas considered are the ski lift stations, commercial facilities and accommodation within the ski resort. PV power production forecast, as well as the other variables, is necessary for the optimization algorithm

in order to predict the behaviour of the system and determine the proper power references to minimize the objective function. Concerning the prediction of the PV power for the V2G optimization, it is assumed that on day  $d$  the expected irradiation for day  $d+1$  is known to forecast the generated power according to the total available PV area. In particular, two different arrangements of PV modules were assumed: flat and tilted plane. For these two types, a PV capacity of  $10 \text{ kW}/120 \text{ m}^2$  and  $10 \text{ kW}/60 \text{ m}^2$  was considered, respectively. Through an estimation of the available surfaces in the ski-resort it has been calculated an area of  $2200 \text{ m}^2$  and  $1570 \text{ m}^2$ , for tilted and flat plane respectively, obtaining a nominal power of the plant of about 0.5 MW.

Irradiance data were obtained through the Copernicus Atmosphere Monitoring Service (CAMS) [246] for the location of the studied resort during the entire 2019 ski season. Through this service it is possible to obtain data with high temporal resolution of Global, Direct and Diffuse solar irradiance for actual weather as well as for clear-sky conditions.

#### 4.3.3.3 LOAD PROFILE

In order to optimise and control the energy flows within the ski resort, it is essential to predict the electrical load profile so as to foresee the upcoming action. The total electricity consumption of the ski resort is due to the ski lifts, accommodation facilities, auxiliary services and to the snow production during necessary periods. In this study, snow-making power profile is estimated by using a variable number of snow guns and only during the night, depending on the ski slopes involved in the process.

#### SKI-LIFT

The ski lifts aim to transport skiers to the top of the slopes, and they work continuously every day during the whole ski season. The power absorbed by a lift motor varies according to many parameters including length, elevation gain, transport speed and capacity. For example, a 4-person chairlift with a 1000 m length, a 400 m elevation gain and a capacity of 2000 pers./h has a maximum power of 415 kW. A fixed speed is typically kept so that the travel time is always constant. Thus, as the number of skiers increases, the power required also increases, varying considerably during the day. The ski resort's opening hours may

differ depending on altitude and location, but they usually run from 8:30 a.m. to 4:30 p.m. throughout the ski season. The largest electrical power consumption contribution is clearly due to ski lifts. For this reason, forecasting the power consumption is necessary to minimize electricity costs during day operations. Due to the lack of measuring equipment on the chairlift supply lines, it is necessary to estimate the power consumption over time in another way. The ski resort has 8 ski lifts with a maximum full-load total power of about 2 MW and a minimum no-load total power of 750 kW. At the beginning of each ski season, a load test is carried out on all chairlifts to certify everything is working properly. During this test, the no-load and full-load active power for each plant is measured by simulating the weight of skiers with sandbags.

The amount of work  $W$  required to move a mass  $m$  between two points at different heights  $h$  is calculated using the law of potential energy. Assuming that the acceleration of gravity  $g$  and the height between the two points are constant, the potential energy is proportional to the mass to be moved. If the ride time interval  $\Delta t_r$  is constant and neglecting friction losses, the required mechanical power  $P_{mec}$  varies linearly with the mass, as shown in (4.14):

$$P_{mec} = \frac{W}{\Delta t_r} = \frac{mgh}{\Delta t_r} \quad (4.14)$$

In this way, using the electrical power measurements from the tests mentioned above and knowing that the power increases with the number of passengers, it is possible to use the turnstile ski pass reading to estimate the active power absorbed by each lift every  $\Delta t$  minutes. The power absorbed  $P_{SL}$  can be express as in (4.15):

$$P_{SL_s} = P_{0_s} + \frac{p_s}{P_{max_s} \cdot \Delta t} (P_{f_s} - P_{0_s}) \quad (4.15)$$

where  $p_s$  is the number of passengers logged in the time period  $\Delta t$  [h],  $P_{max_s}$  is the ski lift nominal capacity [person/h],  $P_{0_s}$  the no-load power [kW] and  $P_{f_s}$  the full-load power [kW] for each plant  $s$ . Using the real data of skier runs provided by the lift operator of the ski resort under investigation, it is then possible to calculate the power consumption

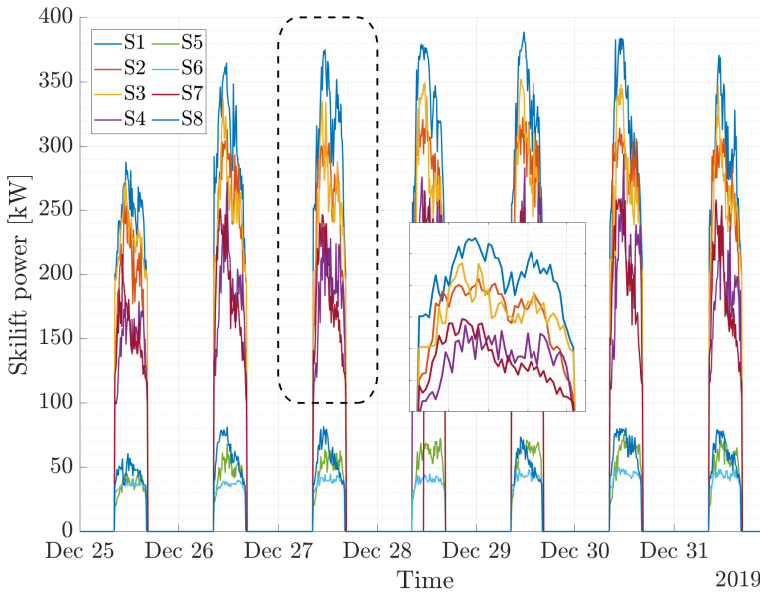


**Figure 4.16:** Ski lifts power estimation during 2019 Christmas holidays ( $\Delta t=10\text{min}$ ). S1-S4,S7 are chairlifts and S5,S6,S8 are platter lifts. (Color online)

for each lift, as shown in Fig. 4.16. As can be seen from the power levels, it is possible to easily identify chairlifts (S1-S4,S7) and platter lifts (S5,S6,S8).

Thanks to these data, it is possible to predict the power in the following 24 hours with good accuracy and real-time data can be used to correct any prediction errors. The advantage of this method is that no additional measuring system is required besides to the turnstile ski pass reading, whose data is nevertheless saved for statistical analysis by the lift operator. Although the use of a power measurement system could provide a better accuracy and thus a more precise prediction, the method used provides a quick and a real-time load estimation and its accuracy is certainly suitable for the purposes of this work. Furthermore, the estimation method is easily scalable for different plant sizes.

#### BASE LOAD CONSUMPTION

Electricity consumption is also represented by a contribution due to the auxiliary services of the ski resort such as restaurants, offices and accommodation. During daylight hours this has a minimal impact on

the total load, which is mainly due to the ski lifts. Nevertheless, as it can be seen from the zoomed area in Fig. 4.16, the ski-lift power decreases during the central hours of the day. It is therefore expected that during this period the base load consumption will increase due to the increased flow of lunchtime users. For this reason, the base load consumption is increased by a certain amount of power proportional to the ski-lifts power reduction during lunchtime (and thus indirectly to  $p_s$ ) and scaled to the maximum daily load. By doing so, days with high power demands and thus more people will have a greater increase in base load during the lunch interval. A certain amount of power during the night is also considered due to auxiliary loads.

### SNOW-MAKING PROCESS

Climate change and the consequences of global warming have a significant impact on snow management in a ski area. Snow melting, as a result of high temperatures and radiation, is the main problem for most ski area and the most common strategy is to produce snow artificially [247]. As mentioned above, snowmaking accounts for about half of the ski resort's electricity consumption. Currently, fan guns, lances and high-pressure cannons are the three types of machines for this process, and they differ in consumption, yield, cost and optimal conditions for snowmaking. Despite this, only low-pressure fan guns will be considered in this analysis as they are the most common due to their high yield and use flexibility. They basically include a fan, a compressor and a series of circularly arranged nozzles that mix water and air for a total power of 20 kW each. About a hundred snow guns (fixed and removable) are installed in the entire ski area. In order to replicate a representative power profile a random number between 70 and 100 snow guns has been chosen within the 30-min resolution. The power profile variation is reflective of both the number of operating guns and the possible variation in power as a function of nighttime temperature. The resort has about twenty slopes located on average at the same altitude. The average length of the slopes is about 800 m with a maximum length of 1.5 km. Most of the slopes are at altitude, except for those that are used to come back to the car parks, which

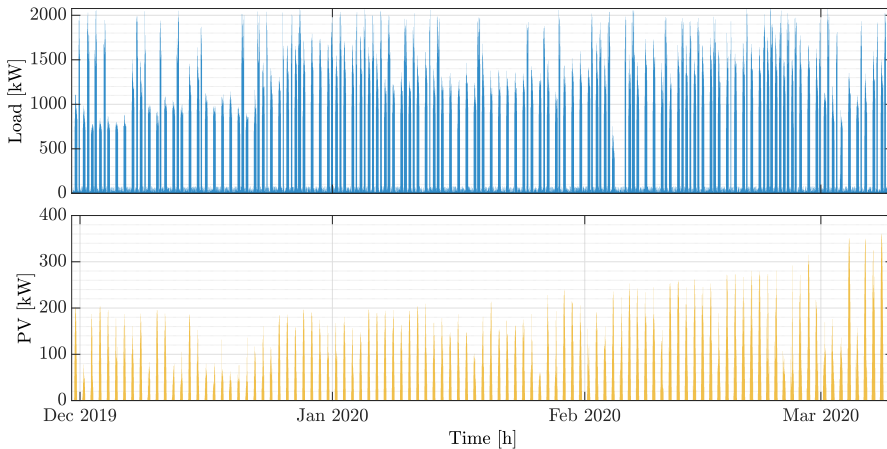


**Figure 4.17:** Load consumption (ski-lift, snow guns and base power) and PV power from season 2019-2020.

have the greatest elevation gain. According to a study carried out by the operator, a skiable area of  $650\,000\text{ m}^2$  was calculated.

Figure 4.17 shows the total load consumption power  $P_L$  (ski-lifts, base load and snow-making) and the PV generated power based on solar irradiance data for the ski-season 2019. These data will be used for all the time scenarios analysed. A higher frequency of power consumption is shown in certain periods of the season. This is caused by the snow-making process that is always started during the night hours in order to take advantage of the lower temperatures and increase the production and quality of snow. The nighttime power profile was created in relation to the information received from the ski-resort.

#### 4.3.3.4 SKIERS

Tourists are divided into two categories: daily and weekly. The daily skiers (DS) arrive after the opening of the lifts and typically start skiing around 10-11 am corresponding to the peak ski-lift load. A small number of these are the more experienced skiers, who arrive before the lifts open and start skiing as soon as the lifts start operating. Daily skiers typically stop skiing before the lifts close and by 3pm the slopes begin to empty naturally (see Fig. 4.16), as it is estimated that an average skier can tolerate a total of 6000 m of vertical gain per day [245]. Experienced skiers stay until the last run and so will leave the resort even an hour after the lifts close. For this reason, it was decided

to simulate EVs presence in different time slots. EV connections for daily skiers are randomly distributed around the opening of the lifts with a higher probability towards late morning and EV disconnections immediately after the lifts stop with full-charged EVs. Daily skiers vary day by day, increasing significantly during weekends and public holidays.

Weekly skiers (WS) arrive at the resort and leave their EV connected for several consecutive days, taking advantage of the accommodation proximity to the slopes. We suppose the number of weekly skiers change randomly over the weeks and they will find a full-charged EV at the end of their stay. In particular, it is assumed that not all CS are always connected to a car. In fact, it was simulated that the number of connected users varies in a probabilistic way according to the estimated daily ski-lift load (only for daily skiers) and according to the period of stay (random number in the range [5 8] days) and absence (random number in the range [1 2] days) of the weekly users. Therefore, the assumed number of CS should only be seen as the actual number of installed CS. The differentiation between weekly and daily skiers implies that the two types of skiers have different dedicated CS. The former will have available the CS of the accommodation while the latter will have dedicated CS provided by the ski-resort in the public parking. As far as CS is concerned, it is assumed that a ski resort reservation system knows in advance the status of each plug so that it can schedule power management. It is assumed that all parameters of interest are estimated from the information that the user enters into the booking application for the use of the charging stations. When a user desires to make a CS reservation, an estimation of the arrival and departure time (which will be the same as the hotel reservation for weekly users) is assumed and, for weekly skiers, for any EV disconnection and connection within their stay. In fact, the simulation includes that a weekly skier may want to visit a nearby place or simply have dinner in a different location with a certain probability. Regarding the initial SOC, this could be estimated through entering the estimated distance the user will travel to get to the ski-resort by assuming an average consumption relative to the type of vehicle and knowing the total battery capacity (again provided by the user during the booking process).

On this aspect, according to a study carried out on 1165 ski tourists, 79% are weekly tourists, only 13% are daily tourists and the remaining 8% are ski instructors or local visitors [248]. This shows the great potential of an EV battery use strategy also during the night hours and not only during daytime, which is the case for daily skiers. The same study also assessed user's attitudes towards renewable energy generation and its aesthetic and environmental impact within the ski resort. It shows that most people are well disposed towards photovoltaics on the buildings and hydroelectric power, also from the environmental and visual impact point of view.

In this work, it was assumed that all EVs have the same battery capacity and charge/discharge power for each time scenario. More detailed information are shown in Section 4.3.6. Moreover, it is assumed that car owners will accept to participate for V2G with certainty thanks to an incentive consisting in a discount on the ski-pass and/or charging for free.

#### 4.3.3.5 ELECTRICITY PRICE PROFILE

The entire resort is supplied by a single HV station with a total contracted capacity of about 10 MW. The power distribution to different zones is done through several MV substations. The current DSO implements a TOU-type energy pricing with two price bands. The peak period is defined from Monday to Friday from 8 a.m. to 8 p.m. while all remaining hours are defined as off-peak. Adopting the current electricity prices provided by the DSO (January 2022), the peak and off-peak period prices are 270.5 €/MWh and 232.7 €/MWh, respectively, with a variation of 16.2%. Network services, system charges, excise taxes and VAT for industrial users are included [249]. Energy selling price is also considered at a fix value with a remuneration of 39.9 €/MWh through the so-called "Ritiro Dedicato" mechanism, which is not a classic FIT but rather regulates the sale of electricity according to the Italian regulation. According to existing regulations, the selling price (also called "Prezzi minimi garantiti") is compensated based on zonal market prices through an economic adjustment. This has not been considered despite the strong distortion of current prices since lower prices belong to common market conditions compared to the current ones.

#### 4.3.4 PROBLEM FORMULATION AND EMS IMPLEMENTATION

In this section, the EMS operations and the mathematical problem formulation are described based on the previous information described in Section 4.3.3. Figure 4.15 shows a general scheme of the proposed control system where the 24-h horizon MPC optimization is performed within the V2G module.

The inputs of the V2G optimisation module are the forecasted PV power, estimated ski lifts power (see Eq. 4.15), the EVs states (initial SOC, arrival and departure times) and the  $CO_2$  emission intensity over 24 hours. The entire optimization and related input vectors of the V2G module are discretized with a time step of 30 minutes. With this interval, all vectors for each time horizon will have a length of 48 elements. The energy purchase and sell prices are taken as known as they are established with the DSO. Snow-making power is also supposed to be known a priori since usually it depends on weather forecast of the following days. The output of the V2G module are the reference powers produced by the V2G optimisation algorithm to be provided to the EVs charging stations. Regarding the V2G aspect, battery degradation is a well-known problem in the literature and a key aspect of cost-effectiveness in storage systems [66, 67, 74]. Despite this, a degradation model is not always included in techno-economic studies [235, 240, 244, 250], leading to overly optimistic results. Due to its considerable influence on the performance of the EVs charge/discharge behaviour and the number of charge cycles, a linear programming approach has been integrated to consider this aspect. Its operation is based on the optimization of maximum and minimum battery energy values as a function of battery replacement cost as shown in [251].

In the following paragraphs, the algorithm governing the operation of V2G services is discussed, whose ultimate objective is to minimise the cost of energy absorbed from the public grid and, jointly, to minimize the  $CO_2$  emissions in different scenarios and strategies.

##### 4.3.4.1 OBJECTIVE FUNCTION

The main goal of the V2G module optimization is to minimise the total cost of the overall ski-resort from different perspectives. It is important to emphasize that in this study the minimization is based

only on operating costs not considering the costs of PV systems and charging stations installation nor the implementation of the proposed EMS. Moreover, the PV plant is assumed in its first year of life for each scenario thus no PV modules degradation is considered. In this study, the total cost to be minimized is the contribution of multiple terms as expressed in (4.16):

$$\min f = \sum_{t=1}^T \alpha_1 (C_E(t) + C_{DEG}(t)) + \alpha_2 C_{CO_2}(t) \quad (4.16)$$

where  $T$  is the total number of intervals in the considered horizon ( $T=48$  in our case),  $C_E$  is the cost function related on energy exchanged with the grid,  $C_{DEG}$  is the EV's batteries degradation cost function and  $C_{CO_2}$  is the  $CO_2$  environmental cost function. The weighted sum method is used to scalarize the two objectives into a single objective by adding each one multiplied by a weight. These weights are chosen in proportion to the relative importance of the single objective [252]:  $\alpha_1$  and  $\alpha_2$  for economic and environmental cost, respectively.

The cost function of the energy exchanged with the grid is the first term that has been analysed. A TOU profile is used by the DSO for selling energy to the ski-resort and the same cost profile is used in this work throughout all the scenarios. Energy cost function is mathematically shown in (4.17):

$$C_E(t) = \Delta t \left( P_{grid}^+(t) \sigma_{B_n}(t) - P_{grid}^-(t) \sigma_{S_n}(t) \right) \quad (4.17)$$

where  $\Delta t$  [h] is the simulation time step resolution,  $P_{grid}^+[MW]$  is the absorbed power from the grid,  $P_{grid}^-[MW]$  is the fed power to the grid,  $\sigma_{B_n}$  is the normalised energy purchase price and  $\sigma_{S_n}$  is the normalised energy selling price, both normalised based on the respective maximum price value.

The second term in the objective function is related to the EV's battery degradation. The purpose of this term is to limit charge and discharge cycles on the basis of estimated battery replacement cost. The battery degradation model is based on [253], where the total replacement cost of the battery and the total energy exchanged during its life (energy throughput) is defined. The degradation algorithm is based on the

minimization of the discharge gap [251] which is eventually minimised in the cost function. The term  $C_{DEG}$  is shown mathematically in (4.18):

$$C_{DEG}(t) = \sum_{i=1}^{EV_{con}} (E_{H_i} - E_{L_i}) \sigma_{BC_n}(t) \quad (4.18)$$

where  $E_H$  and  $E_L$  are the highest and lower energy content during a complete horizon for the  $i$ -th EV,  $EV_{con}$  is the actual number of EV connected to the ski-resort's CS and  $\sigma_{BC_n}$  is the normalised EV's battery degradation cost per kWh based on its maximum value. The last term of (4.16) is the  $CO_2$  emissions environmental cost which is defined in (4.19):

$$C_{CO_2}(t) = \Delta t P_{grid}^+(t) \lambda_{CO_2n}(t) \quad (4.19)$$

where  $\lambda_{CO_2n}$  is the normalised carbon intensity of electricity based on its maximum value. The data concerning  $\lambda_{CO_2}$  in the considered period have been calculated from the type of electric production in the considered electric sector (North Italy IT-NO zone) [225] using different emission factors for each energy resource. The global carbon intensity for the considered ski season is shown in Fig. 2.4 in Chapter 2.

#### 4.3.4.2 CONSTRAINTS

##### GRID

Grid inequalities constraints are used to include the total capacity of the MV cabins in the optimization problem in order to not overcome the rated transformers power. In order to avoid simultaneously nonzero values between the absorbed and the fed powers a binary variable  $y(t)$  is defined.

$$0 \leq P_{grid}^+(t) \leq y(t) P_{grid}^{max}, \forall t \quad (4.20)$$

$$0 \leq P_{grid}^-(t) \leq (1 - y(t)) P_{grid}^{max}, \forall t \quad (4.21)$$

$$P_{grid}(t) = P_{grid}^+(t) - P_{grid}^-(t), \forall t \quad (4.22)$$

$$y(t) \in \{0, 1\}, \forall t \quad (4.23)$$

where  $P_{grid}^{max}[MW]$  is the maximum power of the MV cabins and  $P_{grid}$  is the net grid power. The grid power separation also makes it possible to define different energy sale and purchase prices in the formulation.

### ELECTRIC VEHICLES

EVs constraints are used to define the energy variation model of the battery as well as charging and discharging power limits. Equations (4.24) to (4.27) shows the EV power constraints where each of them is true for each connected  $i$ -th EV.

$$0 \leq P_{EV_i}^{chg}(t) \leq e_i(t) P_{EV_i}^{max} \quad , \forall t \quad (4.24)$$

$$0 \leq P_{EV_i}^{dis}(t) \leq (1 - e_i(t)) P_{EV_i}^{max} \quad , \forall t \quad (4.25)$$

$$P_{EV_i}(t) = P_{EV_i}^{dis}(t) - P_{EV_i}^{chg}(t) \quad , \forall t \quad (4.26)$$

$$e_i(t) \in \{0, 1\} \quad , \forall t \quad (4.27)$$

where  $P_{EV}^{chg}[MW]$  and  $P_{EV}^{dis}[MW]$  are the EV's charging and discharging powers respectively,  $P_{EV}^{max}[MW]$  is the maximum rated power of the EV and  $e(t)$  is a binary variable with the same purposes as  $y(t)$ .

Conversely, equations (4.28) to (4.31) shows the  $i$ -th EV energy constraints.

$$0 \leq E_{EV_i}(t) \leq C_{EV} \quad , \forall t \quad (4.28)$$

$$E_{EV_i}(t) = \begin{cases} 0 & \text{(car not connected)} & \text{for } t < t_{i,arr}^k \\ E_{EV_i,arr} & & \text{for } t = t_{i,arr}^k \\ E_{EV_i}(t-1) + \left( P_{EV_i}^{chg}(t-1)\eta_{EV} - \frac{P_{EV_i}^{dis}(t-1)}{\eta_{EV}} \right) \Delta t & \forall t \in [t_{i,arr}^k + 1, t_{i,dep}^k] \end{cases} \quad (4.29)$$

$$E_{EV_i}(t) = E_{EV_i,dep} \quad , \text{ for } t = t_{i,dep}^k \quad (4.30)$$

$$E_{EV_i}(t) \geq (1 - DoD_{max})C_{EV} \quad , \forall t \quad (4.31)$$

where  $E_{EV}[MWh]$  is the EV battery energy,  $C_{EV}[MWh]$  is the EV battery capacity,  $t_{arr}$  is the EV arrival time,  $t_{dep}$  is the EV departure time,  $E_{EV_{dep}}[MWh]$  is the minimum EV battery energy to be met at  $t_{dep}$  (set to  $C_{EV}$ ),  $E_{EV_{arr}}$  is the EV battery energy at  $t_{arr}$  and  $DoD_{max}$  is the maximum depth-of-discharge of the battery to set a safety energy lower bound (20% of full capacity). In a study regarding the round-trip

efficiency (RTE) for V2G technology [254], the experimental average RTE for a 40 kWh Nissan Leaf is calculated as 87%. In (4.29),  $\eta_{EV}$  is the EV battery charging/discharging efficiencies and its value is set to  $\sqrt{0.87} = 0.93$ . The latter energy equations can be different in terms of time instants within a time horizon. Since a weekly user may decide to disconnect the car within his/her stay period, there may be more than one instant of departure and arrival within the same 24-h interval, as explained in Section 4.3.3.4. This is expressed through the index  $k$  which indicates the number of arrival/departure instant within the time horizon.

#### EV BATTERY DEGRADATION

As already mentioned, EV battery degradation is considered in terms of optimal minimum and maximum energy amount within the considered horizon. For this reason, the constraints (4.32) and (4.33) are used to bound the  $i$ -th EV energy based on the optimization cost used in the objective function.

$$E_{EV_i}(t) \geq E_{L_i} \quad , \forall t \quad (4.32)$$

$$E_{EV_i}(t) \leq E_{H_i} \quad , \forall t \quad (4.33)$$

where  $E_L$  and  $E_H$  are the two optimization variables used for the  $i$ -th EV in (4.18).

#### POWER BALANCE

The power balance related to the system described in Fig. 4.15 is modeled using (4.34):

$$P_{PV}(t) + P_{grid}(t) - P_{SL}(t) + \sum_{i=1}^{EV_{con}} P_{EV_i}(t) - P_{SM}(t) - P_{AUX} = 0 \quad (4.34)$$

$$P_L(t) = P_{SL}(t) + P_{SM}(t) + P_{AUX}(t) \quad (4.35)$$

where  $P_{PV}[MW]$  is the PV power,  $P_{SL}[MW]$  is the ski-lift power,  $P_{SM}[MW]$  is the snow-making power and  $P_{AUX}[MW]$  the base load power. In order to group all the uncontrollable loads, (4.35) defined the total load power  $P_L$  described in Section 4.3.3.3.

#### 4.3.5 EV-CS GROWTH MODEL

The world market for electric cars is rapidly growing. Annual sales of plug-in passenger cars (BEVs and PHEVs) increased from 2 million in 2019, to 3 million in 2020, to 6 million in 2021, of which 3 million in China and 2 million in Europe. In Italy, in 2021 electric cars had an annual market share equal to 9.3%, steadily growing although a lower growth rates compared with the neighboring northern countries such as Austria (20%), Switzerland (13%) or Germany (26%). Trentino-Alto Adige, the region where the sky-resort is located, with 1.8% of the Italian population had 23% of the Italian BEV circulation fleet, equal to 53 thousand passenger cars [255]. Within this framework, we made some assumption about the likely trends in electric car uptake up to the year 2030, taking into account that the sky resort will host both Italian and international tourist <sup>1</sup>. In the following subsection, we explain the assumption made regarding: a) the number of charging stations located in the sky resort and the corresponding electric cars parked at the sky resort; b) the average battery capacity of the electric cars and c) battery replacement costs per kWh. All three assumption will be made with reference to the years 2023 and 2030.

##### 4.3.5.1 THE NUMBER OF CHARGING STATIONS LOCATED IN THE SKY RESORT

The starting point stems from the observation that the hotel and restaurant managers have promptly adapted to the customers' requests for vehicle charging, providing them with 8 charging stations in different hotels. As of 2019 and 2022, there were no public charging stations dedicated to daily skiers. We assumed conservatively that by 2023, at least 2 public charging stations will be made available for 500 cars parked at the sky resort. The assumption is based on the ratio of electric cars over the total circulation fleet equal to 0.3% in 2021. For the year 2030, we predicted that at least 60 of the 500 car parked at the resort will be electric and charged at the resort location. The prediction is based on the evolution of the electric car up in Norway, hence, assuming that Italy will follow a similar penetration path (see Table 4.10). In about a decade, the share of electric cars in the Norwegian fleet

---

<sup>1</sup>According to our informal sources, in the 2019 winter season, 70% of the visitors came from Italy, 15% from the Czech Republic, 5% from Germany, 3% from Poland, and the remaining from other countries.

**Table 4.10:** Passengers EV market share of total new car sales since 2013 [258]

Country	2013	2014	2015	2016	2017	2018	2019	2020	2021
Norway	6.1%	13.8%	22.4%	29.1%	39.2%	49.1%	55.9%	74.7%	86.2%
Italy	0.07%	0.08%	0.09%	0.08%	0.1%	0.26%	0.6%	4.3%	9.3%

increased from a very marginal share to the current 12.1%. Translated to our case study, it implies that 60 of the 500 car will require charging at the sky resort in 2030.

This approach is based on the following considerations. The regional distribution of electric vehicles is heterogeneous in Italy, with a higher prevalence in the north of the country and lower in the south. In particular, the region under consideration (Trentino Alto-Adige) alone has 20% of the circulating fleet of electric cars in Italy [256]. Moreover, the region is among the richest in Italy with an annual average household income equal to 39,028 € (the Italian average is 33,106 €) along with Emilia-Romagna (38,593 €) and Lombardy (37,702 €) [257]. In addition, due to ski-resort location many visitors come from the neighbouring northern countries such as Switzerland or Germany, that are also making huge progress in spurring EV market share. New fully battery electric car registrations in Germany, for example, increased from 63 thousand units in 2019 to 194 thousand in 2020, and to 356 thousand last year, with an EV (BEV+PHEV) sales share rising from 3% to 14% to 26%, respectively [27].

#### 4.3.5.2 AVERAGE BATTERY CAPACITY

The assumption we made regarding the average battery capacity for the year 2023 is based on the observed evolution of the driving range of the BEV on sale in the US market (Figure 4.18) from 2011 to 2021. As can be seen, up to the year 2015 there was considerable growth in the maximum values (associated with the Tesla models), but the majority of the cars sold offered a limited driving range. Only from 2016 on, the average driving range sold in the US market had a significant boost. Using an extrapolation method, we estimated that the medium driving range will be equal to 402 km in 2023 and 512 km in 2030, respectively. Taking as reference the average consumption of the 2018 Nissan Leaf 40 kWh, around 17 kWh/100 km (including summer and

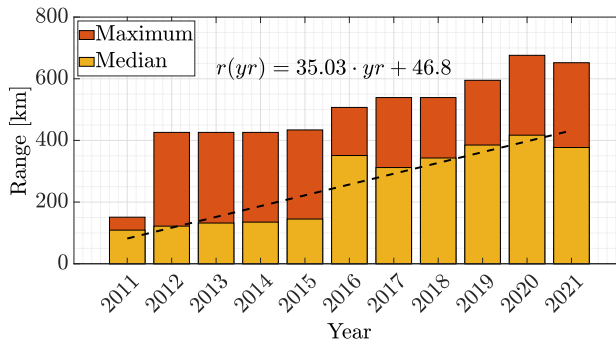


**Figure 4.18:** Range of U.S. market EVs in years 2011-2021 [260]

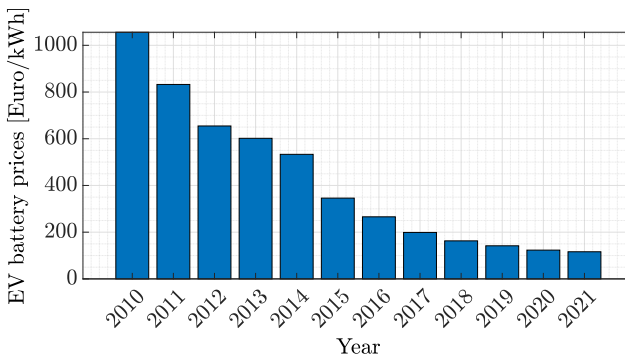


**Figure 4.19:** EV battery pack prices per kWh from 2010 to 2021 [261]

winter driving) [259], we estimated the average battery capacity of the electric cars sold in the market. It resulted a value of 62 kWh in 2023 (as in the Nissan Leaf e+) and 90 kWh in 2030.

#### 4.3.5.3 BATTERY REPLACEMENT COSTS

Battery costs have dramatically declined over the years due to economies of scale and improved production processes. Figure 4.19 shows the fall of average battery prices for electric car batteries over the period 2010 to 2021. In the literature, forecasts for the coming years vary greatly since it is obviously very difficult to predict whether the decline will follow the same trend or the increasing cost of the materials used to produce the batteries will slow down considerably the fall of the battery prices. In light of the uncertainty, we opted not to adopt statistical extrapolation methods but to assume a price reduction rate equal to the one last observed, i.e. 6%. However, since for the purposes of our

**Table 4.11:** Main parameters and values used in the different time scenario simulations.

Parameter	S2019	S2022	S2023	S2030
CS type [DS-WS]	-	-	2 – 8	30 – 30
EV battery [kWh-kW]	-	-	62 – 7	90 – 50
Average initial SOC [%] [DS-WS]	-	-	60.2 – 61	60.1 – 58.2
$\sigma_{BC}$ [€/kWh]	-	-	144.5	95.4
PV (Flat)-(Tilt) [W/m <sup>2</sup> ]	-	83 – 166	83 – 166	83 – 166
$\sigma_B$ (HP)-(LP) [€/MWh]	270.5 – 232.7	270.5 – 232.7	270.5 – 232.7	270.5 – 232.7

model we need an estimate of the battery replacement costs per kWh, we added labour costs (15%) and VAT (22%) to the battery prices. Under these assumptions, we estimated that in 2023 battery replacement costs will be equal to 144.5 €/kWh and in 2030 to 95.4 €/kWh.

### 4.3.6 RESULTS AND DISCUSSIONS

In this section, the results based on several simulations of three possible time scenarios (2022, 2023 and 2030) are shown and discussed. Each scenario describes a different situation regarding the characteristics adopted by the ski resort and the distinctive parameters of the automotive sector in future years. The 2019 season is taken as reference for the data provided by the ski-resort regarding ski-pass turnstile passages and solar irradiance values. The 2019 season is only evaluated to help the reader understand PV system implementation improvements in the 2022 scenario. All the simulations are performed for a complete ski seasons for each scenario.

Table 4.11 shows these information in more detail by including the values used for each feature that characterizes the scenario based on our estimation. For a fair comparison between the different subscenarios, the initial SOC of each EV was chosen randomly within the range of battery usability (in our case the DoD is 80%) and the initial values were kept the same for all charge/discharge strategies within the considered scenarios.

For a more complete analysis, the 2023 and 2030 scenarios were both divided into five subscenarios. Specifically, these are meant to show how the data vary based on three different vehicle charging and discharging strategies and two different environmental optimization as it follows:

- **Dumb:** considers the so-called "dumb charging" in which the vehicle is charged at full power as soon as it is connected to the charging station and does not have the opportunity to discharge energy. This subscenario then shows the results if the ski resort would choose not to adopt any optimization method;
- **Opt-Chg:** considers a charging strategy that is optimized based on total cost and battery degradation minimization but still does not allow energy discharging from the vehicles;
- **V2G:** examines the V2G strategy, in which both charging and discharging powers are minimized based on total cost and battery degradation aspect;
- **V2G&CO2:** analyse to multi-objective optimization between total cost and battery degradation combined with  $CO_2$  emission minimization ( $\alpha_1 = 0.5$  and  $\alpha_2 = 0.5$ );
- **CO2:** considers only the environmental aspect by optimizing only the  $CO_2$  emissions ( $\alpha_1 = 0$  and  $\alpha_2 = 1$ ).

With reference to the 2030 scenario, a sensitivity analysis is made in order to assess the variability of the results by varying the battery replacement cost, the PV production, the EVs number and user type as well as the purchase energy gap price. More details can be found in Section 4.3.7.

#### 4.3.6.1 RESULTS COMPARISON

A comprehensive summary of the performed simulations with the final cumulative values is shown in Table 4.12 that shows the total energy values, costs and the amount of  $CO_2$  emitted calculated during the whole ski season for each specific scenario. In particular, the following values are shown:

- $E_{load}$ : total energy absorbed by loads [MWh]
- $E_{PV}$ : total energy generated by PV plant [MWh]
- $E_{buy}$ : total energy bought from the grid [MWh]
- $E_{sell}$ : total energy sold to the grid [MWh]

- $E_{chg}$ : total charge energy for all the EVs [MWh]
- $E_{dis}$ : total discharge energy from all the EVs [MWh]
- $CO_2$ : total tons of emitted  $CO_2$  due from the purchase of energy [ton]
- $C_{buy}$ : total cost for purchased energy from the grid [€]
- $C_{sell}$ : total cost for sold energy to the grid [€]
- $C_{total}$ : total operational cost covered by the ski resort [€]
- $SC$ : total self-consumption [%]

The self-consumption ( $SC$ ) is defined as the ratio between the amount of total energy locally generated and consumed, and the total energy generated. First of all it is good to analyse the impact between the S2019 and S2022 scenarios regarding the exploitation of a PV system. As expected, the generation of a large part of the total energy required ( $\approx 6.5\%$ ) reduces the amount of energy drawn from the grid and consequently both the total cost and the amount of  $CO_2$  emitted. In terms of  $CO_2$ , there is approximately the same percentage change as it is proportional to the amount of energy taken from the grid. The cost for energy is reduced considerably even though the revenue from the sale of energy is not even comparable to the total cost. In this case, due to the fact that energy consumption takes place mainly during daylight hours (except for snow-making), the self-consumption is very high at 97%. Of course, the lack of a storage system means that it cannot be further increased.

Figure 4.20 shows the values of S2023 (orange) and S2030 (yellow) shown in Table 4.12 for total cost ( $C_{total}$ ), energy absorbed by the grid ( $E_{buy}$ ), tons of  $CO_2$  ( $CO_2$ ) as a percentage variation with respect to the S2022 scenario. Self-consumption ( $SC$ ) is shown as absolute value. In the S2023 scenario there is a slightly change in all the values due to the integration of EVs. The EVs charging process naturally requires the increase of energy purchased from the grid to satisfy this new electrical component that in the case of dumb and optimized charging strategy

**Table 4.12:** Summary table with final cumulative value for each scenario during the whole season.

	S2019		S2022		S2023				S2030			
	Dumb	Opt-Chg	V2G	V2G&CO2	CO2	Dumb	Opt-Chg	V2G	V2G&CO2	CO2		
$E_{load}$ [MWh]	1538,98	1538,98	1538,98	1538,98	1538,98	1538,98	1538,98	1538,98	1538,98	1538,98		
$E_{pv}$ [MWh]	-	99,6	99,6	99,6	99,6	99,6	99,6	99,6	99,6	99,6		
$E_{buy}$ [MWh]	1538,98	1442,36	1450,87	1449,86	1449,28	1450,77	1561,1	1558,9	1561,9	1572		
$E_{sell}$ [MWh]	-	2,98	2,79	1,96	0,79	0,79	0,84	0,08	0	0		
$E_{chg}$ [MWh]	-	-	8,69	8,52	14,72	14,29	26,2	119,44	153,89	155,51		
$E_{dis}$ [MWh]	-	-	-	-	5,61	5,24	15,60	-	31,34	32,75		
CO2 [ton]	586,37	551	554,39	553,90	553,82	552,71	552,37	595,73	594,56	596,97		
$C_{buy}$ [€]	383320	358362	360406	360171	359868	360030	360856	387483	386970	386720		
$C_{sell}$ [€]	-	117	109	77	31	31	31	33	3	0		
$C_{total}$ [€]	383320	358245	360297	360094	359837	359999	360856	387450	386967	386720		
SC [%]	-	97	97,2	98	99,21	99,21	99,21	99,16	99,92	100		
										100		

is merely seen as an additional load. In fact, about 9 MWh of  $E_{chg}$  are required.

As mentioned above, due to the presence of the EVs before the start-up of the plants, they can charge themselves with the PV energy produced and thus slightly increase the self-consumption (97.2%) and reduce the energy sold to the grid. Through the OptChg strategy, the optimization tries to charge the vehicles in the cheapest periods and thus, even if in a negligible way, reduce the cost of purchased energy, increasing the self-consumption up to 98% and consequently reduce the  $CO_2$  emissions. With the introduction of the V2G strategy, there is a clear decrease in the energy sold to the grid which is now stored for later use. As a result, self-consumption increases to around 99.21%. The vehicles contribute 5.61 MWh to the energy balance, i.e. just 0.36% of the total energy required. The total price variation between the three strategies is in the order of hundreds of Euros and compared to the S2022 scenario is below 1%. As it can be perceived, the increase of the total cost due to the introduction of EVs for all the charging strategy is so marginal ( $\approx 2$  k€) compared to the total costs of S2022. The ski-resort could decide to donate the charging energy just to increase its visibility and increase the tourist flow in the area rather than selling energy to the DSO. The  $CO_2$  emissions can be improved by optimising in a multi-objective way also the environmental impact through the introduction of the  $\alpha_2$  factor in the two environmental strategies. However, it can be seen that the change is minimal and brings no significant improvement neither economically nor environmentally.

In the 2030 scenario, due to the higher number of estimated vehicles and higher battery capacity, all quantities increase substantially leading to total cost, energy absorbed and  $CO_2$  emitted exceeding the S2022 reference scenario with higher percentages. Among the three charging strategies, the dumb strategy is the worst regarding cost and SC. In particular, the self-consumption is lower than in the S2023 case with V2G. By implementing the Opt-Chg strategy it can be achieved some improvements. For example, the total cost and the  $CO_2$  are reduced but more important the self-consumption is close to 100%.

With the use of V2G technology and due to the increased purchase of energy for energy arbitrage, the cost is further reduced, albeit minimally.

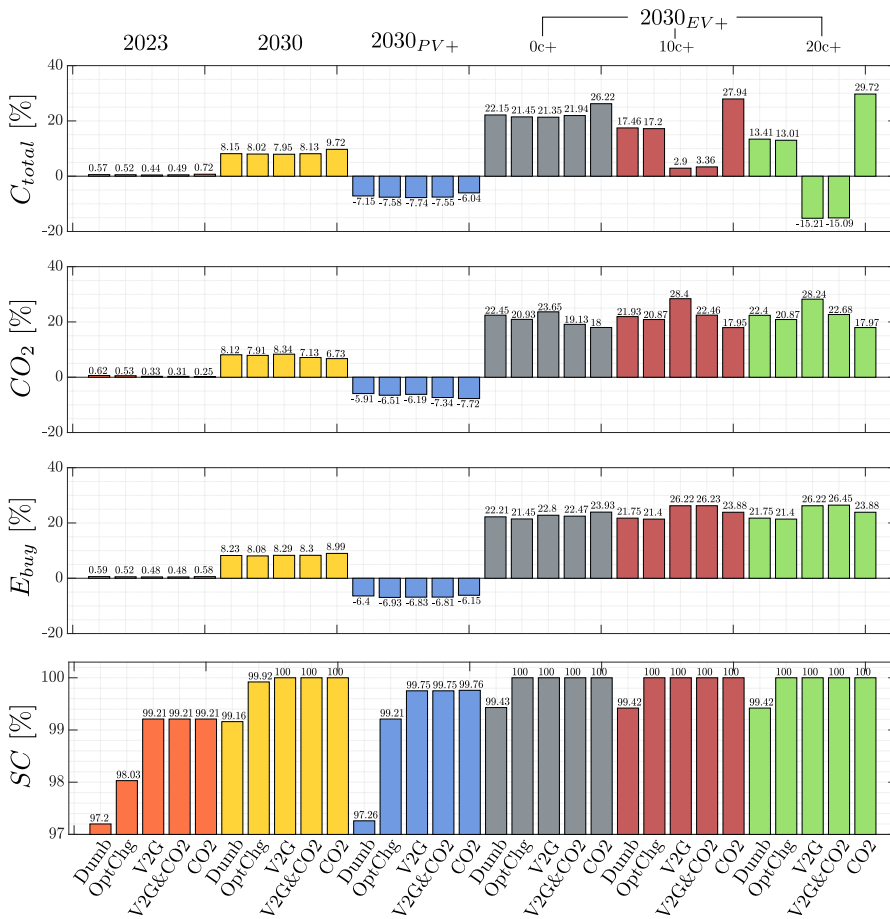


**Figure 4.20:** Final results of future scenarios and sensitivity analysis on PV size, EVs number and purchased gap price. (Color online)

This is not the case for  $CO_2$ , which increases due to the greater energy exchanged with the grid as a result of energy arbitrage. However, this is the first case where all the energy produced is also consumed as sales are zero and self-consumption is at 100%. In this case, the price increase compared to the S2022 scenario is relatively higher ( $\approx 30$  k€) for all strategies and the assumption of donating charging energy may no longer be valid since it is about 8% of the total seasonal cost. It should be noted that in any case these costs will be incurred as, assuming our hypothesis, there will be an increasing demand for charging stations in future years.

By using the V2G&CO2 strategy the cost increases slightly while the purchased energy remains almost unchanged and the  $CO_2$  emission is

reduced to 7.13%. This situation is both economically and environmentally optimal as it jointly minimises both the cost and the environmental impact caused by energy absorption. The  $CO_2$  scenario was also simulated which no longer takes into account the total cost of the ski resort but only the  $CO_2$  emission. As it can be clearly seen, the  $CO_2$  impact is further reduced to the detriment of the total cost, which it is no longer limited by any minimization objective. Assuming the 2030 scenario optimistic from the point of view of the number of installed charging stations, their halving was simulated. The results are affected but the change is less than three percentage points for each charging strategy.

#### 4.3.7 SENSITIVITY ANALYSIS

Although several parameters are able to radically change the behaviour of the results, it was analysed the variation of the main aspects characterising the system: on one side the growth from the perspective of renewable sources exploitation and on the other side the increase in the number and type of users in order to raise the awareness of the reader and to understand where a substantial variation of the results takes place. For this reason, two more macro scenarios are included based on 2030 scenario. As no further assumptions were made in the 2023 and 2030 scenarios regarding a possible increase in PV power capacity compared to 2022, the purpose of the 2030<sub>PV+</sub> scenario is to show how an additional ground-mounted plant with a nominal power of 1 MW and an increase in PV module efficiency of 4% changes the results just shown. Then, in this case, the new 1.6 MW PV plant energy production is 318.59 MWh instead of 99.6 MWh and  $E_{load}$ ,  $E_{chg}$  and  $E_{dis}$  are the same as 2030. As expected, a significant reduction in purchased energy, total cost and amount of  $CO_2$  was achieved. Between the five different optimisations, no particular changes are noticeable due to the constant number of cars used, and the trend between the strategies remains almost similar. In this scenario there is a saving of about 30 k€ on the total cost and an average reduction of 38 tons of  $CO_2$  over the whole season. Although the self-consumption is always higher than in 2022, it has decreased compared to 2030 because the number of cars can not retain all the photovoltaic energy produced by having necessarily to sell it. Compared to the 2019 scenario without any type of RES

generation, the maximum  $CO_2$  and total cost reduction are 7.8% and 13.7%, respectively.

The second analysis introduces the 2030<sub>EV+</sub> scenario where the number of total available CSs was set at 200 in order to put maximum stress on the study despite the knowledge that this number will be difficult to achieve. Out of these 200 CSs, 150 were dedicated to weekly skiers and 50 to daily skiers according to the ratio shown in [248]. To be clear, the nominal power of the photovoltaic system has been kept as in 2030 (0.5 MW) as well as the battery degradation cost. This last macro scenario has been divided into three different variants, each with a certain variation in the price gap of the purchased energy but always preserving the average price of 2030. The aim of this theoretical analysis is to highlight the influence of V2G energy arbitrage as a function of the variation of the energy purchase price gap dependent on renewable energy production (e.g. wind) in the future energy mix. These price variations make it possible to appreciate how the exploitation of V2G to reduce costs is extremely sensitive to these gaps. In particular, the three cases are defined as follow:

- **0c+**: no change in the price gap (270.5 | 232.7 €/MWh)
- **10c+**: the price gap has changed by 10 c€/kWh (320.5 | 182.7 €/MWh)
- **20c+**: the price gap has changed by 20 c€/kWh (370.5 | 132.7 €/MWh)

Regarding the 0c+ case, it can be found the same trend as in 2023 and 2030: the total cost, the  $CO_2$  emission and the purchased energy increase proportional to the number of vehicles whereas the self-consumption already improves in the dumb strategy. Same considerations as in the previous scenarios can be made among the five different optimization cases. Different situations are found for the 10c+ and 20c+ cases. In 10c+ it is possible to highlight how the cost variation has dramatically dropped when the V2G strategy is introduced, resulting in a cost increase of 2.9% compared to 2022. Instead, in the 20c+ case the situation further improves by even reducing costs by 15.21%. Slight cost increases occur with the V2G&CO2 strategy as in the other

scenarios, while in the  $CO_2$  strategy the cost exceeds that of the 0c+ case. This happens because of the anti-phase behavior of the purchase price and  $CO_2$  emissions during the day. The optimizer tries to buy energy during the hours of minimum environmental impact (daylight hours) at the expense of the price range that is at its maximum value. Clearly, this price reduction was expected as, having increased the price gap (in particular having reduced the overnight price), the car fleet makes more use of the night hours to recharge, showing how the night-day price difference has a significant influence on the cost reduction. Like the purchase price gap, the  $CO_2$  emission factor gap will have the same influence on  $CO_2$  optimization strategy. The last analysis is

related to the battery degradation cost of S2030 scenario. The variation of total cost  $C_{total}$ , EVs charging energy  $E_{chg}$ , tons of  $CO_2$  and EVs discharging energy  $E_{dis}$  with a battery degradation cost  $\sigma_{BC}$  equal to 50% and 10% of S2030 cost, with respect to the V2G case, have been analysed. The total cost variation is negligible and the  $CO_2$  increment is close to 1% for both battery costs variation cases. However, the total EV charging and discharging energy have dramatically increased of 51% and 218%, respectively, for the case with the cost at 50%. As we have already discussed, this is because, for the 2030 price gap, the most has already been done from a cost perspective and any other changes are not going to create substantial improvements. In the case where the cost is 10% from the S2030 cost, there is no appreciable change as compared to the case with the cost at 50%.

#### 4.3.8 DISCUSSION OF SIMULATION RESULT

As expected, the integration of a PV system reduces the cost of energy purchased from the grid. With the assumptions made regarding a 0.5 MW PV plant without EVs and 1.6 MW PV plant with EVs integration, a cost and  $CO_2$  reduction of 6% and 13.7%, respectively, is achieved, compared to the scenario without renewable generation.

In both future scenarios, the introduction of EVs causes an increase in total power consumption leading to increased costs and  $CO_2$  in all the charging strategies. By optimising charging and exploiting V2G technology, a slight decrease compared to dumb charging has been obtained, leading to the system selling less and less energy and

therefore increasing self-consumption. Moreover, when the  $CO_2$  is also considered, an optimal trade-off between total cost and  $CO_2$  impact is achieved, albeit in a minor way. Despite ski resorts not being currently involved in the Emission Trading Scheme (EU-ETS), this may happen in the future due to increasingly stringent emission regulations. In this case, an optimized management of the environmental impact will not only be environmentally beneficial but also economically profitable in case of  $CO_2$  allowances exchange.

The energy arbitrage exploitation through V2G technology brings marginal improvements in the studied futures scenarios. However, the results of sensitivity analysis show the great potential of V2G showing the importance of the price gap between TOU bands in this kind of analysis. Different V2G services like peak-shaving, load-leveling or reactive power compensation could bring more benefits in terms of power profile or voltage regulation. Moreover, the question concerning the social aspect naturally arises: will the users be favorable to providing these kinds of services? In which way and to which extent could they be encouraged?

The two main costs of the ski area are the ski lifts and the night-time snow-making. While the former can be reduced by installing an appropriately sized PV system, the latter is more difficult to mitigate as it always takes place at night. In this respect, snow-making could be managed in an optimised way by taking into account temperatures, energy purchase costs and forecasts for the following days in order to predict snow-pack conditions.

## 4.4 A MPC-BASED CONTROL WITH ANN-BASED FORECASTERS FOR JOINTLY ACTING SELF-CONSUMERS

Recent European Community directives introduce Renewable Energy Communities (REC) and Jointly Acting Renewable Self-Consumers (JARSC). Both entities are constituted by communities of residential and/or non-residential prosumers, located in proximity of renewable generators and Electrical Storage Systems (ESS) owned and managed by the REC/JARSCs. These aggregations of prosumers are aimed at providing environmental and economic benefits by maximizing their global self-consumption. In this frame, it is relevant to introduce a control strategy which considers the whole system represented by the REC/JARSCs and performs optimal management of energy production, storage and consumption. The present study proposes a Model Predictive Control (MPC) based control design, targeted at the minimization of electricity cost and equivalent  $CO_2$  emissions, considering the whole ensemble of loads included in multi-apartment block in Milan, Italy, over a 24-h prediction horizon. To exploit the MPC ability of including forecasts in the optimization problem, predictors including Artificial Neural Networks (ANN) are developed for solar irradiance, air temperature, electricity price and carbon intensity. The presented results highlight that the proposed MPC controller provides a significant improvement in electricity cost savings by maximizing self-consumption over the 24-h prediction horizon. Additionally, the equivalent  $CO_2$  emissions are effectively reduced.

### 4.4.1 MOTIVATIONS

New scenarios are disclosing for electric power distribution systems and new opportunities are opening for consumers. The recent directives 2018/2001 [262] and 2019/944 [263] from European Community, which are currently undergoing the transposition process by Member States, are pushing towards an improvement in the valorisation of self-consumption of renewable energy generation, in particular photovoltaic (PV) and wind generation. The articles 21 and 22 of the RED II directive [262] introduce Renewable Self-Consumers (RSC), Jointly Acting Renewable Self-Consumers (JARSC) and Renewable Energy Communi-

ties (REC). RSCs, JARSCs and REC members, “individually or through aggregators, are entitled:

- (a) to generate renewable energy, including for their own consumption, store and sell their excess production of renewable electricity;
- (b) to install and operate electricity storage systems combined with installations generating renewable electricity for self-consumption;
- (c) to maintain their rights and obligations as final consumers;
- (d) to receive remuneration, including, where applicable, through support schemes, for the self-generated renewable electricity that they feed into the grid.

The Member States are transposing these indications in an heterogeneous way. However, the common factor which can be clearly identified is RSCs, JARSCs and RECs being a further instrument pushing the transformation of final consumers into groups of subjects (prosumers) capable of producing, consuming, storing and sharing electrical energy generated by means of renewable energy sources.

Another aspect of relevance, under the light of the recent policies towards decarbonization, is the evaluation of the equivalent emissions of  $CO_2$  generated by the electrical system [264]. At the moment,  $CO_2$  emissions are not included in electricity price for residential users but, considering the relevance of decarbonization targets, it is of interest to consider how to limit  $CO_2$  emissions. It is hence relevant to introduce a control strategy which considers the whole system represented by the REC, JARSCs or RSCs and performs optimal management of energy production, storage and consumption. Consequently, energy flows can be optimized with the aim of maximizing self-consumption and power shared among the REC members or RSCs, which implies a reduction in cost through available incentive mechanisms, and lowering  $CO_2$  equivalent emissions.

#### 4.4.2 RELATED LITERATURE

RECs are extensively debated in the literature. Several authors have already analysed the REC and JARSC frameworks in order to provide

a comprehensive overview of regulations and technical/economic assessments. As an example, [265, 266] aim to review the regulatory frameworks among different EU member states showing that most of the countries have already developed tariffs definition to support REC, although in some countries there is still no clear structure, with different boundaries regarding REC definitions. In [267], a general overview of RECs and RSCs is shown, investigating different aspects regarding the integration of REC and the actual power system, including the ancillary service and demand response perspectives. Moreover, several projects have already been developed around Europe, demonstrating the considerable interest from governments, research institutes, private entities, and end users [268–270]. From the control and optimization aspect, [271] proposes smart metering and electric vehicles charging solutions to increase the self-consumption in a REC by regulating the EV charging power during the day, while [100] has studied machine learning techniques to improve self-consumption on an existing wind-power REC in Belgium.

A multi-agent approach is analysed in [272], where the coordination of a set of shiftable loads is optimized to maximize the self-consumption of a shared PV system in a JARSC building. Increases in self-sufficiency and self-consumption of up to 98% and 81% are obtained, as well as showing the differences between different control architectures. In [273], an innovative power-sharing model is proposed both for JARSC and REC aiming to always make the end user passive towards the grid, so that only one dedicated point of connection is seen as active user. However, no storage has been considered and a real-time control is performed without any optimization method. Finally, in [274, 275] a procedure is proposed for the optimal design of electrical and thermal installations as a function of total costs and  $CO_2$  emissions reduction. In addition to the economic aspect, although important from the point of view of the end user and the community, the environmental perspective plays a key role, especially in this context where the main aim of the incentive includes decarbonization. In fact, more and more attention is also being paid to this aspect in view of a possible introduction of remuneration for the  $CO_2$  emissions avoided [276]. Although different works have been conducted regarding the joint optimization between costs and

carbon intensity in different energy entities with different optimization techniques [50, 203, 242, 277, 278], no work has been found regarding the analysis of REC or JARSCs with a trade-off approach between the two aspects.

From a control perspective, REC and JARSCs represent a form of grid-connected microgrid, the control of which have been largely debated in literature in recent years. When optimal dispatchment of available resources is the main control task, Model Predictive Controllers (MPC) are often considered. Indeed, MPC controllers are particularly suited for microgrid control as they calculate control action as an optimization problem over a defined prediction horizon, which allows integrating available forecasts and constraints in control action calculations. Additionally, since the control action is calculated by means of a constrained optimization problem, MPC controllers are suited to manage different tasks with conflicting requirements [212, 279]. Indeed, some papers propose MPC-based controllers for microgrids [280–286], addressing different tasks spanning from voltage control to economic optimization and hierarchical control. In these regards, it is clear that the MPC control performances are related to forecasts reliability, and significant literature is available for PV generation, electricity price, carbon intensity and load [98, 101, 102, 104, 105, 107, 111, 112, 127, 287–292]. For this tasks, ANN-based predictors proved to be a suitable solution for PV generation forecasts [101, 102, 287].

#### 4.4.3 JARSC SYSTEM DESCRIPTION

In this section, the considered electrical system as well as the scope of this work are detailed. First, a general overview of the different components is presented, followed by a detailed description of the consumption and generation profiles. At the end, the target of the problem is detailed by defining the incentive features of the collective self-consumption framework. As mentioned, the considered system represents a case study located in Milan. Even though all the data used for sizing and simulations are obtained from online databases, it is necessary to define a geographical location to maintain consistency among correlated data (e.g. irradiance and temperature).

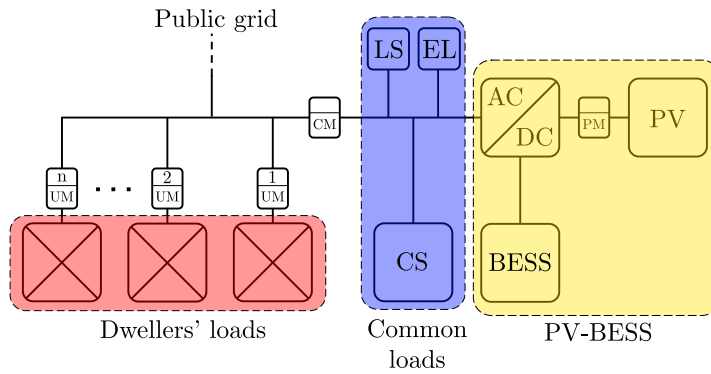


**Figure 4.21:** Considered system electrical schematic.

#### 4.4.3.1 SYSTEM OVERVIEW

The considered system of JARSCs is shown in Fig. 4.21. It is assumed that JARSCs are located in a building in the centre of Milan and consists of twelve apartments, all inhabited by different types of dwellers and families. Each user/apartment has its own energy meter (UM), owned and managed by the DSO. A PV system is installed on the roof of the building, the energy production of which is measured by the production meter (PM). In order to maximize the self-consumption, an “all-in-one” ESS has been included in order to store the surplus PV energy produced in the hours of lower consumption and maximum PV generation for later discharge during periods with small or null PV generation. The ESS includes an inverter, interfacing the DC section with the AC grid and providing PV and/or ESS energy to the common loads, hence improving the total self-consumption. The energy exchanged with the grid is measured through the common utility meter (CM).

The ESS system aims to optimally handle the PV generation by performing the Maximum Power Point Tracking (MPPT) function and manage the charge/discharge battery operation, and includes a Battery Management System (BMS) for balancing the temperatures and the state of charge (SoC) of the battery pack. It is assumed that the power exchanged by the battery can be controlled by an external signal, which will be the output of the MPC control discussed in Section 4.4.4, and that SOC measures/estimation are available from the ESS.

**Table 4.13:** Photovoltaic module technical specification

Electrical Parameter at STC	Symbol	Value
Nominal Power	$P_{mdM}^{STC}$	400 W
Module Efficiency	$\eta_{md}$	22.6%
Rated Voltage	$V_{mdM}^{STC}$	65.8 V
Rated Current	$I_{mdM}^{STC}$	6.08 A
Open-circuit Voltage	$V_{mdOC}^{STC}$	75.6 V
Short-circuit Current	$I_{mdSC}^{STC}$	6.58 A
Current Temperature Coefficient	$\alpha_{md,T}^{\%}$	2.9 mA/°C
Voltage Temperature Coefficient	$\beta_{md,T}^{\%}$	-176.8 mV/°C
Power Temperature Coefficient	$\gamma_{md,T}^{\%}$	-0.29 %/°C

#### 4.4.3.2 PHOTOVOLTAIC SYSTEM

The PV system is designed in order to cover most of the energy consumption of the considered JARSCs. The total energy consumption of the considered JARSCs, detailed in Section 4.4.3.4 and Section 4.4.3.5, is equal to 40 MWh/year. Considering to cover the 85% of the annual energy consumption with the PV generation, and considering that in Milan the annual energy generation of PV systems is roughly 1100 kWh/kWp, the required PV installed power result in 30.9 kW. Since the PV system is the only source of energy present in the microgrid, monocrystalline technology is selected as a common commercial solution. The selected module specifications (manufacturer is unessential and undisclosed) are reported in Table 4.13. To reach the required installed power by means of the selected PV modules, it is possible to use 3 series-connected modules per string and 26 parallel-connected strings, resulting in a total of 78 installed modules, the power of which is equal to 31.2 kWp. Note that this sizing procedure is not optimal from the economic point of view, but it is meant to have enough PV generation to cover most of the JARSCs needs, in order to reduce  $CO_2$  emissions, which is one of the driving reasons for the introduction of REC and JARSCs.

#### 4.4.3.3 STORAGE SYSTEM

With the aim of increasing the building self-consumption, a lithium-ion phosphate storage system has been included in the system under analysis. The sizing of the ESS is based on the energy which should ideally be stored on each day of the year, calculated as the difference

**Table 4.14:** Battery module specifications

Electrical Data	Value
Rated Module Capacity	300 Ah
Efficiency	95%
Rated Voltage	50 V
Rated C-rate	1 C
Depth of Discharge	90 %
Warranty	10 years
Battery Service Life	designed for over 20 years
Cycles	10,000

between PV production and loads energy consumption in daily hours. The sum of said energy over one year is then divided by the number of days of the year in which PV production is larger than loads energy consumption in daily hours, resulting in a starting ESS sizing equal to 63 kWh. The considered ESS is then realized by means of four commercially available modules, each one having a capacity of 15 kWh. In order to reduce the degradation during the lifetime, a maximum Depth-of-Discharge (DoD) has been set in the simulations to comply with the manufacturer specifications. The main parameters of the battery module are listed in Table 4.14.

#### 4.4.3.4 CONSUMERS LOAD PROFILES

As mentioned, the multi-apartment block under investigation consists of twelve apartments, each inhabited by different occupants with different habits. In fact, with the aim of making the evaluation as faithful as possible, a wide spectrum of dwellers with different habits (and, therefore, different load profiles) has been considered. For this purpose, the Load Profile Generator (LPG) simulation tool [293] has been used, which allows automatic generation of residential electrical and water synthetic consumption based on psychological and behavioural profiles of the residents and possible daily activities which can be performed. A list of example consumption profiles is available at [294], the first twelve of which are used as load profiles in this study. The list of the inhabitant's profiles, the corresponding amount of electricity consumption and their contractual power are shown in Table 4.15. In addition, Fig. 4.22 shows the twelve load profiles corresponding to each apartment over

**Table 4.15:** Inhabitants details and electricity consumption over one year.

Type	Consumption [kWh]	Contractual Power [kW]
Couple (F23-M25) both at work	2623	3.5
Couple (F37-M38), with work	1706	3.5
Family (F40-M43-M10), both at work	2613	4
Couple (F45-M50)	2870	5
Family (F35-M40-M13-M6-F4)	4001	5
Jobless (M30)	1265	3.5
Single with work (M23)	1454	3.5
Family (F30-M11-M7)	3227	3.5
Single woman (F34) with work	1733	3
Single man (M40) shift worker	2035	4
Female (F23) student	1563	3
Male (M22) student	1102	3

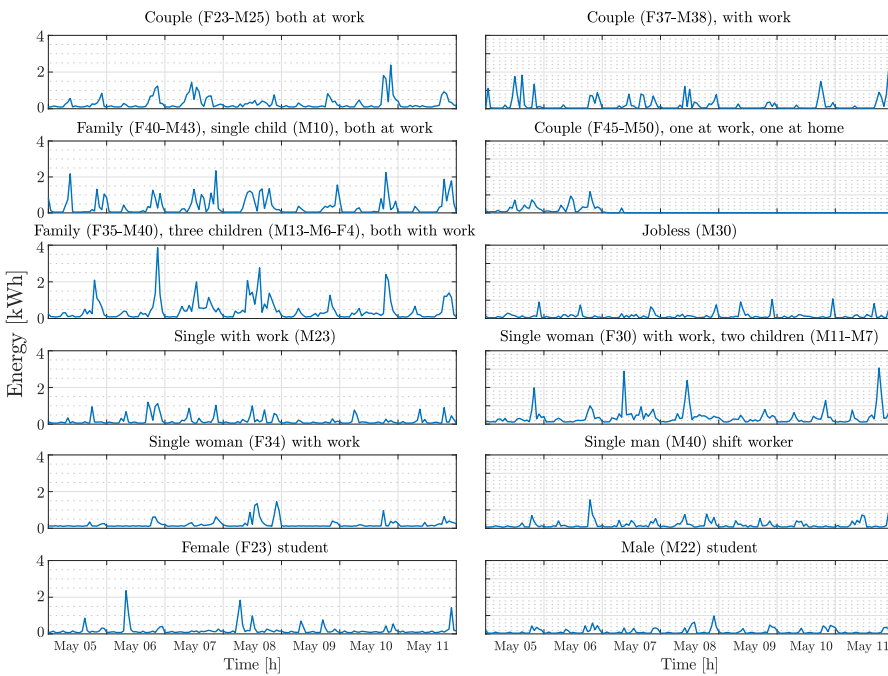


**Figure 4.22:** Example of electrical load profiles of the twelve apartments over one week

one example week throughout the year. One can note that each profile has different properties depending on the presence of inhabitants, possible vacation periods and working hours. This not only makes it possible to correctly evaluate the economic and energy analysis of the problem, but also provides important characteristics on the periods of greatest consumption.

#### 4.4.3.5 COMMON LOAD PROFILE

In multi-flat buildings, there is always a certain amount of electrical load needed for common services, the costs of which are usually divided among the inhabitants according to private agreements, which will not be discussed in this study. The most common loads representing common services are the lighting of shared areas (courtyard, stairs, entrance) and lifters. Consequently, in absence of available data, an energy profile based on statistical considerations was created for lighting and elevators. With regard to lighting, a number of LED bulbs with an average power of 100 W were assumed. Absorption takes place over two time slots: between 5 a.m. and 9 a.m. and between 5 p.m. and midnight. During these time intervals, LED lighting is assumed to absorb, in each 5-min interval, an instantaneous power between 50 W and 150 W, with gaussian distribution and average value equal to 100 W. Concerning the lift, [295] presented a study on different types of lifts highlighting that a significant power consumption generated by residential lifts is caused by the stand-by mode rather than by individual rides. In our model, according to measures presented in [295], an average stand-by power of 250 W was considered. Additionally, with regard to consumption in the running phase, an energy of 50 Wh per single run was assumed. The operating intervals are the same as for lighting with the addition of a lunchtime interval between noon and 2pm. Considering the total number of inhabitants in the building, from 6 to 18 runs for the morning and evening intervals and from 3 to 9 runs for the mid-day interval were considered, with random (gaussian) variations around the average value.

In addition to lifters and lighting, the increase in electric car purchases in recent years has also seen an increase in residential charging stations (wallboxes) as an additional common service for the inhabitants. For this reason, real energy profiles of a 22 kW wallbox for residential use were considered for the charging of two 50 kWh electric vehicles. The two owners mainly use the vehicle for commuting, so that it is charged during the evening/night hours in order to have it fully charged the next morning. Charging is not externally controlled and the power profile is managed by the EV's internal BMS.

#### 4.4.3.6 PHOTOVOLTAIC GENERATION PROFILES

Considering now solar irradiance and air temperature, statistical data are available online, provided by the Photovoltaic Geographical Information System (PVGIS), an online database managed by the European Science Hub [296]. This database provides both hourly profiles for complete years and aggregated data, such as monthly average radiation. Photovoltaic generation can be calculated as a function of solar irradiance and air temperature considering the expressions reported in [286]. Considering that the purpose of this study is the design of an MPC controller, it is clear that also some forecasts of solar irradiance and air temperature would be of help. In these regards, the aggregated data (e.g. average daily profiles per month) available from PVGIS may be considered as a starting point for PV generation prediction. Further discuss on how to integrate statistical data in forecasts are reported in Section 4.4.4.4. The data used in this study are referred to 2016, being it the most recent year for which all data are available for the considered location.

#### 4.4.3.7 ELECTRICITY PRICE AND EQUIVALENT CARBON INTENSITY PROFILES

Being minimization of cost and equivalent  $CO_2$  emissions the target of this study, it is necessary to recall data about those quantities. Considering selling price, it is worth considering that, in Italy, two possibilities are considered. In fact, the surplus of energy production which is not directly consumed or stored to the battery is sold to the public grid. In Italy there are two types of procedures for selling energy to the grid. The first consists of payment by the distributor of a fixed minimum price (PMG - Prezzo Minimo Garantito). The second one consists of payment of energy through the real-time pricing (PO - Prezzo Orario), which varies hourly based on the energy markets and the electricity zone considered. In this study, we assume that the sale of energy is performed via PO, thus taking advantage of the variability of market prices. In these regards, PO values for the year 2016 in the ITA-NORTH electricity market zone were extracted from the database of the European Network of Transmission System Operators for Electricity (ENTSO-E) [225]. Regarding the purchase cost, a variable cost was assumed based on the hourly zonal price by considering a possible implementation of

a real-time pricing (RTP) type market that varies based on the needs of the distributor. System charges, network services, excise taxes, trader's earnings and VAT were added to the PO at typical values for residential customers.

In addition to economic cost, buying energy from the grid does also imply an environmental cost in terms of  $CO_2$  emission. The energy produced carries a carbon dioxide content that depends on the energy mix of the country of production (and neighbouring countries, due to international energy exchange): the carbon intensity is the parameter that allows us to assess this aspect. This value changes considerably within the day hour by hour depending on how much energy is produced from renewable sources compared to production from fossil fuels. Therefore, it is possible to optimize the purchase of energy from the grid, reducing absorption during high-carbon intensity periods (night-time) and increasing absorption during low-carbon hours (daytime). Based on the types of production plants, their emission factors and amount of energy produced, it is possible to calculate the carbon intensity of the electricity of the specific area. The ENTSO-E platform provides the values and types of production on an hourly basis while the emission factors were extracted from the study in [297].

#### 4.4.3.8 INCENTIVE PLAN FOR SHARED ENERGY

As mentioned, recent directives from European Community require Member States to promote forms of self-consumption, including jointly acting self-consumption. From here on, we will refer to the Italian case, assuming that, even if other transposition of the European Directives may be technically different, the common idea driving this incentive system will produce comparable results. Even though detailed discussion on energy pricing will be presented in Sections 4.4.4.3 and 4.4.5 as part of the optimization problem formulation, this subsection aims to describe the operation of the incentive mechanism that should act as a lever for the promotion of REC and RSC. In principle, two different regulation models, namely physical and virtual [298], are possible. However, at present regulation refers only to the virtual one, where the participants in REC or JARSCs share energy by taking advantage of the Distribution System Operator (DSO) existing distribution grid. In this

configuration, each inhabitant is connected through its own connection point (meter), as shown in Fig. 4.21. The electricity system operator GSE (Gestore Sistema Energetico), in order to promote REC/RSCs, rewards local self-consumption by providing an economic incentive. The latter is calculated on the so-called “shared energy”, which is equal to the hourly minimum between the electricity produced and fed into the grid by renewable sources and the electricity consumed by the set of subjects belonging to the REC or by RSCs. Shared energy is rewarded with:

- (a) a compensation due to avoided grid losses and distribution charges of about 11.5 €/MWh;
- (b) an incentive of 100 €/MWh for groups of JARSCs, 110 €/MWh for REC.

In addition, since the energy produced is actually fed into the grid (virtual exchange), said energy is remunerated according to the electricity market. In this case, the common loads are connected upstream of the condominium meter, directly absorbing the PV energy and representing an additional form of self-consumption, which will need to be considered for economic analysis.

#### 4.4.4 SYSTEM MODELLING AND CONTROL DESIGN

In this Section, the main systems models and forecasts used for the simulations described in Section 4.4.5 are presented. As far as the MPC controller is concerned, efficient solvers are available commercially (e.g. Gurobi [299], Cplex [300], etc.), along with specific MATLAB expansions (e.g. Yalmip [301]) to interface standard MATLAB code with the aforementioned commercial solvers. As a consequence, the realization of an MPC controller requires a suitable system model, constraints and cost function, leaving the real problem solution and related issues to specific software.

##### 4.4.4.1 SYSTEM MODEL FOR SIMULATION PURPOSES ELECTRONIC POWER CONVERTER

The considered system includes one converter interfacing PV and ESS to the public distribution system. For the purposes of this study, the system

is considered in quasi-stationary conditions, such that a detailed model of power converters and their control is not required. Consequently, they will be modelled as ideal converters with known efficiency (battery efficiency 95%, PV to grid efficiency 98%).

#### PV SYSTEM MODELLING

For the purposes of this study, the PV modules can be simply modelled by means of their I–V characteristic, which allows determining the maximum power point as a function of ambient temperature and solar irradiance. The exact equations used in this study can be found in [286].

#### ESS MODELLING

Considering the target of this study, an advanced battery model is not needed. The only characteristics which is necessary to model are those related with energy balance, namely State of Charge (SoC) and efficiency. Considering a constant efficiency  $\eta_{batt}$ , and assuming the ESS exchange power  $P_{batt}$  positive if drained, the energy exchanged by the ESS over one discrete time step  $\Delta t$  can be evaluated by means of:

$$E_{batt} = \left( \frac{1 + \text{sgn}(P_{batt})}{2} \frac{1}{\eta_{batt}} - \frac{1 - \text{sgn}(P_{batt})}{2} \eta_{batt} \right) P_{batt} \Delta t \quad (4.36)$$

The ESS SoC variation over one discrete time step  $\Delta t$  can then be evaluated by means of:

$$SoC(k) = SoC(k - 1) - \frac{E_{batt}}{C_{batt}} \quad (4.37)$$

where  $C_{batt}$  is the nominal ESS energy capacity.

#### 4.4.4.2 SYSTEM MODEL FOR MPC CONTROL DESIGN

The desired discrete-time system model is expressed in general form as:

$$\mathbf{x}(k + 1) = \mathbf{A}\mathbf{x}(k) + \mathbf{B}\mathbf{u}(k) \quad (4.38)$$

where  $x$ ,  $u$  are, respectively, the state and input vectors and  $\mathbf{A}$ ,  $\mathbf{B}$  are, respectively, the state and input matrices. In the considered case study,

the only model required is a model of the storage devices SoC, which, combining (4.36), (4.37) can be formulated as:

$$SoC(k+1) = SoC(k) - \frac{P_{batt}(k) \Delta t}{C_{batt}} \left( \frac{1 + \text{sgn}(P_{batt}(k))}{2} \frac{1}{\eta_{batt}} - \frac{1 - \text{sgn}(P_{batt}(k))}{2} \eta_{batt} \right) \quad (4.39)$$

Reformulating (4.39) in terms of states and inputs leads to:

$$x(k+1) = x(k) - \frac{\Delta t}{C_{batt}} u(k) \quad (4.40)$$

where  $x(k) = SoC(k)$ . The control  $u$  is defined as:

$$u(k) = P_{batt}(k) \left( \frac{1 + \text{sgn}(P_{batt}(k))}{2} \frac{1}{\eta_{batt}} - \frac{1 - \text{sgn}(P_{batt}(k))}{2} \eta_{batt} \right) \quad (4.41)$$

such that the control input  $u$  represents a virtual power exchanged with the battery, including efficiency. This allows to use a linear system model (4.40), to include constraint on battery power  $P_{batt}$ , and to map the non-linearity related to battery efficiency (4.41) as a constraint in the optimization problem in a computationally efficient way.

#### 4.4.4.3 OPTIMIZATION PROBLEM FORMULATION

##### VARIABLES

The proposed MPC controller is based on a quite simple model, as detailed in Section 4.4.4.2. However, since it is intended for minimizing costs and  $CO_2$  emissions, it will need to deal with quite a complex cost functions and constraints set. In order to make the problem formulation as clear as possible, a number of auxiliary variables are introduced.

Firstly, a set of continuous variables is necessary to represent the system operating point ( $X_0$ ), states ( $\mathbf{X}$ ), and inputs ( $\mathbf{U}$ ). Note that the homologous variables appearing in Section 4.4.4.2 ( $x, u$ ), indicated with lowercase letters, are referring to a single time step, while variables indicated as bold capital letters ( $\mathbf{X}, \mathbf{U}$ ) are vectors representing variables

over the prediction horizon. Successively, the following variables are defined:

- non-controllable exchanged energy  $\mathbf{E}_{nc[13 \times N]}$ : each column of  $\mathbf{E}_{nc}$  is constituted by the energy absorbed, at one of the  $N$  steps of the prediction horizon, by the 13 connection points reported in Fig. 4.21 when battery power  $P_{batt}$  is null. The first twelve elements of each column represent consumers' absorptions, and hence are strictly positive. The last element of each column includes common loads and PV generation, so that can be negative when PV generation is larger than common load. At each step, the first column of  $\mathbf{E}_{nc}$  is built with real-time measures, while the subsequent  $N - 1$  columns are built with forecast data.
- selling price, buying price and  $CO_2$  equivalent emission vectors  $\mathbf{P}_{sell[1 \times N]}$ ,  $\mathbf{P}_{buy[1 \times N]}$ ,  $\mathbf{CO2}_{[1 \times N]}$ : represent the evolution of selling price, buying price and carbon intensity, respectively, over the  $N$  steps in the prediction horizon. Similarly to matrix  $\mathbf{E}_{nc}$ , the first element of these vector represents a real-time measure, while the following ones are obtained from forecast data.
- battery exchanged power  $\mathbf{P}_{ESS[1 \times N]}$ : control variable over the prediction horizon, related to the system input  $\mathbf{U}$  by means of (4.41), introduced as a constraint. Battery exchanged power  $\mathbf{P}_{ESS}$  is the optimization variable which constitutes the output of the proposed MPC controller, and the first element of  $\mathbf{P}_{ESS}$  is used as control signal  $P_{batt}$  for the ESS and system simulation.
- PV generated power  $\mathbf{P}_{PV[1 \times N]}$ : PV generated power over the prediction horizon. Note that the energy produced by the PV over the prediction horizon is included in  $\mathbf{E}_{nc}$ , but the PV generated power  $\mathbf{P}_{PV}$  is required to define operational constraints.
- exchanged energy  $\mathbf{E}_{[13 \times N]}$ : includes the battery exchanged power in energy balance. The first twelve elements of each column are equal to their counterparts in  $\mathbf{E}_{nc}$ , while the last element is obtained as:

$$\mathbf{E}(13, k) = \mathbf{E}_{nc}(13, k) - P_{ESS}(k) \Delta t, k \in [1, N] \quad (4.42)$$

- shared energy  $\mathbf{E}_{shared[1xN]}$ : energy shared over the prediction horizon, as defined in Section 4.4.3.8. Considering that the energy injected into the grid by the PV/ESS node is identified, for each  $k$ -th step of the prediction horizon, as  $-\mathbf{E}(13, k)$ , each element of  $\mathbf{E}_{shared}$  is defined as:

$$\mathbf{E}_{shared}(k) = \begin{cases} \min\left(\sum_{i=1}^{12} \mathbf{E}(i, k) - \mathbf{E}(13, k)\right) & \text{if } -\mathbf{E}(13, k) > 0 \\ 0 & \text{if } -\mathbf{E}(13, k) \leq 0 \end{cases} \quad (4.43)$$

- sold energy  $\mathbf{E}_{sold[1xN]}$ : energy sold over the prediction horizon, defined as:

$$\mathbf{E}_{sold}(k) = \begin{cases} -\mathbf{E}(13, k) - \mathbf{E}_{shared}(k) & \text{if } -\mathbf{E}(13, k) > \mathbf{E}_{shared}(k) \\ 0 & \text{if } -\mathbf{E}(13, k) \leq \mathbf{E}_{shared}(k) \end{cases} \quad (4.44)$$

- cost matrix  $\mathbf{C}_{[13xN]}$ : defines the energy cost over the prediction horizon. The first twelve elements of each column, being residential users, are defined as:

$$\mathbf{C}(i, k) = VAT(C_{fix}(i) + \mathbf{E}(i, k)\mathbf{P}_{buy}(k)), \quad i \in [1, 12], \quad k \in [1, N] \quad (4.45)$$

where  $C_{fix}(i)$  represents the portion of yearly fixed cost of the  $i$ -th users associated with each hour of the year and  $VAT$  is a coefficient including the value added tax. The last element of each column is quite more complex to be defined, as the PV/ESS node can both buy or sell energy. This results in:

$$\mathbf{C}(13, k) = \begin{cases} VAT(C_{fix}(13) + \mathbf{E}(13, k)\mathbf{P}_{buy}(k)) & \text{if } \mathbf{E}(13, k) \geq 0 \\ VAT C_{fix}(13) - \mathbf{E}_{shared}(k) \cdot (\mathbf{P}_{buy}(k) + Inc) - \mathbf{E}_{sold}(k)\mathbf{P}_{sell}(k) & \text{if } \mathbf{E}(13, k) < 0 \end{cases} \quad (4.46)$$

where  $Inc$  is the aforementioned economic incentive on shared energy.

- $CO_2$  total emission vector  $\mathbf{CO2}_{total[13xN]}$ : defines the total  $CO_2$  emissions over the prediction horizon, defined as:

$$\mathbf{CO2}_{total}(k) = \begin{cases} \mathbf{CO2}(k) \sum_{i=1}^{13} \mathbf{E}(i, k) & \text{if } \sum_{i=1}^{13} \mathbf{E}(i, k) > 0 \\ 0 & \text{if } \sum_{i=1}^{13} \mathbf{E}(i, k) \leq 0 \end{cases} \quad (4.47)$$

## CONSTRAINTS

In the following section, the optimization problem constraints are presented, which are:

- initial operating point: state variables must be equal to the measured battery SoC  $x(k)$  related to the current time instant, according to:

$$\mathbf{X}_0 = x(k) \quad (4.48)$$

- storage SoC is to be limited according to device capacity and DOD provided by the manufacturer, resulting in:

$$1 - DOD \leq \mathbf{X} \leq 1 \quad (4.49)$$

- the vector of control variables over the prediction horizon  $\mathbf{U}$  can be represented, according to (4.41) as:

$$\mathbf{U}(k) = \mathbf{P}_{ESS}(k) \left( \frac{1 + \text{sgn}(\mathbf{P}_{ESS}(k))}{2} \frac{1}{\eta_{batt}} - \frac{1 - \text{sgn}(\mathbf{P}_{ESS}(k))}{2} \eta_{batt} \right) \quad (4.50)$$

- battery exchanged power  $\mathbf{P}_{ESS}$  is to be limited according to converter capability and ESS C-rate, resulting in:

$$-P_{maxC} \leq \mathbf{P}_{ESS} \leq P_{maxD} \quad (4.51)$$

where  $P_{maxC}$  is the maximum charge power and  $P_{maxD}$  is the maximum discharge power;

- it may be useful to consider the possibility of imposing the MPC controller not to buy energy from the grid to charge the battery, regardless of the possible economic convenience of this operation.

In the said case, battery exchanged power  $P_{ESS}$  is to be limited with respect to the PV generated power, resulting in:

$$\mathbf{P}_{ESS} \geq -\mathbf{P}_{PV} \quad (4.52)$$

The implications of this additional constraints will be discussed in Section 4.4.5.

### COST FUNCTION

The cost function to be used for optimization must consider, as mentioned, electricity cost and equivalent  $CO_2$  emissions. Consequently, the following quantities are defined:

$$J_{Cost} = \sum_{k=1}^N \sum_{i=1}^{13} \mathbf{C}(i, k) \quad (4.53)$$

$$J_{CO_2} = \sum_{k=1}^N \mathbf{CO2}_{total}(k) \quad (4.54)$$

where  $J_{Cost}$  represents the total electricity cost over the prediction horizon as a function of the optimization variable  $P_{ESS}$ , while  $J_{CO_2}$  represents the total equivalent  $CO_2$  emissions over the prediction horizon as a function of the optimization variable  $P_{ESS}$ . In addition to these costs, it may be of interest to introduce a further cost term to avoid possible issues related to inconsistencies in forecasts. This additional term is defined as:

$$\mathbf{J}_{prev} = \begin{cases} -(1 - \mathbf{X}(2)) \sum_{i=1}^{13} \mathbf{E}(i, 1) & \text{if } \sum_{i=1}^{13} \mathbf{E}(i, 1) < 0 \\ 0 & \text{if } \sum_{i=1}^{13} \mathbf{E}(i, 1) \geq 0 \end{cases} \quad (4.55)$$

This term is meant to associate an additional cost to energy sold while the battery is not fully charged. In fact, the summation in 4.55 represents the energy sold in the first step of the prediction horizon, while the term  $(1 - \mathbf{X}(2))$  is null when the MPC foresee the battery to be fully charged on the second step of the prediction horizon. The effect of this additional cost on MPC behavior will be discussed in Section 4.4.5.

Defined the single terms (4.53)–(4.55), the desired cost function is defined as:

$$J = \alpha J_{Cost} + \beta J_{CO_2} + \gamma J_{prev} \quad (4.56)$$

where  $\alpha$ ,  $\beta$ ,  $\gamma$  are coefficients used to assess the different priorities in the optimization process. In particular,  $\alpha$ ,  $\beta$  are chosen such that  $\alpha \geq 0$ ,  $\beta \geq 0$ , with  $\alpha + \beta = 1$ , in order to assess the priority of cost vs  $CO_2$  minimization. The term  $\gamma$ , on the contrary, is chosen equal to 1 if the additional cost (4.55) is desired to be considered in the optimization problem, null otherwise.

#### 4.4.4.4 AVAILABLE DATA AND FORECASTS

As mentioned, one of the main strengths of MPC controllers is their ability to exploit available forecasts to optimize control action over the prediction horizon, and obviously the better performances are obtained when the available forecasts are accurate and reliable. Consequently, it is necessary to clarify which data are to be considered as available forecasts for the MPC controller, hence known a priori over the whole prediction horizon, and which ones are to be considered as measured data to be used in system simulation, hence known only in the simulation present and past steps.

#### STATISTICAL PREDICTION OF SOLAR IRRADIANCE, AIR TEMPERATURE, PRICE, $CO_2$ EMISSIONS AND LOADS

As mentioned in Section 4.4.3.6, the PVGIS database [296] provides average daily irradiation and temperature profiles on hourly base for each month of the year. Additionally, it provides daily irradiation and temperature profiles on hourly base for each day of the year. In this study, the average daily profiles of each month have been considered as known and used as available forecast, both for irradiation and temperature, assuming the forecasts of each day of the month to be the same. Analogously, the daily irradiation and temperature profiles of each day has been used as measured data, not known a priori.

As reported in Section 4.4.3.7, hourly price and carbon intensity forecasts are available from online databases. Aggregated data, similar to the ones available for temperature and irradiance, are not available.

Consequently, similar profiles are obtained, for a single day of each month, by averaging the available data of that month, hour by hour, both for price and carbon intensity. This allows using the same approach used for irradiance and temperature, in that the averaged data are used as known statistical predictions, while the original hourly profiles are used as measured data. Lastly, the same approach is applied to load profiles, both users' absorptions and common services absorption, as presented in Section 4.4.3.4 and 4.4.3.5. Averaged profiles are generated and used as known forecast data, while original hourly profiles are used as measured data.

This approach provides long-term predictions with low effort, but it is not very accurate, in that solar irradiance and load absorption in particular are known to be subject to large variations with respect to its average value. For this reason, it is suitable for long-term predictions, where large deviations from the average trend are less likely. For the same reasons, this approach is less suitable for short-term predictions, where irradiance and load variations may be significant and produce more significant effect on system operation. Consequently, a more effective solution for short-term prediction is introduced in the following paragraph.

#### ANN-BASED PREDICTION OF SOLAR IRRADIANCE, AIR TEMPERATURE PRICE AND $CO_2$ EMISSION

As mentioned, the availability of reliable predictions is a key factor for the development of an efficient MPC controller. In these regards, it is of interest to consider machine learning techniques for this task. It is worth considering that, ideally, not only reliable predictions are desired, but the predictor also needs to be as simple as possible to be compatible with real-time applications with no need for expensive high-performance processors. For these reasons, the well-known Feed-Forward Neural Network (FFNN) [302] has been selected to predict both solar irradiance (G) and air temperature (T). Even though FFNNs represent the simplest form of artificial neural networks, their ability to solve complex problems by mapping the relationship between the input and the output using the back-propagation algorithm has been widely demonstrated [303]. In this study, four different neural networks have

been used for prediction of solar irradiance, air temperature, electricity price and carbon intensity.

The first two neural networks are used for prediction of solar irradiance and air temperature, and are obtained from [286]. They work with 15 min sampling time, so that the available profiles have been interpolated to obtain a 15-min time step, processed through the neural network, and resampled to get predictions with 1-hour time step. The ANN architecture consists of one input layer with 12 neurons corresponding to the previous 12 input values from time  $k$  back to time  $k-11$ , one or more hidden layers within a number of neurons estimated during the training process, and one output layer containing 12 output values corresponding to time steps from  $k+1$  up to  $k+12$ , as depicted in Fig. 4.23. The dataset used for the training of the network consists of the 35136 samples. This dataset has been restructured as a matrix of  $N \times M$  dimension where  $N = 12$  rows and  $M = 35124$  columns. The FFNN prediction model can be simply formulated as:

$$Y^N(k+1) = FFNN(Y^N(k)) \quad (4.57)$$

where  $Y^N(k)$  is the column  $k$ ,  $Y^N(k+1)$  corresponds to the next column ( $k+1$ ) and  $N = 1, 2, \dots, 12$ . Given the notation of (4.57), we can conclude that, at time  $k$ , a vector of  $N$  elements  $Y^N$  is provided to the prediction model FFNN which forecasts a vector of  $N$  elements available at time  $k+1$ . The dataset has been divided into two sets: the 80% of the samples has been used for the training, while the remaining 20% has been used for testing the model. With reference to Fig. 4.24, during the first iteration the input and the output of the FFNN correspond to the first and the second columns, respectively. During the second iteration, the input and the output of the FFNN correspond to the second and the third columns, respectively. The method is applied in the same way until the mean square error is less than 10%. The FFNN is then able to predict the next 12 values of solar irradiance and air temperature based on the actual values of the previous 12. The training process has been tuned using the Levenberg-Marquardt algorithm [304] which is available in MATLAB using the *trainlm* network training function [305]. After a number of experiments, the best configuration has been obtained with the structure 12x15x12 (12 neurons in the input layer,

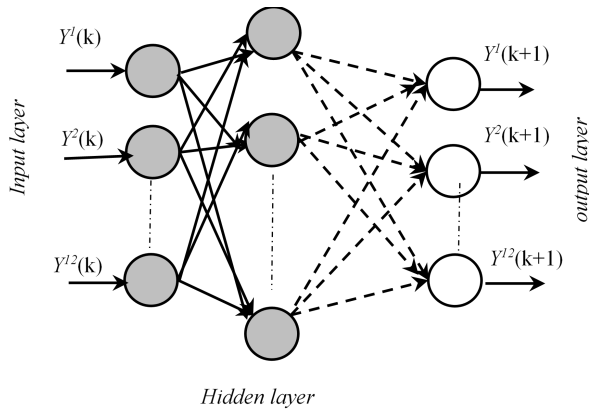


**Figure 4.23:** Feed forward neural network configuration

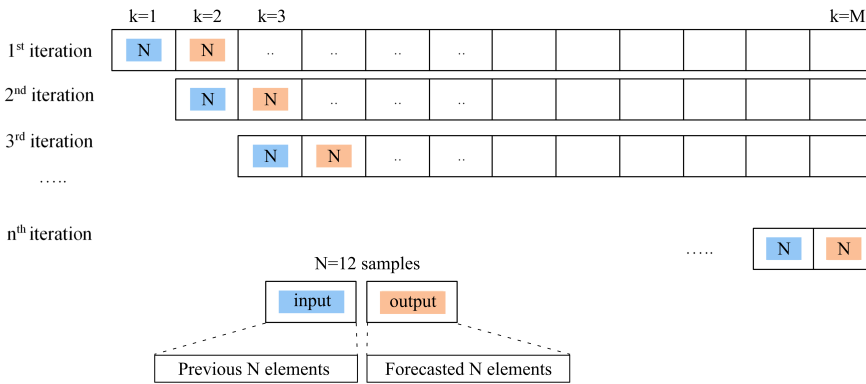


**Figure 4.24:** Multistep ahead forecasting scheme

15 in the hidden layer and 12 in the output layer). Considering the final resample of prediction data, the considered ANN provides a forecast of the next 3 hours, based on the measures over the last 3 hours.

A similar approach has been used to design the other neural networks used in this study, which are aimed at forecasting carbon intensity and price. For carbon intensity predictions, the ANN architecture consists of one input layer with 24 neurons corresponding to the previous 24 input values from time  $k$  back to time  $k-23$ , one or more hidden layers within a number of neurons estimated during the training process, and one output layer containing 3 output values corresponding to time steps from  $k+1$  up to  $k+3$ , as depicted in Fig. 4.23. The dataset used for the training of the network consists of the 52591 samples. This dataset has been restructured as a matrix of  $N \times M$  dimension where  $N = 24$

rows and  $M = 52527$  columns. The FFNN prediction model can be simply formulated as (4.57), with  $N = 1, 2, \dots, 24$ . The dataset has been divided into two sets: the 85% of the samples has been used for the training, while the remaining 15% has been used for testing the model. The method is applied in the same way until the mean square error is less than 10%. The FFNN is then able to predict the next 3 values of carbon intensity based on the actual values of the previous 24. The training process has been tuned using the Levenberg-Marquardt algorithm. After a number of experiments, the best configuration has been obtained with the structure  $24 \times 12 \times 3$  (24 neurons in the input layer, 12 in the hidden layer and 3 in the output layer).

For price predictions, the same procedure used for carbon intensity predictions has been used. In particular, the ANN architecture consists of one input layer with 9 neurons corresponding to the previous 9 input values from time  $k$  back to time  $k-8$ , one or more hidden layers within a number of neurons estimated during the training process, and one output layer containing 3 output values corresponding to time steps from  $k+1$  up to  $k+3$ , as depicted in Fig. 4.23. The dataset used for the training of the network consists of the 54295 samples. This dataset has been restructured as a matrix of  $N \times M$  dimension where  $N = 24$  rows and  $M = 54244$  columns. The training process has been tuned using the Levenberg-Marquardt algorithm. The resulting FFNN is then able to predict the next 3 values of electricity price based on the actual values of the previous 24. After a number of experiments, the best configuration has been obtained with the structure  $9 \times 12 \times 3$  (9 neurons in the input layer, 12 in the hidden layer and 3 in the output layer).

#### INTEGRATION OF REAL-TIME MEASURES AND ANN PREDICTIONS WITH STATISTICAL DATA

The forecasts provided by the ANN-based predictor are then integrated in the overall forecasts: at each time step, the previous 3 measured values of solar irradiance and air temperature are provided as input to the ANN-based predictor, which provides a forecast of the 3 subsequent values of the same quantities. These 3 values substitute the corresponding 3 values of the statistical profiles so that, at each time step, the first 3 steps of the forecasts are those provided by the ANN,

while the following steps are purely statistical forecasts. The same is done for price and carbon intensity ANN, which, even though requiring a different number of inputs, still provide as output a 3-h prediction.

This solution produces adaptive forecasts of the considered quantities, which are updated based on real-time measures at each time step. A similar approach based on averaging of real-time measures and statistical forecasts was proposed in [306] for this same task. However, the addition of the ANN-based predictor proposed in this study significantly increases the accuracy of short-term prediction, which has the most effect on MPC control action, with minimal computational burden increase. The statistical forecast proposed in [306] is used in this study, as a way to ensure a smooth transition between ANN predictions and statistical data. Overall, at each time step  $k$ , the real time measure is acquired, the step  $[k+1; k+3]$  are the forecasts provided by the ANN, and the subsequent three steps  $[k+4; k+6]$  are obtained by means of the statistical forecast proposed in [306] to ensure a smooth connection between ANN prediction and statistical data.

Considering load forecasts, the high volatility of the considered profiles made impossible to use a simple FFNN to generate useful prediction. Indeed, the complexity of the load profile generator [293] used to generate them suggest that a very complex network must be used to obtain reasonable predictions, which is in contrast with the simplicity target of this study. Consequently, the statistical forecast proposed in [306] has been used to connect real-time measures and statistical predictions, with no further forecast techniques applied.

#### 4.4.5 SYSTEM SIMULATION AND RESULTS

In this Section, the numerical simulations performed to assess the effectiveness of the proposed MPC controller are reported. All simulations have been realized as MATLAB code and cover one year of operation. The considered simulations scenarios are described in Section 4.4.5.1, necessary numerical data are reported in Section 4.4.5.2, simulation results are presented in Section 4.4.5.3, while an economic analysis of the presented results is reported in Section 4.4.5.4. Global results are discussed in Section 4.4.6.

#### 4.4.5.1 DEFINITION OF SIMULATION SCENARIOS

In order to assess the proposed control effectiveness, a comprehensive set of simulations have been performed. The considered simulation scenarios are reported in the following.

##### SIMULATION SCENARIO 1: FIRST BENCHMARK SIMULATION

In this scenario, no optimization is performed, and no measures are shared between connection points. The battery is controlled considering only the measures available at the common utility meter (CM) in Fig. 4.21. The power drained from the battery, at each time step  $k$ , is calculated as:

$$P_{batt} = \begin{cases} \frac{E(13,k)}{\Delta t} - P_{PV}(k) & \text{if } 1 - DOD \leq SoC(k) - P_{batt} \frac{\Delta t}{C_{batt}} \leq 1 \\ 0 & \text{otherwise} \end{cases} \quad (4.58)$$

Simulation Scenario 1 basically covers what would be done at the moment in terms of energy management, and will be considered a first reference for the evaluation of optimized simulations. In this case, the battery is charged and discharged in order to cover, if possible, the load at the common utility meter (CM), maximizing its self-consumption. The excess of generation is stored in the ESS for later use for common services if possible, otherwise it is injected into the distribution grid. In this latter case, part of the injected energy will be considered shared energy, depending on the absorptions at the other 12 connection points.

##### SIMULATION SCENARIO 2: SECOND BENCHMARK SIMULATION

In this scenario, no optimization is performed, but measures from connection points 1–12 are shared among JARSCs. The battery is controlled considering the measures available at the 13 connection points in Fig. 4.21. The power drained from the battery, at each time step  $k$ , is calculated as

$$P_{batt} = \begin{cases} \frac{\sum_{i=1}^{13} E(i,k)}{\Delta t} - P_{PV}(k) & \text{if } 1 - DOD \leq SoC(k) - P_{batt} \frac{\Delta t}{C_{batt}} \leq 1 \\ 0 & \text{otherwise} \end{cases} \quad (4.59)$$

Scenario 2 represents a significant improvement over Scenario 1 and is specifically tailored for JARSCs. Consequently, it will be considered a second reference for the evaluation of optimized simulations. In this case, the battery is charged and discharged in order to cover, if possible, the global load at the 13 connection points, maximizing self-consumption and energy shared among JARSCs. The excess of generation is stored in the ESS for later use at among JARSCs if possible, otherwise it is injected into the distribution grid and sold.

### **SIMULATION SCENARIO 3: FIRST OPTIMIZATION SOLUTION**

In this scenario, the considered problem is addressed by means of the MPC controller discussed in Section 4.4.4.2, including constraints (4.48)–(4.51), but not constraint (4.52), and cost function weight  $\gamma = 0$ . Forecasts obtained according to Section 4.4.4.4 are used. Cost functions weights  $\alpha, \beta$  are varied from 0 to 1 by 0.1 steps, with  $\alpha + \beta = 1$ , resulting in a set of eleven simulations highlighting the effect of different (arbitrary) priorities in the optimization problem.

### **SIMULATION SCENARIO 4: SECOND OPTIMIZATION SOLUTION**

In this scenario, the considered problem is addressed by means of the MPC controller discussed in Section 4.4.4.2, including constraints (4.48)–(4.52), and cost function weight  $\gamma = 1$ . Forecasts obtained according to Section 4.4.4.4 are used. Cost functions weights  $\alpha, \beta$  are varied from 0 to 1 by 0.1 steps, with  $\alpha + \beta = 1$ . As mentioned, the additional constraint (4.52) does not allow the MPC controller to buy energy from the grid to charge the battery, which is often contrary to the spirit of reducing  $CO_2$  emissions, at least as long as the energy mix includes fossil fuels. The additional cost term included in the optimization problem by setting  $\gamma = 1$  adds an additional cost to energy sold while the battery is not fully charged, which represents a form of caution against forecast errors. In fact, the MPC controller may decide not to charge the battery and to sell energy during the morning, planning to charge the battery at noon, when the price is usually lower. However, an error in forecasts (e.g. unforeseen shading) can make impossible to charge the battery when planned, causing a lack of energy

during the evening and night, which will force the MPC controller to buy energy from the grid increasing costs and  $CO_2$  equivalent emissions.

#### SIMULATION SCENARIO 5: THIRD OPTIMIZATION SOLUTION

In this scenario, the considered problem is addressed by means of the MPC controller discussed in Section 4.4.4.2, including constraints (4.48)–(4.51), but not constraint (4.52), and cost function weight  $\gamma = 0$ . Ideal forecasts (e.g. perfect forecast of each quantity the forecast of which is used in the optimization problem) are used. Cost functions weights  $\alpha$ ,  $\beta$  are varied from 0 to 1 by 0.1 steps, with  $\alpha + \beta = 1$ . This solution is obviously not feasible in real applications, in that any forecast method will include a certain level of uncertainty. However, it may be useful to consider this scenario too, as it represents the best possible solution of the considered optimization problem, which could be reached in principle with very accurate predictors.

#### 4.4.5.2 NUMERICAL DATA

In this Section, the numerical data necessary for simulation are reported. In addition to the data referenced in Section 4.4.3.7, to determine electricity price it is necessary to calculate fixed costs, energy buying price and energy selling price. Fixed costs are here calculated according to the Italian standard and are available from [307]. They consist of a fixed component and of a component proportional to the contractual power. The numerical values of these fixed cost, for each connection point, are reported in Table 4.16. Energy selling price is assumed equal to the PO referenced in Section 4.4.3.7. Energy buying price is determined considering that, during 2016, the energy component of buying price was, on average, equal to selling price increased by 89%. In addition to energy component, there is another component to be considered, including various fees and customs, on average equal to 0.0586 €/kWh. Lastly, VAT is equal to 10% for the 12 residential connection points, while it is equal to 22% for the last, non-residential connection point.

#### 4.4.5.3 SIMULATION RESULTS

Numerical results from the simulation scenarios detailed in Section 4.4.5.1 are reported in this Section. As mentioned, the performance

**Table 4.16:** JARSCs Fixed electricity costs.

Connection Point	Cost [€/year]	Connection Point	Cost [€/year]
UM1	143.81	UM8	143.81
UM2	143.81	UM9	133.19
UM3	154.43	UM10	154.43
UM4	175.67	UM11	133.19
UM5	175.67	UM12	133.19
UM6	143.81	CM	600.47
UM7	143.81		

indexes used for the evaluation of the presented results are the total electricity cost [€] charged to the JARSCs over one year and the total  $CO_2$  equivalent emissions [kg] generated by the electrical system to provide the JARSCs the total amount of energy bought from the grid over one year. Additional quantities of interest are: total energy [kWh] drained from the ESS over one year, total shared energy [kWh] over one year and total self-consumed energy [kWh] over one year. For ease of comparison among different scenarios, the results in terms of electricity cost [€], total  $CO_2$  equivalent emissions [kg], total energy [kWh] drained from the ESS, total shared energy [kWh], total self-consumed energy [kWh] are reported, respectively, in Table 4.17, Table 4.18, Table 4.19, Table 4.20, and Table 4.21. Additionally, the results of the optimization problem (electricity cost [€], total  $CO_2$  equivalent emissions [kg]) are graphically presented in Fig. 4.25. For reference, the electricity cost and  $CO_2$  equivalent emissions have also been calculated based only of load profiles, which corresponds to what JARSCs would have been charged in absence of PV and ESS. The total cost is, in this case, equal to 9189 €, while the total equivalent  $CO_2$  emissions are equal to 17175 kg.

**Table 4.17:** JARSCs total electricity cost [€] over one year.

Scenario 1	Scenario 2	Scenario 3	Scenario 4	Scenario 5	$\alpha$
5972	5371	5810	5398	5495	0
		5536	5298	5166	0.1
		5469	5264	5069	0.2
		5438	5247	5023	0.3
		5418	5238	5000	0.4
		5408	5233	4991	0.5
		5401	5230	4987	0.6
		5399	5228	4985	0.7
		5397	5228	4984	0.8
		5394	5227	4984	0.9
		5393	5227	4984	1

**Table 4.18:** JARSCs total  $CO_2$  emissions [kg] over one year.

Scenario 1	Scenario 2	Scenario 3	Scenario 4	Scenario 5	$\alpha$
11204	8854	9261	8541	7959	0
		9328	8467	8085	0.1
		9334	8452	8248	0.2
		9401	8438	8400	0.3
		9454	8442	8521	0.4
		9497	8445	8590	0.5
		9535	8453	8633	0.6
		9574	8461	8662	0.7
		9590	8469	8686	0.8
		9603	8467	8711	0.9
		9618	8473	8734	1

**Table 4.19:** JARSCs total energy [kWh] drained from the ESS over one year.

Scenario 1	Scenario 2	Scenario 3	Scenario 4	Scenario 5	$\alpha$
6632	9317	13312	10627	16204	0
		11173	10543	14263	0.1
		11054	10669	14369	0.2
		11331	10778	15185	0.3
		11637	10834	15860	0.4
		11891	10877	16241	0.5
		12144	10907	16452	0.6
		12333	10912	16586	0.7
		12429	10934	16722	0.8
		12526	10959	16831	0.9
		12619	10973	16900	1

**Table 4.20:** JARSCs total shared energy [kWh] over one year.

Scenario 1	Scenario 2	Scenario 3	Scenario 4	Scenario 5	$\alpha$
4648	14749	15949	14651	18120	0
		13206	13906	15237	0.1
		12963	13738	14600	0.2
		13254	13841	14934	0.3
		13600	13933	15461	0.4
		13881	13986	15834	0.5
		14123	14031	16072	0.6
		14306	14068	16229	0.7
		14387	14077	16332	0.8
		14482	14077	16436	0.9
		14536	14104	16504	1

**Table 4.21:** JARSCs total self-consumed energy [kWh] over one year.

Scenario 1	Scenario 2	Scenario 3	Scenario 4	Scenario 5	$\alpha$
10322	6277	7094	6550	8869	0
		7442	7594	9193	0.1
		7764	7894	9952	0.2
		7800	7888	10458	0.3
		7855	7842	10622	0.4
		7872	7822	10650	0.5
		7899	7789	10651	0.6
		7934	7761	10633	0.7
		7964	7748	10666	0.8
		7976	7759	10679	0.9
		8009	7730	10687	1

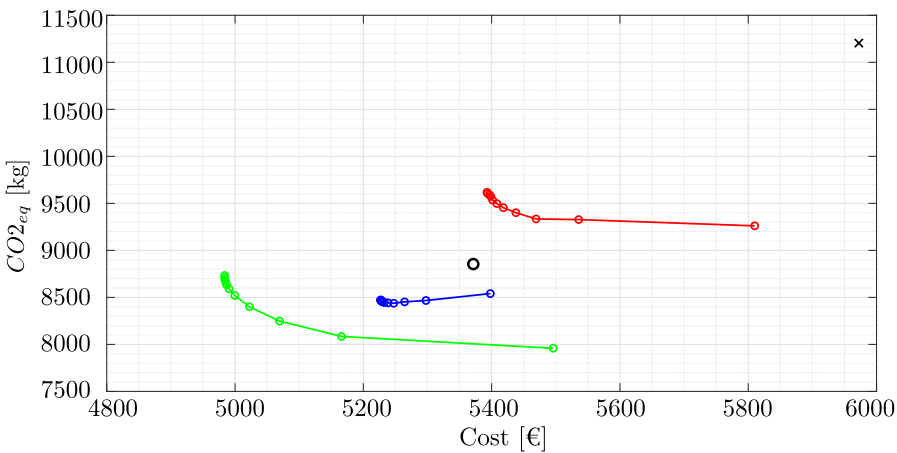


**Figure 4.25:** Graphical representation of simulation results: scenario 1 (black cross), scenario 2 (black circle), scenario 3 (red), scenario 4 (blue), scenario 5 (green)

### SIMULATION SCENARIO 1: FIRST BENCHMARK SIMULATION

As mentioned, this scenario represents the basic benchmark for performance evaluation. The total cost in charge to the JARSCs is equal to 5972 €, while the total  $CO_2$  equivalent emissions are equal to 11204 kg. The total energy drained from the ESS over one year is equal to 6632 kWh, total shared energy over one year is equal to 4648 kWh and total self-consumed energy over one year is equal to 10322 kWh. The results of the optimization problem (electricity cost [€], total  $CO_2$  equivalent emissions [kg]) are identified by a black cross in the solution plane (€ -  $CO_2$ ) graphically presented in Fig. 4.25. All the simulations were performed using a common desktop PC with an Intel Core i5-7500 CPU and 16 GB RAM. The average computational time required for each iteration of the MPC control is, on average, equal to 230 ms. Considering that no particular attention has been dedicated to computational efficiency and that the considered sample time is equal to 1 h, this is more than satisfactory and supports the applicability of the proposed control to real-time applications, with no need for excessive computational requirements.

### SIMULATION SCENARIO 2: SECOND BENCHMARK SIMULATION

This second scenario represents a significant improvement over Scenario 1, in that the measures from connection points 1–12 are collected and used to consider shared energy, in addition to self-consumption, in battery management. The total cost in charge to the JARSCs is equal to 5371 €, while the total  $CO_2$  equivalent emissions are equal to 8854 kg. This corresponds to a 10.1% cost reduction and 21.0%  $CO_2$  emissions reduction. The total energy drained from the ESS over one year is equal to 9317 kWh, total shared energy over one year is equal to 14749 kWh and total self-consumed energy over one year is equal to 6277 kWh. With respect to Scenario 1, the energy drained from the ESS is increased by 40.5%, self-consumed energy is reduced by 39.2% and shared energy is increased by 217.4%. Even though self-consumed energy is the most effective remuneration mechanism for small PV generators, which would suggest that Scenario 2 would not provide any advantage over Scenario 1, the change of the control law from (4.58)

(Scenario 1) to (4.59) (Scenario 2) generates a huge increase in shared energy which, unitedly with the incentive on shared energy selling price, produces a significant improvement in cost and  $CO_2$  emissions over Scenario 1. This can be clearly seen in the graphical representation reported in Fig. 4.25, where the results of the optimization problem in Scenario 2 are identified by a black circle.

### SIMULATION SCENARIO 3: FIRST OPTIMIZATION SOLUTION

This scenario represents the first optimized solution proposed in this study. The results in terms of electricity cost [€], total  $CO_2$  equivalent emissions [kg], total energy [kWh] drained from the ESS, total shared energy [kWh], total self-consumed energy [kWh] are reported, respectively, in Table 4.17, Table 4.18, Table 4.19, Table 4.20, and Table 4.21, for the complete considered range of cost function weights  $\alpha$ ,  $\beta$ .

The minimum total cost in charge to the JARSCs is equal to 5393 €, while the minimum total  $CO_2$  equivalent emissions are equal to 9261 kg. The complete set of results of the optimization problem (electricity cost [€], total  $CO_2$  equivalent emissions [kg]) are identified by red circles in the solution plane (€ -  $CO_2$ ) graphically presented in Fig. 4.25, which exhibits the quite regular behaviour expected from the Pareto frontier of optimization problems. However, Fig. 4.25 also clearly shows that Scenario 3 introduces significant advantage over Scenario 1, but it does not provide better performance than Scenario 2. Further investigation of this disappointing result revealed that the main problem with the optimization problem addressed in Scenario 3 is the relative slow update of the forecasts used. This is caused partially by the inevitable delays in prediction responses, partially by the 1-h sampling time. This creates two main issues:

- the MPC may decide to buy from the grid to charge the battery in prevision of future use, depending on generation, load, carbon intensity and price forecasts. However, this operation is dangerous, in that inevitable errors in previsions may compromise the advantages that the MPC controller planned to obtain. Additionally, buying energy from the grid to charge the ESS may be considered not desirable in terms of  $CO_2$  emissions in general;

- the MPC controller may decide not to charge the battery and to sell energy during the morning, and to charge the battery at noon, when the price is usually lower. However, an error in forecasts (e.g. unforeseen shading) can make impossible to charge the battery when planned, causing a lack of energy during the evening and night, which will force the MPC controller to buy energy from the grid increasing costs and  $CO_2$  equivalent emissions.

On the basis of these considerations, Scenario 4 was developed by adding the additional constraint (4.52), which does not allow the MPC controller to buy energy from the grid to charge the battery, and setting  $\gamma = 1$ . The additional cost term included therefore in the optimization problem adds an additional cost to energy sold while the battery is not fully charged, which represents a form of caution against forecast errors.

#### SIMULATION SCENARIO 4: SECOND OPTIMIZATION SOLUTION

This scenario represents the second optimized solution proposed in this study, in which, in order to avoid the issue emerged in Scenario 3, the cost function weight  $\gamma$  is set  $\gamma = 1$  and the additional constraint (4.52) is included in the optimization problem. The results in terms of electricity cost [€], total  $CO_2$  equivalent emissions [kg], total energy [kWh] drained from the ESS, total shared energy [kWh], total self-consumed energy [kWh] are reported, respectively, in Table 4.17, Table 4.18, Table 4.19, Table 4.20, and Table 4.21, for the complete considered range of cost functions weights  $\alpha, \beta$ .

The minimum total cost in charge to the JARSCs is equal to 5227 €, while the minimum total  $CO_2$  equivalent emissions are equal to 8438 kg. This corresponds to a cost reduction up to 12.5% and a  $CO_2$  emissions reduction up to 24.7% with respect to Scenario 1, and to a cost reduction up to 2.7% and a  $CO_2$  emissions reduction up to 4.7% with respect to Scenario 2. The maximum total energy drained from the ESS over one year is equal to 10973 kWh, maximum total shared energy over one year is equal to 14651 kWh and maximum total self-consumed energy over one year is equal to 7894 kWh. With respect to Scenario

1, the energy drained from the ESS is increased up to 65.5%, self-consumed energy is increased up to 3.5% and shared energy is increased up to 215.2%. With respect to Scenario 2, the energy drained from the ESS is increased up to 17.8%, self-consumed energy is increased up to 70.3% and shared energy is decreased at least of 0.6%. These results highlight that the optimized solution considered in Scenario 4 produces a total shared energy close to the non-optimized solution considered in Scenario 2. However, the optimized solution manages to significantly increase self-consumed energy, which produces benefits in cost and  $CO_2$  emission reduction, at expense of more demanding battery use. The complete set of results of the optimization problem (electricity cost [€], total  $CO_2$  equivalent emissions [kg]) are identified by blue circles in the solution plane (€ -  $CO_2$ ) graphically presented in Fig. 4.25, which clearly shows the advantage gained by means of the proposed MPC controller with respect to non-optimized solution. In the meantime, Fig. 4.25 also shows that the Pareto frontier associated with this optimization problem is not similar to the usually expected hyperbola. This is due to the fact that the additional cost term introduced in Scenario 4 affects the solution of the optimization problem, impeding the MPC to sell energy while the battery is not charged, while the additional constraint (4.52) does not allow the MPC to buy energy to charge the battery. However, Fig. 4.25 shows only two cost terms, which makes impossible to graphically appreciate the effect of three cost terms (a 3-D surface with parametrization of  $\alpha, \beta, \gamma$  would be necessary). Still, Fig. 4.25 highlights that setting  $\alpha < 0.3$  is useless in this scenario, in that the additional cost terms and constraint do not allow for a reduction in  $CO_2$  emissions, such that setting  $\alpha < 0.3$  implies an increase in cost, but not a reduction of  $CO_2$  emissions. Still, it is clear that the additional cost term and constraints allow the MPC to improve over non-optimized solutions and take advantage of available forecasts, the errors included in which were critical for the MPC formulation discussed in the description of Scenario 3.

#### SIMULATION SCENARIO 5: THIRD OPTIMIZATION SOLUTION

This scenario represents the third and last optimized solution proposed in this study, which is intended to disclose the full potential of the con-

sidered MPC control. As mentioned, the additional cost and constraints introduced in Scenario 4 are ditched, and the forecast obtained by the techniques discussed in Section 4.4.4.4 are substituted with ideal predictions, identical to measured data. While the applicability of this scenario is questionable, it is useful to consider it in this Section as it allows to identify the theoretical optimal solution which would be obtained with perfect predictions, providing a measure of the possible improvement theoretically available over Scenario 4. The results in terms of electricity cost [€], total  $CO_2$  equivalent emissions [kg], total energy [kWh] drained from the ESS, total shared energy [kWh], total self-consumed energy [kWh] are reported, respectively, in Table 4.17, Table 4.18, Table 4.19, Table 4.20, and Table 4.21, for the complete considered range of cost functions weights  $\alpha$ ,  $\beta$ .

The minimum total cost in charge to the JARSCs is equal to 4984 €, while the minimum total  $CO_2$  equivalent emissions are equal to 7959 kg. This corresponds to a cost reduction up to 16.5% and a  $CO_2$  emissions reduction up to 29.0% with respect to Scenario 1, and to a cost reduction up to 7.2% and a  $CO_2$  emissions reduction up to 10.1% with respect to Scenario 2, and to a cost reduction up to 4.7% and a  $CO_2$  emissions reduction up to 5.7% with respect to Scenario 4. The maximum total energy drained from the ESS over one year is equal to 16900 kWh, maximum total shared energy over one year is equal to 18120 kWh and maximum total self-consumed energy over one year is equal to 10687 kWh. With respect to Scenario 1, the energy drained from the ESS is increased up to 154.8%, self-consumed energy is increased up to 3.5% and shared energy is increased up to 289.8%. With respect to Scenario 2, the energy drained from the ESS is increased up to 81.4%, self-consumed energy is increased up to 70.3% and shared energy is increased up to 22.9%. With respect to Scenario 4, the energy drained from the ESS is increased up to 54.0%, self-consumed energy is increased up to 35.5% and shared energy is increased up to 23.7%.

#### 4.4.5.4 ECONOMIC ANALYSIS

In this section, a basic analysis of the common economic indicators used for PV/ESS evaluation is reported. Quantities considered are: Levelized Cost of Energy (LCOE) [€cent/kWh], Levelized Cost of Storage (LCOS)

**Table 4.22:** JARSCs economic parameters.

Parameter	Value
System expected life	20 years
Return of equity	0.1 %
Return of debt	4 %
Equity percentage	50 %
Debt percentage	50 %
PV cost	1540 €/kWp
PV degradation rate	0.25 %
Yield of the plant	1100 kWh/kWp
O&M costs	1 %
Battery cost	900 €/kWh
Tax deduction	50% in 10 years
Inflation rate	2 %
Energy inflation rate	2 %
Interest rate	2 %

**Table 4.23:** Economic indicators.

	Scenario 1	Scenario 2	Scenario 4
LCOE [€cent/kWh]	8.87	8.87	8.87
LCOS [€cent/kWh]	18.32	13.04	11.07 - 11.52
Payback Time [years]	15	13	12 - 13
NPV [k€]	20.74	35.26	34.61 - 38.74
Annual Revenue per User [€]	57.62	97.94	96.13 - 107.60

[€cent/kWh], payback time [years], Net Present Value (NPV) [k€], and annual revenue per user [€]. Methodologies for calculation of the aforementioned indicators can be found in [187, 308]. The main data used for calculation of economic indicators are reported in Table 4.22. The numerical values of the considered economic indicators, for each considered scenario, are reported in Table 4.23. A graphical representation of the NPV behaviour over the expected life of the PV/ESS system for Scenarios 1, 2, and 4 is presented in Fig. 4.26, where, for Scenario 4, the less favourable result is reported in orange, while the most favourable result is reported in blue. Since Scenario 3 proved to be of scarce interest and Scenario 5 is intended just as a limit optimal solution, only Scenarios 1, 2, and 4 are discussed.

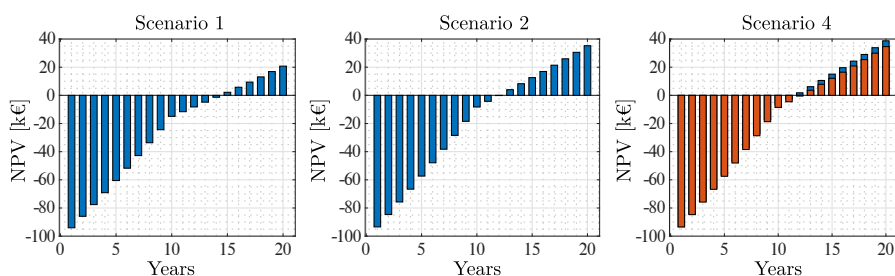


**Figure 4.26:** Graphical representation of NPV behaviour over the expected life of the PV/ESS system for Scenarios 1, 2, and 4

The LCOE, depending only on PV cost and PV production, is common to all scenarios and equal to 8.87 €cent/kWh. The LCOS is equal to 18.32 €cent/kWh in Scenario 1, which is reduced to 13.04 €cent/kWh in Scenario 2 and up to 11.07 €cent/kWh in Scenario 4, due to the increased use of ESS for energy sharing among JARSCs. The payback time is equal to 15 years in Scenario 1, while it is equal to 13 years in Scenarios 2 and can be reduced to up to 12 years in Scenario 4. NPV is equal to 20.74 k€ in Scenario 1, 35.26 k€ in Scenario 2 and increases up to 38.74 k€ in Scenario 4. Annual revenues per user are equal to 57.62 € in Scenario 1, 97.94 € in Scenario 2 and increase up to 107.60 € in Scenario 4. Overall, the economic indicators are not particularly favourable, in that, while it is clear that the installation of the combined PV/ESS system does produce revenues over the expected life of the system, the entity of these revenues is not very significant and payback time is quite long. On the other side, it must be considered that the equivalent  $CO_2$  emission, not considered in economic analysis, are reduced from 17175 kg up to 7959 kg, which corresponds to a reduction up to 53.7%. Considering the target of decarbonization driving the European Directives of reference for RECs and JARSCs, this may be considered quite a significant result. Additionally, it is not hard to foresee that equivalent  $CO_2$  emissions, which at the moment represent an additional cost only for large industrial loads, may in the not so far future be an additional cost also of residential users. In this case, the significant reduction in  $CO_2$  emissions would produce significant economic savings.

#### 4.4.6 DISCUSSION OF SIMULATION RESULT

From a technical perspective, the results discussed in Section 4.4.5.3 show that the proposed MPC controller introduces significant advantages with respect to not optimized solutions, as long as predictions are sufficiently accurate or specific measures to reduce sensitivity to forecasts errors are included in the optimization problem formulation. In these regards, the following issues could be addressed to further improve control performances:

- smaller sampling time: in principle, a smaller sampling time would reduce the sensitivity to forecast errors, in that it allows the MPC controller to re-evaluate its control action more frequently. The MPC controller discussed in this study, due to the 1-h sampling time, cannot update its control action for 1 h after each solution of the optimization problem, which may be a problem in presence of inaccurate forecasts. On the other side, a smaller time step would increase computational burden. However, the results shown in Section 4.4.5.3 suggest that computational time would not be a significant issue. A smaller sampling time would also be beneficial for PV production ANN-based forecaster, in that it would update its prediction more frequently considering real-time measures;
- improved predictors: more efficient predictors would take the solution obtained in Scenario 4 closer to the theoretical optimum discussed in Scenario 5. On the other side, this possible solution is to be cautiously evaluated, since the additional complexity of improved predictors may not be compatible with real-time applications;
- load side demand control: the introduction of demand control policies may produce significant benefits in optimized scenarios, in that load volatility has proven difficult to be predicted. Load side demand control policies would help in that they would make load more regular and predictable, allowing more efficient optimization, and may also allow to partially reshape the load profiles

with respect to generation, price and carbon intensity profiles, allowing a further degree of freedom in the optimization problem.

From an economic perspective, the results discussed in Section 4.4.5.4 highlights that the considered solution does produce revenues over its expected life, but the entity of these revenues is not enough to be an attractive investment form. These results also allow drawing some considerations regarding the incentive plan for JARSCs currently available in Italy. On one side, it is clear that the incentive plan does create an economic advantage for prosumers sharing energy among a group of JARSCs or REC, which is beneficial for the environment in terms of  $CO_2$  emission reduction, and beneficial for the distribution system, which is less likely to suffer from excessive generation. This suggest that, if economic convenience is the main target, a smaller PV/ESS would be better suited for the task, having a shorter payback time due to a higher self-consumption, but generating less savings in terms of electricity bill and smaller reductions in the  $CO_2$  emissions. On the other side, the entity of the incentive is not sufficient to make the installation of a PV/ESS an attractive investment for the energy sharing mechanism. Two possible ways to increase profitability are foreseen:

- remuneration of  $CO_2$  emissions reduction: considering that decarbonization is the driving reason for recent changes in energy market, extending a form of remuneration of  $CO_2$  emission reduction to residential users is reasonable. Considering that the reduction in  $CO_2$  emissions are very significant when, as in this study, the PV/ESS system is designed to cover most of the JARSCs energy needs, an economic recognition of this result would significantly increase profitability of larger PV/ESS systems over smaller ones, which would perfectly fit the decarbonization task;
- power sharing solutions: physical power sharing [273], not using the DSO system as a mean for virtual energy exchange, would not benefit from incentive on shared energy. However, the average energy selling price resulting from the present study, including incentives, is roughly equal to 16 €cent/kWh, while the energy

buying price is, on average, roughly equal to 24 €cent/kWh. From these data, the increased self-consumption obtained from power sharing would be 50% more convenient than sharing energy through the DSO infrastructure. On the other side, the power sharing requires additional converters, cables and switchboards, the cost of which is to be included in economic evaluation. However, this study seems to suggest that power sharing, even if not yet covered by standards, may be a more profitable solution than virtual energy exchange through the DSO grid.

## 4.5 DISCUSSION

In contrast to Chapter 3, which focused primarily on an analysis of power electronic components and their control for efficiency improvements and V2G services, this chapter presented different studies on the optimization of energy flows within microgrids integrating electric vehicles trying to answer the second research question (Q2). The main goal is to minimize the economic costs and  $CO_2$  emissions caused by grid power generation through the use of MPC controllers that use future predictions in order to act in advance on controllable energy flows such as storage systems and if possible, the charging power of the vehicles themselves.

In the study presented in Section 4.2, the use of eMPC in EV charging stations based on PV and BESS, taking into account uncertainties is analysed. The explicit formulation is based on the mapping of critical regions (CRs) by the use of Multi-parametric Programming (MPP). The uncertainties considered are: PV production, SoC, electricity price,  $CO_2$  emissions, and the EV power consumption. The algorithm proposed was tested in two different testbeds, one using a commercial PC and the other using a dSPACE real-time platform. The results showed that the eMPC is a good candidate for the real-time energy management as it can run offline while the results can be stored in a lookup table. This reduces the online optimization time when the actual values of the uncertainties are known. The eMPC should only evaluate the critical regions stored in the lookup-table and set the new control variables at every sampling time. The evaluation of the critical regions takes less than 1 second

for any of the two platforms tested. Thus, eMPC could be used in a low cost platform to run real time energy management. However, the number of CRs for the current application can grow exponentially when the prediction horizon increases, affecting the computation time offline. Besides the electricity price, the proposed algorithm also takes into account the  $CO_2$  emissions due to the mix energy from the grid as part of the uncertainties and constraints.

In Section 4.3, the integration of a photovoltaic system, electric vehicles and V2G technology has been analysed in a ski resort located in Trentino-Alto Adige. The study presents and analyses the current situation and future possibilities in three different scenarios for the years 2022, 2023 and 2030, each with different charging strategies. The development of an EMS based on MPC technique allowed us to evaluate a possible economic and environmental performance, in terms of total costs and  $CO_2$  emissions. The availability of real data relating to skier flows at the ski-lift turnstiles allowed us to estimate the power absorbed by the plants, in order to obtain a correct and reliable evaluation of the energy consumption of the ski resort. Thanks to the automotive growth models introduced in Section 4.3.5, it was possible to estimate the most important parameters, such as the number of cars, as well as the capacity and price of battery replacement for future scenarios.

In the last study introduced in Section 4.4, an MPC-based control algorithm coupled with an ANN-based predictor for optimal management of JARSCs is presented. The proposed algorithm evaluates the control action over a one-day prediction horizon, considering available forecasts of PV production, electricity price, carbon intensity and load, and minimizes a cost function including electricity cost and equivalent  $CO_2$  emissions. Five simulation scenarios are presented and discussed, highlighting the effectiveness of the proposed control design, which produces a cost reduction up to 12.5% and a  $CO_2$  emissions reduction up to 24.7%. An essential economic evaluation of the considered system shows that the revenues are not large and payback time are quite long, but reduction in  $CO_2$  emissions up to 53.7% are obtained by means of the considered PV/ESS system. Lastly, a brief discussion identified the

main technical and economic aspects worth of further study in order to improve the considered system performance.

## CONCLUSIONS

In this thesis work, we aimed to study energy management processes and optimization strategies for the integration of electric vehicles with the electric grid and their interfacing with renewable power generation and storage systems from an economic and environmental perspective. Several experimental validations have been developed at the University of Trieste and at the Christian-Albrechts-Universität (CAU) in Kiel, leading to outcomes that resulted in several research publications. Following the introductory chapter, the work has been divided into two main macro themes that seek to answer the following research questions: (i) in which ways can electric vehicles be integrated into the current electric system and what are the challenges to be considered? (ii) which energy management strategies can be exploited and which objectives can be achieved in systems that integrate electric vehicles?

The first theme addressed the integration of electric vehicles by starting from the low level, that is, analyzing the electronic structures and components required to connect electric vehicles to the grid. The theme focused on analyzing two DAB converter topologies from the perspective of losses and their interface with EV batteries. In addition, solutions were proposed for improving efficiency during vehicle-to-grid (V2G) operations and the simulation of a V2G system under construction at the University of Trieste, Italy, has been shown.

The second theme, on the other hand, targeted on the study of energy flow management within nano- and microgrids integrating electric vehicles. The topic focused on the implementation of Model Predictive Control (MPC) approaches that govern energy flows taking into account

system uncertainties, prediction of variables through neural networks, and economic and environmental aspects. In this regard, an experimental study of the photovoltaic charging station at the University of Trieste, a study on V2G technology within an Alpine ski-resort, and a study related to Jointly Acting Renewable Self-Consumers (JARSCs) in the context of energy communities have been presented.

In the following, conclusions and future developments within the scope of work are drawn.

Electrification of energy consumption and transportation, and increasing electricity generation from renewable sources are the way to effectively implement current decarbonization policies and make the energy sector economically sustainable. Electric vehicles may become key co-players in decreasing greenhouse gas emissions, reducing costs, and actively supporting the power grid through V2G technology. However, their integration into the power grid plays a key role and needs to be studied thoroughly.

Due to the variable conditions typical of charging processes, it is necessary to carefully evaluate the topology of converters employed, taking into account normalized losses versus rated power in order to compare devices in a fair way. The use of a single-phase or three-phase DAB converter depends on the applications and system constraints on volume, harmonic content, and acceptable current stress. In general, an optimal-efficiency charging trajectory can always be found, albeit at the expense of charging times which may be a hard constraint. However, implementing a maximum-efficiency strategy is straightforward and allows for increased efficiency compared to other charging strategies. In this context, future work may include an MPC approach that, based on the efficiency model, both optimizes losses and charging times.

In contrast, the use of optimized control techniques for the integration of electric vehicles can bring significant benefits if their charging is controlled differently from traditional methods. In the study related to the photovoltaic charging station in Section 4.2, it is shown how it is possible to take into account the uncertainties of the variables involved with an explicit MPC controller and optimize the energy flows accord-

ing to the considered objectives, achieving excellent computational performance compared to classical MPC methods. Speaking of benefits, from the study related to EV integration in a ski-resort in Section 4.3, it can be concluded that the use of electric vehicles to minimize costs and environmental impact through V2G is beneficial even if in a small way and strongly depends on the operating conditions and future scenarios of the automotive market. However, a different situation will arise when  $CO_2$  minimization will be economically remunerated as already done for industrial consumers. The latest study focused primarily on a group of jointly acting renewable self-consumers (JARSC) in a condominium where common loads include an EV charging station. The benefits from the optimal management of energy flows both economically and environmentally are considerable, producing a decrease in costs of up to 12.5% and a reduction in  $CO_2$  emissions of up to about 25%. Future work may include exploitation of V2G within renewable energy communities and the usage of other types of energy carriers such as hydrogen in order to study fuel cell vehicles integration.



## REFERENCES

- [1] H.-O Rama, Debra Roberts, M. Tignor, E.S. Poloczanska, Katja Mintenbeck, A. Alegría, Marlies Craig, S. Langsdorf, S. Löschke, Vincent Möller, Andrew Okem, B. Rama, and Sina Ayanlade. *Climate Change 2022: Impacts, Adaptation and Vulnerability Working Group II Contribution to the Sixth Assessment Report of the Intergovernmental Panel on Climate Change*. Aug. 2022.
- [2] William F. Lamb, Thomas Wiedmann, Julia Pongratz, Robbie Andrew, Monica Crippa, Jos G. J. Olivier, Dominik Wiedenhofer, Giulio Mattioli, Alaa Al Khourdajie, Jo House, Shonali Pachauri, Maria Figueroa, Yamina Saheb, Raphael Slade, Klaus Hubacek, Laixiang Sun, Suzana Kahn Ribeiro, Smail Khennas, Stephane de la Rue du Can, Lazarus Chapungu, Steven J. Davis, Igor Bashmakov, Hancheng Dai, Shobhakar Dhakal, Xianchun Tan, Yong Geng, Baihe Gu, and Jan Minx. "A review of trends and drivers of greenhouse gas emissions by sector from 1990 to 2018". en. In: *Environmental Research Letters* 16.7 (June 2021). Publisher: IOP Publishing, p. 073005.
- [3] Yongqi Sun, Sicong Tian, Philippe Ciais, Zhenzhong Zeng, Jing Meng, and Zuotai Zhang. "Decarbonising the iron and steel sector for a 2 °C target using inherent waste streams". en. In: *Nature Communications* 13.1 (Jan. 2022), p. 297.
- [4] Simon Tomažič, Goran Andonovski, Igor Škrjanc, and Vito Logar. "Data-Driven Modelling and Optimization of Energy Consumption in EAF". en. In: *Metals* 12.5 (May 2022), p. 816.
- [5] Goran Andonovski and Simon Tomažič. "Comparison of data-based models for prediction and optimization of energy consumption in electric arc furnace (EAF)". en. In: *IFAC-PapersOnLine*.

- 10th Vienna International Conference on Mathematical Modelling MATHMOD 2022 55.20 (Jan. 2022), pp. 373–378.
- [6] Jesús D. Hernández, Luca Onofri, and Sebastian Engell. “Modeling and Energy Efficiency Analysis of the Steelmaking Process in an Electric Arc Furnace”. en. In: *Metallurgical and Materials Transactions B* (Sept. 2022).
- [7] Johannes Dock and Thomas Kienberger. “Techno-economic case study on Oxyfuel technology implementation in EAF steel mills – Concepts for waste heat recovery and carbon dioxide utilization”. en. In: *Cleaner Engineering and Technology* 9 (Aug. 2022), p. 100525.
- [8] Nicola Blasuttigh. “Electric arc furnaces for steel production: energy modelling and innovative control solutions”. PhD thesis.
- [9] *ABS SISAK to secure competitive and green steel production in Croatia* ‹ Danieli. en.
- [10] Peter Berrill, Eric J. H. Wilson, Janet L. Reyna, Anthony D. Fontanini, and Edgar G. Hertwich. “Decarbonization pathways for the residential sector in the United States”. en. In: *Nature Climate Change* 12.8 (Aug. 2022), pp. 712–718.
- [11] Benjamin D. Leibowicz, Christopher M. Lanham, Max T. Brozynski, José R. Vázquez-Canteli, Nicolás Castillo Castejón, and Zoltan Nagy. “Optimal decarbonization pathways for urban residential building energy services”. en. In: *Applied Energy* 230 (Nov. 2018), pp. 1311–1325.
- [12] M. J. S. Zuberi, J. Chambers, and M. K. Patel. “Techno-economic comparison of technology options for deep decarbonization and electrification of residential heating.” en. In: *Energy Efficiency* 14.7 (Sept. 2021), p. 75.
- [13] Xiwang Xiang, Minda Ma, Xin Ma, Liming Chen, Weiguang Cai, Wei Feng, and Zhili Ma. “Historical decarbonization of global commercial building operations in the 21st century”. en. In: *Applied Energy* 322 (Sept. 2022), p. 119401.

- [14] Shufan Zhang, Minda Ma, Xiwang Xiang, Weiguang Cai, Wei Feng, and Zhili Ma. “Potential to decarbonize the commercial building operation of the top two emitters by 2060”. en. In: *Resources, Conservation and Recycling* 185 (Oct. 2022), p. 106481.
- [15] STEVEN Nadel and CHRIS Perry. “Electrifying space heating in existing commercial buildings: opportunities and challenges”. In: *American Council for an Energy-Efficient Economy (ACEEE) Publication* (2020).
- [16] *World Energy Outlook 2020 – Analysis*. en-GB.
- [17] *Transport sector CO2 emissions by mode in the Sustainable Development Scenario, 2000-2030 – Charts – Data & Statistics*. en-GB.
- [18] *A European Strategy for Low-Emission Mobility — European Environment Agency*. en. Policy Document.
- [19] Steven Nadel. “Electrification in the Transportation, Buildings, and Industrial Sectors: a Review of Opportunities, Barriers, and Policies”. en. In: *Current Sustainable/Renewable Energy Reports* 6.4 (Dec. 2019), pp. 158–168.
- [20] Runsen Zhang and Shinichiro Fujimori. “The role of transport electrification in global climate change mitigation scenarios”. en. In: *Environmental Research Letters* 15.3 (Feb. 2020), p. 034019.
- [21] *Can car manufacturers meet customer expectations for ACES mobility? | McKinsey*.
- [22] Marie Rajon Bernard, Dale Hall, and Nic Lutsey. “Update on electric vehicle uptake in European cities”. en. In: (2021). Publisher: International Council on Clean Transportation.
- [23] Gavin Bridge and Erika Faigen. “Towards the lithium-ion battery production network: Thinking beyond mineral supply chains”. en. In: *Energy Research & Social Science* 89 (July 2022), p. 102659.

- [24] Ruby T. Nguyen, Roderick G. Eggert, Mike H. Severson, and Corby G. Anderson. “Global Electrification of Vehicles and Intertwined Material Supply Chains of Cobalt, Copper and Nickel”. en. In: *Resources, Conservation and Recycling* 167 (Apr. 2021), p. 105198.
- [25] Han Hao, Yong Geng, James E. Tate, Feiqi Liu, Kangda Chen, Xin Sun, Zongwei Liu, and Fuquan Zhao. “Impact of transport electrification on critical metal sustainability with a focus on the heavy-duty segment”. en. In: *Nature Communications* 10.1 (Nov. 2019). Number: 1 Publisher: Nature Publishing Group, p. 5398.
- [26] M. Naumanen, T. Uusitalo, E. Huttunen-Saarivirta, and R. van der Have. “Development strategies for heavy duty electric battery vehicles: Comparison between China, EU, Japan and USA”. en. In: *Resources, Conservation and Recycling* 151 (Dec. 2019), p. 104413.
- [27] *Global EV Outlook 2022 – Analysis*. en-GB.
- [28] Carlo Cunanan, Manh-Kien Tran, Youngwoo Lee, Shinghei Kwok, Vincent Leung, and Michael Fowler. “A Review of Heavy-Duty Vehicle Powertrain Technologies: Diesel Engine Vehicles, Battery Electric Vehicles, and Hydrogen Fuel Cell Electric Vehicles”. en. In: *Clean Technologies* 3.2 (June 2021). Number: 2 Publisher: Multidisciplinary Digital Publishing Institute, pp. 474–489.
- [29] Emir Çabukoglu, Gil Georges, Lukas Küng, Giacomo Pareschi, and Konstantinos Boulouchos. “Battery electric propulsion: An option for heavy-duty vehicles? Results from a Swiss case-study”. en. In: *Transportation Research Part C: Emerging Technologies* 88 (Mar. 2018), pp. 107–123.
- [30] European Commission, Directorate-General for Research, and Innovation. *Electrification of the transport system : expert group report*. Publications Office, 2018.

- [31] Andrew W. Thompson and Yannick Perez. “Vehicle-to-Everything (V2X) energy services, value streams, and regulatory policy implications”. en. In: *Energy Policy* 137 (Feb. 2020), p. 111136.
- [32] Kang Miao Tan, Vigna K Ramachandaramurthy, and Jia Ying Yong. “Integration of electric vehicles in smart grid: A review on vehicle to grid technologies and optimization techniques”. In: *Renewable and Sustainable Energy Reviews* 53 (2016), pp. 720–732.
- [33] Joeri Van Mierlo, Maitane Berecibar, Mohamed El Baghdadi, Cedric De Cauwer, Maarten Messagie, Thierry Coosemans, Valéry Ann Jacobs, and Omar Hegazy. “Beyond the State of the Art of Electric Vehicles: A Fact-Based Paper of the Current and Prospective Electric Vehicle Technologies”. en. In: *World Electric Vehicle Journal* 12.1 (Mar. 2021), p. 20.
- [34] KM Bhargavi, NS Jayalaxmi, Sheetal Malagi, and Vinay Kumar Jadoun. “Integration of Plug-in Electric Vehicles in Smart Grid: A Review”. In: *2020 International Conference on Power Electronics & IoT Applications in Renewable Energy and its Control (PARC)*. IEEE, 2020, pp. 214–219.
- [35] Asaad Mohammad, Ramon Zamora, and Tek Tjing Lie. “Integration of Electric Vehicles in the Distribution Network: A Review of PV Based Electric Vehicle Modelling”. In: *Energies* 13.17 (2020), p. 4541.
- [36] Mario Mezzarobba, Alberto Tessarolo, **Nicola Blasuttigh**, Alessandro Massi Pavan, Simone Castellan, and Stefano Pastore. “Technologies for Electric Vehicle Utilization for Electric Power Optimal Management”. In: *2021 AEIT International Conference on Electrical and Electronic Technologies for Automotive (AEIT AUTOMOTIVE)*. Nov. 2021, pp. 1–6.
- [37] Francesco Giordano, Alessandro Ciocia, Paolo Di Leo, Andrea Mazza, Filippo Spertino, Alberto Tenconi, and Silvio Vaschetto. “Vehicle-to-Home Usage Scenarios for Self-Consumption Improvement of a Residential Prosumer With Photovoltaic Roof”.

- In: *IEEE Transactions on Industry Applications* 56.3 (Mar. 2020), pp. 2945–2956.
- [38] Xuan Hou, Jun Wang, Tao Huang, Tao Wang, and Peng Wang. “Smart Home Energy Management Optimization Method Considering Energy Storage and Electric Vehicle”. In: *IEEE Access* 7 (2019). Conference Name: IEEE Access, pp. 144010–144020.
- [39] David Borge-Diez, Daniel Icaza, Emin Açıkkalp, and Hortensia Amaris. “Combined vehicle to building (V2B) and vehicle to home (V2H) strategy to increase electric vehicle market share”. en. In: *Energy* 237 (Dec. 2021), p. 121608.
- [40] Paolo Lazzeroni, Sergio Olivero, Maurizio Repetto, Federico Stirano, and Marc Vallet. “Optimal battery management for vehicle-to-home and vehicle-to-grid operations in a residential case study”. en. In: *Energy* 175 (May 2019), pp. 704–721.
- [41] Vitor Monteiro, JG Pinto, and João Luiz Afonso. “Operation modes for the electric vehicle in smart grids and smart homes: Present and proposed modes”. In: *IEEE Transactions on Vehicular Technology* 65.3 (2015), pp. 1007–1020.
- [42] Vitor Monteiro, Joao Catalao, Tiago Sousa, JG Pinto, Marcello Mezaroba, and Joao L Afonso. “Improved voltage control for the electric vehicle operation in V2H mode as an off-line UPS in the context of smart homes”. In: *EAI Endorsed Transactions on Energy Web* 7.25 (2020).
- [43] Parag Jose Chacko and Meikandasivam Sachidanandam. “An optimized energy management system for vehicle to vehicle power transfer using micro grid charging station integrated Gridable Electric Vehicles”. en. In: *Sustainable Energy, Grids and Networks* 26 (June 2021), p. 100474.
- [44] Roberto Alvaro, Jairo González, Carlos Gamallo, Jesús Fraile-Ardanuy, and Davy Luk Knapen. “Vehicle to vehicle energy exchange in smart grid applications”. In: *2014 International Conference on Connected Vehicles and Expo (ICCVE)*. ISSN: 2378-1297. Nov. 2014, pp. 178–184.

- [45] Mohammed Shurrab, Shakti Singh, Hadi Otrok, Rabeb Mizouni, Vinod Khadkikar, and Hatem Zeineldin. “An Efficient Vehicle-to-Vehicle (V2V) Energy Sharing Framework”. In: *IEEE Internet of Things Journal* 9.7 (Apr. 2022). Conference Name: IEEE Internet of Things Journal, pp. 5315–5328.
- [46] Abdullah Dik, Siddig Omer, and Rabah Boukhanouf. “Electric Vehicles: V2G for Rapid, Safe, and Green EV Penetration”. en. In: *Energies* 15.3 (Jan. 2022). Number: 3 Publisher: Multidisciplinary Digital Publishing Institute, p. 803.
- [47] Paulo RC Mendes, Luis Valverde Isorna, Carlos Bordons, and Julio E Normey-Rico. “Energy management of an experimental microgrid coupled to a V2G system”. In: *Journal of Power Sources* 327 (2016), pp. 702–713.
- [48] Gabriel Antonio Salvatti, Emerson Giovani Carati, Rafael Cardoso, Jean Patric da Costa, and Carlos Marcelo de Oliveira Stein. “Electric vehicles energy management with V2G/G2V multifactor optimization of smart grids”. In: *Energies* 13.5 (2020), p. 1191.
- [49] C Battistelli, L Baringo, and AJ Conejo. “Optimal energy management of small electric energy systems including V2G facilities and renewable energy sources”. In: *Electric Power Systems Research* 92 (2012), pp. 50–59.
- [50] Mahmoud M. Gamil, Tomonobu Senjyu, Hasan Masrur, Hiroshi Takahashi, and Mohammed Elsayed Lotfy. “Controlled V2Gs and battery integration into residential microgrids: Economic and environmental impacts”. en. In: *Energy Conversion and Management* 253 (Feb. 2022), p. 115171.
- [51] K Mahmud, S Morsalin, YR Kafle, and GE Town. “Improved peak shaving in grid-connected domestic power systems combining photovoltaic generation, battery storage, and V2G-capable electric vehicle”. In: *2016 IEEE International Conference on Power System Technology (POWERCON)*. IEEE, 2016, pp. 1–4.

- [52] Harun Turker, Ahmad Hably, and Seddik Bacha. “Housing peak shaving algorithm (HPSA) with plug-in hybrid electric vehicles (PHEVs): Vehicle-to-Home (V2H) and Vehicle-to-Grid (V2G) concepts”. In: *4th International Conference on Power Engineering, Energy and Electrical Drives*. IEEE, 2013, pp. 753–759.
- [53] Zhenpo Wang and Shuo Wang. “Grid Power Peak Shaving and Valley Filling Using Vehicle-to-Grid Systems”. In: *IEEE Transactions on Power Delivery* 28.3 (July 2013). Conference Name: IEEE Transactions on Power Delivery, pp. 1822–1829.
- [54] Nuh Erdogan, Fatih Erden, and Mithat Kisacikoglu. “A fast and efficient coordinated vehicle-to-grid discharging control scheme for peak shaving in power distribution system”. In: *Journal of Modern Power Systems and Clean Energy* 6.3 (May 2018). Conference Name: Journal of Modern Power Systems and Clean Energy, pp. 555–566.
- [55] Noor Aziz, Murtaza Ali Shah, and Muhammad Ubaid Mehmood. “Vehicle to Grid (V2G) for Peak Shaving: New Trend, Benefits, and Issues”. en. In: *International Journal of Computing and Communication Networks* 1.2 (Dec. 2019). Number: 2, pp. 27–37.
- [56] Giuseppe Buja, Manuele Bertoluzzo, and Christian Fontana. “Reactive power compensation capabilities of V2G-enabled electric vehicles”. In: *IEEE transactions on power electronics* 32.12 (2017), pp. 9447–9459.
- [57] Rubi Rana and Bendik Nybakk Torsater. “Coordinated Voltage Support with Reactive Power from High-power Charging Stations for EVs”. In: *2021 IEEE Madrid PowerTech* (June 2021).
- [58] Patricio A Mendoza-Araya, Phillip J Kollmeyer, and Daniel C Ludois. “V2G integration and experimental demonstration on a lab-scale microgrid”. In: *2013 IEEE Energy Conversion Congress and Exposition*. IEEE, 2013, pp. 5165–5172.
- [59] Madhuri P Jadhav and VN Kalkhambkar. “Frequency Regulation by Electric Vehicle”. In: *2018 International Conference on*

*Current Trends towards Converging Technologies (ICCTCT)*. IEEE, 2018, pp. 1–6.

- [60] Sid-Ali Amamra and James Marco. “Vehicle-to-Grid Aggregator to Support Power Grid and Reduce Electric Vehicle Charging Cost”. In: *IEEE Access* 7 (2019), pp. 178528–178538.
- [61] Huachun Han, Di Huang, Dan Liu, and Qiang Li. “Autonomous frequency regulation control of V2G (Vehicle-to-grid) system”. In: *2017 29th Chinese Control And Decision Conference (CCDC)*. IEEE, 2017, pp. 5826–5829.
- [62] Keyhaneh Janfeshan, Mohammad AS Masoum, and Sara Deilami. “V2G application to frequency regulation in a microgrid using decentralized fuzzy controller”. In: *Proceedings of 2014 International Conference on Modelling, Identification & Control*. IEEE, 2014, pp. 361–364.
- [63] Willett Kempton, Victor Udo, Ken Huber, Kevin Komara, Steve Letendre, Scott Baker, Doug Brunner, and Nat Pearre. “A test of vehicle-to-grid (V2G) for energy storage and frequency regulation in the PJM system”. In: *Results from an Industry-University Research Partnership* 32 (2008).
- [64] Jasna Tomić and Willett Kempton. “Using fleets of electric-drive vehicles for grid support”. In: *Journal of Power Sources* 168.2 (June 2007), pp. 459–468.
- [65] Christopher G Hoehne and Mikhail V Chester. “Optimizing plug-in electric vehicle and vehicle-to-grid charge scheduling to minimize carbon emissions”. In: *Energy* 115 (2016), pp. 646–657.
- [66] Samuel Pelletier, Ola Jabali, Gilbert Laporte, and Marco Veneroni. “Battery degradation and behaviour for electric vehicles: Review and numerical analyses of several models”. In: *Transportation Research Part B: Methodological* 103 (2017), pp. 158–187.
- [67] Sekyung Han, Soohee Han, and Hirohisa Aki. “A practical battery wear model for electric vehicle charging applications”. In: *Applied Energy* 113.C (2014), pp. 1100–1108.

- [68] Olivier Tremblay and Louis-A Dessaint. “Experimental validation of a battery dynamic model for EV applications”. In: *World Electric Vehicle Journal* 3 (2009), pp. 13–16.
- [69] Markus Einhorn, Fiorentino Valerio Conte, Christian Kral, and Jürgen Fleig. “Comparison, Selection, and Parameterization of Electrical Battery Models for Automotive Applications”. In: *IEEE Transactions on Power Electronics* 28.3 (Mar. 2013), pp. 1429–1437.
- [70] Bogdan-Adrian Enache, Emilian Lefter, and Constantin Stoica. “Comparative study for generic battery models used for electric vehicles”. In: May 2013, pp. 1–6.
- [71] Chengke Zhou, Kejun Qian, Malcolm Allan, and Wenjun Zhou. “Modeling of the cost of EV battery wear due to V2G application in power systems”. In: *IEEE Transactions on Energy Conversion* 26.4 (2011), pp. 1041–1050.
- [72] Duo Rick Shang and Guodong Sun. “Electricity-price arbitrage with plug-in hybrid electric vehicle: Gain or loss?” In: *Energy Policy* 95 (2016), pp. 402–410.
- [73] Dominik Pelzer, David Ciechanowicz, and Alois Knoll. “Energy arbitrage through smart scheduling of battery energy storage considering battery degradation and electricity price forecasts”. In: *2016 IEEE Innovative Smart Grid Technologies-Asia (ISGT-Asia)*. IEEE, 2016, pp. 472–477.
- [74] Kotub Uddin, Tim Jackson, Widanalage D Widanage, Gael Chouchelamane, Paul A Jennings, and James Marco. “On the possibility of extending the lifetime of lithium-ion batteries through optimal V2G facilitated by an integrated vehicle and smart-grid system”. In: *Energy* 133 (2017), pp. 710–722.
- [75] Alexander Kies. “Joint optimisation of arbitrage profits and battery life degradation for grid storage application of battery electric vehicles”. In: *Journal of Physics: Conference Series*. Vol. 977. IOP Publishing, 2018, p. 012005.

- [76] Florian Wankmüller, Prakash R. Thimmapuram, Kevin G. Gallagher, and Audun Botterud. “Impact of battery degradation on energy arbitrage revenue of grid-level energy storage”. In: *Journal of Energy Storage* 10 (Apr. 2017), pp. 56–66.
- [77] Ridoy Das, Yue Wang, Krishna Busawon, Ghanim Putrus, and Myriam Neaimeh. “Real-time multi-objective optimisation for electric vehicle charging management”. In: *Journal of Cleaner Production* 292 (2021), p. 126066.
- [78] Daniel Burmester, Ramesh Rayudu, Winston Seah, and Daniel Akinyele. “A review of nanogrid topologies and technologies”. en. In: *Renewable and Sustainable Energy Reviews* 67 (Jan. 2017), pp. 760–775.
- [79] Lexuan Meng, Eleonora Riva Sanseverino, Adriana Luna, Tomislav Dragicevic, Juan C. Vasquez, and Josep M. Guerrero. “Microgrid supervisory controllers and energy management systems: A literature review”. en. In: *Renewable and Sustainable Energy Reviews* 60 (July 2016), pp. 1263–1273.
- [80] Amrutha Raju Battula, Sandeep Vuddanti, and Surender Reddy Salkuti. “Review of Energy Management System Approaches in Microgrids”. en. In: *Energies* 14.17 (Jan. 2021), p. 5459.
- [81] Sadaqat Ali, Zhixue Zheng, Michel Aillerie, Jean-Paul Sawicki, Marie-Cécile Péra, and Daniel Hissel. “A Review of DC Microgrid Energy Management Systems Dedicated to Residential Applications”. en. In: *Energies* 14.14 (Jan. 2021), p. 4308.
- [82] Abdellatif Elmouatamid, Radouane Ouladsine, Mohamed Bakhouya, Najib El Kamoun, Mohammed Khaidar, and Khalid Zine-Dine. “Review of Control and Energy Management Approaches in Micro-Grid Systems”. en. In: *Energies* 14.1 (Jan. 2021), p. 168.
- [83] Fang Yang, Xianyong Feng, and Zhao Li. “Advanced Microgrid Energy Management System for Future Sustainable and Resilient Power Grid”. In: *IEEE Transactions on Industry Applications* 55.6 (Nov. 2019), pp. 7251–7260.

- [84] Muhammad Fahad Zia, Elhoussin Elbouchikhi, and Mohamed Benbouzid. “Microgrids energy management systems: A critical review on methods, solutions, and prospects”. en. In: *Applied Energy* 222 (July 2018), pp. 1033–1055.
- [85] Pavitra Sharma, Hitesh Dutt Mathur, Puneet Mishra, and Ramesh C. Bansal. “A critical and comparative review of energy management strategies for microgrids”. en. In: *Applied Energy* 327 (Dec. 2022), p. 120028.
- [86] Utpal Kumar Das, Kok Soon Tey, Mehdi Seyedmahmoudian, Saad Mekhilef, Moh Yamani Idna Idris, Willem Van Deventer, Bend Horan, and Alex Stojcevski. “Forecasting of photovoltaic power generation and model optimization: A review”. en. In: *Renewable and Sustainable Energy Reviews* 81 (Jan. 2018), pp. 912–928.
- [87] Sobrina Sobri, Sam Koohi-Kamali, and Nasrudin Abd. Rahim. “Solar photovoltaic generation forecasting methods: A review”. en. In: *Energy Conversion and Management* 156 (Jan. 2018), pp. 459–497.
- [88] Ismail Kaaya, Julián Ascencio-Vásquez, Ismail Kaaya, and Julián Ascencio-Vásquez. *Photovoltaic Power Forecasting Methods*. en. Publication Title: Solar Radiation - Measurement, Modeling and Forecasting Techniques for Photovoltaic Solar Energy Applications. IntechOpen, Apr. 2021.
- [89] A. Massi Pavan, S. Vergura, A. Mellit, and V. Lughì. “Explicit empirical model for photovoltaic devices. Experimental validation”. en. In: *Solar Energy* 155 (Oct. 2017), pp. 647–653.
- [90] A. Rezaee Jordehi. “Parameter estimation of solar photovoltaic (PV) cells: A review”. en. In: *Renewable and Sustainable Energy Reviews* 61 (Aug. 2016), pp. 354–371.
- [91] Maria Carmela Di Piazza, Massimiliano Luna, and Gianpaolo Vitale. “Dynamic PV Model Parameter Identification by Least-Squares Regression”. In: *IEEE Journal of Photovoltaics* 3.2 (Apr. 2013). Conference Name: IEEE Journal of Photovoltaics, pp. 799–806.

- [92] Shuijia Li, Wenyin Gong, and Qiong Gu. “A comprehensive survey on meta-heuristic algorithms for parameter extraction of photovoltaic models”. en. In: *Renewable and Sustainable Energy Reviews* 141 (May 2021), p. 110828.
- [93] Alberto Dolara, Sonia Leva, and Giampaolo Manzolini. “Comparison of different physical models for PV power output prediction”. en. In: *Solar Energy* 119 (Sept. 2015), pp. 83–99.
- [94] Giuseppina Ciulla, Valerio Lo Brano, Vincenzo Di Dio, and Giovanni Cipriani. “A comparison of different one-diode models for the representation of I–V characteristic of a PV cell”. en. In: *Renewable and Sustainable Energy Reviews* 32 (Apr. 2014), pp. 684–696.
- [95] Sofiane Kichou, Santiago Silvestre, Letizia Guglielminotti, Llanos Mora-López, and Emilio Muñoz-Cerón. “Comparison of two PV array models for the simulation of PV systems using five different algorithms for the parameters identification”. en. In: *Renewable Energy* 99 (Dec. 2016), pp. 270–279.
- [96] Meng Wang, Jinqing Peng, Yimo Luo, Zhicheng Shen, and Hongxing Yang. “Comparison of different simplistic prediction models for forecasting PV power output: Assessment with experimental measurements”. en. In: *Energy* 224 (June 2021), p. 120162.
- [97] Adel Mellit, Alessandro Massi Pavan, Emanuele Ogliari, Sonia Leva, and Vanni Lughi. “Advanced Methods for Photovoltaic Output Power Forecasting: A Review”. en. In: *Applied Sciences* 10.2 (Jan. 2020). Number: 2 Publisher: Multidisciplinary Digital Publishing Institute, p. 487.
- [98] Xiaoqiao Huang, Qiong Li, Yonghang Tai, Zaiqing Chen, Jun Zhang, Junsheng Shi, Bixuan Gao, and Wuming Liu. “Hybrid deep neural model for hourly solar irradiance forecasting”. en. In: *Renewable Energy* 171 (June 2021), pp. 1041–1060.
- [99] Alfredo Nespoli, Emanuele Ogliari, Sonia Leva, Alessandro Massi Pavan, Adel Mellit, Vanni Lughi, and Alberto Dolara.

- “Day-ahead photovoltaic forecasting: A comparison of the most effective techniques”. In: *Energies* 12.9 (2019), p. 1621.
- [100] Z. de Grève, J. Bottieau, D. Vangulick, A. Wautier, P.-D. Dapoz, A. Arrigo, J.-F. Toubeau, and F. Vallée. “Machine learning techniques for improving self-consumption in renewable energy communities”. English. In: *Energies* 13.18 (2020).
- [101] Jiaqi Qu, Zheng Qian, and Yan Pei. “Day-ahead hourly photovoltaic power forecasting using attention-based CNN-LSTM neural network embedded with multiple relevant and target variables prediction pattern”. en. In: *Energy* 232 (Oct. 2021), p. 120996.
- [102] Deniz Korkmaz. “SolarNet: A hybrid reliable model based on convolutional neural network and variational mode decomposition for hourly photovoltaic power forecasting”. en. In: *Applied Energy* 300 (Oct. 2021), p. 117410.
- [103] Adel Mellit and Alessandro Massi Pavan. “A 24-h forecast of solar irradiance using artificial neural network: Application for performance prediction of a grid-connected PV plant at Trieste, Italy”. In: *Solar Energy* 84.5 (2010), pp. 807–821.
- [104] Donghun Lee and Kwanho Kim. “PV power prediction in a peak zone using recurrent neural networks in the absence of future meteorological information”. en. In: *Renewable Energy* 173 (Aug. 2021), pp. 1098–1110.
- [105] Fermín Rodríguez, Alice Fleetwood, Ainhoa Galarza, and Luis Fontán. “Predicting solar energy generation through artificial neural networks using weather forecasts for microgrid control”. en. In: *Renewable Energy* 126 (Oct. 2018), pp. 855–864.
- [106] H.S. Hippert, C.E. Pedreira, and R.C. Souza. “Neural networks for short-term load forecasting: a review and evaluation”. In: *IEEE Transactions on Power Systems* 16.1 (Feb. 2001). Conference Name: IEEE Transactions on Power Systems, pp. 44–55.
- [107] Gholamreza Memarzadeh and Farshid Keynia. “Short-term electricity load and price forecasting by a new optimal LSTM-NN

- based prediction algorithm”. en. In: *Electric Power Systems Research* 192 (Mar. 2021), p. 106995.
- [108] Hesham K. Alfares and Mohammad Nazeeruddin. “Electric load forecasting: Literature survey and classification of methods”. In: *International Journal of Systems Science* 33.1 (Jan. 2002), pp. 23–34.
- [109] Arunesh Kumar Singh, Ibraheem, S. Khatoon, Md. Muazzam, and D. K. Chaturvedi. “Load forecasting techniques and methodologies: A review”. In: *2012 2nd International Conference on Power, Control and Embedded Systems*. Dec. 2012, pp. 1–10.
- [110] Ashraful Haque and Saifur Rahman. “Short-term electrical load forecasting through heuristic configuration of regularized deep neural network”. en. In: *Applied Soft Computing* 122 (June 2022), p. 108877.
- [111] Léonard Tschora, Erwan Pierre, Marc Plantevit, and Céline Robardet. “Electricity price forecasting on the day-ahead market using machine learning”. en. In: *Applied Energy* 313 (May 2022), p. 118752.
- [112] Wendong Yang, Shaolong Sun, Yan Hao, and Shouyang Wang. “A novel machine learning-based electricity price forecasting model based on optimal model selection strategy”. en. In: *Energy* 238 (Jan. 2022), p. 121989.
- [113] Rafał Weron. “Electricity price forecasting: A review of the state-of-the-art with a look into the future”. en. In: *International Journal of Forecasting* 30.4 (Oct. 2014), pp. 1030–1081.
- [114] Jakub Nowotarski and Rafał Weron. “Recent advances in electricity price forecasting: A review of probabilistic forecasting”. en. In: *Renewable and Sustainable Energy Reviews* 81 (Jan. 2018), pp. 1548–1568.
- [115] Deepak Singhal and K. S. Swarup. “Electricity price forecasting using artificial neural networks”. en. In: *International Journal of Electrical Power & Energy Systems* 33.3 (Mar. 2011), pp. 550–555.

- [116] Athanasios Ioannis Arvanitidis, Dimitrios Bargiotas, Dimitrios Kontogiannis, Athanasios Fevgas, and Miltiadis Alamaniotis. “Optimized Data-Driven Models for Short-Term Electricity Price Forecasting Based on Signal Decomposition and Clustering Techniques”. en. In: *Energies* 15.21 (Jan. 2022). Number: 21 Publisher: Multidisciplinary Digital Publishing Institute, p. 7929.
- [117] Intergovernmental Panel on Climate Change and Ottmar Edenhofer, eds. *Climate change 2014: mitigation of climate change: Working Group III contribution to the Fifth Assessment Report of the Intergovernmental Panel on Climate Change*. OCLC: ocn892580682. New York, NY: Cambridge University Press, 2014.
- [118] Ion V. Ion and Antoaneta Ene. “Evaluation of Greenhouse Gas Emissions from Reservoirs: A Review”. en. In: *Sustainability* 13.21 (Oct. 2021), p. 11621.
- [119] A. Levasseur, S. Mercier-Blais, Y.T. Prairie, A. Tremblay, and C. Turpin. “Improving the accuracy of electricity carbon footprint: Estimation of hydroelectric reservoir greenhouse gas emissions”. en. In: *Renewable and Sustainable Energy Reviews* 136 (Feb. 2021), p. 110433.
- [120] Daniel Nugent and Benjamin K. Sovacool. “Assessing the lifecycle greenhouse gas emissions from solar PV and wind energy: A critical meta-survey”. en. In: *Energy Policy* 65 (Feb. 2014), pp. 229–244.
- [121] Diptyaroop Maji, Ramesh K. Sitaraman, and Prashant Shenoy. “DACF: day-ahead carbon intensity forecasting of power grids using machine learning”. In: *Proceedings of the Thirteenth ACM International Conference on Future Energy Systems*. e-Energy '22. New York, NY, USA: Association for Computing Machinery, June 2022, pp. 188–192.
- [122] *Electricity Maps - Live 24/7 CO<sub>2</sub> emissions of electricity consumption*. en-US.
- [123] *Carbon Intensity UK*.

- [124] *US Power Sector Emissions*. en. text/html. Archive Location: <https://emissionsindex.org/> Publisher: CMU Power Sector Carbon Index. Nov. 2022.
- [125] *Tracking emissions in the US electricity system*.
- [126] Hannah Ritchie, Max Roser, and Pablo Rosado. “Energy”. In: *Our World in Data* (Oct. 2022).
- [127] Neeraj Dhanraj Bokde, Bo Tranberg, and Gorm Bruun Andresen. “Short-term CO2 emissions forecasting based on decomposition approaches and its impact on electricity market scheduling”. en. In: *Applied Energy* 281 (Jan. 2021), p. 116061.
- [128] Alasdair RW Bruce, Lyndon Ruff, James Kelloway, Fraser MacMillan, and Alex Rogers. “Carbon intensity forecast methodology”. In: *National Grid ESO: Warwick, UK*. 20 (2021).
- [129] Bo Tranberg, Olivier Corradi, Bruno Lajoie, Thomas Gibon, Iain Staffell, and Gorm Bruun Andresen. “Real-time carbon accounting method for the European electricity markets”. en. In: *Energy Strategy Reviews* 26 (Nov. 2019), p. 100367.
- [130] Nicolae Scarlat, Matteo Prussi, and Monica Padella. “Quantification of the carbon intensity of electricity produced and used in Europe”. en. In: *Applied Energy* 305 (Jan. 2022), p. 117901.
- [131] Roberto Turconi, Alessio Boldrin, and Thomas Astrup. “Life cycle assessment (LCA) of electricity generation technologies: Overview, comparability and limitations”. en. In: *Renewable and Sustainable Energy Reviews* 28 (Dec. 2013), pp. 555–565.
- [132] Jacques A. de Chalendar and Sally M. Benson. “A physics-informed data reconciliation framework for real-time electricity and emissions tracking”. en. In: *Applied Energy* 304 (Dec. 2021), p. 117761.
- [133] **Nicola Blasuttigh**, Hamzeh Beiranvand, Thiago Pereira, and Marco Liserre. “Comparative Study of Single-phase and Three-phase DAB for EV Charging Application”. In: *2022 24th European Conference on Power Electronics and Applications (EPE'22 ECCE Europe)*. Sept. 2022, pp. 1–9.

- [134] **Nicola Blasuttigh**, Hamzeh Beiranvand, Thiago Pereira, Simone Castellan, and Marco Liserre. “Efficiency trade-off-oriented analysis for the integration of dc-dc converter and battery pack in V2G applications”. In: *ECCE2022 - Energy Conversion Congress and Exposition, 2022*. Sept. 2022.
- [135] Hamzeh Beiranvand, **Nicola Blasuttigh**, Thiago Pereira, S.H. Noehren, H. Krueger, Alessandro Massi Pavan, and Marco Liserre. “ $\eta_{max}$ -Charging Strategy for Lithium-Ion Batteries of EVs in V2G Applications”. In: *ECCE2022 - Energy Conversion Congress and Exposition, 2022*. Sept. 2022.
- [136] Simone Castellan, **Nicola Blasuttigh**, Roberto Menis, Alessandro Massi Pavan, Mario Mezzarobba, and Giuseppe Buja. “Design and simulation of a vehicle-to-grid system”. In: *2020 6th International Conference on Electric Power and Energy Conversion Systems (EPECS)*. IEEE, 2020, pp. 69–74.
- [137] Chunhua Liu, KT Chau, Diyun Wu, and Shuang Gao. “Opportunities and challenges of vehicle-to-home, vehicle-to-vehicle, and vehicle-to-grid technologies”. In: *Proceedings of the IEEE* 101.11 (2013), pp. 2409–2427.
- [138] Hauke van Hoek, Markus Neubert, and Rik W De Doncker. “Enhanced modulation strategy for a three-phase dual active bridge—Boosting efficiency of an electric vehicle converter”. In: *IEEE Transactions on Power Electronics* 28.12 (2013), pp. 5499–5507.
- [139] Angshuman Sharma and Santanu Sharma. “Review of power electronics in vehicle-to-grid systems”. In: *Journal of Energy Storage* 21 (2019), pp. 337–361.
- [140] M Di Benedetto, A Lidozzi, L Solero, F Crescimbin, and S Bifaretti. “Hardware design of SiC-based Four-Port DAB Converter for Fast Charging Station”. In: *2020 IEEE Energy Conversion Congress and Exposition (ECCE)*. IEEE, 2020, pp. 1231–1238.
- [141] Rik WAA De Doncker, Deepakraj M Divan, and Mustansir H Kheraluwala. “A three-phase soft-switched high-power-density

- DC/DC converter for high-power applications”. In: *IEEE transactions on industry applications* 27.1 (1991), pp. 63–73.
- [142] Lucas Mondardo Cúnico, Zedequias Machado Alves, and André Luís Kirsten. “Efficiency-Optimized Modulation Scheme for Three-Phase Dual-Active-Bridge DC–DC Converter”. In: *IEEE Transactions on Industrial Electronics* 68.7 (2020), pp. 5955–5965.
- [143] Asier Garcia-Bediaga, Irma Villar, Alejandro Rujas, Ion Etxeberria-Otadui, and Alfred Rufer. “Analytical models of multiphase isolated medium-frequency DC–DC converters”. In: *IEEE Transactions on Power Electronics* 32.4 (2016), pp. 2508–2520.
- [144] Florian Krismer. “Modeling and optimization of bidirectional dual active bridge DC-DC converter topologies”. en. PhD thesis. ETH Zurich, 2010.
- [145] D Segaran, Donald Grahame Holmes, and Brendan Peter McGrath. “Comparative analysis of single and three-phase dual active bridge bidirectional DC-DC converters”. In: *2008 Australasian Universities Power Engineering Conference*. IEEE, 2008, pp. 1–6.
- [146] Takushi Jimichi, Murat Kaymak, and Rik. W. De Doncker. “Comparison of single-phase and three-phase dual-active bridge DC-DC converters with various semiconductor devices for offshore wind turbines”. In: *2017 IEEE 3rd International Future Energy Electronics Conference and ECCE Asia (IFEEC 2017 - ECCE Asia)*. June 2017, pp. 591–596.
- [147] Hauke van Hoek, Markus Neubert, Albert Kroeber, and Rik W. De Doncker. “Comparison of a single-phase and a three-phase dual active bridge with low-voltage, high-current output”. In: *2012 International Conference on Renewable Energy Research and Applications (ICRERA)*. Nov. 2012, pp. 1–6.
- [148] Ryo Haneda and Hirofumi Akagi. “Design and Performance of the 850-V 100-kW 16-kHz Bidirectional Isolated DC–DC Converter Using SiC-MOSFET/SBD H-Bridge Modules”. In: *IEEE*

*Transactions on Power Electronics* 35.10 (Oct. 2020), pp. 10013–10025.

- [149] Alberto Rodriguez Alonso, Javier Sebastian, Diego G Lamar, Marta M Hernando, and Aitor Vazquez. “An overall study of a Dual Active Bridge for bidirectional DC/DC conversion”. In: *2010 IEEE Energy Conversion Congress and Exposition*. IEEE, 2010, pp. 1129–1135.
- [150] Pugliese Sante. “Power Converters and Control Systems for DC Smart Grids and Smart Transformers Applications”. PhD thesis. Jan. 2018.
- [151] Zhe Zhang and Michael A. E. Andersen. “High frequency AC inductor analysis and design for dual active bridge (DAB) converters”. en. In: *2016 IEEE Applied Power Electronics Conference and Exposition (APEC)*. Long Beach, CA, USA: IEEE, Mar. 2016, pp. 1090–1095.
- [152] HARISH RAMAKRISHNAN. “Design Guide: TIDA-010054 Bi-Directional, Dual Active Bridge Reference Design for Level 3 Electric Vehicle Charging Stations”. In: *Texas instruments*. 2019.
- [153] Kenny George. “Design and Control of a Bidirectional Dual Active Bridge DC-DC Converter to Interface Solar, Battery Storage, and Grid-Tied Inverters”. In: (2015).
- [154] Elkin Edilberto Henao-Bravo, Carlos Andrés Ramos-Paja, Andrés Julián Saavedra-Montes, Daniel Gonzalez-Montoya, and Julian Sierra-Perez. “Design method of dual active bridge converters for photovoltaic systems with high voltage gain”. In: *Energies* 13.7 (2020), p. 1711.
- [155] Hamzeh Beiranvand, Esmael Rokrok, and Marco Liserre. “ $V_f$ -constrained  $\eta\rho$ -pareto optimisation of medium frequency transformers in ISOP-DAB converters”. en. In: *IET Power Electronics* 13.10 (Aug. 2020), pp. 1984–1994.
- [156] *Document Library | Wolfspeed*. en-us.

- [157] Hamzeh Beiranvand, Esmaeel Rorok, and Marco Liserre. “Theoretical Evaluation of Semiconductor Loss Components Behavior in ISOP-DAB Converters”. In: *2019 IEEE 13th International Conference on Compatibility, Power Electronics and Power Engineering (CPE-POWERENG)*. Apr. 2019, pp. 1–7.
- [158] Hafiz Abu Bakar Siddique. “The three-phase dual-active bridge converter family : modeling, analysis, optimization and comparison of two-level and three-level converter variants; 1. Auflage”. en. PhD thesis. RWTH Aachen University, 2019.
- [159] Bin Chen. “Analysis of Effect of Winding Interleaving on Leakage Inductance and Winding Loss of High Frequency Transformers”. en. In: *Journal of Electrical Engineering & Technology* 14.3 (May 2019), pp. 1211–1221.
- [160] K. Venkatachalam, Charles Sullivan, T. Abdallah, and H.E. Tacca. “Accurate prediction of ferrite core loss with nonsinusoidal waveforms using only Steinmetz parameters”. In: *2002 IEEE Workshop on Computers in Power Electronics, 2002. Proceedings*. July 2002, pp. 36–41.
- [161] N. Fritz, M. Rashed, S. Bozhko, F. Cuomo, and P. Wheeler. “Analytical modelling and power density optimisation of a single phase dual active bridge for aircraft application”. In: *The Journal of Engineering* (2019), pp. 3671–3676.
- [162] Irma Villar, Asier Garcia-Bediaga, Unai Viscarret, Ion Etxeberria-Otadui, and Alfred Rufer. “Proposal and validation of medium-frequency power transformer design methodology”. In: *2011 IEEE Energy Conversion Congress and Exposition*. Sept. 2011, pp. 3792–3799.
- [163] Irma Villar, Unai Viscarret, Ion Etxeberria-Otadui, and Alfred Rufer. “Global Loss Evaluation Methods for Nonsinusoidally Fed Medium-Frequency Power Transformers”. In: *IEEE Transactions on Industrial Electronics* 56.10 (Oct. 2009), pp. 4132–4140.
- [164] Hauke Van Hoek. “Design and operation considerations of three-phase dual activa bridge converters for low-power applications

- with wide voltage ranges”. en. PhD thesis. RWTH Aachen University, 2017.
- [165] Malik Ali Judge, Asif Khan, Awais Manzoor, and Hasan Ali Khattak. “Overview of smart grid implementation: Frameworks, impact, performance and challenges”. en. In: *Journal of Energy Storage* 49 (May 2022).
- [166] Christopher Betzin, Holger Wolfschmidt, and Matthias Luther. “Electrical operation behavior and energy efficiency of battery systems in a virtual storage power plant for primary control reserve”. en. In: *International Journal of Electrical Power & Energy Systems* 97 (Apr. 2018), pp. 138–145.
- [167] Nataly Bañol Arias, Seyedmostafa Hashemi, Peter Bach Andersen, Chresten Træholt, and Rubén Romero. “Distribution System Services Provided by Electric Vehicles: Recent Status, Challenges, and Future Prospects”. In: *IEEE Transactions on Intelligent Transportation Systems* 20.12 (Dec. 2019). Conference Name: IEEE Transactions on Intelligent Transportation Systems, pp. 4277–4296.
- [168] Elpiniki Apostolaki-Iosifidou, Paul Codani, and Willett Kempton. “Measurement of power loss during electric vehicle charging and discharging”. en. In: *Energy* 127 (May 2017), pp. 730–742.
- [169] Sajad Esmailirad, Ali Ghiasian, and Abdorreza Rabiee. “An Extended M/M/K/K Queueing Model to Analyze the Profit of a Multiservice Electric Vehicle Charging Station”. In: *IEEE Transactions on Vehicular Technology* 70.4 (Apr. 2021). Conference Name: IEEE Transactions on Vehicular Technology, pp. 3007–3016.
- [170] Md Mejbaul Haque, Peter Wolfs, Sanath Alahakoon, Bjorn Sturmborg, Mithulan Nadarajah, and Firuz Zare. “DAB Converter with Q Capability for BESS/EV Applications to Allow V2H/V2G Services”. In: *IEEE Transactions on Industry Applications* (2021), pp. 1–1.

- [171] F.M. Gatta, A. Geri, S. Lauria, M. Maccioni, and F. Palone. “Battery energy storage efficiency calculation including auxiliary losses: Technology comparison and operating strategies”. In: *2015 IEEE Eindhoven PowerTech*. June 2015, pp. 1–6.
- [172] Anton Kersten, Manuel Kuder, Emma Grunditz, Zeyang Geng, Evelina Wikner, Torbjörn Thiringer, Thomas Weyh, and Richard Eckerle. “Inverter and Battery Drive Cycle Efficiency Comparisons of CHB and MMSP Traction Inverters for Electric Vehicles”. In: *2019 21st European Conference on Power Electronics and Applications (EPE '19 ECCE Europe)*. Sept. 2019, P.1–P.12.
- [173] Armin Jafari, Mohammad Samizadeh Nikoo, Furkan Karakaya, and Elison Matioli. “Enhanced DAB for efficiency preservation using adjustable-tap high-frequency transformer”. In: *IEEE Transactions on Power Electronics* 35.7 (2019), pp. 6673–6677.
- [174] Iman Aghabali, Jennifer Bauman, Phillip J. Kollmeyer, Yawei Wang, Berker Bilgin, and Ali Emadi. “800-V Electric Vehicle Powertrains: Review and Analysis of Benefits, Challenges, and Future Trends”. In: *IEEE Transactions on Transportation Electrification* 7.3 (Sept. 2021), pp. 927–948.
- [175] Amirreza Poorfakhraei, Mehdi Narimani, and Ali Emadi. “A Review of Multilevel Inverter Topologies in Electric Vehicles: Current Status and Future Trends”. In: *IEEE Open Journal of Power Electronics* 2 (2021), pp. 155–170.
- [176] Christian Jung. “Power Up with 800-V Systems: The benefits of upgrading voltage power for battery-electric passenger vehicles”. In: *IEEE Electrification Magazine* 5.1 (Mar. 2017), pp. 53–58.
- [177] Andrew Meintz, Jiucui Zhang, Ram Vijayagopal, Cory Kreutzer, Shabbir Ahmed, Ira Bloom, Andrew Burnham, Richard B. Carlson, Fernando Dias, Eric J. Dufek, James Francfort, Keith Hardy, Andrew N. Jansen, Matthew Keyser, Anthony Markel, Christopher Michelbacher, Manish Mohanpurkar, Ahmad Pesaran, Don Scofield, Matthew Shirk, Thomas Stephens, and Tanvir Tanim.

- “Enabling fast charging – Vehicle considerations”. en. In: *Journal of Power Sources* 367 (Nov. 2017), pp. 216–227.
- [178] A Kersten. “Modular Battery Systems for Electric Vehicles based on Multilevel Inverter Topologies - Opportunities and Challenges”. en. PhD thesis. 2021.
- [179] Uwe Drofenik and Johann W. Kolar. “A General Scheme for Calculating Switching- and Conduction-Losses of Power Semiconductors in Numerical Circuit Simulations of Power Electronic Systems”. In: *in Proc. of the 2005 International Power Electronics Conf. (IPEC’05)*, pp. 4–88686.
- [180] Min Chen and Gabriel A Rincon-Mora. “Accurate electrical battery model capable of predicting runtime and IV performance”. In: *IEEE transactions on energy conversion* 21.2 (2006), pp. 504–511.
- [181] Yang Chen, Yan Ma, Peng Duan, and Hong Chen. “Estimation of State of Charge for Lithium-ion Battery Considering Effect of Aging and Temperature”. In: *2018 37th Chinese Control Conference (CCC)*. July 2018, pp. 8472–8477.
- [182] Lin Chen, Mo Zhang, Yunhui Ding, Shuxiao Wu, Yijing Li, Gang Liang, Hao Li, and Haihong Pan. “Estimation the internal resistance of lithium-ion-battery using a multi-factor dynamic internal resistance model with an error compensation strategy”. en. In: *Energy Reports* 7 (Nov. 2021), pp. 3050–3059.
- [183] Reinhold Koch. “On-line Electrochemical Impedance Spectroscopy for Lithium-Ion Battery Systems”. de. PhD thesis. Technische Universität München Fakultät für Elektrotechnik und Informationstechnik, 2017.
- [184] Oskar Theliander, Anton Kersten, Manuel Kuder, Weiji Han, Emma Grunditz, and Torbjorn Thiringer. “Battery Modeling and Parameter Extraction for Drive Cycle Loss Evaluation of a Modular Battery System for Vehicles Based on a Cascaded H-Bridge Multilevel Inverter”. In: *IEEE Transactions on Industry Applications* 56 (Sept. 2020).

- [185] Yuejiu Zheng, Minggao Ouyang, Xuebing Han, Languang Lu, and Jianqiu Li. “Investigating the error sources of the online state of charge estimation methods for lithium-ion batteries in electric vehicles”. en. In: *Journal of Power Sources* 377 (Feb. 2018), pp. 161–188.
- [186] Matthias Kuipers, Philipp Schröer, Thomas Nemeth, Hendrik Zappen, Alexander Blömeke, and Dirk Uwe Sauer. “An Algorithm for an Online Electrochemical Impedance Spectroscopy and Battery Parameter Estimation: Development, Verification and Validation”. en. In: *Journal of Energy Storage* 30 (Aug. 2020), p. 101517.
- [187] Alessandro Massi Pavan, Vanni Lughi, and Mariangela Scorrano. “Total Cost of Ownership of electric vehicles using energy from a renewable-based microgrid”. In: *2019 IEEE Milan PowerTech*. IEEE, 2019, pp. 1–6.
- [188] Murat Yilmaz and Philip T. Krein. “Review of the Impact of Vehicle-to-Grid Technologies on Distribution Systems and Utility Interfaces”. In: *IEEE Transactions on Power Electronics* 28.12 (Dec. 2013). Conference Name: IEEE Transactions on Power Electronics, pp. 5673–5689.
- [189] N. Z. Xu and C. Y. Chung. “Reliability Evaluation of Distribution Systems Including Vehicle-to-Home and Vehicle-to-Grid”. In: *IEEE Transactions on Power Systems* 31.1 (Jan. 2016). Conference Name: IEEE Transactions on Power Systems, pp. 759–768.
- [190] Yanchong Zheng, Songyan Niu, Yitong Shang, Ziyun Shao, and Linni Jian. “Integrating plug-in electric vehicles into power grids: A comprehensive review on power interaction mode, scheduling methodology and mathematical foundation”. en. In: *Renewable and Sustainable Energy Reviews* 112 (Sept. 2019), pp. 424–439.
- [191] Morris Brenna, Federica Foiadelli, and Michela Longo. “The exploitation of vehicle-to-grid function for power quality im-

- provement in a smart grid”. In: *IEEE Transactions on Intelligent Transportation Systems* 15.5 (2014), pp. 2169–2177.
- [192] HSVS Kumar Nunna, Swathi Battula, Suryanarayana Doolla, and Dipti Srinivasan. “Energy management in smart distribution systems with vehicle-to-grid integrated microgrids”. In: *IEEE Transactions on Smart Grid* 9.5 (2016), pp. 4004–4016.
- [193] Vítor Monteiro, J. G. Pinto, and João L. Afonso. “Improved vehicle-for-grid (iV4G) mode: Novel operation mode for EVs battery chargers in smart grids”. en. In: *International Journal of Electrical Power & Energy Systems* 110 (Sept. 2019), pp. 579–587.
- [194] Md Jan E Alam, Kashem M Muttaqi, and Danny Sutanto. “Effective utilization of available PEV battery capacity for mitigation of solar PV impact and grid support with integrated V2G functionality”. In: *IEEE Transactions on Smart Grid* 7.3 (2015), pp. 1562–1571.
- [195] Hasan Mehrjerdi and Elyas Rakhshani. “Vehicle-to-grid technology for cost reduction and uncertainty management integrated with solar power”. en. In: *Journal of Cleaner Production* 229 (Aug. 2019), pp. 463–469.
- [196] Shigenori Inoue and Hirofumi Akagi. “A Bidirectional DC–DC Converter for an Energy Storage System With Galvanic Isolation”. In: *IEEE Transactions on Power Electronics* 22.6 (Nov. 2007), pp. 2299–2306.
- [197] Chunting Mi, Hua Bai, Chongwu Wang, and Sonya Gargies. “Operation, design and control of dual H-bridge-based isolated bidirectional DC–DC converter”. In: *IET Power Electronics* 1.4 (2008), pp. 507–517.
- [198] GmbH dSPACE. *dSPACE GmbH*. en.
- [199] GmbH Plexim. “The simulation platform for power electronic systems”. In: *User Manual Version 4.4* (2019).
- [200] Hirofumi Akagi, Edson Hirokazu Watanabe, and Mauricio Aredes. *Instantaneous power theory and applications to power conditioning*. John Wiley & Sons, 2017.

- [201] Simone Castellan, Giuseppe Buja, and Roberto Menis. “Single-phase power line conditioning with unity power factor under distorted utility voltage”. In: *International Journal of Electrical Power & Energy Systems* 121 (2020), p. 106057.
- [202] Gregory L Plett. *Battery management systems, Volume I: Battery modeling*. Artech House, 2015.
- [203] Ana Cabrera-Tobar, Alessandro Massi Pavan, **Nicola Blasuttigh**, Giovanni Petrone, and Giovanni Spagnuolo. “Real time Energy Management System of a photovoltaic based e-vehicle charging station using Explicit Model Predictive Control accounting for uncertainties”. en. In: *Sustainable Energy, Grids and Networks* 31 (Sept. 2022), p. 100769.
- [204] Ana Cabrera-Tobar, **Nicola Blasuttigh**, Alessandro Massi Pavan, Vanni Lughì, and Giovanni Petrone. “Energy, environmental and economic analysis of a real photovoltaic based charging station”. en. In: *14th International Conference of the International Association for Mathematics and Computer in Simulation (ELECTRIMACS)*. 2022, p. 6.
- [205] Ana Cabrera-Tobar, **Nicola Blasuttigh**, Alessandro Massi Pavan, Vanni Lughì, Giovanni Petrone, and Giovanni Spagnuolo. “Energy scheduling and performance evaluation of a real e-vehicle charging station”. In: *Electronics* (2022).
- [206] **Nicola Blasuttigh**, Stefano Pastore, Mariangela Scorrano, Romeo Danielis, and Alessandro Massi Pavan. “Vehicle-to-Ski: A V2G Optimization-Based Cost and Environmental Analysis for a Ski Resort”. In: *Sustainable Energy Technologies and Assessments* (2022).
- [207] Simone Negri, Federico Giani, **Nicola Blasuttigh**, Alessandro Massi Pavan, Adel Mellit, and Enrico Tironi. “Combined model predictive control and ANN-based forecasters for jointly acting renewable self-consumers: An environmental and economical evaluation”. en. In: *Renewable Energy* (July 2022).

- [208] Samy Faddel, Ali T. Al-Awami, and M. A. Abido. “Fuzzy Optimization for the Operation of Electric Vehicle Parking Lots”. en. In: *Electric Power Systems Research* 145 (Apr. 2017), pp. 166–174.
- [209] Sayyad Nojavan, Majid Majidi, and Kazem Zare. “Performance improvement of a battery/PV/fuel cell/grid hybrid energy system considering load uncertainty modeling using IGDT”. en. In: *Energy Conversion and Management* 147 (Sept. 2017), pp. 29–39.
- [210] Alfredo Vaccaro, Marina Petrelli, and Alberto Berizzi. “Robust Optimization and Affine Arithmetic for Microgrid Scheduling under Uncertainty”. In: *2019 IEEE International Conference on Environment and Electrical Engineering and 2019 IEEE Industrial and Commercial Power Systems Europe (EEEIC / I&CPS Europe)*. 2019, pp. 1–6.
- [211] Carlos Bordons, Félix Garcia-Torres, and Miguel A. Ridao. *Model predictive control of microgrids*. eng. Advances in industrial control. Cham: Springer, 2020.
- [212] Jiefeng Hu, Yinghao Shan, Josep M. Guerrero, Adrian Ioinovici, Ka Wing Chan, and Jose Rodriguez. “Model predictive control of microgrids – An overview”. en. In: *Renewable and Sustainable Energy Reviews* 136 (Feb. 2021), p. 110422.
- [213] Alessandra Parisio, Evangelos Rikos, and Luigi Glielmo. “A Model Predictive Control Approach to Microgrid Operation Optimization”. In: *IEEE Transactions on Control Systems Technology* 22.5 (2014), pp. 1813–1827.
- [214] Jongwoo Choi, Jeong-In Lee, Il-Woo Lee, and Suk-Won Cha. “Robust PV-BESS Scheduling for a Grid With Incentive for Forecast Accuracy”. In: *IEEE Transactions on Sustainable Energy* 13.1 (2022), pp. 567–578.
- [215] Adhithya Ravichandran, Shahin Sirouspour, Pawel Malysz, and Ali Emadi. “A Chance-Constraints-Based Control Strategy for Microgrids With Energy Storage and Integrated Electric Vehi-

- cles”. In: *IEEE Transactions on Smart Grid* 9 (2018), pp. 346–359.
- [216] Alessandro Alessio and Alberto Bemporad. “A Survey on Explicit Model Predictive Control”. In: *Nonlinear Model Predictive Control: Towards New Challenging Applications*. Ed. by Lalo Magni, Davide Martino Raimondo, and Frank Allgöwer. Berlin, Heidelberg: Springer Berlin Heidelberg, 2009, pp. 345–369.
- [217] Iosif Pappas, Dustin Kenefake, Baris Burnak, Styliani Avraamidou, Hari S. Ganesh, Justin Katz, Nikolaos A. Diangelakis, and Efstratios N. Pistikopoulos. “Multiparametric Programming in Process Systems Engineering: Recent Developments and Path Forward”. In: *Frontiers in Chemical Engineering* 2 (2021).
- [218] Richard Oberdieck, Nikolaos A. Diangelakis, Ioana Nascu, Maria M. Papathanasiou, Muxin Sun, Styliani Avraamidou, and Efstratios N. Pistikopoulos. “On multi-parametric programming and its applications in process systems engineering”. In: *Chemical Engineering Research and Design* 116 (2016), pp. 61–82.
- [219] Siyuan Wang, Xuanding Wang, and Wenchuan Wu. “Cloud Computing and Local Chip-Based Dynamic Economic Dispatch for Microgrids”. In: *IEEE Transactions on Smart Grid* 11.5 (2020), pp. 3774–3784.
- [220] Georgios M. Kopanos and Efstratios N. Pistikopoulos. “Reactive Scheduling by a Multiparametric Programming Rolling Horizon Framework: A Case of a Network of Combined Heat and Power Units”. In: *Industrial & Engineering Chemistry Research* 53.11 (2014). \_eprint: <https://doi.org/10.1021/ie402393s>, pp. 4366–4386.
- [221] Ning Tian, Huazhen Fang, and Yebin Wang. “Real-Time Optimal Charging for Lithium-Ion Batteries via Explicit Model Predictive Control”. In: *2019 IEEE 28th International Symposium on Industrial Electronics (ISIE)*. 2019, pp. 2001–2006.
- [222] *Model Predictive Control Toolbox Documentation - MathWorks Italia*.

- [223] A. Bemporad, M. Morari, V. Dua, and E.N. Pistikopoulos. “The explicit solution of model predictive control via multiparametric quadratic programming”. In: *Proceedings of the 2000 American Control Conference. ACC (IEEE Cat. No.00CH36334)*. Vol. 2. 2000, 872–876 vol.2.
- [224] Martin Herceg, Michal Kvasnica, Colin Neil Jones, and Manfred Morari. “Multi-Parametric Toolbox 3.0”. In: *2013 European Control Conference (ECC)* (2013), pp. 502–510.
- [225] *ENTSO-E - European Network of Transmission System Operators for Electricity*.
- [226] Andrés Gersnoviez, María Brox, and Iluminada Baturone. “High-Speed and Low-Cost Implementation of Explicit Model Predictive Controllers”. In: *IEEE Transactions on Control Systems Technology* 27.2 (2019), pp. 647–662.
- [227] Nina M. Pestereva, Nina Yu Popova, and Lev M. Shagarov. “Modern Climate Change and Mountain Skiing Tourism: the Alps and the Caucasus”. eng. In: *European Researcher* 30 (2012), pp. 1602–1617.
- [228] Robert Steiger, Daniel Scott, Bruno Abegg, Marc Pons, and Carlo Aall. “A critical review of climate change risk for ski tourism”. In: *Current Issues in Tourism* 22.11 (July 2019), pp. 1343–1379.
- [229] Daniel Scott, Geoff McBoyle, and Alanna Minogue. “Climate change and Quebec’s ski industry”. In: *Global Environmental Change* 17.2 (2007), pp. 181–190.
- [230] Moncef Krarti. “Feasibility Study of Distributed Energy Generation at a Colorado Ski Resort”. In: *Energy Sustainability*. Vol. 56857. American Society of Mechanical Engineers, 2015, V002T16A002.
- [231] Tyler Farrell. “Evaluating the Potential for Renewable Energy Technology at US Ski Resorts”. In: (2019).

- [232] Enrico Cervi, Daniele Bosich, and Giorgio Sulligoi. “Assessment of an Alpine Microgrid in a Ski Resort for Integrating RES and Electrical Mobility”. In: *2020 IEEE International Conference on Environment and Electrical Engineering and 2020 IEEE Industrial and Commercial Power Systems Europe (EEEIC/I&CPS Europe)*. IEEE, 2020, pp. 1–6.
- [233] Muhammad Umair Mutarraf, Yajuan Guan, Luona Xu, Chun-Lien Su, Juan C. Vasquez, and Josep M. Guerrero. “Electric cars, ships, and their charging infrastructure – A comprehensive review”. en. In: *Sustainable Energy Technologies and Assessments* 52 (Aug. 2022), p. 102177.
- [234] Abdulgader Alsharif, Chee Wei Tan, Razman Ayop, Abdulha-keem Dobi, and Kwan Yiew Lau. “A comprehensive review of energy management strategy in Vehicle-to-Grid technology integrated with renewable energy sources”. en. In: *Sustainable Energy Technologies and Assessments* 47 (Oct. 2021), p. 101439.
- [235] Chitchai Srithapon, Prasanta Ghosh, Apirat Siritaratiwat, and Rongrit Chatthaworn. “Optimization of electric vehicle charging scheduling in urban village networks considering energy arbitrage and distribution cost”. In: *Energies* 13.2 (2020), p. 349.
- [236] Fady Y Melhem. “Optimization methods and energy management in smart grids”. PhD Thesis. Université Bourgogne Franche-Comté, 2018.
- [237] Masoud Honarmand, Alireza Zakariazadeh, and Shahram Jaidid. “Integrated scheduling of renewable generation and electric vehicles parking lot in a smart microgrid”. en. In: *Energy Conversion and Management* 86 (Oct. 2014), pp. 745–755.
- [238] Ning Wang, Bo Li, Yan Duan, and Shengling Jia. “A multi-energy scheduling strategy for orderly charging and discharging of electric vehicles based on multi-objective particle swarm optimization”. en. In: *Sustainable Energy Technologies and Assessments* 44 (Apr. 2021), p. 101037.

- [239] Zahra Azimi, Rahmat-Allah Hooshmand, and Soodabeh Soleymani. “Energy management considering simultaneous presence of demand responses and electric vehicles in smart industrial grids”. en. In: *Sustainable Energy Technologies and Assessments* 45 (June 2021), p. 101127.
- [240] Federica Laureri, L Puliga, Michela Robba, Federico Delfino, and G Odena Bulto. “An optimization model for the integration of electric vehicles and smart grids: Problem definition and experimental validation”. In: *2016 IEEE International Smart Cities Conference (ISC2)*. IEEE, 2016, pp. 1–6.
- [241] Olusola Bamisile, Sandra Obiora, Qi Huang, Eric C. Okonkwo, Oluseyi Olagoke, Akeem Shokanbi, and Ravinder Kumar. “Towards a sustainable and cleaner environment in China: Dynamic analysis of vehicle-to-grid, batteries and hydro storage for optimal RE integration”. en. In: *Sustainable Energy Technologies and Assessments* 42 (Dec. 2020), p. 100872.
- [242] Tom Terlouw, Tarek AlSkaif, Christian Bauer, and Wilfried van Sark. “Multi-objective optimization of energy arbitrage in community energy storage systems using different battery technologies”. In: *Applied Energy* 239 (2019), pp. 356–372.
- [243] Pietro Elia Campana, Luca Cioccolanti, Baptiste Francois, Jakub Jurasz, Yang Zhang, Maria Varini, Bengt Stridh, and Jinyue Yan. “Li-ion batteries for peak shaving, price arbitrage, and photovoltaic self-consumption in commercial buildings: A Monte Carlo Analysis”. In: *Energy Conversion and Management* 234 (2021), p. 113889.
- [244] Francesco Giordano, Francesco Arrigo, Cesar Diaz-Londono, Filippo Spertino, and Fredy Ruiz. “Forecast-Based V2G Aggregation Model for Day-Ahead and Real-Time Operations”. In: *2020 IEEE Power & Energy Society Innovative Smart Grid Technologies Conference (ISGT)*. IEEE, Feb. 2020, pp. 1–5.
- [245] *Private communication with operator*. 2021.
- [246] *Solar radiation | Copernicus*.

- [247] Robert Steiger and Marius Mayer. “Snowmaking and climate change”. In: *Mountain Research and Development* 28.3 (2008), pp. 292–298.
- [248] Ulrike Pröbstl, Alexandra Jiricka, and Florian Hindinger. *Renewable energy in winter sports destinations—desired, ignored or rejected?* na, 2011.
- [249] ARERA - *Autorità di Regolazione Energia Reti e Ambiente*.
- [250] Qin Yan, Bei Zhang, and Mladen Kezunovic. “Optimized operational cost reduction for an EV charging station integrated with battery energy storage and PV generation”. In: *IEEE Transactions on Smart Grid* 10.2 (2018), pp. 2096–2106.
- [251] Chiara Bordin, Harold Oghenetajiri Anuta, Andrew Crossland, Isabel Lascurain Gutierrez, Chris J Dent, and Daniele Vigo. “A linear programming approach for battery degradation analysis and optimization in offgrid power systems with solar energy integration”. In: *Renewable Energy* 101 (2017), pp. 417–430.
- [252] R. Marler and Jasbir Arora. “The weighted sum method for multi-objective optimization: New insights”. In: *Structural and Multidisciplinary Optimization* 41 (June 2010), pp. 853–862.
- [253] Abire O David and Irfan Al-Anbagi. “EVs for frequency regulation: cost benefit analysis in a smart grid environment”. In: *IET Electrical Systems in Transportation* 7.4 (2017), pp. 310–317.
- [254] Wouter Schram, Nico Brinkel, Gilbert Smink, Thijs van Wijk, and Wilfried van Sark. “Empirical Evaluation of V2G Round-trip Efficiency”. In: *2020 International Conference on Smart Energy Systems and Technologies (SEST)*. Sept. 2020, pp. 1–6.
- [255] Energy Strategy. *Smart Mobility Report 2020*. Tech. rep. 2020, p. 490.
- [256] ACI - *Automobile Club Italia*. it. Sept. 2022.
- [257] Istat - *Istituto Nazionale di Statistica*.
- [258] Wikipedia. *Electric car use by country*. en. Feb. 2022.

- [259] Mariangela Scorrano, Romeo Danielis, Stefano Pastore, Vanni Lughi, and Alessandro Massi Pavan. “Modeling the Total Cost of Ownership of an Electric Car Using a Residential Photovoltaic Generator and a Battery Storage Unit—An Italian Case Study”. en. In: *Energies* 13.10 (Jan. 2020), p. 2584.
- [260] *EPA finds median range of EVs dropped in 2021*. en.
- [261] *Battery Price Declines Slow Down in Latest Pricing Survey - Bloomberg*.
- [262] *Directive (EU) 2018/2001 of the European Parliament and of the Council of 11 December 2018 on the promotion of the use of energy from renewable sources*.
- [263] *Directive (EU) 2019/944 of the European Parliament and of the Council of 5 June 2019 on common rules for the internal market for electricity and amending Directive 2012/27/EU*. en. Doc ID: 32019L0944 Doc Sector: 3 Doc Title: Directive (EU) 2019/944 of the European Parliament and of the Council of 5 June 2019 on common rules for the internal market for electricity and amending Directive 2012/27/EU (recast) (Text with EEA relevance.) Doc Type: L Usr\_lan: en.
- [264] *Directive 2003/87/EC of the European Parliament and of the Council of 13 October 2003 establishing a system for greenhouse gas emission allowance trading within the Union and amending Council Directive 96/61/EC*. en. Doc ID: 02003L0087-20210101 Doc Sector: 0 Doc Title: Directive 2003/87/EC of the European Parliament and of the Council of 13 October 2003 establishing a system for greenhouse gas emission allowance trading within the Union and amending Council Directive 96/61/EC (Text with EEA relevance)Text with EEA relevance Doc Type: L Usr\_lan: en.
- [265] S. Cejka, D. Frieden, and D. Kitzmüller. “Implementation of self-consumption and energy communities in Austria’s and EU member states’ national law: A perspective on system integration and grid tariffs”. In: *CIREN 2021 - The 26th International*

*Conference and Exhibition on Electricity Distribution*. Vol. 2021. Sept. 2021, pp. 3254–3258.

- [266] Dorian Frieden, Andreas Tuerk, Josh Roberts, Stanislas D’Herbemont, Andrej F. Gubina, and Benjamin Komel. “Overview of emerging regulatory frameworks on collective self-consumption and energy communities in Europe”. In: *2019 16th International Conference on the European Energy Market (EEM)*. Sept. 2019, pp. 1–6.
- [267] Maria Luisa Di Silvestre, Mariano Giuseppe Ippolito, Eleonora Riva Sanseverino, Giuseppe Sciumè, and Antony Vasile. “Energy self-consumers and renewable energy communities in Italy: New actors of the electric power systems”. en. In: *Renewable and Sustainable Energy Reviews* 151 (Nov. 2021), p. 111565.
- [268] Joint Research Centre (European Commission), Andreas Uihlein, and Aura Caramizaru. *Energy communities: an overview of energy and social innovation*. eng. LU: Publications Office of the European Union, 2020.
- [269] Catalina Alexandra Sima, Claudia Laurenta Popescu, Mihai Octavian Popescu, Mariacristina Roscia, George Seritan, and Cornel Panait. “Techno-economic assessment of university energy communities with on/off microgrid”. en. In: *Renewable Energy* 193 (June 2022), pp. 538–553.
- [270] Lin Herenčić, Mislav Kirac, Hrvoje Keko, Igor Kuzle, and Ivan Rajšl. “Automated energy sharing in MV and LV distribution grids within an energy community: A case for Croatian city of Križevci with a hybrid renewable system”. en. In: *Renewable Energy* 191 (May 2022), pp. 176–194.
- [271] Giuseppe Barone, Giovanni Brusco, Daniele Menniti, Anna Pinnarelli, Gaetano Polizzi, Nicola Sorrentino, Pasquale Vizza, and Alessandro Burgio. “How Smart Metering and Smart Charging may Help a Local Energy Community in Collective Self-Consumption in Presence of Electric Vehicles”. en. In: *Energies* 13.16 (Jan. 2020), p. 4163.

- [272] G. Pontes Luz, M. C. Brito, J. M. C. Sousa, and S. M. Vieira. “Coordinating shiftable loads for collective photovoltaic self-consumption: A multi-agent approach”. en. In: *Energy* 229 (Aug. 2021), p. 120573.
- [273] Gianfranco Di Lorenzo, Sara Rotondo, Rodolfo Araneo, Giovanni Petrone, and Luigi Martirano. “Innovative power-sharing model for buildings and energy communities”. en. In: *Renewable Energy* 172 (July 2021), pp. 1087–1102.
- [274] Matteo Zatti, Matteo Moncecchi, Marco Gabba, Alberto Chiesa, Filippo Bovera, and Marco Merlo. “Energy Communities Design Optimization in the Italian Framework”. en. In: *Applied Sciences* 11.11 (Jan. 2021), p. 5218.
- [275] Edwin S. Pinto, Luis M. Serra, and Ana Lázaro. “Optimization of the design of polygeneration systems for the residential sector under different self-consumption regulations”. en. In: *International Journal of Energy Research* 44.14 (2020), pp. 11248–11273.
- [276] Idiano D’Adamo. “The profitability of residential photovoltaic systems. A new scheme of subsidies based on the price of CO<sub>2</sub> in a developed PV market”. In: *Social Sciences* 7.9 (2018), p. 148.
- [277] Alonzo Sierra Rodriguez, Tiago de Santana, Iain MacGill, N.j. Ekins-Daukes, and Angèle Reinders. “A feasibility study of solar PV-powered electric cars using an interdisciplinary modeling approach for the electricity balance, CO<sub>2</sub> emissions, and economic aspects: The cases of The Netherlands, Norway, Brazil, and Australia”. en. In: *Progress in Photovoltaics: Research and Applications* 28.6 (2020), pp. 517–532.
- [278] Andrea Bartolini, Francesco Carducci, Carlos Boigues Muñoz, and Gabriele Comodi. “Energy storage and multi energy systems in local energy communities with high renewable energy penetration”. en. In: *Renewable Energy* 159 (Oct. 2020), pp. 595–609.

- [279] James Rawlings, David Mayne, and Moritz Diehl. *Model predictive control: theory, computation and design*. 2nd edition. Santa Barbara: Nob Hill Publishing, LLC, 2020.
- [280] Marcelo M. Morato, José Vergara-Dietrich, Eugene A. Esparcia, Joey D. Ocon, and Julio E. Normey-Rico. “Assessing demand compliance and reliability in the Philippine off-grid islands with Model Predictive Control microgrid coordination”. en. In: *Renewable Energy* 179 (Dec. 2021), pp. 1271–1290.
- [281] Alessio La Bella, Stefano Raimondi Cominesi, Carlo Sandroni, and Riccardo Scattolini. “Hierarchical Predictive Control of Microgrids in Islanded Operation”. In: *IEEE Transactions on Automation Science and Engineering* 14.2 (Apr. 2017). Conference Name: IEEE Transactions on Automation Science and Engineering, pp. 536–546.
- [282] Alessio La Bella, Simone Negri, Riccardo Scattolini, and Enrico Tironi. “A Two-Layer Control Architecture for Islanded AC Microgrids with Storage Devices”. In: *2018 IEEE Conference on Control Technology and Applications (CCTA)*. Aug. 2018, pp. 1421–1426.
- [283] Pulkit Nahata, Alessio La Bella, Riccardo Scattolini, and Giancarlo Ferrari-Trecate. “Hierarchical Control in Islanded DC Microgrids With Flexible Structures”. In: *IEEE Transactions on Control Systems Technology* 29.6 (Nov. 2021). Conference Name: IEEE Transactions on Control Systems Technology, pp. 2379–2392.
- [284] J. M. Manzano, J. R. Salvador, J. B. Romaine, and L. Alvarado-Barrios. “Economic predictive control for isolated microgrids based on real world demand/renewable energy data and forecast errors”. en. In: *Renewable Energy* 194 (July 2022), pp. 647–658.
- [285] Chuanshen Wu, Shan Gao, Yu Liu, Tiancheng E. Song, and Haiteng Han. “A model predictive control approach in microgrid considering multi-uncertainty of electric vehicles”. en. In: *Renewable Energy* 163 (Jan. 2021), pp. 1385–1396.

- [286] Simone Negri, Federico Giani, Alessandro Massi Pavan, Adel Mellit, and Enrico Tironi. “MPC-based control for a stand-alone LVDC microgrid for rural electrification”. en. In: *Sustainable Energy, Grids and Networks* (May 2022), p. 100777.
- [287] A. Mellit, A. Massi Pavan, and V. Lughi. “Deep learning neural networks for short-term photovoltaic power forecasting”. en. In: *Renewable Energy* 172 (July 2021), pp. 276–288.
- [288] Mario A. Tovar Rosas, Miguel Robles Pérez, and E. Rafael Martínez Pérez. “Itineraries for charging and discharging a BESS using energy predictions based on a CNN-LSTM neural network model in BCS, Mexico”. en. In: *Renewable Energy* 188 (Apr. 2022), pp. 1141–1165.
- [289] Ali Agga, Ahmed Abbou, Moussa Labbadi, and Yassine El Houm. “Short-term self consumption PV plant power production forecasts based on hybrid CNN-LSTM, ConvLSTM models”. en. In: *Renewable Energy* 177 (Nov. 2021), pp. 101–112.
- [290] Kacem Gairaa, Cyril Voyant, Gilles Notton, Saïd Benkaciali, and Mawloud Guermoui. “Contribution of ordinal variables to short-term global solar irradiation forecasting for sites with low variabilities”. en. In: *Renewable Energy* 183 (Jan. 2022), pp. 890–902.
- [291] Arkadiusz Jędrzejewski, Jesus Lago, Grzegorz Marcjasz, and Rafał Weron. “Electricity Price Forecasting: The Dawn of Machine Learning”. In: *IEEE Power and Energy Magazine* 20.3 (May 2022), pp. 24–31.
- [292] Marin Cerjan, Ivana Krželj, Marko Vidak, and Marko Delimar. “A literature review with statistical analysis of electricity price forecasting methods”. In: *Eurocon 2013*. July 2013, pp. 756–763.
- [293] Noah Daniel Pflugradt. “Modellierung von Wasser und Energieverbräuchen in Haushalten”. ger. PhD thesis. Aug. 2016.
- [294] *Load Profile Generator*.

- [295] Aníbal de Almeida, Carlos Patrao, João Fong, Rui Araújo, Urbano Nunes, Luc Rivet, Urs Lindegger, Maurizio Nanetti, Walter Cariani, Antonio Disi, Laura Manduzio, Claudio Viola, Simon Hirzel, Elisabeth Dütschke, Julia Oberschmidt, Tobias Fleiter, Tadeusz Skoczkowski, Arkadiusz Węglarz, Ryszard Zwierchanowski, and Krzysztof Kisiel. *E4 - Energy Efficient Elevators and Escalators (Technical Report)*. Mar. 2010.
- [296] *PVGIS Photovoltaic Geographical Information System*. en.
- [297] Antonio Caputo. *Fattori di emissione atmosferica di gas a effetto serra nel settore elettrico nazionale e nei principali Paesi Europei*. Tech. rep. 317/2020. ISPRA, 2020.
- [298] *Gli schemi di Autoconsumo Collettivo e le Comunità dell'Energia*. it-IT.
- [299] *Gurobi - The Fastest Solver - Gurobi*.
- [300] *CPLEX Optimizer - Italia | IBM*.
- [301] *YALMIP*. en.
- [302] N. K. Sinha and Madan M. Gupta, eds. *Soft computing and intelligent systems: theory and applications*. Academic Press series in engineering. San Diego: Academic Press, 2000.
- [303] ROBERT Hecht-nielsen. “III.3 - Theory of the Backpropagation Neural Network\*\*Based on “nonindent” by Robert Hecht-Nielsen, which appeared in Proceedings of the International Joint Conference on Neural Networks 1, 593–611, June 1989. © 1989 IEEE.” en. In: *Neural Networks for Perception*. Ed. by Harry Wechsler. Academic Press, Jan. 1992, pp. 65–93.
- [304] Jorge J Moré. “The Levenberg-Marquardt algorithm: implementation and theory”. In: *Numerical analysis*. Springer, 1978, pp. 105–116.
- [305] SN Sivanandam and SN Deepa. *Introduction to neural networks using Matlab 6.0*. Tata McGraw-Hill Education, 2006.

- [306] Ilaria Bendato, Andrea Bonfiglio, Massimo Brignone, Federico Delfino, Fabio Pampararo, and Renato Procopio. “A real-time Energy Management System for the integration of economical aspects and system operator requirements: Definition and validation”. en. In: *Renewable Energy* 102 (Mar. 2017), pp. 406–416.
- [307] *ARERA - Condizioni economiche per i clienti del mercato tutelato.*
- [308] Domenico Mazzeo. “Nocturnal electric vehicle charging interacting with a residential photovoltaic-battery system: a 3E (energy, economic and environmental) analysis”. en. In: *Energy* 168 (Feb. 2019), pp. 310–331.

## ABOUT THE AUTHOR

Nicola Blasuttigh was born in Cividale del Friuli (Italy) on July 26th 1991. He received the B.Sc. degree in Information Engineering in 2015 and the M.Sc. degree in Electrical and Control Systems Engineering in 2019, both from the University of Trieste (Italy). He is currently a PhD student of the Department of Engineering and Architecture at the University of Trieste. His research interests include power converters, photovoltaic systems and microgrids management with renewable energy and electric vehicle integration.



# LIST OF PUBLICATIONS

## JOURNAL PUBLICATIONS

Simone Negri, Federico Giani, **Nicola Blasuttigh**, Alessandro Massi Pavan, Adel Mellit, and Enrico Tironi. “Combined model predictive control and ANN-based forecasters for jointly acting renewable self-consumers: An environmental and economical evaluation”. en. In: *Renewable Energy* (July 2022)

Ana Cabrera-Tobar, Alessandro Massi Pavan, **Nicola Blasuttigh**, Giovanni Petrone, and Giovanni Spagnuolo. “Real time Energy Management System of a photovoltaic based e-vehicle charging station using Explicit Model Predictive Control accounting for uncertainties”. en. In: *Sustainable Energy, Grids and Networks* 31 (Sept. 2022), p. 100769

**Nicola Blasuttigh**, Stefano Pastore, Mariangela Scorrano, Romeo Danielis, and Alessandro Massi Pavan. “Vehicle-to-Ski: A V2G Optimization-Based Cost and Environmental Analysis for a Ski Resort”. In: *Sustainable Energy Technologies and Assessments* (2022)

Ana Cabrera-Tobar, **Nicola Blasuttigh**, Alessandro Massi Pavan, Vanni Lughì, Giovanni Petrone, and Giovanni Spagnuolo. “Energy scheduling and performance evaluation of a real e-vehicle charging station”. In: *Electronics* (2022)

## CONFERENCE PUBLICATIONS

Simone Castellan, **Nicola Blasuttigh**, Roberto Menis, Alessandro Massi Pavan, Mario Mezzarobba, and Giuseppe Buja. “Design

and simulation of a vehicle-to-grid system”. In: *2020 6th International Conference on Electric Power and Energy Conversion Systems (EPECS)*. IEEE, 2020, pp. 69–74

Mario Mezzarobba, Alberto Tassarolo, **Nicola Blasuttigh**, Alessandro Massi Pavan, Simone Castellan, and Stefano Pastore. “Technologies for Electric Vehicle Utilization for Electric Power Optimal Management”. In: *2021 AEIT International Conference on Electrical and Electronic Technologies for Automotive (AEIT AUTOMOTIVE)*. Nov. 2021, pp. 1–6

**Nicola Blasuttigh**, Hamzeh Beiranvand, Thiago Pereira, and Marco Liserre. “Comparative Study of Single-phase and Three-phase DAB for EV Charging Application”. In: *2022 24th European Conference on Power Electronics and Applications (EPE’22 ECCE Europe)*. Sept. 2022, pp. 1–9

**Nicola Blasuttigh**, Hamzeh Beiranvand, Thiago Pereira, Simone Castellan, and Marco Liserre. “Efficiency trade-off-oriented analysis for the integration of dc-dc converter and battery pack in V2G applications”. In: *ECCE2022 - Energy Conversion Congress and Exposition, 2022*. Sept. 2022

Hamzeh Beiranvand, **Nicola Blasuttigh**, Thiago Pereira, S.H. Noehren, H. Krueger, Alessandro Massi Pavan, and Marco Liserre. “ $\eta_{max}$ -Charging Strategy for Lithium-Ion Batteries of EVs in V2G Applications”. In: *ECCE2022 - Energy Conversion Congress and Exposition, 2022*. Sept. 2022

Ana Cabrera-Tobar, **Nicola Blasuttigh**, Alessandro Massi Pavan, Vanni Lughì, and Giovanni Petrone. “Energy, environmental and economic analysis of a real photovoltaic based charging station”. en. In: *14th International Conference of the International Association for Mathematics and Computer in Simulation (ELECTRIMACS)*. 2022, p. 6

## ACKNOWLEDGEMENTS

The doctoral experience has been challenging but has allowed me to have some unique experiences. In these few lines I would like to thank the amazing people who supported me and those with whom I had the pleasure to work.

First of all I would like to thank my supervisor, Prof. Thomas Parisini who, despite everything, constantly supported and encouraged me on this journey by always giving me good advice and positivity, despite my cosmic pessimism.

Special thanks to my second supervisor, Prof. Alessandro Massi Pavan, who gave me the opportunity to study amazing topics, who supported me from a research and personal point of view, and who was able to look forward by creating unique opportunities that gave a direction to this path and work. Thank you.

Also thanks to Prof. Simone Castellan for his valuable advice and contributions in some of the results I have obtained.

I could not omit to thank Prof. Marco Liserre, who hosted me in Kiel in his large "family" where I was welcomed by amazing people with whom I immediately bonded. In particular, Hamzeh Beiranvand and Thiago Pereira for their time, support in research and advice for the future. Thanks to all the pasta friends, Federico, Clara, Riccardo (S. & M.), Emilio, Luca, Giuseppe, Xiang, Francisco and all the scientific team and staff.

Special thanks to Sante. We shared work, experiments and ideas but also pizzas, philosophical discussions and far too long and cold bike rides. I wish you all the best.

Thanks to Erica, Cestil, Slejko and Marco M., colleagues but above all friends who have always helped me in my time of need by giving me advice, suggestions and support during this journey.

Thanks to the (now former) Branco, the Azzalini-Cisottos family, Giulia, Edo and to all the friends with whom I spent fun and chilling moments outside the university.

My biggest thanks goes to my parents, Sofia and Giovanni, without whom I would not have reached this achievement. Super thanks also to the remaining part of the family, Anna, Simone and the little Bianca, because you have always been there. This dissertation is for all of you.

Last but not least, I would like to thank my girlfriend Chiara, the woman of my life, to whom this dissertation is dedicated. For always being by my side, for being there for me during these tough years, for your love and for making every day special.

Nicola